



NRL/MR/7320--07-9019

# Validation Test Report for the $1/8^\circ$ Global Navy Coastal Ocean Model Nowcast/Forecast System

CHARLIE N. BARRON  
A. BIROL KARA  
ROBERT C. RHODES  
CLARK ROWLEY  
LUCY F. SMEDSTAD

*Ocean Dynamics and Prediction Branch  
Oceanography Division*

January 24, 2007

Approved for public release; distribution is unlimited.

# REPORT DOCUMENTATION PAGE

*Form Approved*  
*OMB No. 0704-0188*

Public reporting burden for this collection of information is estimated to average 1 hour per response, including the time for reviewing instructions, searching existing data sources, gathering and maintaining the data needed, and completing and reviewing this collection of information. Send comments regarding this burden estimate or any other aspect of this collection of information, including suggestions for reducing this burden to Department of Defense, Washington Headquarters Services, Directorate for Information Operations and Reports (0704-0188), 1215 Jefferson Davis Highway, Suite 1204, Arlington, VA 22202-4302. Respondents should be aware that notwithstanding any other provision of law, no person shall be subject to any penalty for failing to comply with a collection of information if it does not display a currently valid OMB control number. **PLEASE DO NOT RETURN YOUR FORM TO THE ABOVE ADDRESS.**

<b>1. REPORT DATE (DD-MM-YYYY)</b> 24-01-2007		<b>2. REPORT TYPE</b> Memorandum Report		<b>3. DATES COVERED (From - To)</b>	
<b>4. TITLE AND SUBTITLE</b>  Validation Test Report for the 1/8° Global Navy Coastal Ocean Model Nowcast/Forecast System				<b>5a. CONTRACT NUMBER</b>	
				<b>5b. GRANT NUMBER</b>	
				<b>5c. PROGRAM ELEMENT NUMBER</b> PE0603207N	
<b>6. AUTHOR(S)</b>  Charlie N. Barron, A. Birol Kara, Robert C. Rhodes, Clark Rowley, and Lucy F. Smedstad				<b>5d. PROJECT NUMBER</b>	
				<b>5e. TASK NUMBER</b>	
				<b>5f. WORK UNIT NUMBER</b> 73-5091-17-5	
<b>7. PERFORMING ORGANIZATION NAME(S) AND ADDRESS(ES)</b>  Naval Research Laboratory Oceanography Division Stennis Space Center, MS 39529-5004				<b>8. PERFORMING ORGANIZATION REPORT NUMBER</b>  NRL/MR/7320--07-9019	
<b>9. SPONSORING / MONITORING AGENCY NAME(S) AND ADDRESS(ES)</b>  Office of Naval Research One Liberty Center 875 North Randolph Street Arlington, VA 22203-1995				<b>10. SPONSOR / MONITOR'S ACRONYM(S)</b>  SPAWAR	
				<b>11. SPONSOR / MONITOR'S REPORT NUMBER(S)</b>	
<b>12. DISTRIBUTION / AVAILABILITY STATEMENT</b>  Approved for public release; distribution is unlimited.					
<b>13. SUPPLEMENTARY NOTES</b>					
<b>14. ABSTRACT</b>  The global Naval Coastal Ocean Model (NCOM) is a 1/8° global application of NCOM developed by the Naval Research Laboratory (NRL) for use at the Naval Oceanographic Office (NAVOCEANO) as a part of an assimilative ocean model nowcast/forecast system. Global NCOM is the first operational global ocean model that has sufficient resolution to be eddy-permitting. Global NCOM supports predictions of ocean currents, temperatures, salinity, sea surface height, and sound speed both directly and by providing initial and boundary conditions for higher-resolution nested ocean models. The forecast system addresses Navy requirements for Numerical Modeling (METOC 9801), High Resolution Surface and Subsurface Currents (METOC 9308), Littoral Salinity Prediction (METOC 9902), and Air-Sea Drift Prediction (METOC 9115). This validation test report describes global NCOM, its use in an assimilative forecast system, and evaluation of assimilative and non-assimilative products using independent climatologies and observations.					
<b>15. SUBJECT TERMS</b> NCOM      Global ocean model      Ocean transport MODAS      Ocean temperature					
<b>16. SECURITY CLASSIFICATION OF:</b>			<b>17. LIMITATION OF ABSTRACT</b>	<b>18. NUMBER OF PAGES</b>	<b>19a. NAME OF RESPONSIBLE PERSON</b> Charlie Barron
<b>a. REPORT</b> Unclassified	<b>b. ABSTRACT</b> Unclassified	<b>c. THIS PAGE</b> Unclassified			UL

# CONTENTS

<b>1. INTRODUCTION .....</b>	<b>1</b>
<b>2. SYSTEM COMPONENTS .....</b>	<b>3</b>
<b>Navy Coastal Ocean Model .....</b>	<b>3</b>
<b>NCOM Data Assimilation.....</b>	<b>6</b>
<b>NCOM River Database.....</b>	<b>7</b>
<b>3. TESTING RESULTS .....</b>	<b>9</b>
<b>Experiments .....</b>	<b>9</b>
<b>Global Means .....</b>	<b>9</b>
<i>Atlantic Hemisphere .....</i>	<i>10</i>
<i>Indian Hemisphere.....</i>	<i>10</i>
<i>Pacific Hemisphere.....</i>	<i>11</i>
<b>Frontal Location,Eddy Kinetic Energy, and SSH Variability.....</b>	<b>11</b>
<i>Gulf Stream.....</i>	<i>12</i>
<i>Kuroshio .....</i>	<i>13</i>
<i>Indian Ocean .....</i>	<i>14</i>
<i>South China Sea.....</i>	<i>15</i>
<b>SSH .....</b>	<b>16</b>
<b>Upper Ocean Buoy Time Series .....</b>	<b>20</b>
<b>SST .....</b>	<b>20</b>

<b>Temperature Profiles .....</b>	<b>22</b>
<b>Mixed Layer Depth .....</b>	<b>23</b>
<b>Drifters .....</b>	<b>24</b>
<b>Current Sections.....</b>	<b>25</b>
<i>Western Atlantic.....</i>	<i>25</i>
<i>Western Pacific.....</i>	<i>26</i>
<i>Equatorial Pacific.....</i>	<i>26</i>
<b>Transports.....</b>	<b>27</b>
<b>Forecasts.....</b>	<b>27</b>
<b>Event Comparisons .....</b>	<b>29</b>
<i>Kuroshio Extension.....</i>	<i>29</i>
<i>Arabian Sea .....</i>	<i>29</i>
<i>Persian Gulf.....</i>	<i>30</i>
<i>Oregon coast.....</i>	<i>30</i>
<b>4. BOUNDARY CONDITIONS .....</b>	<b>32</b>
<b>    Regridding.....</b>	<b>32</b>
<b>    Tides.....</b>	<b>32</b>
<i>General Tide Products.....</i>	<i>32</i>
<i>Tides for SWAFS boundary conditions .....</i>	<i>33</i>
<i>Adding tides for regional solutions.....</i>	<i>33</i>
<b>    Evaluation .....</b>	<b>34</b>
<i>Regional tide solution .....</i>	<i>34</i>

<i>SWAFS boundary conditions</i> .....	34
<b>Other Applications</b> .....	<b>36</b>
<i>Nested or Relocatable NCOM</i> .....	36
<b>5. SUMMARY, CONCLUSIONS AND RECOMMENDATIONS</b> .....	<b>37</b>
<b>6. ACKNOWLEDGEMENTS</b> .....	<b>41</b>
<b>7. REFERENCES</b> .....	<b>42</b>
<b>8. TABLE OF ACRONYMS</b> .....	<b>48</b>

# VALIDATION TEST REPORT FOR THE 1/8° GLOBAL NAVY COASTAL OCEAN MODEL NOWCAST/FORECAST SYSTEM

## 1. INTRODUCTION

One of the primary concerns driving the development of U.S. Navy global models has been improving performance and nesting support in shelf and nearshore regions with short notice applicability anywhere on the globe. A global implementation of the Navy Coastal Ocean Model (NCOM) is a product of the effort to meet this need. The 1/8° Global NCOM has been developed at the Naval Research Laboratory (NRL) for transition to operations at the Naval Oceanographic Office (NAVOCEANO) (Barron *et al.*, 2003). NCOM itself (Martin, 2000) has been under development at NRL since 1998 as an upgrade to NRL's Sigma Z-level Model (SZM; Martin *et al.*, 1998).

An effort to develop and transition a global nowcast/forecast system based on a global version of NCOM began in 1999. NCOM is the final transition of the NRL baseline global system that was a progression of planned ocean analysis and forecast systems delivered for Navy operations (Rhodes *et al.*, 2002). This began in FY99 with an ocean analysis capability, the Modular Ocean Data Assimilation System (MODAS; Fox *et al.*, 2002b), which was followed in FY01 with the delivery of the 1/16° global Navy Layered Ocean Model (NLOM; Smedstad *et al.*, 2003) with the required resolution to properly resolve mesoscale ocean dynamics. The baseline system has been completed by the delivery of a 1/8° global version of the NCOM. The NCOM component provides higher vertical resolution in the mixed layer for improved upper-ocean prediction and boundary conditions for higher resolution coastal models. In joining the operational model suite at NAVOCEANO, NCOM extends prognostic model coverage to the global ocean, including coastal regions (with at-rest depth maintained at a minimum of 5 m) and the Arctic and southern oceans. This baseline system provides the Navy with the first global ocean analysis/prediction capability for fleet support. It is also a contribution to the operational phase of the multi-national Global Ocean Data Assimilation Experiment (GODAE; International GODAE Steering Team, 2000).

Global NCOM products benefit a variety of oceanographic applications. Its standard daily output provides a medium-resolution (midlatitude nominally 14 km or 1/8° latitude) ocean nowcast/forecast capability for 3 to 5 days. It is a source of boundary conditions for nested high-resolution fixed and relocatable coastal forecasting systems. These relocatable systems contain models that can rapidly be set up and run with reasonable ease and high fidelity in any region of the world's oceans. Fixed and relocatable nested systems within global NCOM have been configured with one or more sub-nests with horizontal resolutions varying from 7 km to 1 km or less (Shulman *et al.*, 2004; Whitehouse *et al.*, 2005). Global NCOM's relatively high vertical resolution and options for using more sophisticated surface mixed layer formulation have the potential to improve upper ocean nowcasts by allowing the cycling of NCOM forecasts of sea surface temperature (SST) and mixed-layer depth (MLD) with the MODAS or other SST analysis systems. In a daily cycling system, NCOM 24-hour forecasts would serve as the initial analysis fields, replacing the 24-hour persistence of the prior analysis. Surface current nowcasts

and forecasts from NCOM may support search and rescue operations and optimum track ship routing. New global NCOM capabilities under development include hosting a nested Arctic ice model and providing the ocean portion of a coupled air-ocean forecast system.

Studies performed by NRL evaluate NCOM performance for upper ocean nowcast and forecast skill. The skill assessment provides measures of performance and model error that can be used to improve the real-time assimilation and provide a baseline for future upgrades to the global modeling system. This skill assessment is performed by differencing various forecasts with analyses that correspond to the forecasted times. These assessments have identified present limitations, *e.g.*, an overall cold SST bias, slated to be addressed in future upgrades.

This report discusses the various system components of NCOM and some of the validation results for the NCOM system. The model was spun up from rest with climatological initial conditions and forcing for six years. It was then integrated in assimilative mode for one year before beginning the validation period. During the spin-up phase, global rivers were added and various parameters were initially tuned. For the model running in a non-assimilative simulation mode, there are comparisons including mean sea surface height (SSH) and kinetic energy (KE), SST, mixed layer depth, and sea surface salinity (SSS) with time series from tide gauge data, buoy data and Pathfinder SST data. In the assimilative model runs, SSH comparisons with global tide gauge sea level data that the model does not assimilate and SST comparisons with similarly unassimilated buoy data are shown. Also, nowcast positions of major fronts and eddies from NCOM are compared to NAVOCEANO frontal analysis products and ocean color data. Validations of global SST forecasts are discussed. Recently published journal articles provide additional information and discussion the configuration and validation of global NCOM (Barron *et al.*, 2004; Barron *et al.*, 2006; Kara *et al.*, 2006).

## 2. SYSTEM COMPONENTS

### Navy Coastal Ocean Model

The physics and numerics of NCOM (Martin, 2000), are based largely on the Princeton Ocean Model (POM) as described in Blumberg and Mellor (1987), with some aspects from SZM (Martin *et al.*, 1998), and with some additional features. Detailed descriptions of the controlling equations and numerical implementations are given in Barron *et al.* (2006).

NCOM has a free surface and is based on the primitive equations and the hydrostatic, Boussinesq, and incompressible approximations. Surface boundary conditions for NCOM are wind stress for the momentum equations, surface heat flux for the temperature equation, and effective surface salt flux for the salinity equation. In the operational global NCOM these are interpolated from fields produced by the Navy Operational Global Atmospheric Prediction System (NOGAPS; Rosmond *et al.*, 2002) provided by the Fleet Numerical Meteorology and Oceanography Center (FNMOC). The bottom boundary conditions are the bottom drag for the momentum equations, which is parameterized by a quadratic drag law, and zero flux for the temperature and salinity equations.

NCOM can be forced directly with new surface heat fluxes rather than recalculating the surface turbulent fluxes from the bulk formulae. However, in such cases strong SST relaxation is usually required, a common feature as in other ocean general circulation models. In NCOM, the relaxation is incorporated into modification of the latent and sensible heat fluxes. While this approach reduces nowcast SST error, damping on the evolution of forecast SST or SST variability may be too strong under such a forcing scheme. Thus it will be difficult to assess important SST forcing mechanisms uniquely in time and space.

Horizontal mixing coefficients are calculated with the Smagorinsky (1963) scheme or a grid-cell Reynolds number scheme where the mixing coefficients are determined from a specified grid-cell Reynolds number. Minimum values for the coefficients are specified for both schemes. Vertical mixing coefficients are calculated using the Mellor-Yamada Level 2 (Mellor and Yamada, 1974) or Level 2.5 (Mellor and Yamada, 1982) turbulence models. The Level 2 model can optionally include the Richardson-number-based mixing enhancement scheme of Large *et al.* (1994), which provides for weak mixing at the edge of a turbulent boundary layer for Richardson numbers above the normal critical value of about 0.25 up to a value of 0.7. For the Level 2.5 scheme, the surface flux of turbulent kinetic energy is specified as in Craig and Banner (1994). The global NCOM system in this study utilizes Smagorinsky horizontal mixing and Mellor-Yamada Level 2 vertical mixing with the Large *et al.* (1994) enhancement. Two density options are available in NCOM 2.3: the Friedrich and Levitus (F-L) (1972) polynomial approximation of the equation of state, and the adaptation by Mellor (1991) of the United Nations Educational Scientific and Cultural Organization (UNESCO) equation of state (Millero *et al.*, 1980; Millero and Poisson 1981). Global NCOM opts for the F-L equation, which is faster but less accurate at depth than the Mellor equation. We have assumed that F-L has sufficient accuracy relative to the other sources of error in the model, but have not performed a detailed analysis quantifying the time benefit versus performance cost in global NCOM.

The spatial finite differences are mainly second order with options for some higher-order differences. There is an option for the quasi-third order upwind advection scheme described by Holland *et al.* (1998) for momentum and/or scalars, and an option for the Flux-Corrected

Transport (FCT) advection scheme (Zalesak, 1979) for scalars. The FCT scheme avoids advective overshoots but increases running time by about 50%. Global NCOM in this report employs the third-order upwind advection but not the relatively expensive FCT. Temporal differencing is leapfrog with an Asselin (1972) filter to suppress timesplitting. All terms are treated explicitly in time except for the solution for the free surface and vertical diffusion. In the solution for the free surface, the horizontal surface pressure gradient terms in the depth-averaged momentum equations and the divergence terms in the depth-averaged continuity equation are evenly split between the old and new time levels to minimize the damping of surface waves. In the vertical diffusion terms, the field being diffused is evaluated fully at the new time level to avoid diffusive overshoots and vertical gradient reversals.

The free-surface mode is calculated implicitly; therefore, the surface pressure gradients and the divergence terms in the surface elevation equation have a component at the new time level being calculated. Horizontal mixing and quadratic bottom drag is time-lagged as required for stability, avoiding timesplitting problems. Vertical mixing is fully implicit with vertical eddy coefficient evaluated using time-lagged values of the model fields to avoid exciting the timesplitting behavior of the leapfrog scheme.

In the vertical, NCOM can use  $z$  (fixed) coordinates with a free surface, full  $\sigma$  (terrain following) coordinates, or hybrid  $\sigma/z$  coordinates. These vertical grid configurations are depicted in Fig. 1. The NCOM vertical grid uses  $\sigma$  coordinates from the surface down to a user-specified depth  $z_s$  and  $z$ -levels below (Fig. 1c). Discussion of the motivation for this grid design is presented in Barron *et al.* (2006). The upper,  $\sigma$  portion of the grid is divided into layers as in POM with each  $\sigma$  layer being a fixed fraction of the total depth occupied by the  $\sigma$  layers. On the lower,  $z$ -level portion of the grid, the bottom depth is rounded to the nearest specified  $z$ -level. The model can be configured to run completely in  $\sigma$  mode or with any number of  $\sigma$  over  $z$ -levels, i.e., as long as at least one  $\sigma$  layer is included to accommodate the free surface. For the  $\sigma$ -level portion of the grid, the form of the NCOM equations is similar to that presented by Blumberg and Mellor (1987) except that the depth in the equations is replaced by  $\min(H, z_s)$ , where  $H$  is the bottom depth.

The global model configuration of NCOM uses 41  $\sigma$ - $z$  level surfaces, resulting in 40 material levels in the vertical. Of these 41 surfaces, 19 are  $\sigma$ -coordinate interfaces in the upper 137 m, and 21 are  $z$ -coordinate levels below 137 to 5500 m, and one, surface 21, behaves as a  $\sigma$ -coordinate on the bottom for depths shallower than 137 m and as a fixed 137 m  $z$ -coordinate for deeper depths. Surface one is the free surface, but free surface variations are proportionally divided among all but the bottom  $\sigma$  interface. Interfaces are at depths determined by logarithmic stretching such that the uppermost material layer thickness is 1 m and the bottom  $z$ -interface is at 5500 m. The 137 m  $\sigma$ - $z$  interface is selected as a surface that generally intersects land along an isobath close to or shallower than the shelf break. Thus the  $\sigma$ - $z$  transition lies between the inner and middle shelf, where  $\sigma$  coordinates are clearly appropriate, and the shelf break and slope, where  $z$ -levels are desired to maintain minimum upper level thickness and avoid the problems associated with  $\sigma$  coordinates in regions of steep topography. Where the water is shallower than 137 m, primarily in the shelf region, the 19  $\sigma$ -coordinate material levels follow the bottom to improve representation of response to topographic features. In deeper water, the vertical resolution of the  $\sigma$ -coordinate layers at rest increases from 1m at the surface to about 20 m at the  $\sigma$ - $z$  interface. Grid cell wetting or drying is not supported, and the shallowest bottom depth allowed is 5 m. The model depth and coastline are based on NRL DBDB2, a global, 2-minute gridded topography produced at NRL (D. Ko, [http://www7320.nrlssc.navy.mil/DBDB2\\_WWW](http://www7320.nrlssc.navy.mil/DBDB2_WWW)).

The availability of this Beta version of NRL DBDB2 bathymetry two-minute database was announced 4 June 2002. Improvements in bathymetry remain an ongoing topic of interest within the operational oceanography community, as many raw bathymetry sets have not undergone adequate quality control.

NCOM is coded for an orthogonal curvilinear horizontal grid as in POM (Blumberg and Herring 1987). Global NCOM horizontal grid dimensions are 2048x1280. Fig. 2 depicts the horizontal grid used in global NCOM, a rotated, reprojected bipolar grid with a transition zone (Murray, 1996). South of 32°N the grid is spherical with meridional stretching. Between 32°N and 71°30'S the stretching maintains a cell aspect ratio of 1, meaning that the zonal grid spacing in km is equal to the meridional grid spacing in km. This aspect ratio of unity is used to improve the accuracy of horizontal finite-difference calculations. South of 71°30'S to the southern limit of 78°27'S the meridional grid spacing is held constant, allowing grid cells to become meridionally elongated in order to avoid excessive concentration of nodes and computational effort in the south polar extremes of the domain. A transition zone begins at 32°N, linking the spherical grid in the south to the reprojected bipolar grid north of 47°20'N. North of 32°N, model x-coordinates are no longer parallel with lines of latitude. Reprojected pole locations at 47°20'N were selected in Canada and Russia to isolate the most highly distorted portions of the domain over land and maintain a grid cell aspect ratio near 1 over active water regions. Fig. 3 illustrates the relative distortion of the Arctic after mapping to the logically rectangular model domain. The resolution of the grid varies spatially due to the stretching, leaving the grid spacing near 20 km at the equator, 5-10 km in the Arctic, and 14 km or 1/8° latitude at 45°S (midlatitude). Boundary conditions are periodic in the primarily zonal i dimension, closed on the Antarctic j boundary and mapped on the Arctic j boundary to allow uninterrupted communication where the j boundary matches across the Arctic seam.

Operationally and for these simulations, the NCOM model forcing is calculated from the following time-varying atmospheric fields: wind stress, air temperature, air mixing ratio, and net solar radiation. Where available, these are taken from FNMOC NOGAPS (Rosmond *et al.*, 2002). Operational runs use forcing at 3-hour time steps, but the archives used for the 1997-2002 hindcast runs stored only 6-hourly fields. The hindcast simulations in 1997 employed atmospheric data from the European Center for Medium-range Weather Forecasting (ECMWF; Gibson *et al.*, 1997) for fields other than wind stress because appropriate NOGAPS data prior to 1998 are not in the NRL archive. Sensible and latent heat fluxes are strongly dependent on SST, so these are calculated every time step using the NCOM model SST in bulk formulations that include the effect of air-sea stability through the exchange coefficients (Kara *et al.*, 2002). The annual SST cycle is built into the model to a limited extent via the bulk formulation link between SST and atmospheric air temperature, which follows the annual cycle of atmospheric temperature. Including air temperature in the formulations for latent and sensible heat flux along with model SST in the bulk formulation automatically provides a physically realistic tendency towards the correct SST (Kara *et al.*, 2003a). Although radiation fluxes also depend on SST to some extent, these fluxes are obtained directly from NOGAPS in order to use the atmospheric cloud mask. Additional studies are investigating alternate representations of the heat flux and mixing terms to account for biases in model results.

## NCOM Data Assimilation

NCOM assimilates temperature and salinity fields produced by MODAS. Developed at NRL (Fox *et al.*, 2002a), MODAS consists of climatological databases plus over 200 programs and utilities for combining irregularly sampled remote-sensed data and in-situ measurements to create 3D estimates of temperature and salinity over the global ocean. MODAS performs quality checking and optimum interpolation of ocean observations (Bretherton *et al.*, 1976), including temperature, salinity, and SSH.

The MODAS2D SSH and SST are gridded by optimum interpolation using altimeter (Jacobs *et al.*, 2002) and Multi-Channel SST (MCSST) data products from NAVOCEANO (Barron and Kara, 2006). MCSST data are obtained from multiple 5-channel Advanced Very High Resolution Radiometer (AVHRR) instruments aboard polar orbiting satellites (May *et al.*, 1998). For the fields it prepares for global NCOM, MODAS uses SSH from the assimilative 1/16° NLOM, (Smedstad *et al.*, 2003). A detailed description and discussion of the NLOM's prediction capabilities is given in Wallcraft *et al.* (2003) and Smedstad *et al.*, (2003). MODAS constructs synthetic temperature and salinity fields from input fields of SST and steric SSH. Steric SSH is the integrated difference of the actual specific volume anomaly minus the specific volume anomaly of an ideal water column with 35 salinity and 0°C potential temperature, in this case integrated over the upper 1000 m (Boebel and Barron, 2003). Climatological SST and steric SSH from the MODAS bimonthly database are subtracted to give SST and steric SSH anomalies relative to the climatology. MODAS then uses equations determined from historical correlations to project estimated temperature anomalies at standard depths downward from these surface anomalies. For example, a zero anomaly in SST and a -1.0 °C anomaly in SSH may project an anomaly of -2.2 °C in 200 m temperature for a particular location. The local climatological temperature profile is then added to the profile of anomalies, producing a profile of synthetic temperature. MODAS then uses location-specific climatological temperature-salinity relationships at each standard depth to estimate the synthetic salinity profile. Temperature from MODAS is converted to potential temperature for use in NCOM. These salinity and potential temperature fields are filled to provide assimilated data for NCOM in a format that encompasses the entire model grid.

Global NCOM assimilation uses NLOM SSH rather than MODAS2D SSH to take advantage of the improved nowcast skill of the NLOM dynamics over the MODAS statistical model and the ability of NLOM to better quantify the steric component of SSH for the synthetic calculations. Changes in steric SSH produce no changes in bottom pressure, so a model can calculate a steric SSH by subtracting the height proportional to the calculated bottom pressure anomaly from the total height. An altimeter observes total SSH without distinguishing steric versus non-steric contributions. NLOM assimilates the total height and internally attributes the signal to dynamically appropriate sources. The NLOM SSH anomaly used to derive NCOM assimilation fields is the NLOM estimate of steric SSH anomaly, which is the NLOM SSH minus NLOM climatological SSH minus the SSH anomaly equivalent to the NLOM bottom pressure anomaly.

NLOM SSH does not extend over regions shallower than 200m or north of 66°N, and it is not reliable south of 55°S. Because the non-steric component of total SSH is proportionally larger in shallow water and in high latitudes (Shriver and Hurlburt, 2000), direct use of MODAS2D SSH is problematic in the same areas in the absence of information on how to partition the signal between steric and non-steric components. Thus in these regions, MODAS

synthetic profiles are calculated using SST only, and a linear blend is applied to transition between regions of SST only and full SSH/SST synthetics (Fox *et al.*, 2002a).

Global NCOM is dependent upon the 1/16° NLOM to provide the required resolution to properly resolve mesoscale ocean dynamics. As stated in the introduction, this nowcast/forecast global system is the operational global system at the Naval Oceanographic Office and all components are vital to determining meaningful model results. Even though NCOM is the most visible component of the global nowcast/forecast system, as it is the final product, the absence of the global NLOM SSH would negatively impact the NCOM results, to the point of having poor skill in regions of significant front or mesoscale eddy activity.

Data preparation for the NCOM model begins with SST from MODAS2D and SSH from NLOM. Subtracting the NLOM climatological mean SSH from daily steric SSH yields a SSH deviation, which is passed along with MODAS2D SST to the MODAS dynamic climatology module for calculation of synthetic temperature and salinity profiles. At this stage, available *in situ* observations can be assimilated into the 3D analyses. For the present study, no *in situ* data have been included, allowing all *in situ* observations to be used for independent validation. After converting temperature to potential temperature, the 3D potential temperature and salinity fields are interpolated to the model grid.

Data assimilation used in NCOM is done using two mechanisms: (1) adjustment of heat and salinity fluxes at the surface, and (2) relaxation toward subsurface temperature and salinity profiles. In both cases, the assimilation is applied each time step with strength proportional to the product the deviation field multiplied by the gridded weighting function, where the deviation field is the difference between the model and assimilation fields, and the weighting field reflects the relative confidence between the model and the data. This slow data insertion technique allows the model to incrementally adjust to the data with minimal dynamic disruption (Rhodes *et al.*, 2002). Preparation of the data fields for assimilation is independent of the NCOM assimilation itself, allowing the model to accommodate a variety of approaches to preparing the observational analyses, such as incorporating *in situ* data within the MODAS structure or linking NCOM into a cycling multi-variate optimal interpolation or variational scheme. The limitations on the assimilation procedures are dependent upon operational time constraints and computational resources.

## **NCOM River Database**

One purpose of Global NCOM is to provide a global capability to initialize, nest, and evaluate fixed and relocatable coastal ocean models. In support of that objective, a database of river flow estimates is needed. Perry *et al.* (1996) provides a start with estimates of annual mean river discharges for 981 of the world's largest rivers. However, many rivers exhibit a strong seasonal variability, which we would like to reflect in our ocean models. Through the use of multiple internet sources and published data sets we have expanded on the Perry (1996) data to provide a global database of monthly mean river discharge and incorporated this data in global and nested NCOM runs (Barron and Smedstad, 2002). Where data for a given river are not sufficient for constructing a monthly mean, a seasonal cycle is inferred from nearby rivers and scaled to the appropriate annual mean. Real time discharge rates are rarely available for any rivers outside of the United States, so monthly means are likely to be the best available estimate of real time flow for analyses and forecasts in most areas.

Barron and Smedstad (2002) examined the impact of using climatological monthly mean river discharge instead of annual mean discharge by using either set of means to predict daily river discharge over two years for 28 of the largest rivers in the United States for which daily discharges were recorded. The study found that monthly climatological means were superior to various annual climatological means in most cases and were particularly well suited for representing discharges from rivers located in the upper midlatitude band from 39°N to 67°N. With the major exception of the Mississippi River, rivers that discharge into the Gulf of Mexico were difficult to represent using any climatology, likely due to the irregular, episodic nature of storm-events which result in large discharge variations.

Monthly river outflow can contribute to more accurate seasonal representation of areas near coastlines. Seasonality particularly affects the polar areas, where river outflow can become quite small during winter months and quite large during the summer melting season. Even when seasonality is not important, the nearshore distribution of salinity in a model using river sources is likely to be superior to the distribution based on gridded global climatologies. These are likely to smooth out or miss nearshore gradients inadequately sampled by sparse historical hydrographic observations. Fig. 4 provides one of the clearest indications of the impact that including rivers has on nearshore properties. Several major rivers along the western coast of Africa empty into the eastern equatorial Atlantic, including the Congo and Niger rivers. Although relaxation to MODAS surface salinity does produce realistic salinity distribution in the open ocean, in coastal regions, inclusion of major rivers significantly modifies nearshore salinity stratification. For example, the general freshening along the coast at 4°N is evident in the case without rivers due to relaxation to MODAS salinity. Thus addition of rivers produces a more pronounced salinity minimum which can be attributed to the Ogooué (Gabon), the Ntem, Nyong, Sanaga and Wouri (Cameroon), and the Cross (Nigeria) rivers.

### 3. TESTING RESULTS

#### Experiments

Before performing any interannual NCOM simulations, the model was first spun-up over 6 years from a static climatological initial state to statistical energy equilibrium. This spin-up was forced with monthly Hellerman-Rosenstein (1983) mean wind stress and climatological surface heat fluxes obtained from NOGAPS. The model simulation was then extended in data-assimilative mode for 1997, forced with 6-hourly NOGAPS wind stress and modified ECMWF atmospheric fluxes, as discussed earlier. Results from 1997 are not part of the validation, thus allowing a full year for the model to adjust from its climatological state to a realistic hindcast state suitable for evaluation. Interannual experiments following 1997 use corresponding “real-time” 6-hourly atmospheric wind and thermal forcing from NOGAPS. The validations focus on two interannual  $1/8^\circ$  global NCOM model simulations: (1) free-running (i.e., atmospheric forcing only), and (2) assimilative (i.e., with ocean data assimilation of MODAS temperature and salinity fields). The assimilative case corresponds to the operational implementation (although excluding *in situ* observations), while the free-running case provides a reference for assessing standalone model skill and impact of assimilation. Both simulations start from the same initial state on 1 January 1998. The free running experiment covers three full years, 1998-2000, while the assimilative experiment extends almost six years to 2003 and continues in real-time. Over the period covered in this validation test report, both simulations use nowcast-quality NOGAPS wind, NOGAPS thermal forcing and MODAS+NLOM assimilation fields. To allow assessment of forecast skill without the overhead of running daily forecasts, 7-day free-running forecasts are initiated from the assimilative restart files every 15 days. This collection of model simulations is used to examine the performance of NCOM in representing ocean properties and circulation on daily time scales, with emphasis on model performance for upper ocean quantities. Additional validations using a multi-year NCOM experiment run in near-real time are reported in more detail by Kara *et al.* (2006).

#### Global Means

Global mean and standard deviation fields from global NCOM are presented to provide an accessible reference to the basic ocean solution provided by the global model and to illustrate the impact of data assimilation on large scale model features. SSH, SST, SSS, surface speed, and surface KE are each presented in three hemispheric views, focusing on the Atlantic, Indian, and Pacific Ocean basins, respectively. Plots of the 3-year 1998-2000 mean fields are shown for each data type. Reference grid lines denote every  $30^\circ$  of longitude and every  $15^\circ$  of latitude. Standard deviation plots convey variability information for SSH, SST, SSS and surface speed. The corresponding plot reflecting variability of KE is the plot of mean eddy kinetic energy (EKE).

$$\text{mean(EKE)} = \text{mean(KE)} - \text{KM} = 0.5 * (\sigma_u^2 + \sigma_v^2) * (n-1)/n$$

where  $\sigma_u$  and  $\sigma_v$  are the standard deviations of eastward (u) and northward (v) velocity and n is the number of realizations in the sample. KM is the kinetic energy calculated from the means of u and v velocity components.

## Atlantic Hemisphere

For the hemisphere centered on the Atlantic basin, the most prominent features evident in the SSH (Fig. 5) are the North Atlantic and South Atlantic gyres. The Gulf Stream stands out as a region of particularly high SSH variability, indicating a high level of eddy activity; this area is discussed in more detail in a later section. Assimilation tightens the SSH gradients in the gyres, and increases SSH variability in the main Gulf Stream and Loop Current while reducing SSH variability in the South Atlantic, Antarctic Circumpolar Current (ACC) and Caribbean Sea.

Global SST (Fig. 6) shows that assimilation leads to warmer surface temperatures in the subtropical and tropical Atlantic while reducing overall SST variability, which is maximum north of the Gulf Stream. In particular, assimilation reduces the cold SST tongue in the eastern equatorial Pacific, perhaps indicating that the La Niña conditions prevalent from late 1998 through most of 2000 were overstated in the free-running model. SSS (Fig. 7) is very similar between the assimilative and free-running cases, reflecting the relatively low confidence in, and thus weak relaxation to, surface salinity data. In terms of salinity, the primary difference between the cases results from addition of river inflow to the assimilative run, introducing localized changes that are difficult to detect in long term global statistics other than enhanced low salinity plumes and increased SSS variability in the vicinity of major rivers such as the Amazon, Orinoco and Plata along the east coast of South America, the Mississippi emptying into the northern Gulf of Mexico, and the Congo along the west coast of Africa.

Plots of mean speed (Fig. 8) in the Atlantic hemisphere clearly trace the dominant western boundary and equatorial currents. The impact of assimilation is most evident in the equatorial and Gulf Stream regions. Around the equator, the south equatorial current is dominant for the free-running case while the north equatorial current is prevalent in the assimilative case. The free-running case has higher standard deviation of surface speed in the tropics, but the standard deviation of surface speed is higher at mid to northern latitudes in the assimilative case. Assimilation also extends the Gulf Stream much farther east and minimizes the northward overshoot seen in the free-running case just offshore of Cape Hatteras. In the plots of kinetic energy (Fig. 9), the pathway and eastward extension of the Gulf Stream is better defined after the assimilation, while the free-running case has more energetic mean currents in the Caribbean and shedding of Agulhas eddies around South Africa. Additional work is underway tuning the assimilation scheme to better represent distributions of currents and eddy variability (Barron *et al.*, submitted).

## Indian Hemisphere

For the Indian Ocean, primary differences in SSH between the free running and assimilative cases (Fig. 10) are evident in the SSH variability, which after assimilation is lower in the eastern ACC and south of Madagascar, relocated in the South Equatorial Current, and somewhat increased in the Arabian Sea and Bay of Bengal. SST (Fig. 11) means are similar between the two experiments, with a stronger signal of cool upwelling off the coast of Somalia evident in the free-running case. Salinity on these scales is similar as well (Fig. 12), with a notable exception of higher salinity variability in the assimilative case in the northern Bay of Bengal due to fresh water inflow from the Ganges-Bramaputra system. Influence of river plumes is also evident along the coasts of Thailand and China. Examination of surface speed (Fig. 13) and kinetic energy (Fig. 14) reveals stronger western boundary currents and higher speed variability in the free-running case. One hypothesis under investigation is that the procedure to

calculate synthetic temperature profiles does not adequately account for differences between the mean MODAS and mean NLOM height structure of the western boundary currents. If NLOM has a tighter gradient in its mean, then SSH deviations from the NLOM mean do not represent the full gradient when they are treated as deviations from the MODAS mean SSH. Based on these results, model studies are underway to examine the impact of assimilation using alternate instantaneous and mean SSH fields, with a focus in western boundary current regions.

### **Pacific Hemisphere**

Plots of SSH in the Pacific (Fig. 15) show assimilation improves the structure of the main gyres in the north and south Pacific and a dramatic eastward extension of the Kuroshio and a stronger height signal for the East Australia Current (EAC). SST (Fig. 16) after assimilation is generally warmer, the cool signal from equatorial upwelling is less prominent, and SST variability is reduced in the mid to high latitudes, particularly along the south coast of Alaska and the Aleutians. Multi-year SSS conditions (Fig. 17) show no notable differences between the free-running and assimilative cases, with any riverine influence very much on the periphery from the Pacific perspective. Finally, surface speed (Fig. 18) and kinetic energy (Fig. 19) in the Pacific clearly indicate the prominence of the equatorial currents, which are stronger and have a larger meridional extent in the free-running case. The assimilative case has a better Kuroshio extension but, in the EAC, the Alaska Stream and the East Kamchatka Current have been greatly weakened. Preliminary studies have found that a more realistic Alaska Stream results if the differences between the MODAS and NLOM mean SSH are more properly included during the production of synthetic temperature profiles (Barron *et al.*, submitted).

### **Frontal Location, Eddy Kinetic Energy, and SSH Variability**

Regional zooms of model fields allow a more detailed examination of data assimilation impact and the regional accuracy or deficiency of global NCOM simulations. Looking at large scale features through sea surface height or mean current location, we qualitatively assess the fidelity of the model's representation of basic circulation features. EKE provides a measure of the variability in the basic circulation of the model. Where available, these means are compared with relevant observed climatologies. At this stage the basic features of global NCOM are compared with the basic circulation of the Shallow-Water Analysis and Forecast System (SWAFS) Northworld model as well. Since global NCOM is to serve as a replacement for the SWAFS Northworld model, we highlight differences between the basic circulations of the two models integrated over the same time interval. Improvements are to be expected as NCOM, though not touted as a high horizontal resolution model, still has a higher resolution than the 1/4° SWAFS. Other factors also will be identified to justify this replacement.

Information on the position of fronts in the western North Atlantic and western North Pacific can be extracted from the daily NAVOCEANO Ocean Front and Eddy Bogus as described in NAVMETOCCOMINST 3140.24A procedures for preparing bogus data. These front bogus files are series of labeled coordinates that indicate the estimate of the front position for that day as determined from analysis of infrared imagery, where the "front" is a line of transition between warm and cold water. Each point is tagged with a quality flag indicating the percentage of confidence in the front position. The confidence level is set to 100 if the front is clearly visible on a given day. To maintain continuity, front position at obscured points is estimated by persistence from the past or interpolation from neighboring points and the

confidence flag is reduced. Confidence in bogus position continues to decrease as a region continues to be obscured. To create mean front locations for this study, the data for a selected front were binned in  $0.5^\circ$  longitude bins, appropriate for the primarily east-west fronts considered. Within each bin, a mean and standard deviation of front latitude was calculated and paired with the midpoint longitude of the bin. Only bogus points with a confidence of 85% or higher were used. The archive of front boguses has data for approximately 85% of the days between 17 September 1998 and the present, limiting the range over which means can be computed. Thus the mean 1998-2000 front positions are biased toward the latter two years, while means from September 2002 – May 2003 are unbiased in time.

## Gulf Stream

In the North Atlantic, the Gulf Stream is a key circulation feature of deep-water interest. Fig. 20 shows a zoom of the Gulf Stream region with mean and mean  $\pm 1$  standard deviation 1998-2000 position of the Gulf Stream north wall. Looking at mean surface currents, Fig. 20a reveals that free-running global NCOM favors a small overshoot north due to delayed separation from the coast and an unrealistic Gulf Stream path due east at about  $35^\circ$  N, common features in free-running models at this resolution and are consistent with the two Gulf Stream pathways found in linear solutions (Townsend *et al.*, 2000). EKE is very high near  $70^\circ$ W (Fig. 20b), reflecting excessive instability in this region of the free-running Gulf Stream. Fig. 20c,d reveal the impacts of data assimilation on the Gulf Stream pathway, eliminating most of the northward overshoot and producing a pathway in better agreement with observations. Results from 100 m (Fig. 21) provided a clearer indication of the eastward extension of the Gulf Stream pathway through data assimilation.

Ample historical data for evaluation of model eddy kinetic energy are available in the North Atlantic. Although strictly speaking we will examine eddy kinetic energy per unit mass, having units  $\text{cm}^2/\text{s}^2$ , we will neglect the “per unit mass” tag and refer to this quantity as EKE. Fig. 22 shows mean global NCOM EKE at 5 m depth for 1998-2002, to be compared with mean EKE derived from historical North Atlantic surface drifter observations in the 1990s (Fig. 23) (Fratantoni, 2001). While similar to the assimilative case in most respects, the free-running case in the Caribbean Sea and north of  $60^\circ$ N has higher surface EKE, in better agreement with observations. Also, NCOM in either mode does not reproduce the tongue of high EKE extending north of  $50^\circ$ N east of Newfoundland and the Grand Banks. This tongue of EKE is associated with the North Atlantic Loop Current, which is poorly simulated in NCOM and most other ocean models. Generally, these results indicate a need to adjust the assimilation procedure in certain areas, a topic discussed more fully in the final section of this report. In the vicinity of the Gulf Stream, model EKE from the assimilative case agrees reasonably well with the historical observations, although it underestimates the maximum drifter Gulf Stream EKE by 15-30%.

At 700m, model EKE (Fig. 24) can again be compared with climatological means, in this case means compiled from SOFAR float observations (Fig. 25) (Schmitz, 1996; Owens, 1984; Owens, 1991; Richardson, 1993). EKE at 700 m in the assimilative case is generally higher and in closer agreement with historical observations, showing the two regions of relatively high EKE south of Nova Scotia and Newfoundland. The assimilative case also eliminates the spurious EKE maximum seen in the free-running results where the Gulf Stream separates from the coast. As

was the case at the surface, the extrema in the assimilative global NCOM EKE are well located but fall 15-30% short of the observed maxima.

For comparisons with the SWAFS assimilative  $1/4^\circ$  northworld model, statistics from both northworld and assimilative global NCOM are calculated over the periods of archived SWAFS data, which were only available from 9/1/2002 – 5/31/2003 for surface fields and 11/15/2002 – 5/15/2003 for subsurface data. Mean front locations are calculated over the period of available SWAFS surface data. To avoid false conclusions in comparisons between SSH based on different color tables or color ranges, for plotting purposes the mean SSH of the SWAFS data is adjusted for each plot to equal the mean NCOM SSH averaged over the plot area.

Fig. 26 shows surface comparisons between global NCOM and northworld SWAFS. The main Gulf Stream pathway between the models is similar in extent with location in agreement with observations (Fig. 26b,d). The mean core of the Gulf Stream has somewhat better continuity in SWAFS, partly due to a low evident in the pathway of both models at  $66^\circ\text{W}$ , which appears to be stronger and less separated from the Gulf Stream in NCOM. In SSH (Fig. 26a,c), SWAFS is seen to have a much tighter recirculation gyre concentrated south of  $35^\circ\text{N}$  and west of  $70^\circ\text{W}$  (Fig. 26c), leading to a spurious localized recirculation current along  $65^\circ\text{W}$  (Fig. 26d). Two other unrealistic features are detectable in the mean SWAFS SSH: a trough of low SSH between the shelf break and Gulf Stream after separation, and a SSH low over the northern end of the Bahamas. Circulation patterns corresponding to these SSH features are evident at 500 m (Fig. 27). A strong, spurious southward current along the slope, too shallow to be the deep western boundary current, is evident in SWAFS (Fig. 27d) but not NCOM (Fig. 27b). Also, the pass between Florida and Grand Bahamas at  $26^\circ\text{N}$  is shallower than 500 m in SWAFS, while it should extend to a minimum depth between 600 and 700 m as in NCOM. The shallow sill in SWAFS diverts deep flow east of the Bahama Banks and leads to a spurious two-path Gulf Stream at 500 m between  $27^\circ\text{N}$  and  $30^\circ\text{N}$ . At 500 m the Gulf Stream is significantly stronger in NCOM west of  $65^\circ\text{W}$  but somewhat less continuous to the east. EKE at 500 m (Fig. 27a,c) is similar between the two cases.

## **Kuroshio**

In the North Pacific, the Kuroshio is a key circulation feature of deep-water interest. Fig. 28 shows a zoom of the mean surface currents and EKE for the Kuroshio region similar to what was discussed previously for the Gulf Stream. Fig. 28a depicts a weaker Kuroshio mean current for the free-running case compared to the assimilative case (Fig. 28c). The mean EKE results for the two cases (Fig. 28b,d) show similar results with the assimilative case showing much more realistic energy patterns that correspond with the mean frontal analysis. The EKE from the free running case indicates a slight overshoot of the Kuroshio near  $145^\circ\text{E}$  which is not as evident in the mean surface current results. Another difference between the two cases is that the Kuroshio is much stronger to the east in the assimilative case and is much more realistic compared to the overlaid frontal analysis.

Another difference is the unrealistic position of the Kuroshio meander near  $140^\circ\text{E}$  in the free-running case compared with the frontal analysis that is in much better agreement with the location of the meander in the assimilative case. This difference is also indicated in the mean surface kinetic energy depicted by the high energy in the free-running case at the position of the unrealistic meander discussed above, which is not seen in the assimilative results. Results from

100 m (Fig. 29) provide similar results of the more eastward penetration of the Kuroshio in the assimilative case and the unrealistic meander position in the non-assimilative case.

Fig. 30 shows the mean NCOM EKE for the Kuroshio at 5m depth and 500 m depth for 1998-2002 from the free-running and assimilative cases similar to the Atlantic results shown earlier. As in earlier results, the assimilative model (Fig. 30b,d) produces more realistic eastward penetration of the Kuroshio and more tightly constrains the current east of 140°E than the free-running NCOM (Fig. 30a,c). These results are consistent with the earlier surface results with the frontal positions overlain.

Similar to the Gulf Stream results discussed previously, comparisons of NCOM with the SWAFS northworld model were also performed in the Kuroshio. Fig. 31 shows surface comparisons between the two systems. The main Kuroshio pathway location for the systems is similar and in reasonable agreement with observations (Fig. 31b,d). However, NCOM has stronger currents and is more inertial farther to the east, especially east of 155°E. The SWAFS system shows several unrealistic large re-circulation gyres just south of the Kuroshio from 135°E to 145°E. The gyre at 142°E in the SWAFS system as shown in the mean SSH (Fig. 31a) is a spurious circulation that is indicative of premature separation of the Kuroshio and causes a discontinuous Kuroshio in SWAFS that is not in agreement with the frontal analysis in this region, while NCOM, which does not show this feature (Fig. 31c), has a continuous front and compares better with the bogus in this area. The strong re-circulation gyres seem to contribute to the lack of eastward penetration of the front in SWAFS. SWAFS also shows an unrealistic penetration of the Kuroshio into the East China Sea near 128°E that is not shown in Global NCOM and is not in agreement with the frontal analysis. These features are also evident in the results at 500 m (Fig. 32), especially the SWAFS gyre at 142°E and the differences in the front between the two systems (Fig. 32a,c) just downstream from this feature.

## Indian Ocean

Fig. 33 and Fig. 34 show a zoom of the Indian Ocean region from the global NCOM for the free-running and assimilative cases. The mean current speed and EKE from 1998-2000 for the surface (Fig. 33) and 100 m (Fig. 34) from the two cases are much more similar than for the results in the Gulf Stream and Kuroshio discussed earlier. A possible reason for the smaller differences is that the dynamics of the largest variations in Indian Ocean circulation are more deterministic at basin scales than those of the Atlantic and Pacific. The monsoon changes in wind forcing produce some of the most significant variations in Indian Ocean circulation (Schott and McCreary, 2001). Also, this zoom only considers the region north of 30°S, thus excluding the Agulhas retroflexion that would have instabilities similar to the western boundary currents in the other basins. The 1/8° model resolution is more adequate for this lower latitude region of Indian Ocean dynamics than it is for either the Kuroshio or Gulf Stream. One notable difference is the reduced strength of the western boundary current in the Indian Ocean. This may be due to discrepancies between the NLOM and MODAS height fields along the western boundary, where a tight front in NLOM is not resolved in the MODAS climatological SSH, resulting in weak gradients in the assimilation field. Methods to improve the data assimilation here are discussed in the final section.

Fig. 35 shows the mean SSH over the Indian Ocean from Global NCOM (Fig. 35a) and SWAFS northworld (Fig. 35b) for the winter monsoon period (November 15, 2002 to March 15, 2003). There are notable differences between the two systems especially in the south Indian

Ocean near the southern boundary of the SWAFS grid, but for the purposes of this comparison, it is better to focus on the Arabian Sea, which is an important area of Navy interest. In addition, there is a nested higher resolution SWAFS regional model for the northern Indian Ocean (IO) that can also be compared for this region. Fig. 36 shows zooms of the Arabian Sea for SSH and surface currents overlain on speed for assimilative global NCOM (Fig. 36a,b), SWAFS northworld (Fig. 36c,d) and SWAFS IO nest (Fig. 36e,f). To assist in evaluating these results, Fig. 37 depicts the prevalent observed circulation in the Indian Ocean (Schott and McCreary, 2001). NCOM and the SWAFS results have striking differences, with NCOM results much closer to the typical patterns. The SWAFS systems show very strong mean currents along the coast that are not realistic based on the mean IO circulation. There are strong mean mesoscale features in the SWAFS solutions and particularly in the IO nest that are not observed. The global NCOM has a mean circulation pattern that is more consistent with the expected mean flow patterns during the winter monsoon. The strong front in SSH and corresponding strong currents seen across the Arabian Sea at 8°N are not observed features of a mean winter monsoon circulation. There appear to be some problems with the SWAFS solutions and the reasons for these problems are not known, but the global NCOM mean circulation is an improvement over SWAFS in this area.

### South China Sea

Fig. 38 shows a zoom of the South China Sea region from the global NCOM for the free-running and assimilative cases. The mean surface EKE from 1998-2000 for both runs (Fig. 38a,b) reveals only minor differences, with a slight reduction in surface EKE in the assimilative case, most notably east of the Luzon Strait, which may indicate the assimilative case reduces the magnitude and frequency of intrusions of the Kuroshio through the strait. Surface EKE in the assimilative case is also somewhat reduced in the central South China Sea, the Sulu Sea, and the northern Suluwesi Sea. Mean surface currents (Fig. 38c,d) show some changes in the basic pattern within the South China Sea, but more notable is the increased intrusion of the Mindanao Current retroflexion into the Suluwesi Sea. Fig. 38f reveals that the assimilation has set up an anti-cyclonic circulation pattern within the Suluwesi Sea, and a weaker shift to a cyclonic circulation at 500m is also detectable within the Sulu Sea (Fig. 38e). In the final discussion, assimilation adjustments are discussed for this region. Relatively isolated basins like the Sulu Sea pose difficulty, because they often have significantly different background steric height anomalies, causing boundary effects between adjacent seas. This is noticeable in the decreased mean currents in the South China Sea in the assimilative case. For the Sulu Sea, its isolated water below 500m is significantly warmer than the ambient Pacific temperatures at the same depths, leading to larger background steric height anomaly in the surrounding Pacific when integrating from the same depth.

Fig. 39 shows comparisons of global NCOM and SWAFS northworld for this region. The NCOM (Fig. 39a,c,e) and SWAFS (Fig. 39b,d,f) results for mean SSH, mean 5 m currents and speed, and mean 100 m currents and speed are shown. As in the Indian Ocean, there are large differences between the assimilative NCOM and SWAFS solutions. Several strong features of the mean SWAFS results in this region are inconsistent with observed circulation patterns in the South China Sea (i.e. Fang *et al.*, 1998). The lack of transport in SWAFS through the Makassar Strait at 118°E is attributable to the incomplete global domain of SWAFS northworld which does

not allow for circulation south of Africa and Australia, and thus does not encompass the processes responsible for the Indonesian Throughflow.

As demonstrated later using NCOM's observed velocity cross-sections, NCOM shows a realistic Kuroshio pathway in crossing the Luzon Strait between the Philippines and Taiwan (Fig. 39c,e). Metzger and Hurlburt (2001) identifies this as a dual pathway that includes a shallow intrusion into the South China Sea before passing east of Taiwan and a secondary pathway that passes east of the Babuyan Islands in the Luzon Strait. In contrast, SWAFS shows a deep Kuroshio intrusion into the South China Sea with the Kuroshio then exiting through the Taiwan Strait, west of Taiwan, contrary to observations (Fig. 39d,f). This may be facilitated by the unrealistically deep Taiwan Strait in SWAFS, greater than 100m vs. between 50m and 100m for the observed still depth.

Another unrealistic feature of SWAFS is the penetration of a strong jet near 13°N into the South China Sea through the Philippine Islands. In addition, SWAFS shows an unrealistic, strong gyre in the southwestern South China Sea that crosses between the deep water of the South China Sea (northeastern part) and the shallow Sunda Shelf (southwestern part), contrary to the expectations from conservation of potential vorticity. This may be facilitated by the unrealistically deep SWAFS topography over the Sunda Shelf (and other places in the region) (Fig. 39f), possibly to accommodate the use of sigma coordinates everywhere. The SSH plots (Fig. 39a,b) show that SWAFS misses the observed cyclonic gyre in the northern South China Sea that is seen in the NCOM SSH. As in the Indian Ocean, the global NCOM solution is more realistic and compares favorably with observed mean features in the South China Sea.

## SSH

Since global NCOM has been developed to predict ocean quantities in both open ocean and coastal regions, it is necessary to examine model performance in as many places as possible by including both coastal and open ocean locations. For SSH, intercomparisons between the model experiments and independent observations are performed using sea level measurements from a total of 282 tide gauges located in different regions of the global ocean (Fig. 40). The data are considered in year-long time segments to mitigate the effects of data gaps while allowing validation over a variety of intra-annual time scales. To avoid misleading comparisons over short or sparse time series, only stations with more than 100 measurements in a given year are included in the analysis. Using these criteria, the 282 stations yield 612 year-long time series for daily comparisons during 1998-2001. A more detailed discussion of validation of global NCOM using these data is given by Barron *et al.* (2004).

The sea level data from these tide gauges are maintained by the Joint Archive for Sea Level (JASL) Center, which is a cooperative effort between the U.S. National Oceanographic Data Center (NODC) and the University of Hawaii Sea Level Center (Caldwell and Merrifield 1992). JASL acquires, quality controls, manages, and distributes sea level data over the global ocean, including hourly data from regional and national sea level networks. At JASL the data are inspected and obvious errors, such as data spikes and time shifts, are corrected. Gaps less than 25 hours are interpolated. This quality-controlled JASL data set is presently the largest global collection of sea level measurements. For NCOM-data comparisons we use daily averaged detided sea level data from JASL over the period from 1998 to 2001. The tide gauges are located both at islands in the open ocean and in coastal regions where the depth of the water is often very shallow and the continental shelf varies from wide to minimal. The variety and coverage of the

tide gauge locations make these data very useful in validating daily NCOM SSH over the global ocean.

In order to compare the sea level time series from JASL with those from NCOM, daily SSH values from each tide gauge are first adjusted for the inverse barometer effect (e.g., Gill 1982). The inverse barometer correction provides a simple approximation of the sea level response to forcing from air pressure changes. The correction requires knowledge of daily mean atmospheric pressure sea level at all 282 tide gauge locations. For this purpose, a time series of daily averaged mean sea level was extracted at each tide gauge location from archived NOGAPS mean sea level pressure fields. The time series of pressure every 6 hours were filtered using a 13-point boxcar filter, a simple weighted average with uniform weight. Thus, daily pressure values are at each day a 72 hour mean centered on that day. Using standard values for gravitational acceleration and water density,  $g = 9.8\text{m}\cdot\text{s}^{-2}$  and  $\rho = 1025\text{kg}\cdot\text{m}^{-3}$ , we calculated the height adjustment coefficient for the inverse barometer effect as  $dh/dp = 0.9955 \text{ cm mb}^{-1}$ . If  $P$  is atmospheric pressure in mb,  $P_{\text{std}}$  is the standard pressure, and  $h_0$  is the initial height, the adjusted height at standard pressure,  $h_{\text{stdp}}$ , is given by

$$h_{\text{stdp}} = h_0 + (P - P_{\text{std}}) \cdot dh/dp$$

The inverse barometer adjustment of 0.9955 cm is added (subtracted) to (from) the sea level observation for pressure 1 mb above (below) a standard reference value of 1013.3 mb. In summary, the inverse barometer correction is a height increase where the NOGAPS pressure is high (the sea level would be higher in the absence of high pressure) and a height decrease where the NOGAPS pressure is low. The barometer correction is applied to the observed SSH time series at each individual tide gauge location. This transforms the sea level to what it would be under the standard atmospheric pressure, allowing it to be directly compared with the global NCOM SSH, which does not account for atmospheric pressure. For validation purposes this is entirely equivalent to using the inverse barometer approximation to add the effects of atmospheric pressure to NCOM. As an example, the inverse barometer correction is shown for Tofino, located on the Canadian coast at (49°N, 126°W) in Fig. 41. The most obvious effect of the barometric correction is a change in the standard deviation of SSH. While the standard deviation of SSH is 22 cm for the original tide gauge data, it becomes 16 cm after applying the inverse barometric correction in 1998.

There should be no expectation that the mean would be the same between NCOM SSH and any tide gauge or between any two tide gauges because each SSH is quantified with respect to an essentially arbitrary reference level. In the case of a tide gauges, each measurement is defined relative to a local standard, while in the case of global NCOM, SSH is defined to have a global area-weighted average of zero. To reconcile the difference in reference means, the annual mean is removed from both time series before performing model-data comparisons. In the case of locations which have data voids in a given year, the NCOM and observation means are calculated for both model and gauge data only for the days when daily gauge observations are available, and those means are removed from their respective time series. Model-data comparisons are performed for each individual year from 1998 to 2001, separately, because our purpose is to measure the performance of NCOM on daily and monthly time scales from 1998 to 2001. We applied no smoothing on sea level data to eliminate some of high frequency effects due to wind and thermal atmospheric forcing used in the model.

For time series data, we emphasize three statistical metrics to evaluate differences between the models and observations: correlation coefficient  $R$ , root-mean-square difference

RMS, and skill score SS. More complete explanations of these quantities are given by Barron *et al.* (2004) and Murphy (1988). Skill Score (SS) is given by

$$SS = R^2 - (\text{conditional bias}) - (\text{unconditional bias}),$$

where conditional bias is due to the bias in standard deviation and unconditional bias is due to bias in the mean. In the case of SSH, non-dimensional SS measures the accuracy of NCOM SSH relative to tide gauge SSH. The SS is 1.0 for perfect NCOM predictions, and can be negative if the NCOM prediction has normalized amplitudes larger than the correlation or large biases in the mean (Murphy and Epstein, 1989). For SSH comparisons in this study, differences in the mean values have been removed from the data; mean differences are not removed for other data types. Thus for SSH, SS deviates from  $R^2$  purely due to conditional bias. The value of  $R^2$  can be considered a measure of “potential” skill, i.e., the skill that we can obtain by eliminating bias in standard deviation and the mean.

De-meaned daily SSH values from  $1/8^\circ$  NCOM (both free-running and data assimilative) and JASL at various locations located near the USA, Canada, Japan, Australia and Ecuador are shown in Fig. 42. Daily SSH values from the  $1/8^\circ$  NCOM were extracted at the tide gauge locations for the model-data comparisons. As evidenced from the daily tide gauge time series, the SSH changes over time might be quite different at each location. Model results are shown separately for free-running and data assimilative simulations. Overall, it is noteworthy that even the free-running NCOM is able to simulate SSH, including its seasonal variations well. This is especially evident for Atlantic City, USA, located at ( $39^\circ\text{N}, 74^\circ\text{W}$ ), Prudhoe Bay, USA, located at ( $70^\circ\text{N}, 149^\circ\text{W}$ ) and for Santa Cruz, Ecuador, located at ( $1^\circ\text{S}, 90^\circ\text{E}$ ).

Using only one statistical metric might not be sufficient to assess differences in performance of  $1/8^\circ$  NCOM between various tide gauge locations, as seen in Table 1. For example, the RMS difference value of 9.95 cm near Atlantic City located at ( $39^\circ\text{N}, 74^\circ\text{W}$ ) is larger than that of 9.38 cm near Cocos, Australia ( $12^\circ\text{S}, 97^\circ\text{E}$ ) when analyzing the free-running  $1/8^\circ$  NCOM simulation. This might give the indication that SSH prediction from the model at Atlantic City is worse than at Cocos. However, an examination of the non-dimensional SS values reveals a SS value of 0.43 at Atlantic City that is larger than the value of 0.34 at Cocos. Thus, NCOM SSH prediction at Atlantic City is relatively better than the one at Cocos. This is due to the fact that the SSH standard deviation from the tide gauge at Atlantic City (13.22 cm) is larger than at Cocos (11.54 cm), contributing to the relatively large RMS difference at Atlantic City. Thus, the non-dimensional SS analysis serves to clarify the distinction between the two cases. The non-dimensional SS value is especially useful when evaluating relative model performance at two locations, where one has little seasonal cycle and the other has a large seasonal cycle. Because the standard deviations of SSH from the tide gauges are different, RMS difference might yield misleading results.

We now examine spatial variation of the statistical results over the global ocean in each year. Fig. 43 shows R values calculated between SSH values from the JASL tide gauge data and results from the data assimilative simulation from  $1/8^\circ$  NCOM at all locations in 1998, 1999, 2000 and 2001. The analysis is presented when calculating R values based on 1-day and 30-day running averaged time series separately. A notable improvement in R values is evident after applying a 30-day running average to the daily SSH time series. This is seen at tide gauge stations located near the Japan Sea for all analyzed years. Similarly, a substantial increase in R values is seen at tide gauge locations near the U.S. and Canada coasts. Most of the tide gauges over the open ocean are located between  $100^\circ\text{E}$  and  $160^\circ\text{W}$  over the global ocean. For these stations, correlations tend to be larger near the equator and smaller near  $20^\circ\text{N}$  or  $20^\circ\text{S}$ , perhaps

reflecting the larger and thus better resolved equatorial scales. Stations are plotted in order of decreasing correlation, so that a station with lower correlation will never be obscured behind a station with higher correlation.

The model success in predicting SSH can also be seen in nondimensional SS values (Fig. 44). The stations are plotted in order of decreasing SS, similar to the correlation plots. Any positive SS indicates model skill in predicting SSH, with perfect skill over the year indicated by a SS of one. Positive skill is indicated over most of the global ocean, with negative skill primarily for scattered stations in the central basins or along western boundaries. Skill is particularly high in eastern boundary regions, which may reflect relatively higher dependence on direct local wind forcing.

We summarize the results by providing median values of each statistical metric for each year rather than providing individual statistical values at each tide gauge location. Median RMS, R and SS values are given in Table 2. These were calculated using 1-day and 30-day running averages of SSH time series from tide gauges and  $1/8^\circ$  NCOM. In the median statistics analysis, there are a total of 189, 181, 151 and 91 tide gauges based on the daily averaged SSH time series and 187, 177, 137 and 90 tide gauges based on the 30-day running averaged time series in 1998, 1999, 2000 and 2001, respectively.

Both free-running and assimilated  $1/8^\circ$  NCOM simulations reproduce the correct SSH phase with median  $R > 0.70$  in all years. All median SS values are positive, showing the success of the model. Ocean data assimilation in the model always improves the median SS value, and this remarkable improvement is especially evident in 2000 when using either 1-day or 30-day statistics. Overall, the median RMS differences are approximately 6 cm and 3 cm in all years from 1998 to 2001 when using 1-day and 30-day statistics, respectively.

Finally, overall NCOM performance in predicting SSH is assessed for the 4-year period during 1998-2001 by combining tide gauge statistics from all years. This yields a total of 612 (591) year-long SSH time series over 1998-2001 based on the 1-day (30-day running average) statistics, representing over 200,000 individual comparisons. It should be noted that we only use tide gauge locations which have at least 100 day-long SSH time series in a given year. For each set of statistics we also calculate class intervals for RMS difference, R and SS to examine the distribution of statistical metrics using histograms. As seen from Fig. 45, there are 134 (146) year-long tide gauge time series that have RMS differences between 2 and 3 cm from the free-running (data-assimilative)  $1/8^\circ$  NCOM simulations when using the 30-day running averages of time series. Most of the R values are  $> 0.7$ , and assimilation generally improves R values. A notable improvement from the data assimilation in predicting SSH is seen from the SS class intervals. There are a total of 118 year-long tide gauge time series where the free-running  $1/8^\circ$  NCOM simulations did not yield skillful SSH prediction ( $SS < 0$ ). With data assimilation this number is reduced to 71 out of 591 cases. This improvement even more notable because SSH is not directly assimilated; assimilation of profiles of temperature and salinity leads to generally improved calculations of SSH.

The statistics are substantially improved by using a 30-day versus a 1-day running average. In part, this is due to the temporal resolution of the altimeter data as evidenced by the larger percentage-wise improvement in RMS difference from data assimilation with the 30-day running averaged time series (Fig. 46). The median RMS difference is 5.98 cm (3.63 cm) when using daily (30-day running averaged) time SSH time series in the free-running model-data comparisons. Similarly, the median RMS difference is 5.77 cm (3.36 cm) when using daily (30-day running averaged) time SSH time series in the data-assimilative model-data comparisons.

There are approximately 52% (66%) cases when  $R > 0.7$  calculated from daily (30-day running averaged) SSH time series for the free-running model simulations. In the case of the data-assimilative model simulations, approximately 61% (75%) cases have  $R > 0.7$  when using daily (30-day running averaged) SSH time series in calculations. Based on the SS class intervals we conclude that free-running model resulted in approximately 20% (118 out of 591 tide gauges) unrealistic predictions and data-assimilative model resulted in approximately 12% (71 out of 591 tide gauges) unskillful predictions ( $SS < 0$ ) during 1998-2001. Low skill stations are scattered among stations of positive skill, but show a tendency toward the western boundary current regions and islands of the south-central Pacific.

## Upper Ocean Buoy Time Series

Upper ocean quantities from NCOM are validated in part using buoy time-series observations reported from three sources: (1) the Tropical Atmosphere-Ocean (TAO) array (McPhaden *et al.*, 1998), (2) the Pilot Research Moored Array (PIRATA) (Servain *et al.*, 1998), and (3) the National Oceanic Data center (NODC) database, accessed from the internet site <http://www.nodc.noaa.gov/BUOY/buoy.html>. The TAO array, located in the equatorial Pacific Ocean, consists of approximately 70 buoys between  $8^{\circ}\text{S}$  -  $8^{\circ}\text{N}$  and  $137^{\circ}\text{E}$  -  $95^{\circ}\text{W}$ . The PIRATA is an array of 12 buoys in the Tropical Atlantic and is very sparse in comparison to the TAO buoys. The NODC database holds different types of buoy observations collected by the National Data Buoy Center (NDBC), and these buoys are located in the Gulf of Mexico and along the U.S. eastern and western coasts, Great Lakes, Hawaii and Alaska coasts. Because NCOM does not assimilate any buoy data over the period of this study, validating model results using buoy observations from TAO, PIRATA, and NDBC serves as an independent verification. All the buoys monitor different upper ocean quantities. These buoy observations (or calculated quantities) include daily-averaged time series of SST, SSS, mixed-layer depth (MLD), subsurface temperatures, and subsurface salinities. The TAO and PIRATA buoys do not directly report MLD, but they provide subsurface temperatures measured at several depths down to 500 m from which MLD can be calculated. There were no subsurface temperature time series available from the NDBC buoys. Therefore, no MLD time series from the NDBC buoys are used for the NCOM intercomparisons. We use buoy series that do not have a lot of data voids. When a few data voids were found in the time series, they were filled using linear interpolation.

## SST

A set of 81 moored buoys is used for the NCOM SST intercomparisons, equivalent to over 30,000 comparisons. These include 38 TAO buoys, 4 PIRATA buoys and 41 NDBC buoys located in different regions of the global ocean (Fig. 47). There are buoys located in relatively shallow coastal locations (most of the NDBC buoys) and in the open ocean (the TAO, PIRATA, and a few of the NDBC buoys). All the buoys report hourly SST measured at a depth of approximately 1 m below the sea surface. An assessment of instrumental accuracies indicates errors of about  $0.03^{\circ}\text{C}$  for buoy SST (Freitag *et al.*, 1994). We extracted from these buoys a set of 219 unassimilated year-long buoy time series for model validation from 1998-2000.

For the model-data comparisons, daily-averaged buoy SSTs were formed. No smoothing was applied to the original values. Daily snapshot SSTs from NCOM were also extracted at the buoy locations. Note that the average latitude/longitude positions of the buoys are used to extract SST from the model grid although buoy locations can change from day to day, and they may also

change by a few km whenever a mooring is recovered and a new one redeployed. It should be remembered that NCOM used in this study assimilates  $1/8^\circ$  MODAS SST analysis of satellite IR data, so the model-data comparisons presented here also include the MODAS SST to indicate for SST the appropriateness and effectiveness of the model assimilation procedure. Also note that the MODAS analyses used for comparison and assimilation use MCSST observations only, leaving the *in situ* observations independent for validation purposes.

Fig. 48 show daily SST time series from the buoy observations, NCOM, and MODAS during 1998 and 1999. As examples to illustrate the model assessment procedure used for buoy SST, detailed model-data comparison results are shown for nine buoy locations. These are chosen to represent different regions over the global ocean. Three are eastern equatorial Pacific TAO buoys (Fig. 48;  $0^\circ\text{N}, 125^\circ\text{W}$ ;  $0^\circ\text{N}, 140^\circ\text{W}$ ;  $2^\circ\text{S}, 110^\circ\text{W}$ ;). These sources record the  $\sim 6^\circ\text{C}$  cooling in ambient SST associated with the 1998 El Niño to La Niña transition. All cases tend to be cool during El Niño, perhaps because the MODAS climatology used to fill cloudy, data-sparse regions prior to assimilation is cooler than the extreme El Niño water. Agreement is significantly closer during La Niña, even for the free-running case. SSTs in the assimilative case tend to lag the observations and MODAS assimilation fields during the El Niño to La Niña transition, perhaps indicating a need for stronger relaxation to MODAS SST near the equator.

The remaining sample time series are from 1999. Four are NDBC buoys around the United States: a coastal buoy in the Gulf of Mexico (Fig. 49a;  $30^\circ\text{N}, 89^\circ\text{W}$ ), a buoy over the inner shelf of the U.S. mid-Atlantic Bight (Fig. 49b;  $40^\circ\text{N}, 73^\circ\text{W}$ ), a deep water NDBC buoy off the central California coast (Fig. 49c;  $38^\circ\text{N}, 130^\circ\text{W}$ ), and a high-latitude buoy off Alaska just south of Prince William Sound (Fig. 49d;  $60^\circ\text{N}, 147^\circ\text{W}$ ). The remaining two are a PIRATA buoy from the central equatorial Atlantic ( $10^\circ\text{S}, 10^\circ\text{W}$ ) and a TAO buoy from the western Pacific equatorial warm pool ( $2^\circ\text{N}, 156^\circ\text{E}$ ). All cases indicate reasonable correspondence between the observations, assimilation SSTs (MODAS) and the assimilative model. The agreement between the data and the free running case is also fairly good in most regions save the western Pacific equatorial warm pool (Fig. 49f), where the free running case is about  $2^\circ\text{C}$  cooler. About 10% of the time series for this comparison are from the western equatorial Pacific region  $5^\circ\text{S}-8^\circ\text{N}$ ,  $147^\circ\text{E}-165^\circ\text{E}$ , so the relatively large errors in the free running case for this region will have a significant impact on the final statistics. Fig. 50 summarizes the results for the entire data set. Compared to the buoy observations, assimilative NCOM SST has a root mean squared difference (RMSD) of  $0.54^\circ\text{C}$  and a mean correlation of 0.95. Additional comparisons between global NCOM and buoy time series may be found in Kara *et al.* (2006).

Comparisons were also made with monthly means from the 9 km Pathfinder SST climatology (Casey and Cornillon, 1999). The Pathfinder fields are based on the same AVHRR data used by the MODAS2D SST products, but the processing used by Pathfinder is independent from the NAVOCEANO data used by MODAS, with potentially different results. The MODAS SST data are a real-time operational product, while the Pathfinder are a reanalysis long after the observation time. We regridded NCOM to the Pathfinder grid and computed a difference at each point for which Pathfinder had a value. NCOM and Pathfinder means for October 2000 are shown in Fig. 51. The pathfinder monthly means were a composite of cloud-free observations in each grid cell over a month. Thus some grid cells might be a mean of 30 observations while others might represent a single observation. NCOM mean monthly SST fields are a mean of snapshots from each day of the month and have no missing data. Pathfinder regions with no data are indicated in grey (Fig. 51c) and are excluded from the comparison statistics. NCOM fields are noticeably smoother than the Pathfinder composites, probably due both to real variations not

captured by the model or its forcing and to the cloud-induced sampling irregularities in Pathfinder.

To compare NCOM and Pathfinder, we subtracted Pathfinder monthly means from the corresponding means of free-running and data-assimilative NCOM. Examples for October 2000 are shown in Fig. 52. These show that for October 2000, NCOM tends to be warmer than Pathfinder in high latitudes and in the eastern edges of the ocean basins, and cooler than Pathfinder for much of the ocean interior. Fig. 53 summarizes the data comparisons with time series of mean error and RMS error from 1998-2000. These results confirm that free-running global NCOM has a significant cold bias relative to Pathfinder and assimilative NCOM. We will examine this bias more with the evaluation of 7-day NCOM forecasts. Assimilative NCOM has a global cold bias of  $-0.09^{\circ}\text{C}$  relative to Pathfinder, with most of this bias occurring in 1998-1999. Overall bias for assimilative NCOM in 2000 appears to be negligible. Global RMS difference is  $1.36^{\circ}\text{C}$  for free-running NCOM and  $0.75^{\circ}\text{C}$  for assimilative NCOM during 1998-2000.

To analyze global SST forecast bias over operationally-relevant forecast scales, we compared means of forecast fields to corresponding means of analysis nowcast fields. Mean SST files were calculated for each 24-hour forecast increment over 1998-2002. For example, we calculated a mean of 48-hour forecasts. SST means were calculated for the corresponding SST nowcast analyses and subtracted from the forecast means. This global forecast bias for SST bias is shown in Fig. 54. The analyses indicate a slight global SST bias of  $-0.009^{\circ}\text{C}$  for 24 hour forecasts and  $-0.05^{\circ}\text{C}$  for 7-day forecasts. Although these biases are well within observational precision, they do indicate a tendency in the model which will be addressed by future refinement.

## Temperature Profiles

Unlike the NDBC buoys, both TAO and PIRATA buoys report subsurface temperatures measured at various depths from surface down to 500 m. The buoys reporting subsurface temperatures can be considered under two categories based on the water depths at which subsurface measurements are taken. These groups are identified in Fig. 55, which indicates the positions of buoys providing 95 unassimilated, year-long time series of temperature profiles used for validation of NCOM temperature profiles for 1998-2001, representing of 34,000 profiles. Type I buoys, in the equatorial Atlantic and western equatorial Pacific, have sensors at 1, 20, 40, 60, 80, 100, 120, 140, 180, 300 and 500 m. Type II buoys, in the central and eastern equatorial Pacific, mount sensors at 1, 25, 50, 75, 100, 125, 150, 200, 250, 300 and 500 m. An assessment of instrumental accuracies indicates about  $0.1^{\circ}\text{C}$  for subsurface temperature (Freitag *et al.*, 1994). Similar to SST, a few missing values were filled using linear interpolation. For model-data comparisons, no smoothing was applied to buoy subsurface temperatures, and no buoy temperatures were used in NCOM assimilation. NCOM subsurface and MODAS climatological temperatures were interpolated to the observation depths for each type of buoy.

Statistics resulting from the standard suite of time series model data comparisons are presented in Fig. 56. Distinguishable differences are evident between the two sets of buoys and between the models and climatology. The impact of the SST cold bias is seen in Fig. 56a, where for the model results, both sets have a  $0.2^{\circ}\text{C}$  or colder bias in the upper 50 m. For the western equatorial Pacific (set II) buoys, climatology has a slight cold bias in the upper 50 m that grows to  $0.5^{\circ}\text{C}$  cold down to 150 m. The bias of the model is fairly uniform  $-0.25^{\circ}\text{C}$  for the western buoys down to 150 m. In contrast, the climatological bias of the eastern equatorial Pacific and equatorial Atlantic buoys is warm in the upper 300 m, reaching a maximum of  $1.5^{\circ}\text{C}$  at 100 m.

The mean bias probably reflects a preponderance of La Niña or absence of El Niño conditions in 1998-2001 relative to the MODAS climatology. The model mean bias for the eastern buoys varies between  $\pm 0.5^\circ\text{C}$  and is smaller in magnitude than the climatological bias at all depths other than the upper 20m, a reflection of the model cold SST bias.

The case of RMS error is presented in Fig. 56. By this measure, for the eastern buoys global NCOM is superior to climatology for all depths between 20 m and 300 m and otherwise equivalent; the situation is reversed for the western equatorial Pacific buoys. In an absolute sense climatology is significantly worse in the western than eastern region. Model performance is similar in each region, with maximum RMS error at quite different depths, 80 m for eastern Pacific and equatorial Atlantic and 150 m for the western equatorial Pacific. Fig. 56d shows that these depths correspond to the maximum standard deviation from the observations, interpreted to be the base of the thermocline. Global NCOM correctly locates the base of the thermocline in both sets of buoys, while climatology has the base of the thermocline too deep for the Atlantic and eastern Pacific buoys. Correlation (Fig. 56c) is superior for the model over climatology and above 0.85 for the upper 100 m in both cases. At deeper depths the relative performance of model and climatology is mixed for correlation. Skill score (Fig. 56e) is above 0.7 for the model at all depths above 100 m for the eastern buoys and all depths above 200 m for the western buoys, meaning the models have maximum skill above to just below the base of the thermocline. In both cases skill score shows high model performance in the upper 300 m and superior model performance relative to climatology in the upper 100-150 m.

## Mixed Layer Depth

Temperature comparisons from the prior section showed the relatively high performance of the model in predicting temperature itself in the upper 100-150 m, but examining the mixed layer will determine whether the better individual temperatures translates into an improved derived quantity, mixed layer depth (MLD). MLD is calculated from the same set of buoys used in the comparisons of temperature profile but limited to 1998-2000, as shown in Fig. 57. Surface ocean layer depth can be calculated at these buoy locations because subsurface temperatures from buoy, NCOM, MODAS and MODAS climatology are available.

There are two commonly used surface ocean layer depth definitions: (1) an isothermal layer depth (ILD), and (2) an isopycnal layer depth (MLD). The methodology for inferring the ILD and MLD used in this paper is fully described by Kara *et al.* (2000a), showing that MLD is best defined using a variable density definition. In brief, the ILD [MLD] can be summarized in its simplest form as being the depth at the base of an isothermal [isopycnal] layer, where the temperature [density] has changed by a fixed value of  $\Delta T$  [ $\Delta\sigma_t$ ] from the temperature [density] at a reference depth of 10 m. For the isopycnal layer this means  $\Delta\sigma_t = \sigma_t(T+\Delta T, S, P) - \sigma_t(T, S, P)$ , where P is set to zero. Density is usually calculated using an equation of state with no pressure dependence (Millero *et al.*, 1980; Millero and Poisson, 1981).

While daily salinity values from NCOM, MODAS and MODAS climatology are available at the buoy locations in 1998-2000, daily collocated salinity measurements from buoys were not available. To be consistent with all products, we calculated true surface ocean layer depth based on the ILD definition (temperature-based) rather than MLD definition (density-based via salinity). It is noted that specific attention needs to be given to calculation of layer depth, especially in the equatorial Pacific due to existence of barrier layers as explained by Kara *et al.* (2000b). Although the ILD definition with a  $\Delta T$  value of  $0.5^\circ\text{C}$  is approximately equal to

optimal MLD at the equatorial ocean, this constant value can be quite variable from one location to another (Kara *et al.*, 2003b). Thus, we use a location-specific  $\Delta T$  value determined at each buoy location obtained from the annual mean  $\Delta T$  map of Kara *et al.* (2003a). This annual mean field provides spatial variation of  $\Delta T$  values at each  $1^\circ \times 1^\circ$  grid cell, allowing us to obtain an ILD that is equivalent to the optimal MLD at each buoy location. This is referred to as MLD.

Fig. 58 shows an example of the mixed layer depth superimposed on temperature profiles for the upper 150 m for a 2001 buoy in the central equatorial Pacific. Climatology produces a very smooth estimate of MLD, with somewhat more daily variability introduced in the MLD from NLOM-based MODAS synthetics which are assimilated by global NCOM. Realistic variability in MLD is evident only in the global NCOM case. MLD in both the observations and model varies around 90-100 m depth. Overall, the model results for the comparisons with observations show a 19 m RMS error, 8 m shallow bias and -0.21 skill score for predicting MLD for these buoys. Thus even though skill in predicting temperature in the upper 150m is above 0.5 and mostly above 0.7, the model does not show overall skill in predicting the derived MLD. The roughly 10% shallow bias in mixed layer depth needs to be addressed to allow the model top have predictive skill for MLD in the equatorial Pacific. This is discussed further in the section on model recommendations.

## Drifters

Webb Dewitt, recently retired from FNMOC, evaluated the global currents from NCOM by using surface velocity fields from the assimilative global NCOM to advect simulated drifters. For validation, Dewitt used a set of World Ocean Circulation Experiment (WOCE) drifter trajectories from June – November 2000, a controlled data set that he had hand-edited for quality control and sampling bias. Observed trajectories were divided into 7-day segments, and simulated drifters were inserted into the model velocity field at the start time and locations of these segments.

Fig. 59 depicts a set of WOCE drifter observations (black) and NCOM drifter simulations (green) in the North Atlantic for a 7-day period in 2002. This example illustrates the difficulty of simulations with a small number of drifters in regions with eddies and energetic fronts. Two WOCE drifters are in the vicinity of the Gulf Stream, near  $67^\circ\text{W}$ . The northern one is being advected along the main Gulf Stream, while the southern one is trapped in an eddy; both features are evident in the NCOM height field. However, slight errors in time and position of fronts cause the NCOM drifter fates to be different. In NCOM, the eddy has not yet pinched off from the Gulf Stream, so both NCOM drifters are transported around the pre-separation Gulf Stream loop. At  $47^\circ\text{W}$ , NCOM has prematurely pinched off a cold core ring south of the Gulf Stream, causing the NCOM trajectory to travel the short distance north of the cold core ring while the observed trajectory travels around the pre-separation cold loop. A similar difference occurs at  $57^\circ\text{W}$ , where the NCOM drifter is entrained into a warm core ring while the observed trajectory remains in the current core. In these regions, an ensemble approach to trajectory prediction might be more appropriate.

In any case, a large number of trajectories are necessary to make any meaningful statements regarding relative prediction fidelity. Thus on the plots of summary statistics for trajectories simulated by global NCOM and persistence (no movement), a 95% confidence interval is provided. This interval assumes a normal distribution for the statistic of end point separation, an assumption that may or may not be true in each of the regions. The regions include

the equatorial Pacific (Fig. 60a), equatorial Indian (Fig. 60b), South Atlantic (Fig. 61a), equatorial Atlantic (Fig. 61b), and western Atlantic (Fig. 61c), the last of which includes the Gulf Stream. NCOM trajectories in this evaluation prove better than persistence in all regions but the western Atlantic, where NCOM is slightly worse but negligibly different compared with the large confidence interval due to the small sample size and high variability. Only the equatorial Pacific has a sufficient sample size to show that NCOM predicts trajectories that are significantly superior to persistence. An approach we did not try but which might be useful would be a calculation using ensembles of predicted trajectories with small deviations in starting time and location. This might prove to be a superior trajectory estimate and a more discriminating statistic.

## Current Sections

The 3-year 1998-2000 mean velocity fields for the assimilative  $1/8^\circ$  global NCOM are sampled to allow comparisons with historical mean velocity sections found in various published sources. In all cases the specific dates used to compute the means are different, generally not overlapping, and typically over a shorter time period in the historical records. Thus errors attributable to interannual or stochastic variability account for some of the differences between the samples. However, similarities between the model and observed sections add to confidence in the NCOM simulations, while differences may point to model deficiencies in addition to natural variation.

### Western Atlantic

The published source for the historical figures used in these comparisons is Schmitz (1996), which itself adapted the figures from an even earlier source (Richardson *et al.*, 1969). Locations of sections are shown in Fig. 62a in the source depiction and Fig. 62b as applied to extraction from global NCOM. Note that the original oblique Straits of Florida section has been converted to a purely meridional section for extraction from NCOM because the vector transformation has not been formulated for calculating and plotting NCOM currents normal to a oblique section. For the same reason, comparison with the Cape Fear (final) section has been omitted. Also note that although the label on the original plot for section III (Fig. 65) indicates  $24^\circ 45'$ , comparison with Fig. 62a, Fig. 64a, and the extraction from global NCOM indicate this is probably a typographical error which should read  $25^\circ 45'$ ; the latter latitude is used for the comparison. The complete set of comparisons is shown in Fig. 63, with an additional mean without direct comparison at  $27^\circ\text{N}$  (Fig. 66) to include a commonly referenced section. Overall the NCOM sections compare reasonably well to current patterns observed in the historical data. Peak NCOM currents tend to be 40-60 cm/s low in the southern sections and 80cm/s low in the northernmost section off Cape Fear. Models typically output currents in the Gulf Stream at a lower value than is realistic (Schmitz, personal communication.) In addition, the finer details of bathymetry in the observed sections are not replicated in the relatively coarse NCOM grid. Irregularities in the extracted currents, possibly due to a combination of regridding issues and unresolved boundary processes, are evident particularly clearly in Fig. 66, Fig. 67b and Fig. 68b. Relatively weaker currents in Section I (Fig. 63b) may be a combined effect of a zonal versus oblique section, broader opening in the model, or diversion of water east of Cuba.

## Western Pacific

Fig. 70 locates seven sections in the vicinity of Taiwan along which mean currents from the assimilative  $1/8^\circ$  global NCOM were extracted for comparison with historical means from various sources. Extractions from global NCOM in the western Pacific tend to have smoother features in the currents and bathymetry than the historical observations, a consequence of the coarseness of the model relative to the historical surveys. In general, the major attributes of the sections are replicate reasonably well in strength and position by global NCOM.

For the section across the Luzon Strait, data from ADCP observations in Fig. 71a (Liang *et al.*, 2003) agrees well with the historical mean from assimilative NCOM (Fig. 71b). In the northern half of this section, both sets of results indicate a strong mean western intrusion of the Kuroshio into the South China between  $20^\circ\text{N}$  and  $21^\circ\text{N}$ . A mean return current of approximately equal strength flows eastward between  $21^\circ\text{N}$  and the southern coast of Taiwan. For the westward intrusion, NCOM produces a mean subsurface (50-150 m) inflow in the southern half of the section that is stronger than observed, perhaps due to some impeding islands not included at the global resolution. This excess subsurface inflow in the southern half of the section results in NCOM subsurface inflow weaker at these depths than the observed mean at  $21.5^\circ\text{N}$ .

The east-west section through the Luzon Strait (Fig. 72) shows similarly close agreement. Relatively strong northward currents pass on either side of a weak return or quiescent region centered along the Strait at  $121.5^\circ\text{E}$ . The strong, small scale recirculation along the axis of the Strait is not resolved by the global model.

Fig. 73a (Liang *et al.*, 2003) shows northward velocity across four sections east of Taiwan. Agreement is similar to that seen in the Gulf Stream, with maximum currents in the model 10-20 cm less than the observed extrema and the strongest gradients adjacent to the boundary somewhat smoothed. A somewhat circuitous section near the northern end of Taiwan (Fig. 74a; Lee *et al.*, 2001) it approximated as an east-west slice from NCOM. The westward intensification of the Kuroshio agrees between the sections, but the model is slightly weaker and less concentrated against the western boundary, an indication that at this resolution the model is insufficiently inertial to fully represent this feature. This section also highlights the relative coarseness of the model bathymetry in comparison with observations at this level of detail.

## Equatorial Pacific

Fig. 75 locates an along-equator and a cross-equator section used from validations of global NCOM in the equatorial Pacific. Along the equator, we compare model results (Fig. 76b) with the mean eastward current (Fig. 76a) as calculated by Johnson *et al.* (2001) using ADCP observations from 1991-1999. Note that in contrast to most of the velocity sections in this paper which show speed directed normal to the section, Fig. 76 contours speed tangential to the equator. Also in contrast to most other comparisons, the model includes far more resolution and detail than to the observations. Both show a mean westward flow at the surface, the South Equatorial Current (SEC), extending to a depth of about 50 m in the west and shallowing to about 25m in the east. Under this both show a mean eastward Equatorial Undercurrent (EUC) with peak speed around 90 cm/s. The undercurrent core shallows from between 150-200 m in the east to between 75-125 m in the west. Global NCOM produces a more continuous EUC, slightly stronger than the observations in the east and slightly weaker in the west. Many of these differences may be attributable to sampling error or bias due to insufficient sampling over El Niño/La Niña cycles. Overall agreement is quite good.

A cross equator section and associated normal velocity cross section are depicted in Fig. 77 (Johnson *et al.*, 2001). From south to north, the features of interest are a westward SEC between 8°S and 5°N, an eastward EUC centered on the equator, and an eastward North Equatorial Countercurrent (NECC) north of 5°S. The SEC is divided into two lobes, one on either side of the equator, with the stronger and narrow lobes on the northern side. The SEC and NECC agree well in strength and position between the observation and model, particularly in the upper 150 m. Differences in the weak currents below 150 m are in the insubstantial details. The EUC is slightly narrower in the model and stretches the EUC too deep below 150 m, likely a consequence of insufficient resolution for representing the EUC at these depths. As in the other current sections, overall agreement was good. For the collocated temperature cross section (Fig. 78), the 25°C isotherm barely outcrops in NCOM but remains submerged in the observations. The strength of the thermocline appears slightly stronger in the observations. The depth of 13°C isotherm, near the base of the thermocline, follows a similar path in both cases while shallowing from near 250 m at 8°S to near 175 m at 8°N and includes local depth minima on either side of the equator.

## Transports

Another source of model validation is through comparison with observed mean transports through various straits or defined sections. A comprehensive list of transports calculated for sections all over the world is presented in Table 3. We will examine the transports in more detail for selected regions. For example, annual mean transports through the Intra-American Sea obtained from the global NCOM are compared to the observed transports in Fig. 79. We begin by focusing on this region was chosen because there are a large number of observations in the Caribbean and Greater Antilles passages. With the availability of recent observations, meaningful estimates of the average passage transports and their ranges of variability provide an excellent source for model-data comparisons. We use the summaries of observed transport estimates from Johns *et al.* (2002) for our observation standards in this region. It is noted that transport values reported in this paper come from a variety of different sources using different methods, including derivation from velocity measurements. For this comparison, the transport values from NCOM were obtained using only a 2-year mean during 1998-1999. NCOM transports agree fairly well with the observations in most of the sections. Some of the differences may be attributable to interannual variability between the 2-year model mean and the various observation periods and averaging intervals of the observations. We note that the largest NCOM inflow into the Caribbean is shifted slightly northward relative to the historical observations in the Lesser Antilles. This is true for both the assimilative and free-running cases. As noted previously, the assimilative NCOM has relatively low EKE in the Caribbean, suggesting that modifications to the assimilation procedure may particularly improve fidelity in this region.

## Forecasts

To evaluate global NCOM forecasts, we initialized 7-day free-running forecasts after every 15 days of integration of the assimilative global NCOM run from 1998-2002. These are the forecasts used in producing the analysis of bias in forecast SST (Fig. 54). Initial assessments of forecast skill quantify the ability of the model forecasts to replicate subsequent model analyses with full assimilation. We will examine two statistics for two fields, mean error and RMS error, where the mean of each is over space and/or time, for SSH and SST. Forecasts are evaluated for

ability to predict the subsequent model nowcast within assimilation. For comparison, we also calculate the errors in using persistence of the analysis field on the forecast day. For example, on day 1 we make a nowcast, a 24-hour forecast, and a 48-hour forecast. On day 2, we subtract the day 2 nowcast from the day 1 nowcast to calculate a 24-hour persistence error, and we subtract the day 2 nowcast from the day 1 24-hour forecast to calculate a 24-hour forecast error. On day 3, we subtract the day 3 nowcast from the day 1 nowcast to calculate a 24-hour persistence error, and the day 3 nowcast from the day 1 48-hour forecast to calculate the 48-hour forecast error. These ocean forecasts use nowcast quality atmospheric forcing, so errors in the forecasts in these evaluations are attributable to the ocean model and not due to sup-optimal atmospheric forcing.

Global summary results for SSH and SST are reported in Fig. 80 and Fig. 81. In both cases, forecast has smaller absolute error and mean squared error, where the mean is over the globe and time from 1998-2002. Relative forecast skill over persistence is higher for SSH than for SST. Plan views of forecast errors provide insight into the spatial distribution of forecast errors, indicating where relative forecast skill is high and where it has problems. Fig. 82 illustrates the forecast and persistence errors in the Gulf Stream and Kuroshio regions. Relative forecast errors as seen in Fig. 82 are particularly good on the mid-Atlantic coast and in the Yellow Sea because the dynamic response on the inner shelf is largely a deterministic response to the wind forcing. By using hindcast winds, we eliminated errors due to the atmospheric forecast and thus were able to accurately forecast deterministic processes. Relative forecast skill is lower along the main fronts, reflecting the free-running difficulty in representing these frontal dynamics at  $1/8^\circ$  resolution. Results for the Agulhas region and Indian Ocean (Fig. 83) show similar overall skill, with relative difficulty evident in representing the dynamics of the Agulhas Retroflection at  $1/8^\circ$ .

Recall that for the global 1998-2002 mean, forecast SST over 7 days showed only modest improvement over persistence (Fig. 81). Analysis of the spatial distribution of errors (Fig. 84-Fig. 85) demonstrates that a good deal of variation is masked by the overall global mean similarity. For almost the entire ocean, forecast SST clearly has errors smaller than persistence, but at some points immediately adjacent to land, the model forecast has errors that are quite large, in excess of  $1.5^\circ\text{C}$ . We attribute these errors to inadequate land masking of the regridded NOGAPS global atmospheric forcing. We receive the NOGAPS data after it has been regridded from its native grid to a uniform  $1^\circ \times 1^\circ$  lat-lon grid. In this regridding, we lose the ability to reference the atmospheric fields to their native land-sea mask. Because atmospheric stress and heat flux values typically have large gradients between land and sea points, problems can arise if forcing values appropriate to land are applied to ocean areas. In the assimilative model, relaxation to the MODAS2D SST mitigates the effect of inappropriate forcing, but this relaxation is not present in the free-running forecasts. A likely solution is to use the atmospheric forcing directly from its native grid with a native grid land mask. A less attractive solution, but perhaps appropriate in a hindcast case where the native-grid data are not available, would be to use the present regridded atmospheric products with application of a more conservative land mask and then filling sea values to the nearshore regions. A third option would be to extend the assimilation of analysis SST into the forecast period with appropriate time/space weighting as reflected in the expected relative errors.

## **Event Comparisons**

A validated real time, fully global ocean modeling system not only continually provides model nowcasts and forecasts wherever they are needed, but also affords a level of confidence in these products based on the verified level of performance in prior products. These global products may be of sufficient resolution and detail to be used as standalone products, or they may be used as initial and boundary conditions for specialized, higher-resolution models that focus on a limited time and area of interest. In either case, it is the fundamental level of confidence afforded by the prior model validation, knowledge of the places and circumstances in which the global system is strong or suspect, that is of essential value for results from the global system.

Another value of the global system is that validation can occur when and where observations are available. Since we are unable to sample the ocean thoroughly at all times and places, or to anticipate all times and locations for which detailed observations are required, we must rely on systems combining ocean observations and models, in which the observations are used for independent model validation or assimilated to keep the models on track. We thereby have increased confidence in model analyses and predictions that extend to times and locations devoid of supporting observational data.

In this set of event comparisons, we survey a variety of observational sources for corroboration of model snapshots. Some of these episodic data sets are suited for quantitative comparisons and similar to data previously used in more comprehensive comparisons, such as sea surface height from a deployed buoy or sections of ocean currents from a shipboard ADCP. Other observations are applied in ways indirect in terms of the quantities being measured. These are primarily used for qualitative comparisons of feature location using gradients of visible color or other wavelengths from satellites.

### **Kuroshio Extension**

In the same way that mean NAVOCEANO front analyses were used to validate the location of mean fronts, a set of frontal analyses for a particular day can be used to validate the corresponding surface expression of a global NCOM snapshot. Three plots (Fig. 86) are shown for 11 November 2001, each overlaid with the Kuroshio north wall frontal analysis for the same date. All show adequate agreement between the model fronts and observations, indicating that the details in front location from NLOM SSH (Fig. 86a) are successfully transmitted to global NCOM (Fig. 86b,c) via the assimilation of NLOM-based MODAS synthetic temperature and salinity.

### **Arabian Sea**

The next event comparison focuses on a region of continuing Navy interest, the northwestern Arabian Sea. During 30 September – 7 October 2002, a fairly clear composite image of the diffuse attenuation coefficient at 532 nm (Fig. 87a) was produced from analyses of Moderate Resolution Imaging Spectroradiometer (MODIS) data by the Ocean Optics section at NRL (Ocean Color at <http://www7300.nrlssc.navy.mil/products.html>). A span over several days is used to piece together cloud-free sections into a composite that has relatively low cloud contamination but is sufficiently synoptic over the observed scales to reasonably represent mesoscale ocean features. Global NCOM SSH (Fig. 87b) is extracted for 3 October 2002, the midpoint time of the MODIS composite. The two images show similar patterns of alternating

cyclonic and anticyclonic eddies along the coast of Somalia. Eddies located by SSH extrema and closed circulation patterns in the global NCOM analysis agree well with MODIS features delineated by gradients in diffuse attenuation coefficient. NCOM relies on assimilation of NLOM-based MODAS temperature and salinity fields to keep eddy fields in agreement with reality. Thus this successful comparison implies that the assimilation procedure is successfully transferring essential front and eddy information from NLOM and MODAS2D SST.

### **Persian Gulf**

In the Persian Gulf, another region of high Navy interest, an evaluation of NCOM SSH is made for the period shortly before the official start of Operation Iraqi Freedom, 20 March 2003. A snapshot of  $1/8^\circ$  global NCOM SSH and surface currents is shown in Fig. 88a. Animations over this region indicate a range in excess of 1m for the non-tidal SSH variations in the northwestern and southern Persian Gulf with time scales of one day to a week. A Navy buoy deployed in late January 2003 measured sea level at a point in the northwestern Persian Gulf until damaged in mid-March. Its SSH signal has been detided and demeaned over the comparison period, as was done in prior global SSH validation. Comparisons of the buoy observations with the independent  $1/8^\circ$  global NCOM results referenced to the same mean (Fig. 88b) demonstrates the high level of accuracy of the model predictions in this area. Correlation was 0.89 over the two months of this comparison. Note that since the buoy time series was less than an entire year in duration, it was not included in the global statistics.

### **Oregon coast**

The Northeast Pacific Long Term Observation Program at Oregon State University (Smith *et al.*, 2001) has conducted oceanographic surveys along the Oregon Coast from 1997-2003. The cruise reports and additional information are available online from their website at <http://ltop.coas.oregonstate.edu/~ctd>. We have extracted plots of ADCP velocity sections from 1999-2002 from these reports for use in validation of NCOM currents in this region. Twelve of these sections are included with corresponding NCOM results and some discussion in Fig. 89 - Fig. 94. Note that the ADCP data do not extend shallower than 15 m and often omit the zone nearest to the shore. Also, the NCOM results are snapshots for a single instant in time, while the observations are over a 1-2 day survey. The relatively long interval may alias tidal or other frequency variations on scales similar to or smaller than the survey duration.

Despite these limitations, in many cases these global NCOM results are quite similar to the observations, at least for the larger scale features. Fig. 89 shows a particularly nice scenario in which the model replicates a reversal in the surface currents seen across a section surveyed on two consecutive days. The model and observations agree on the timing of the reversal within at least 24 hours, with a more precise determination requiring more details on the individual observations.

Late September 1999 was a period when the model was in poor agreement with the observations. The data are from 22-25 September over two sections, one along  $44.6^\circ\text{N}$  from September 22-23 (Fig. 90a,c) and the other along  $43.2^\circ\text{N}$  from September 24-25. Over this time span the global model results are structurally similar but in almost  $180^\circ$  directional disagreement with the data.

Over the remaining sections and times, the larger scale current structure is fairly consistent between the model and observations. The deep structure is typically smoother in the

model. The global model, with approximately 14 km horizontal grid spacing in this area, has insufficient intrinsic resolution to represent the sharp boundary fronts (Fig. 92), detailed topographic features, or sub-grid scale (horizontal and deeper vertical) details in the observations. The 1° spacing of the NOGAPS atmospheric forcing is similarly insufficient to provide hope of replicating the fine details of the measurements.

## 4. BOUNDARY CONDITIONS

### Regridding

The complex curvilinear,  $\sigma$ -z grid used for global NCOM has useful computational characteristics for representing the world ocean but is somewhat inconvenient for standard methods of representing or using gridded data. Typically, programs which display or ingest data for various applications prefer data on a regularly spaced grid. Since global NCOM is to be used to provide initial and boundary for horizontal domains which are not a direct subset of its global grid, a general method for data regridding has been developed. The generic regridding package for global NCOM builds on some of the logic from Spherical Coordinate Remapping and Interpolation Package developed by Jones (1998). Regridding is done on a point by point basis, allowing extraction of the data on random points, finite element grids, curvilinear horizontal grids, or regular constant-interval lat-lon grids, the standard used for data display. To save time and memory, the regridding program attempts to identify and load the minimum convenient data subset needed for the data extraction. Filling and masking is typically done on the output grid. Since the regridding usually treats any point that falls adjacent to a model water point as a water point, the regridding tends to overestimate the extent of water and should be remasked using the more precise bathymetry appropriate to the subset domain.

Regridding currents are a relatively difficult problem because of the staggered computational c-grid that does not collocate u and v velocity values. For a general regrid, the global NCOM velocity vectors are loaded, interpolated from the c-grid to the temperature points (referred to as a-grid points). Once collocated, the vector components are rotated from +i,+j components relative to the curvilinear computational grid to east, north components relative to geographic coordinates. These geographic coordinates are then interpolated to the output points and, if necessary, rotated to the output computational grid and possibly interpolated as vector components to an output computational staggered c-grid. At present, the subject of surface or bottom boundary conditions from global NCOM has not been discussed. This could perhaps be a future topic of research if there were sufficient interest from potential recipients of such boundary conditions.

### Tides

#### General Tide Products

There are two types of products for which tidal velocities and water levels are required. The first is to produce boundary conditions for nested models that require a full (i.e., global NCOM plus tide) solution along their open boundaries, and the second is to provide the full solution over areas where regional model solutions including tides are not available.

A similar approach is taken for each of these. In each case, a tide model solution for surface height and depth-averaged velocity is computed at each required location (grid points for regions, boundary points for nesting), and added linearly to the interpolated global surface height and velocity solution.

Two tide models are available. The first is the PCTides 2D tide- and wind-driven sea level prediction model, which can be configured to cover the region of interest and forced with global tide model heights along the boundary and IHO tide station data in the interior (Blain, *et*

*al.*, 2002). This approach requires that PCTides be configured on a domain larger than the true area of interest, so that the PCTides solution is not merely a copy of the global model solution that is applied at the PCTides boundary. The second tide model is the global tide solution referred to here as the Oregon State University (OSU) model (<http://www.oce.orst.edu/po/research/tide/index.html>; Egbert, Bennett, and Foreman (1994); Egbert and Erofeeva (2002)). The OSU model is produced using a barotropic model and assimilating Topex/Poseidon sea surface height observations. The set of 10 constituent (M2, S2, N2, K2, K1, O1, P1, Q1, Mf, Mm) amplitudes and phases for the tide height and barotropic transport is computed on a 1440x721, 0.25-degree latitude-longitude grid. The constituent data and extraction software are provided on an anonymous ftp server (accessible at <ftp://ftp.oce.orst.edu/dist/tides/Global>). The OSU tide solution is provided here as a simpler, more robust, and more efficient approach.

### **Tides for SWAFS boundary conditions**

The global NCOM support for SWAFS nests represents an improvement on the support from the present northworld SWAFS domain, as described above. The northworld SWAFS domain supports the Americas, Northwest Pacific, and North Indian Ocean SWAFS nests. The northworld implementation of the Princeton Ocean Model writes to disk boundary condition arrays for 3 external mode variables (elevation and depth-averaged velocity components), and 7 internal mode variables (three velocity components, temperature, salinity, and two turbulent kinetic energy fields for the mixed-layer model). Boundary conditions are written every five internal-mode time steps, which is every fifty minutes. Values are saved at the northworld grid points, for arrays dimensioned five grid points across the nest boundary, and an irregular number of grid points along the nest boundary (that is, dimensioned by the size of the overlapping northworld MPI sub-domains in the along-boundary direction).

To replace this support from the SWAFS northworld, the latitude-longitude-depth locations were calculated for the northworld grid points where data are currently saved to support the SWAFS nests, using the SWAFS northworld code and grid data. These values are stored in separate files for each nest boundary.

A standard global NCOM regridding routine is used to extract the corresponding surface elevation, depth-averaged velocity, horizontal velocity, temperature, and salinity at the northworld grid points, at the NCOM output times (presently, every three hours). Modified versions of the OSU tide extraction routines are used to compute tidal sea level and depth-averaged tidal velocity at the same horizontal locations, at the required fifty-minute interval. A final routine reads the stored global NCOM and OSU fields, interpolates the global NCOM data in time to the SWAFS output time, adds the global NCOM and OSU heights and velocities, adjusts the global NCOM horizontal velocity to the new depth-averaged value, and writes the boundary condition files in the present format of the northworld data.

Note that the vertical velocity and turbulence fields used in the SWAFS boundary conditions are not supported by the global NCOM output, and so are specified with uniform values ( $w=0.$ ,  $q2=q2l=1.e-8$ ).

### **Adding tides for regional solutions**

The global NCOM support for regional areas is fairly similar. A description of the desired region (i.e., latitude/longitude range and resolution, and depth levels) is passed to the

same regridding and OSU solution extraction routines. The time interval of the output is specified in minutes and defaults to one hour. The global NCOM solution for sea level and depth-averaged velocity is added to the OSU tide solution, and the global NCOM horizontal velocity is adjusted to the new depth-averaged value. The final variable set includes the sea level, depth-averaged velocity components, horizontal velocity components, temperature, and salinity, in NetCDF format.

## **Evaluation**

### **Regional tide solution**

A regional tide solution for the domain 100°W to 55°W, 5°N to 55°N at 1/8° resolution was implemented as a test of the NCOM/OSU regional postprocessing. The post-processing of NCOM output to produce a combined NCOM/OSU prediction is not very different from the production of NCOM-only output. The daily runs for 01-06 Dec 2003 were compared with the operational SWAFS Americas configuration for the same run days, using the observed water levels at the Duck, NC USACE pier tide gauge (NOAA/NOS/CO-OPS station 8651370; data available online at <http://www.co-ops.noaa.gov>). Unfortunately, comparing coarse-resolution model surface heights with coastal tide stations means taking model values at grid points right along the model ocean/land boundary. In this case, the relative amplitudes of water levels obtained by interpolating model fields to the tide gauge location may be influenced by the interpolation process, and we are only looking at data from one tide gauge as an example of the types of results obtained from the NCOM/OSU combination (that is, a degree of caution is in order in evaluating these results).

Fig. 95 shows the water levels obtained from the Duck, NC tide gauge along with sea surface heights obtained from the NCOM/OSU post-processing output, and SWAFS Americas operational model output. These outputs are shown from six consecutive days from December 1-6, 2003. The SWAFS Americas output are archived every 2 h, the NCOM/OSU data are obtained every 1 h, and the observed water levels are evaluated every 6 min. The comparisons reveal that the interpolated NCOM/OSU water levels display approximately the right amplitude and phase (this is determined largely by the OSU tide model solution, and that the 2-3 day trend over the forecast period (this can include wind-driven set-up and set-down in NCOM) is captured with varying skill. Both models get correct phase, but NCOM is closer on amplitude.

### **SWAFS boundary conditions**

A version of the SWAFS pacnest code was ported to the NAVOCEANO MSC IBM SP4 and compiled with automatic parallelization to improve the wallclock time to complete these runs. These runs were made using 32-bit real values for all fields. The initial restart file for both runs is a modified copy of the operational SWAFS pacnest restart file valid 23 May 2003. The initial surface-height running-mean and ice thickness fields were also taken from the operational run. All other input files except the boundary conditions were converted to 32-bit real IEEE files. The forcing fields and observational data were taken from the archive maintained by NAVOCEANO.

Two runs were configured. The first used the archived SWAFS northworld boundary conditions from the operational SWAFS pacnest archive, and the second used a time series of

boundary condition files compiled using global NCOM output and the OSU tide model as above. The boundary condition files were not converted to 32-bit IEEE format.

Three further modifications were made to initialize the NCOM/OSU run. The SWAFS temperature and salinity fields in the restart file were replaced with the global NCOM temperature and salinity fields valid on 23 May 2003. The Princeton Ocean Model background temperature and salinity fields in the “grid file” were replaced with the 2-year mean global NCOM temperature and salinity fields. At the same time, the horizontally-uniform background or reference density field in the “grid file” was also replaced with a new field calculated from the present pacnest code density subroutine.

The two model runs were integrated from 24 May to 19 July 2003 in hindcast mode; that is, only the 24 hindcast to bring the model up to the nowcast time each day was performed. No forecast results are evaluated here.

To examine the impact of using global NCOM with OSU tides as a replacement for SWAFS northworld for boundary conditions, we compared paired runs of the SWAFS pacnest, one with the original northworld boundary conditions, the other using the NCOM/OSU boundary conditions. The goal here is to determine whether using NCOM/OSU boundary conditions degrades the interior of the SWAFS solution. Fig. 96-Fig. 105 show horizontal and vertical sections of temperature, salinity, and zonal and meridional velocity. A subjective evaluation shows that the interior solution can differ substantially from the host-model solution at the boundary for both the SWAFS northworld and NCOM/OSU runs. Fig. 106-Fig. 109 show examples of the across-boundary variation in the temperature and along- and across-boundary velocity fields. In many respects, the interior solutions after the 56-day integration appear qualitatively similar, though obviously the use of a different host model does yield a quantitatively different interior. A similar pair of forecast runs will provide quantitative metrics for changes in forecast skill, but will require more resources.

It is possible that over the course of a longer integration, a departure of the SWAFS pacnest climate from the global NCOM host may cause larger, possibly adverse across-boundary gradients to evolve. Our experience with initializing the NCOM/OSU run shown here indicates that replacing the interior solution of the SWAFS pacnest with a snapshot of the global NCOM temperature and salinity fields in the future is an option. The SWAFS pacnest appears to settle the initial shock after about one week of integration in data-assimilating mode.

To evaluate the use of the OSU tide model to provide tidal heights and currents at the boundary, the interior SWAFS pacnest sea surface height simulation is compared with GLOSS/CLIVAR (Global Sea Level Observing System) tide gauge data (available online at the University of Hawaii Sea Level Center; [ilikai.soest.hawaii.edu/uhslc/data1.html](http://ilikai.soest.hawaii.edu/uhslc/data1.html)). Six stations were identified in the SWAFS pacnest domain, all on the Japanese coast (Fig. 110). Fig. 111 shows an example of the 24 May – 19 July time series from one station, with the observed water levels, and corresponding sea surface height time series from the SWAFS pacnest with northworld boundary conditions, and SWAFS pacnest with NCOM/OSU boundary conditions, individually de-meaned. Fig. 112 shows the last ten days from each of the tide gauge time series, along with the two model time series. Here, the two model time series are interpolated to the tide gauge position using the same interpolation, so differences are attributable to the model configuration changes and (more likely) the different host model. Table 4 lists the correlation coefficients calculated for each time-interpolated model time series with the observed water levels (means removed). The NCOM/OSU-hosted solution appears to better reproduce the observations.

As part of the debugging and monitoring process for the near real-time NCOM run boundary-condition post-processing, a similar pair of 32-bit SWAFS ionest integrations was configured beginning 11 Nov 2003 for the NCOM/OSU-hosted run, and 13 Nov 2003 for the SWAFS northworld-hosted run. The NCOM/OSU run was initialized using the approach described above for the SWAFS pacnest runs, with a SWAFS ionest restart file updated with global NCOM temperature and salinity fields valid 11 Nov 2003. The ionest “grid file” was also updated as above. The two test integrations do not include the most recent modifications to the operational code, including the heat-flux adjustment parameter used to modify the SWAFS-driven heat fluxes Fig. 113.

Fig. 114 provides an overview of the surface temperature and salinity fields from the operational SWAFS ionest run and the two test runs valid 07 December 2003. Fig. 115-Fig. 116 show the 20 m temperature, salinity, and zonal and meridional velocities in the area of the northeast Arabian Sea where a “temporary erasure” box was recently implemented in the operational code to control unrealistic surface temperatures.

Fig. 117-Fig. 120 present the temperature, salinity, and two velocity components along the SWAFS ionest open boundary for the two test runs valid 07 Dec 2003. The use of NCOM/OSU-derived boundary condition data does not appear to degrade the SWAFS solution.

These results show the SWAFS northworld-hosted run has the same problems the operational run has had since the assimilation of MODAS synthetics was turned off. It appears that the problem is related to a bad reference density field in the “grid file.” Fig. 121 shows the reference density field from the “grid file” of the northworld-hosted run (i.e., the operational version modified to 32-bit IEEE format) and the new “grid file,” in which the reference density field was replaced. The reference density field appears to have been incorrectly interpolated to the model  $\sigma$ -coordinate grid. The background temperature and salinity fields have similar interpolation errors.

## **Other Applications**

### **Nested or Relocatable NCOM**

In addition to providing boundary conditions for regional SWAFS, global NCOM is also used for initial and/or boundary conditions for nested NCOM domains on either fixed or relocatable domains. Fig. 122 depicts some of these regional domains. Examples online at [http://www7320.nrlssc.navy.mil/IASNFS\\_WWW/](http://www7320.nrlssc.navy.mil/IASNFS_WWW/) show real time and hindcast results from the IAS. Global NCOM also provides initial and boundary conditions for a nested relocatable model in support of *Prestige* oil spill clean-up activities off the coast of Spain.

## 5. SUMMARY, CONCLUSIONS AND RECOMMENDATIONS

This report has described the components of the NCOM modeling system and presented the validation tests of the model. The system consists of the model, the associated databases, the assimilation system, and the data extraction and regridding. The model is NCOM version 2.3 implemented on a fully global curvilinear domain with  $1/8^\circ$  midlatitude resolution. Assimilation consists of 2-D adjustment of surface fluxes and 3-D relaxation to, or slow-insertion of, temperature and salinity field produced by MODAS. MODAS itself derives its fields from regression of synthetic profiles of temperature and salinity using operational  $1/8^\circ$  MODAS-2D SST and  $1/16^\circ$  global NLOM SSH analyses. The associated databases consist of the NCOM river data base, OSU global tide constituent databases, and NRL DBDB2 bathymetry regridded to the NCOM grid. The data extraction provides a generic regridding and filling capability with optional filling, masking and addition of tides. Additional software simplifies extraction of boundary conditions appropriately formatted for SWAFS nests presently embedded in the SWAFS northworld domain. The global model is forced by operational FNMOG wind and thermal fields and assimilates data produced via systems operational at NAVOCEANO.

Overall the model shows reasonable performance over a series of studies designed to test ability to represent upper ocean conditions and circulation. For the discussion, we will focus on those aspects of the model or regions of the global solution that have relatively significant errors or otherwise do not meet expected performance levels.

Global NCOM is ultimately limited by present operational constraints on time and resource to make the best allocation of resources to provide solutions of sufficient quality for support over global scales. Thus while model results would potentially improve with finer horizontal and vertical grids, shorter time steps are also required when one increases spatial resolution. Thus a doubling of the horizontal and vertical resolution implies that (1) internal storage requirements increase by a factor of eight, (2) external requirements increase by a factor of eight, assuming the same sampling frequency, and (3) computer run time increases by at least a factor of 16. The choice to use a  $1/8^\circ$  global grid with 40 vertical material levels, focused toward the surface with a maximum at-rest surface layer thickness of 1 m, is an attempt to best allocate resources for a timely, affordable and useful system. Features and ocean processes on horizontal scales of 10 km or less cannot be represented by such a global model; these are instead relegated to nested models of smaller, regional domains with increasing resolution. Some of the differences between observations and model results are attributable to processes or variations too small to be resolved in the bathymetry, forcing, or observations available for assimilation. Features such as these are noted, but for the discussion and recommendation we focus on shortcomings or other aspects of the model which may be improved under potential action items for future development. In addition to the choices of the model grid, additional choices have been made regarding various model parameterizations, subroutines, relaxation space and time scales, and other aspects. These have been subject to limited refinement and exploration, implying that a better combination, at least for some region or aspect of the global ocean, can be discovered. We will try to identify sensitivity studies for refinement for these aspects of the model. More sensitivity studies will be considered in the future.

None of the validation data were assimilated into global NCOM directly or indirectly prior to their use for validation, maintaining their unambiguous independence for validation purposes. Presently, for global application only the MCSST observations are assimilated after

their use for validation. This leads to one recommendation for development: additional observation data streams in the global assimilation system. Regional MODAS operationally assimilates *in situ* temperature profiles, and this capability could be extended to the global system given present computational capacity and recent improvements in distributed processing under MODAS. While similar to the assimilative case in most respects, the free-running case in the Caribbean Sea and north of 60°N has higher surface EKE, in better agreement with observations. These results indicate a need to adjust the assimilation procedure in certain areas, a topic discussed more fully in the final section of this report. Alternative assimilation systems such as NRL Coupled Ocean Data Assimilation (NCODA), which makes a variety of observations available to models, could also be paired with global NCOM as these prove operationally viable and preferable.

Global NCOM solutions in high latitudes are likely to be deficient for two reasons: poor or missing high-latitude results in NLOM and absence of an ice model or adequate ice treatment. Global NLOM is subglobal, excluding ocean regions north of 65°N. MCSST observations are often sparse in the high latitudes as well, so the quality of MODAS SST-only synthetics at these latitudes is likely to be lower as well. North of 80°N global NCOM assimilates the GDEM-3 climatology, which was found superior to MODAS climatology here, there being no SSH and virtually no SST observations to support accurate MODAS synthetics over the pole. Thus the assimilation fields are likely to be relatively less accurate over the North Pole and high north latitudes. In addition, there is no ice model in the present implementation of global NCOM. The southern ocean is likely to have poorer assimilation fields as well. Global NLOM skill degrades south of about 45°S-50°S due to artificial methods preventing outcropping of its upper layers, so south of 45°S the assimilation field is linearly weighted to become an SST-only based synthetic at 53°S. So the assimilation fields south of 53°S and north of 64°N receive no benefit from altimetry. NCOM solutions do presently have a pseudo ice mask to prevent continual dropping of polar temperatures below freezing, arbitrarily capping minimum temperature at 0.5°C below the freezing point of water at the present salinity and thereby storing some thermal deficit to delay reheating. But the Arctic solution is expected to be of limited use without coupling with an ice model. Proposed solutions to these deficiencies are to add a coupled ice model (had been expected to start in 2003, perhaps delayed by funding), adding a real-time ice mask using satellite-derived ice products, and blending in MODAS2D altimetry with NLOM to extend altimeter data to higher latitudes. The extension of altimetry data to high latitudes would not be warranted before a solution for removing non-steric SSH signals, a relatively large problem in high latitudes, has been developed and operationally implemented.

Another problem associated with assimilation of NLOM data is the lack of NLOM coverage on the continental shelves. In the standard MODAS analysis, SSH is not used in depths shallower than 200m because of the relatively large contribution of non-steric height signal in shallow depths. SST-only synthetics are used shallower than 200 m, combined SSH-SST synthetics are used deeper than 600 m, and the two are blended together for zones with bottom depths between 200 m and 600 m. Since NLOM removes the steric signal but does not include shelf, its solution is applicable to at least within a grid point are two of its boundary. By starting to turn off the NLOM signal at 600 m, NCOM is likely getting a reduced signal if any from legitimate SSH variations near the NLOM boundary.

To calculate synthetic temperature using combined surface height and temperature information, MODAS requires both a normal SST field and an SSH field that is a deviation from the MODAS climatological steric height anomaly. Presently the NLOM steric SSH is

differenced with its own mean, and this field is treated as a deviation from the MODAS steric height. The problem arises where the MODAS mean is significantly different from the NLOM mean, where perhaps MODAS has a smoother mean or does not resolve a given feature. Consider for example the Aleutians. A mean Alaska stream is produced in free-running NCOM in good agreement with observations. However, this current is much weaker in the assimilative case. The SSH signal for the current is quite narrow and steady in NLOM, but is much weaker in global NCOM. Thus NLOM interprets this signal as part of its mean, while MODAS interprets it as a deviation from the mean. This discrepancy causes a negative impact from assimilation in this region. A similar result was seen along the western coast of Africa in the comparison of the free and assimilative models in the Indian Ocean hemisphere. Pathways and perhaps strength of other western boundary current such as the Gulf Stream or Kuroshio may also be improved by addressing this issue. Efforts are continuing to account for the difference in the MODAS and NLOM mean, with preliminary results showing a good affect in the Aleutians, Kuroshio and Gulf Stream. Accounting for differences between the NLOM and MODAS means, combined with extending SST+NLOM SSH synthetics closer to 200 m, should improve the strength and position of assimilative boundary currents in global NCOM. Special care is required in regions with an isolated deep basin such as the Sulu Sea, eastern Bay of Bengal, and Celebes Sea, or gradients in the steric height may produce artificial recirculation along the boundaries between basins. A consequence of this is seen in the excessive penetration of the North Equatorial Current into the Celebes Sea.

Skill in predicting SST is expected to be improved by a combination of factors. Comparisons of SST forecasts with unassimilated MCSSTS demonstrate problems in the SST immediately adjacent to land areas. The suggested source is bleeding of land values for heat flux and wind stress into ocean regions due to using winds not on the atmospheric native grid with an applied native atmospheric grid land mask. The solution proposed is to acquire operational fields on the native grid, apply the native grid land mask, and then regrid for ocean model forcing. This may improve the forecasts in areas of the strongest western boundary currents, where forecast errors are currently highest.

Problems in SST in the equatorial Pacific warm pool in particular and an overall slight cold bias in SST forecasts has multiple solutions which must be tested in combination with the shallow bias in MLD in the equatorial regions. One solution is to modify the ocean attenuation for solar radiation from a clear-water setting to a setting derived from an available climatology of attenuation coefficient. This will tend to transfer more solar radiation to the surface and less to the deeper regions, tending to offset the bias seen in the eastern Pacific (Type I) profiles. However this will tend to increase the shallow bias in MLD, so we will also test modifications of the coefficients in the Mellor-Yamada mixing scheme and possibly investigate applications of other mixing schemes that have shown promise in HYCOM and other models. The validation SST also had scattered problems with checkerboard mixing, a problem that has been addressed in the transitioned version of the model.

Validation also shows of the ability on NCOM boundary conditions to SWAFS nests presently supported by SWAFS northworld and to provide combined NCOM-OSU tide solutions at comparison tide stations. One of the primary concerns driving the development of U.S. Navy global models has been improved performance and nesting support in shelf and nearshore regions with short notice applicability anywhere on the globe. The NCOM higher vertical resolution in the mixed layer improves upper-ocean prediction and boundary conditions for higher resolution coastal models. This global nowcast/forecat system provides the Navy with the

first global ocean analysis/prediction capability for fleet support. It is the first operational eddy-permitting global model that includes the Arctic and shelf regions to the coast. With NLOM and MODAS, it completes a global system that makes best use of operationally-available computational resources to provide current, elevation, temperature, salinity and sound speed nowcasts and forecasts to meet both planned and unforeseen operational Navy needs.

## 6. ACKNOWLEDGEMENTS

This work was funded by the NRL 6.4 Large-scale Models and 6.4 Ocean Data Assimilation projects, managed by the Space and Naval Warfare Systems Command under program element 0603207N. The numerical simulations were performed on the NAVOCEANO IBM-SP3 at Stennis Space Center, Mississippi using grants of computer time from the Department of Defense High Performance Computing Modernization Program. Critical evaluation and advice was provided by the members of the review panel: Frank Bub (NAVOCEANO), Chris DeHaan (NAVOCEANO), John Kindle (NRL) and Bill Schmitz (USM/WHOI(ret.)). The authors would like to thank the numerous NRL contributors for their support in global NCOM development and validation. Among these are Jan Dastugue for help in web page development and graphics, Peter Flynn for work on NCOM visualization, Harley Hurlburt for insight as a technical advisor, Dong Ko for developments in assimilation, bathymetry and grid refinement, Paul Martin for NCOM code development and expert modeling advice, Ruth Preller for discussions on ice modeling, and Alan Wallcraft for scalable, portable NCOM code development. Advice for validations in various regions or for particular datasets was given by Rick Allard, Dan Fox, John Harding (NRL/NAVOCEANO), Joe Metzger, Steve Piacsek, Shelley Riedlinger, Jay Shriver, and Tammy Townsend. Additional contributions on global NCOM validation and visualization were provided by Webb Dewitt (FNMOC), research associates Germana Peggion (UNO) and Ole Martin Smedstad (PSI), U.S. Naval reservists LCDR Karen Ebersole and CDR Stuart Walker, post doctoral researcher Luis Zamudio (FSU), and SEAP summer student Maclean Campbell.

## 7. REFERENCES

- Asselin, R., 1972: Frequency filter for time integrations. *Mon. Wea. Rev.*, **100**, 487-490.
- Barron, C. N., and A. B. Kara, 2006: Satellite-based daily SSTs over the global ocean. *Geophys. Res. Lett.*, **33**, L15603, doi:10.1029/2006GL026356.
- Barron, C.N., A.B. Kara, H.E. Hurlburt, C. Rowley, and L.F. Smedstad, 2004: Sea surface height predictions from the Global Navy Coastal Ocean Model (NCOM) during 1998-2001. *J. Atmos. Oceanic Technol.*, 21(12), 1876-1894.
- Barron, C.N., A.B. Kara, P.J. Martin, R.C. Rhodes, and L.F. Smedstad, 2006: Formulation, implementation and examination of vertical coordinate choices in the global Navy Coastal Ocean Model (NCOM). *Ocean Modelling*, **11**, 347-375, doi:10.1016/j.ocemod.2005.01.004.
- Barron, C.N., R.C. Rhodes, L.F. Smedstad, P.J. Martin, and A.B. Kara, 2003: Global Ocean Nowcasts and Forecasts with the Navy Coastal Ocean Model (NCOM). 2003 *NRL Review*, 175-178.
- Barron, C.N., and L.F. Smedstad, 2002: Global river inflow within the Navy Coastal Ocean Model. Proceedings to Oceans 2002 MTS/IEEE Conference, 29-31 October 2002, 1472-1479.
- Barron, C.N., L.F. Smedstad, J.M. Dastugue, and O.M. Smedstad, submitted: Evaluation of ocean models using observed and simulated drifter trajectories: Impact of sea surface height on synthetic profiles for data assimilation. *J. Geophys. Res.*
- Blain, C.A., R.H. Preller, and A.P. Rivera, 2002: Tidal prediction using the Advanced Circulation Model (ADCIRC) and a relocatable PC-based System. *Oceanography*, **15**, 77-87.
- Boebel, O., and C. Barron, 2003: A comparison of in-situ float velocities with altimeter derived geostrophic velocities. *Deep Sea Res. II*, **50**, 119-139.
- Blumberg, A.F., and H.J. Herring, 1987: Circulation modelling using orthogonal curvilinear coordinates. In: Nihoul, J., and B. Jamart (Eds.), *Three-Dimensional Models of Marine and Estuarine Dynamics*, Elsevier Oceanography Series, **45**, 55-88.
- Blumberg, A.F., and G.L. Mellor, 1987: A description of a three-dimensional coastal ocean circulation model. In: Heaps, N. (Ed.) *Three-Dimensional Coastal Ocean Models*, Amer. Geophys. Union, New York, 208 pp.
- Bretherton, F.P., R.E. Davis, and C.B. Fandry, 1976: A technique for objective analysis and design of oceanographic experiments applied to MODE-73. *Deep Sea Res.*, **23**, 559-582.

- Caldwell, P., and M. Merrifield, 1992: Building an archive of tropical sea level data. *Earth System Monitor*, **3**, 3-6.
- Casey, K.S. and P. Cornillon, 1999: A comparison of satellite and *in situ* based sea surface temperature climatologies. *J. Climate*, **12**, 1848-1863.
- Craig, P.D., and M.L. Banner, 1994: Modeling wave-induced turbulence in the ocean surface layer. *J. Phys. Oceanogr.*, **24**, 2546-2559.
- Egbert, G.D., A F. Bennett, and M.G.G. Foreman, 1994: TOPEX/Poseidon tides estimated using a global inverse model. *J. Geophys. Res.*, **99**, 24821-24852.
- Egbert, G. and L. Erofeeva, 2002: Efficient inverse modeling of barotropic ocean tides. *J. Atmos. Oceanic Technol.*, **19**, 183-204.
- Fang, G., W. Fang, Y. Fang and K. Wang, 1998. A survey of studies on the South China Sea upper ocean circulation, *Acta Oceanographica Taiwanica*, **37**, 1-16.
- Fratantoni, D.M., 2001: North Atlantic surface circulation during the 1990's observed with satellite-tracked drifters. *J. Geophys. Res.*, **106**, 22067-22093.
- Fox, D.N., W.J. Teague, C.N. Barron, M.R. Carnes, and C.M. Lee, 2002a. The Modular Ocean Data Assimilation System (MODAS). *J. Atmos. Oceanic Technol.*, **19**, 240-252.
- Fox, D.N., C.N. Barron, M.R. Carnes, M. Booda, G. Peggion, and J.V. Gurley, 2002b. The Modular Ocean Data Assimilation System. *Oceanography*, **15**, 22-28.
- Freitag, H.P., Y. Feng, L.J. Mangum, M.J. McPhaden, J. Neander, and L.D. Stratton, 1994: Calibration, procedures and instrumental accuracy estimates of TAO temperature, relative humidity and radiation measurements. NOAA Tech. Memo, ERL PMEL-104, 32 pp. [Available from PMEL, 7600 Sand Point Way, Seattle, WA 98115, USA.]
- Friedrich, H., and S. Levitus, 1972: An approximation to the equation of state for sea water, suitable for numerical ocean models. *J. Phys. Oceanogr.*, **2**, 514-517.
- Gibson, J.K., P. Kållberg, S. Uppala, A. Hernandez, A. Nomura, and E. Serrano, 1997: ERA description. ECMWF Re-Analysis Project Report Series, No. **1**, 72 pp. [Available from ECMWF, Shinfield Park, Reading RG2 9AX, UK.]
- Gill, A.E., 1982: *Atmosphere-Ocean Dynamics*, Academic, San Diego, 662 pp.
- Hellerman, S., and M. Rosenstein, 1983: Normal monthly wind stress over the world ocean with error estimates. *J. Phys. Oceanogr.*, **13**, 1093-1104.
- Holland, W.R., J.C. Chow, and F.O. Bryan, 1998: Application of a third-order upwind scheme in the NCAR ocean model. *J. Climate*, **11**, 1487-1493.

- International GODAE Steering Team, 2000: Global Ocean Data Assimilation Experiment Strategic Plan. GODAE Report #6. Published by the GODAE International Project Office, c/o Bureau of Meteorology, Melbourne, Australia, 26 pp.
- Jacobs, G.A., C.N. Barron, D.N. Fox, K.R. Whitmer, S. Klingenberger, D. May, and J.P. Blaha, 2002: Operational altimeter sea level products. *Oceanography*, **15**, 13-21.
- Johns, W.E., T.L. Townsend, D.M. Fratantoni, and W.D. Wilson, 2002: On the Atlantic inflow to the Caribbean Sea. *Deep Sea Res. I*, **49**, 211-243.
- Johnson, G.C., M.J. McPhaden, and E. Firing, 2001: Equatorial Pacific ocean horizontal velocity, divergence, and upwelling. *J. Phys. Oceanogr.*, **31**, 839-849.
- Jones, P.W., 1998: SCRIP: A Spherical Coordinate Remapping and Interpolation Package. <http://www.acl.lanl.gov/climate/software/SCRIP/>. Los Alamos National Laboratory Software Release LACC 98-45.
- Kara, A.B., C.N. Barron, P.J. Martin, L.F. Smedstad, and R.C. Rhodes, 2006: Validation of interannual simulations from the 1/8° global Navy Coastal Ocean Model (NCOM). *Ocean Modelling*, **11**, 376-398, doi:10.1016/j.ocemod.2005.01.003.
- Kara, A.B., P.A. Rochford, and H.E. Hurlburt, 2003a: Mixed layer depth variability over the global ocean. *J. Geophys. Res.*, **108**, 3079, doi:10.1029/2000JC000736.
- Kara, A.B., A.J. Wallcraft, and H.E. Hurlburt, 2003b: Climatological SST and MLD predictions from a global layered ocean model with an embedded mixed layer. *J. Atmos. Oceanic Technol.*, **20**, 1616-1632.
- Kara, A.B., P.A. Rochford, and H.E. Hurlburt, 2002: Air-sea flux estimates and the 1997-1998 ENSO event. *Bound.-Layer Meteor.*, **103**, 439-458.
- Kara, A.B., P.A. Rochford, and H.E. Hurlburt, 2000a: An optimal definition for ocean mixed layer depth. *J. Geophys. Res.* 105, 16803-16821.
- Large, W.G., J.C. McWilliams, and S.C. Doney, 1994: Oceanic vertical mixing: A review and a model with a nonlocal boundary layer parameterization. *Rev. Geophys.*, **32**, 363-403.
- Kara, A.B., P.A. Rochford, and H.E. Hurlburt, 2000b: Mixed layer depth variability and barrier layer formation over the North Pacific Ocean. *J. Geophys. Res.*, **105**, 16783-16801.
- Large, W.G., J.C. McWilliams, and S.C. Doney, 1994: Oceanic vertical mixing: A review and a model with a non-local boundary layer parameterization. *Rev. Geophys.*, **32**, 363-403.
- Lee, T.N., W.E. Johns, C.T. Liu, D. Zhang, R. Zantopp and Y. Yang, 2001: Mean transport and seasonal cycle of the Kuroshio east of Taiwan with comparison to the Florida Current. *J. Geophys. Res.*, **106**, 22143-22158.

- Liang, W.D., T.Y. Tang, Y.J. Yang, M.T. Ko, and W.S. Chuang, 2003. Upper-ocean currents around Taiwan, *Deep Sea Res. II*, **6-7**, 1085-1105.
- Martin, P.J., 2000: Description of the Navy Coastal Ocean Model Version 1.0. NRL Report No. NRL/FR/7322/00/9962, 45pp. [Available from NRL, Code7322, Bldg. 1009, Stennis Space Center, MS 39529-5004, USA.]
- Martin, P.J., G. Peggion, and K.J. Yip, 1998: A comparison of several coastal ocean models. NRL Report No. NRL/FR/7322/97/9692, 96pp. [Available from NRL, Code7322, Bldg. 1009, Stennis Space Center, MS 39529-5004, USA.]
- May, D.A., M.M. Parmer, D.S. Olszewski, and B.D. McKenzie, 1998: Operational processing of satellite sea surface temperature retrievals at the Naval Oceanographic Office. *Bull. Amer. Met. Soc.*, **79**, 397-407.
- McPhaden, M.J., A.J. Busalacchi, R. Cheney, J.R. Donguy, K.S. Gage, D. Halpern, M. Ji, P. Julian, G. Meyers, G.T. Mitchum, P.P. Niiler, J. Picaut, R.W. Reynolds, N. Smith, and K. Takeuchi, 1998: The Tropical Ocean-Global Atmosphere (TOGA) observing system: A decade of progress. *J. Geophys. Res.*, **103**, 14169-14240.
- Metzger, E.J. and H.E. Hurlburt, The importance of high horizontal resolution and accurate coastline geometry in modeling South China Sea inflow, *Geophys. Res. Lett.*, **28**, 1059-1062, 2001.
- Mellor, G.L., 1991: An equation of state for numerical models of oceans and estuaries. *J. Atmos. Oceanic Technol.*, **8**, 609-611.
- Mellor, G.L., and T. Yamada, 1982: Development of a turbulence closure model for geophysical fluid problems. *Rev. Geophys. Space Phys.*, **20**, 851-875.
- Mellor, G.L., and T. Yamada, 1974: A hierarchy of turbulence closure models for planetary boundary layers. *J. Atmos. Sci.*, **31**, 1791-1806.
- Millero, F.J., and A. Poisson, 1981: International one-atmosphere equation of state of seawater. *Deep Sea Res. I*, **28**, 625-629.
- Millero, F.J., C.-T. Chen, A. Bradshaw, and K. Schleicher, 1980: A new high pressure equation of state for seawater. *Deep Sea Res. I*, **27**, 255-264.
- Murphy, A.H., and E.S. Epstein, 1989: Skill scores and correlation coefficients in model verification. *Mon. Wea. Rev.*, **117**, 572-581
- Murphy, A.H., 1988: Skill scores based on the mean square error and their relationships to the correlation coefficient. *Mon. Wea. Rev.*, **116**, 2417-2424.
- Murray, R.J., 1996: Explicit generation of orthogonal grids for ocean models. *J. Computational Phys.*, **126**, 251-273.

- Owens, W.B., 1991: A statistical description of the mean circulation and eddy variability in the northwestern Atlantic using SOFAR floats. *Prog. Oceanog.*, **28**, 257-303.
- Owens, W.B., 1984: A Synoptic and statistical description of the Gulf Stream and subtropical gyre using SOFAR floats. *J. Phys. Oceanogr.*, **14**, 104-113.
- Perry, G.D., P.B. Duffy, and N.L. Miller, 1996: An extended data set of river discharges for validation of general circulation models. *J. Geophys. Res.*, **101**, 21339-21349.
- Rhodes, R.C., H.E. Hurlburt, A.J. Wallcraft, C.N. Barron, P.J. Martin, E.J. Metzger, J.F. Shriver, D.S. Ko, O.M. Smedstad, S.L. Cross, and A.B. Kara, 2002: Navy real-time global modeling systems. *Oceanography*, **15**, 29-43.
- Richardson, P.L., 1993: A census of eddies observed in North Atlantic SOFAR float data. *Prog. Oceanog.*, **31**, 1-50.
- Richardson, W.S., W.J. Schmitz Jr., and P.P. Niiler, 1969: The velocity structure of the Florida Current from the Straits of Florida to Cape Fear. *Deep Sea Res.*, supp. to **16**, 225-231.
- Rosmond, T.E., J. Teixeira, M. Peng, T.F. Hogan, and R. Pauley, 2002: Navy Operational Global Atmospheric Prediction System (NOGAPS): Forcing for ocean models. *Oceanography*, **15**, 99-108.
- Schmitz, W.J., 1996: *On the World Ocean Circulation: Volume I. Some Global Features/North Atlantic Circulation*. Woods Hole Oceanog. Inst. Tech. Rept. WHOI-96-03, 150 pp.
- Schott, F.A. and J.P. McCreary Jr., 2001: The monsoon circulation of the Indian Ocean. *Prog. Oceanog.*, **51**, 1-123.
- Servain, J., A.J. Busalacchi, M.J. McPhaden, A.D. Moura, G. Reverdin, M. Vianna, and S.E. Zebiak, 1998: A Pilot Research Moored Array in the Tropical Atlantic (PIRATA). *Bull. Amer. Met. Soc.*, **79**, 2019-2031.
- Shriver, J.F. and H.E. Hurlburt, 2000: The effect of upper ocean eddies on the non-steric contribution to the barotropic mode. *Geophys. Res. Lett.*, **27**, 2713-2716.
- Shulman I., J. C. Kindle, S. deRada, S. C. Anderson, B. Penta and P. J. Martin, 2004: Development of a hierarchy of nested models to study the California Current System. Estuarine and Coastal Modeling, proceedings of the 8th International Conf., Edited by Malcom Spalding and H. Lee Butler, 74-88.
- Smagorinsky, J., 1963: General circulation experiments with the primitive equations. I: The basic experiment. *Mon. Wea. Rev.*, **91**, 99-164.
- Smedstad, O.M., H.E. Hurlburt, E.J. Metzger, R.C. Rhodes, J.F. Shriver, A.J. Wallcraft, and A.B. Kara, 2003: An operational eddy-resolving 1/16° global ocean nowcast forecast system. *J. Mar. Res.*, 40-41, 341-361.

- Smith, R.L., A. Huyer and J. Fleischbein, 2001: The coastal ocean off Oregon from 1961 to 2000: is there evidence of climate change or only of Los Niños? *Prog. Oceanogr.*, **49**, 63-93.
- Townsend, T.L., H.E. Hurlburt, and P.J. Hogan, 2000: Modeled Sverdrup flow in the North Atlantic from 11 different wind stress climatologies. *Dyn. Atmos. Oceans*, **32**, 373-417.
- Wallcraft, A.J., A.B. Kara, H.E. Hurlburt, and P.A. Rochford, 2003: The NRL Layered Global Ocean Model (NLOM) with an embedded mixed layer sub-model: Formulation and tuning. *J. Atmos. Oceanic Technol.*, **20**, 1601-1615.
- Whitehouse, B.G., P. Hines, D. Ellis and C.N. Barron, 2004: Rapid environmental assessment within NATO. *Sea Technol.*, **45**(11), 10-14.
- Yu, X., and M.J. McPhaden, 1999: Seasonal variability of the equatorial Pacific. *J. Phys. Oceanogr.*, **29**, 925-947.
- Zalesak, S.T., 1979: Fully multidimensional flux-corrected transport algorithms for fluid. *J. Comp. Phys.*, **31**, 33.

## 8. TABLE OF ACRONYMS

ACC	Antarctic Circumpolar Current
AVHRR	Advanced Very High Resolution Radiometer
CLIVAR	Climate Variability and Predictability Program
COMINST	Communications Instructions
EAC	East Australia Current
ECMWF	European Center for Medium-range Weather Forecasting
EKE	Eddy Kinetic Energy
FCT	Flux-Corrected Transport
FNMOC	Fleet Numerical Meteorology and Oceanography Center
GLOSS	Global Sea Level Observing System
GODAE	Global Ocean Data Assimilation Experiment
IHO	International Hydrographic Office
IEEE	Institute of Electrical and Electronics Engineers
ILD	Isothermal Layer Depth
JASL	Joint Archive for Sea Level
KE	Kinetic Energy
MCSST	Multi-Channel SST
MLD	Mixed-layer depth
MODAS	Modular Ocean Data Assimilation System
MPI	Message Passing Interface
NAVMETOC	Naval Meteorology and Oceanography
NAVOCEANO	Naval Oceanographic Office
NCOM	Navy Coastal Ocean Model
NCODA	NRL Coupled Ocean Data Assimilation
NDBC	National Data Buoy Center
NetCDF	Network Common Data Format
NOAA	National Oceanic and Atmospheric Administration
NODC	National Oceanographic Data Center
NLOM	Navy Layered Ocean Model
NRL	Naval Research Laboratory
OSU	Oregon State University
PIRATA	Pilot Research Moored Array in the Tropical Atlantic
POM	Princeton Ocean Model
SS	Skill Score
SSH	Sea Surface Height
SSS	Sea Surface Salinity
SST	Sea Surface Temperature
SWAFS	Shallow-Water Analysis and Forecast System
SZM	Sigma Z-level Model
TAO	Tropical Atmosphere Ocean
UNESCO	United Nations Educational Scientific and Cultural Organization
USACE	United States Army Corps of Engineers
WOCE	World Ocean Circulation Experiment

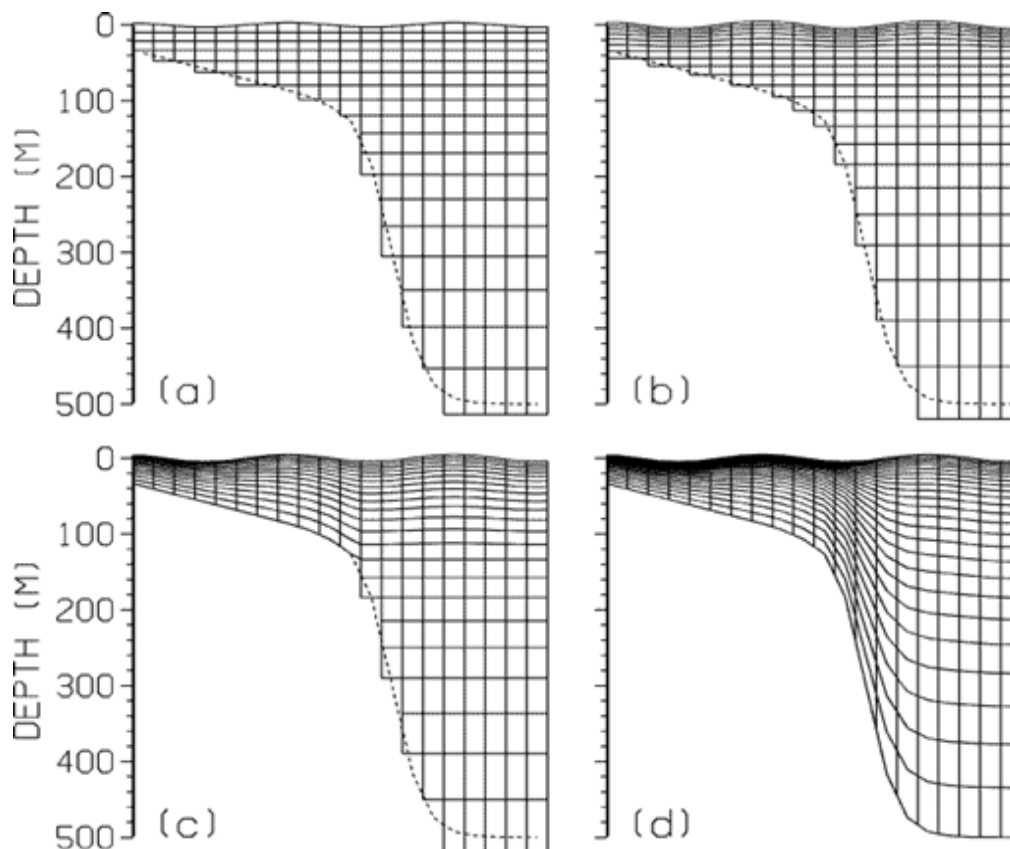


Fig. 1 – An illustration of the NCOM vertical grid: (a) a single  $\sigma$ -level at the surface and z-levels below, (b) several  $\sigma$ -levels at the surface with z-levels below, (c)  $\sigma$ -levels to a depth over most of the shelf and z-levels to the bottom over the slope and abyss, or (d)  $\sigma$ -levels everywhere. Global NCOM follows case c with a  $\sigma$ -z transition at 137m.

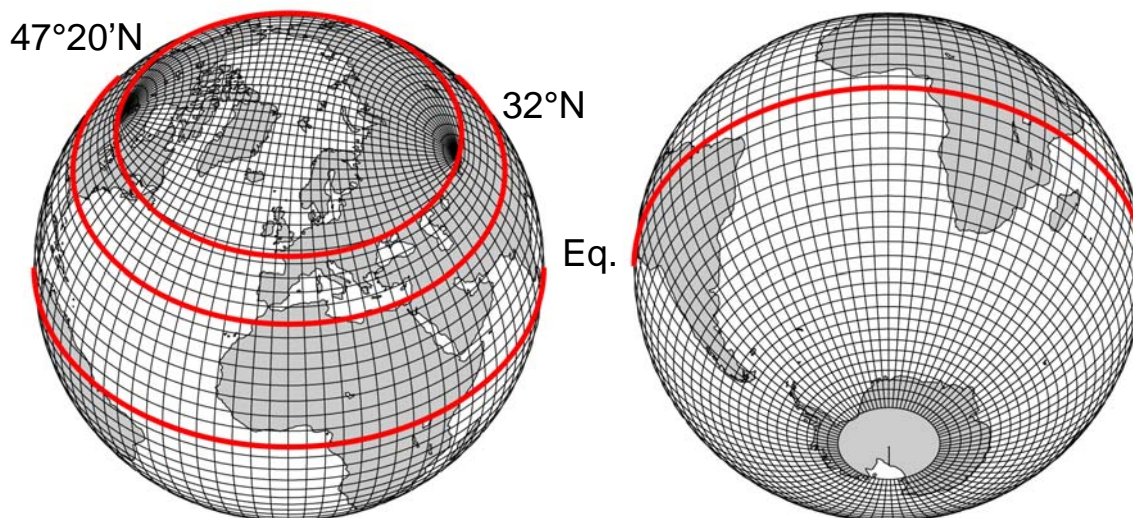


Fig. 2 – An illustration of the horizontal grid used in global NCOM. The equator is delineated in red, as are the limits of the transition zone between  $32^{\circ}\text{N}$  and  $47^{\circ}20'\text{N}$ . By placing poles in Russia and Canada, grid distortion is minimized over oceanic portions of the domain.

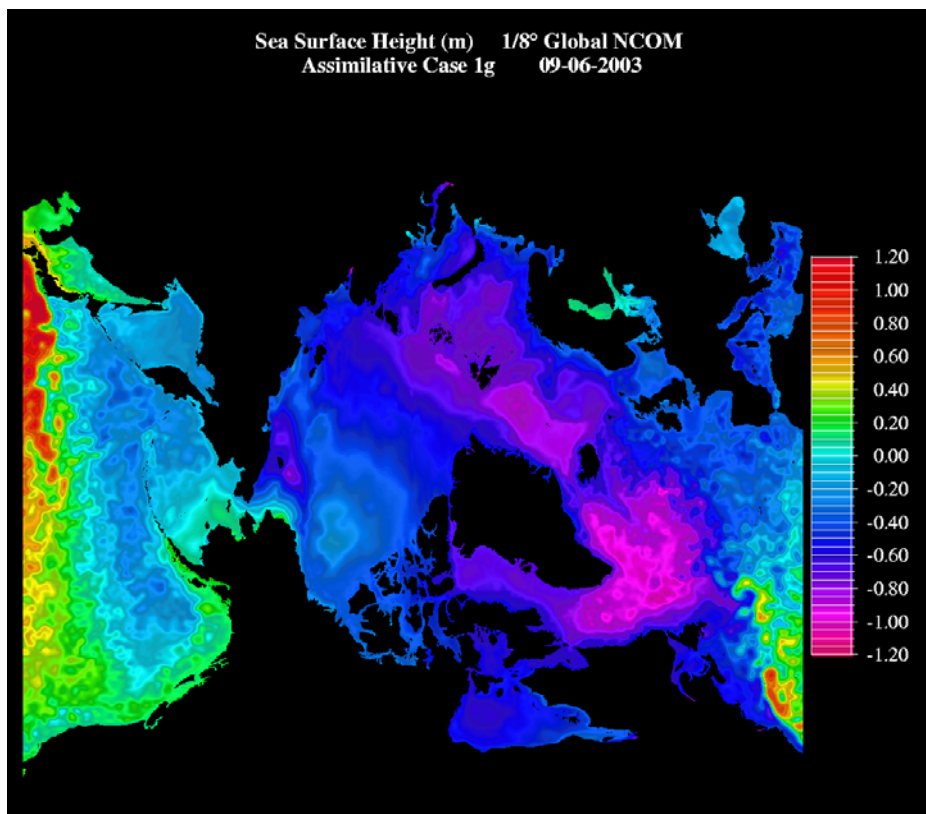


Fig. 3 – Snapshot of Arctic sea surface height. The plot is a rectangular dump of this portion of the domain and indicates the relative grid distortion of various Arctic features. Distortion is greatest in areas near the singularities, such as Hudson Bay.

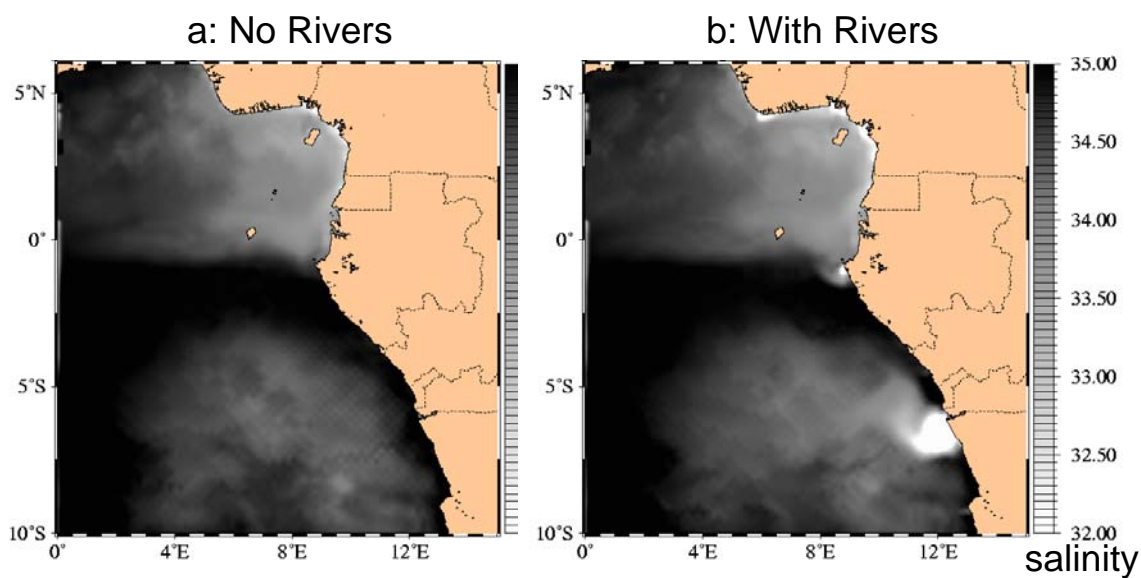


Fig. 4 – Snapshots of surface salinity along the coast of West Africa in June 1997 global NCOM simulations (a) without and (b) with rivers. Although relaxation to MODAS surface salinity does produce realistic distribution in the open ocean, in coastal regions, including major rivers significantly modifies nearshore salinity stratification.

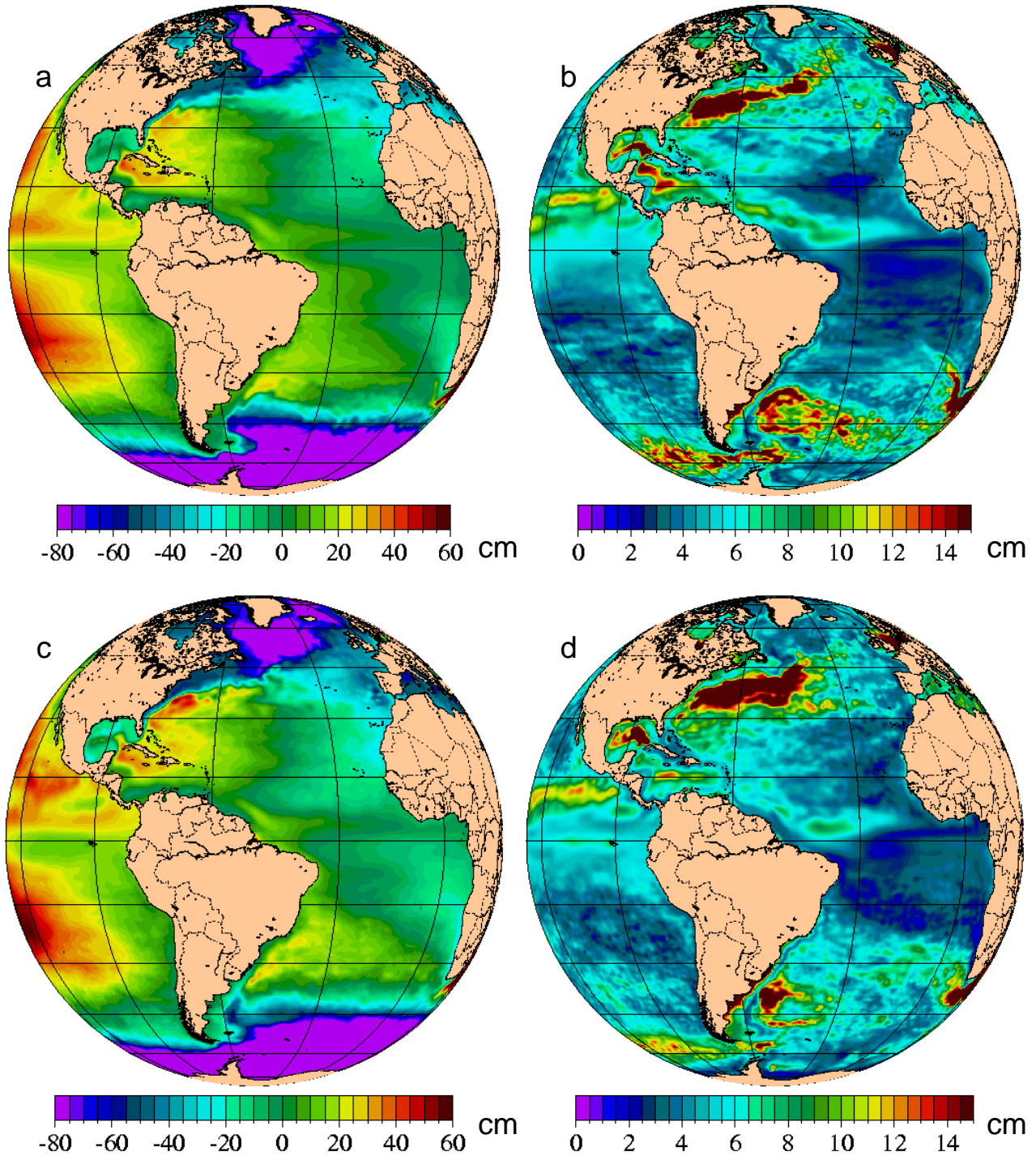


Fig. 5 – Atlantic hemispheric view of mean 1998-2000 SSH (left; a, c) and SSH standard deviation (right; b, d) for free-running (top; a, b) and assimilative (bottom; c, d)  $1/8^\circ$  global NCOM. NCOM is forced with NOGAPS wind and thermal fluxes. The assimilative case relaxes to MODAS synthetic temperature and salinity derived from  $1/8^\circ$  MODAS2D SST and  $1/16^\circ$  NLOM SSH and the statistics of the historical hydrographic data base.

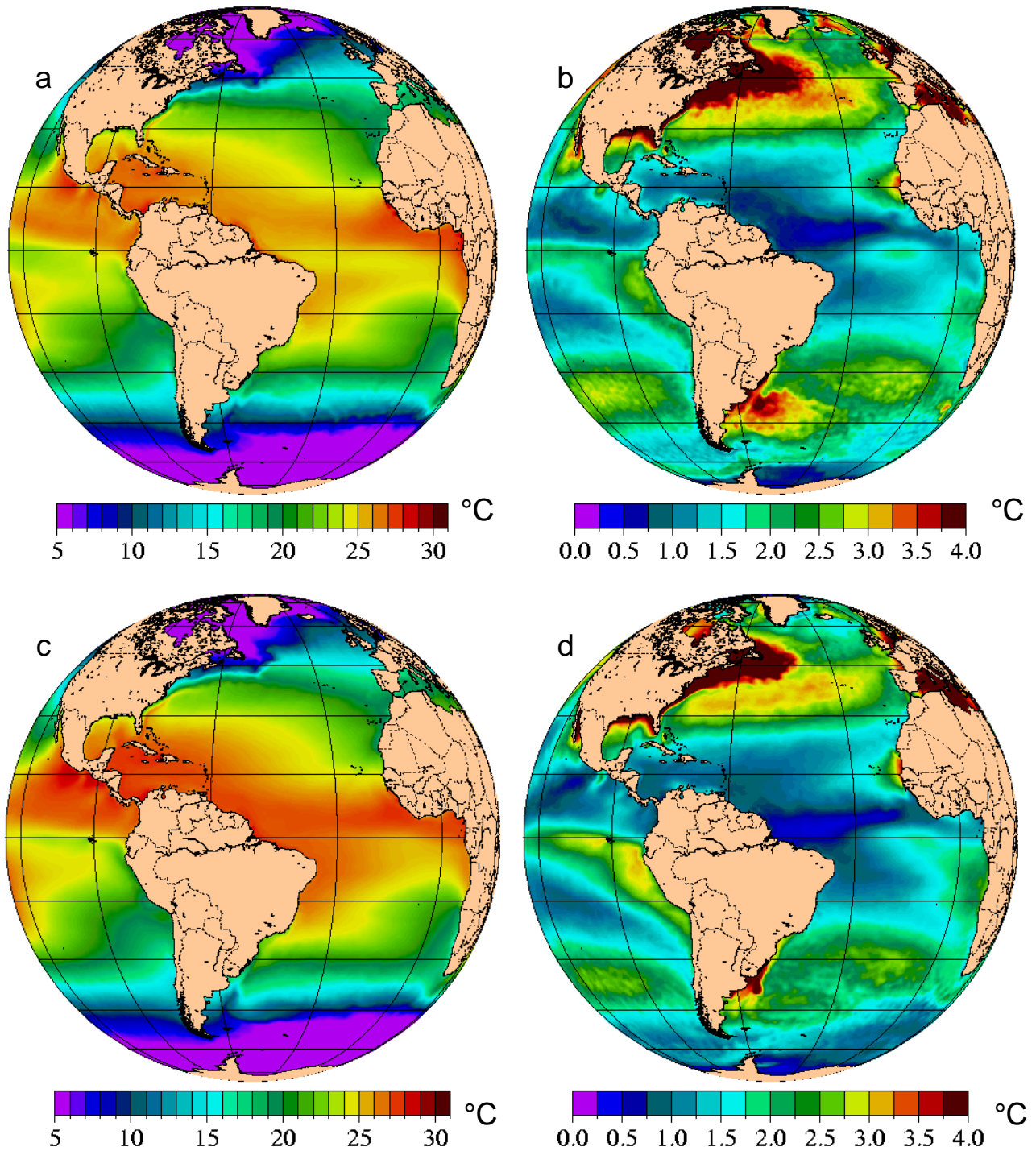


Fig. 6 – Atlantic hemispheric view of mean 1998-2000 SST (left;a,c) and SST standard deviation (right;b,d) for free-running (top;a,b) and assimilative (bottom;c,d)  $1/8^\circ$  global NCOM. NCOM is forced with NOGAPS wind and thermal fluxes. The assimilative case relaxes to MODAS synthetic temperature and salinity derived from  $1/8^\circ$  MODAS2D SST and  $1/16^\circ$  NLOM SSH.

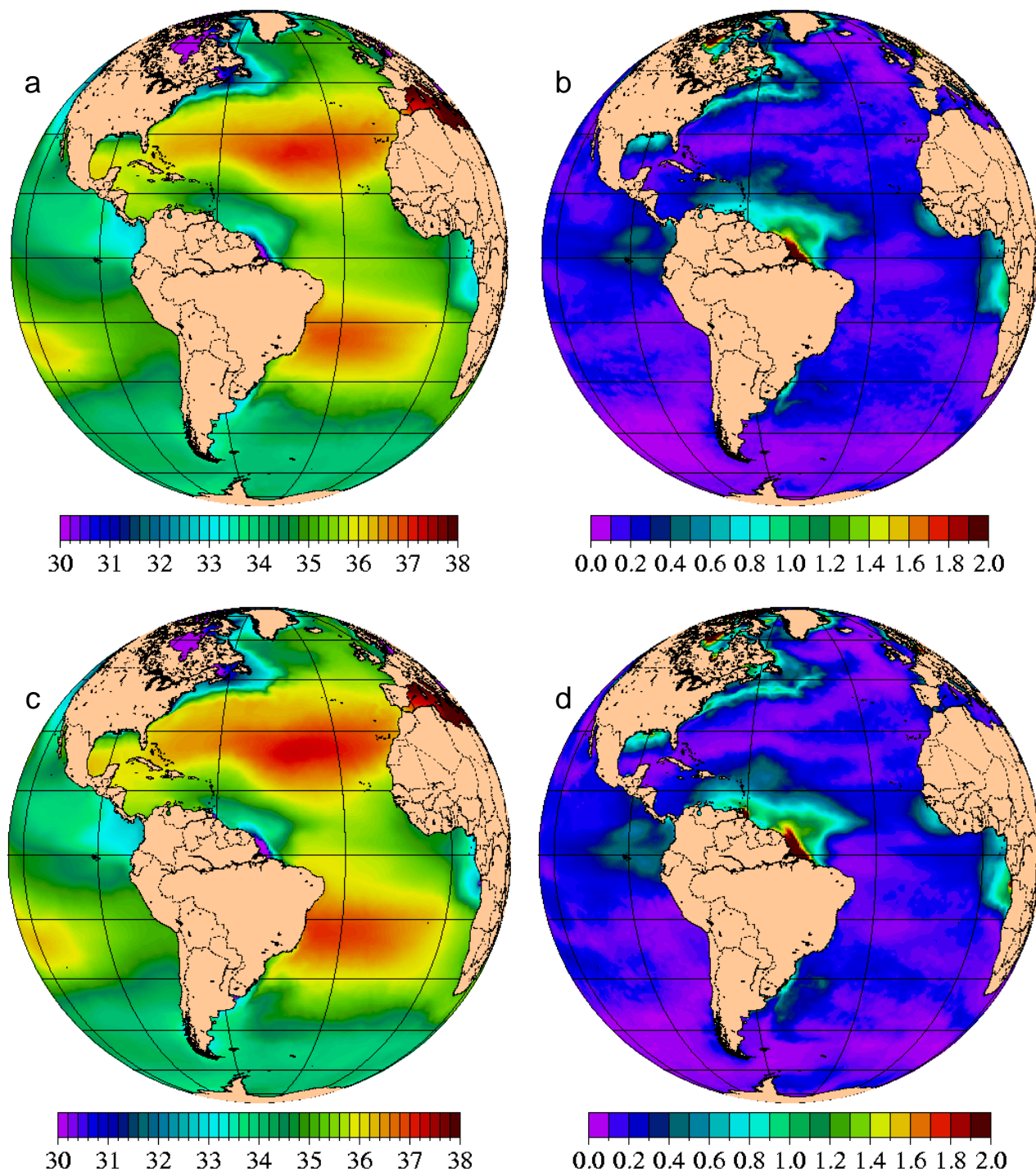


Fig. 7 – Atlantic hemispheric view of mean 1998-2000 SSS (left; a,c) and SSS standard deviation (right; b,d) for free-running (top; a,b) and assimilative (bottom; c,d)  $1/8^\circ$  global NCOM. NCOM is forced with NOGAPS wind and thermal fluxes. The assimilative case relaxes to MODAS synthetic temperature and salinity derived from  $1/8^\circ$  MODAS2D SST and  $1/16^\circ$  NLOM SSH.

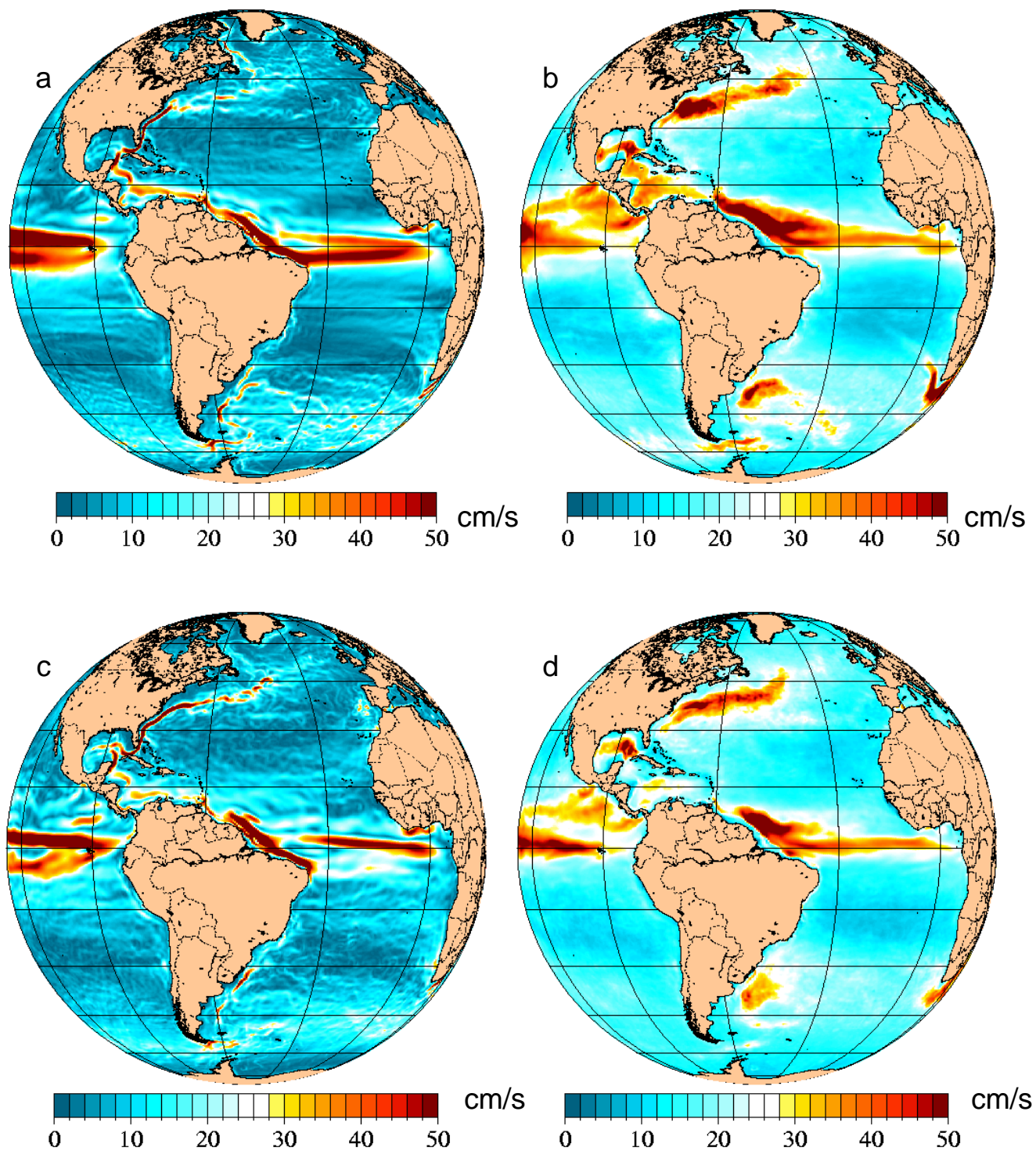


Fig. 8 – Atlantic hemispheric view of mean 1998-2000 surface speed (left; a,c) and surface speed standard deviation (right; b,d) for free-running (top; a,b) and assimilative (bottom; c,d)  $1/8^\circ$  global NCOM. NCOM is forced with NOGAPS wind and thermal fluxes. The assimilative case relaxes to MODAS synthetic temperature and salinity derived from  $1/8^\circ$  MODAS2D SST and  $1/16^\circ$  NLOM SSH.

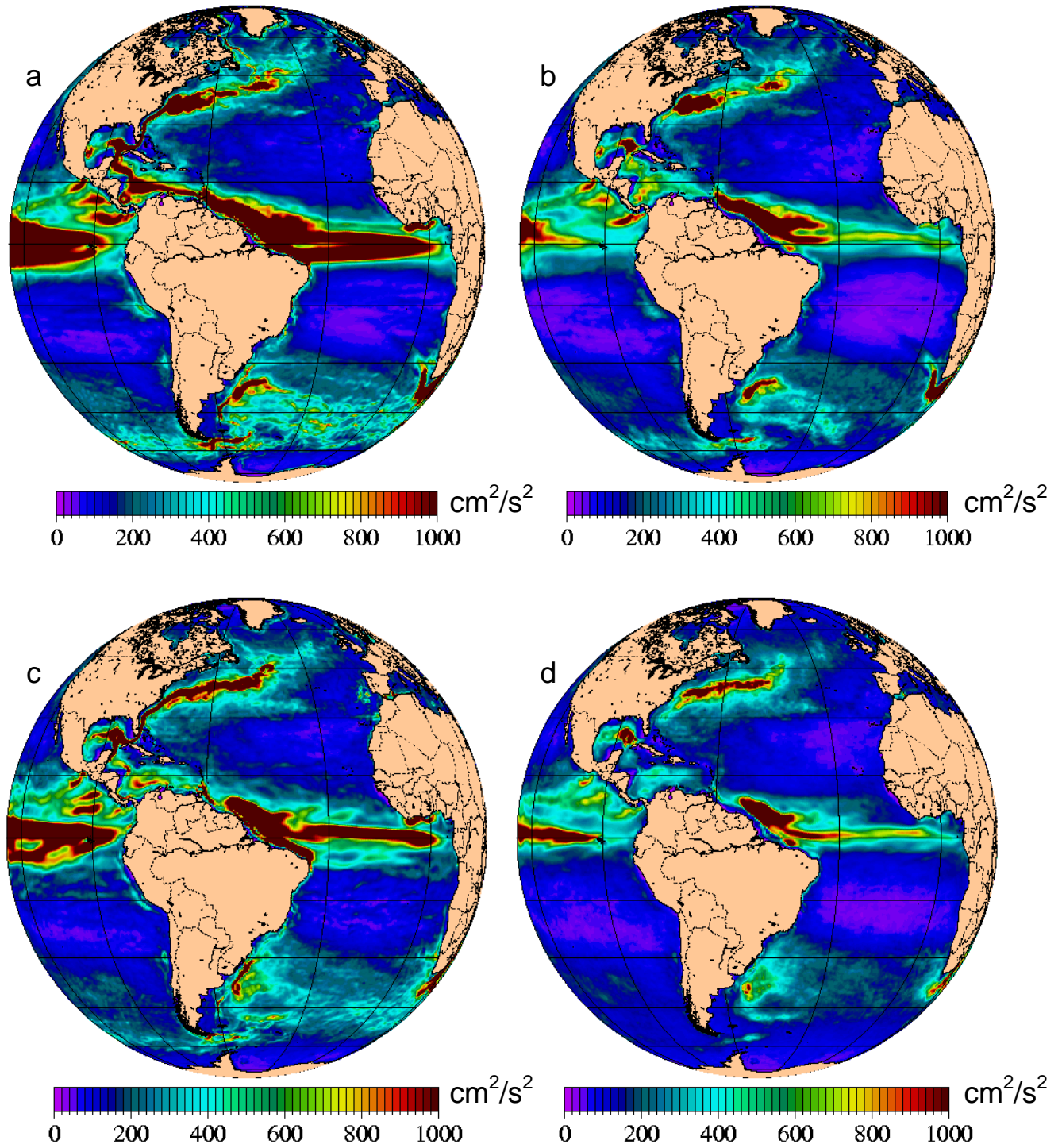


Fig. 9 – Atlantic hemispheric view of mean 1998-2000 surface kinetic energy (left; a,c) and surface EKE (right; b,d) for free-running (top; a,b) and assimilative (bottom; c,d)  $1/8^\circ$  global NCOM. NCOM is forced with NOGAPS wind and thermal fluxes. The assimilative case relaxes to MODAS synthetic temperature and salinity derived from  $1/8^\circ$  MODAS2D SST and  $1/16^\circ$  NLOM SSH.

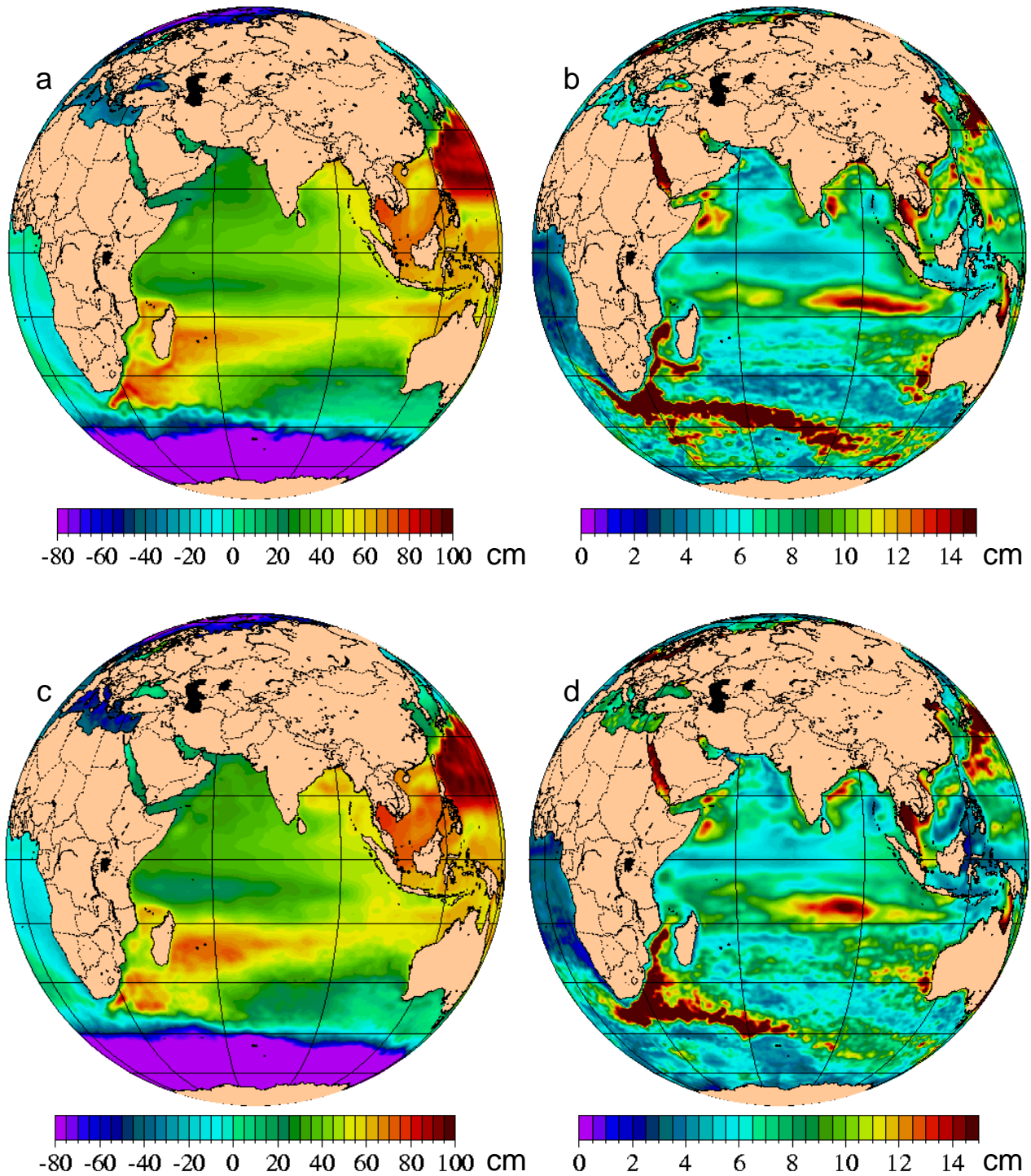


Fig. 10 – Indian hemispheric view of mean 1998-2000 SSH (left;a,c) and SSH standard deviation (right;b,d) for free-running (top;a,b) and assimilative (bottom;c,d)  $1/8^\circ$  global NCOM. NCOM is forced with NOGAPS wind and thermal forcing. The assimilative case relaxes to MODAS synthetic temperature and salinity derived from  $1/8^\circ$  MODAS2D SST and  $1/16^\circ$  NLOM SSH.

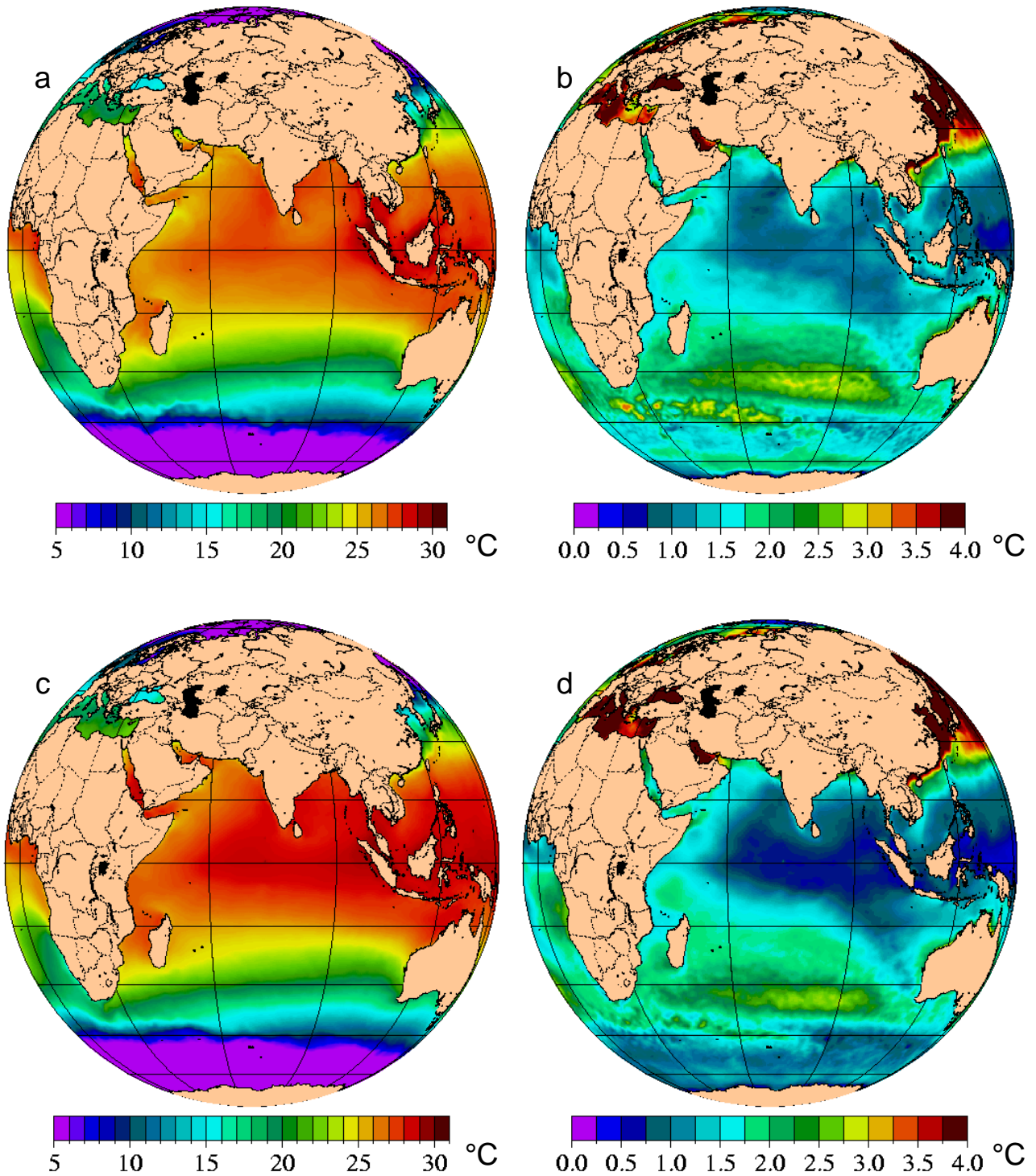


Fig. 11 – Indian hemispheric view of mean 1998-2000 SST (left;a,c) and SST standard deviation (right;b,d) for free-running (top;a,b) and assimilative (bottom;c,d)  $1/8^\circ$  global NCOM. NCOM is forced with NOGAPS wind and thermal forcing. The assimilative case relaxes to MODAS synthetic temperature and salinity derived from  $1/8^\circ$  MODAS2D SST and  $1/16^\circ$  NLOM SSH.

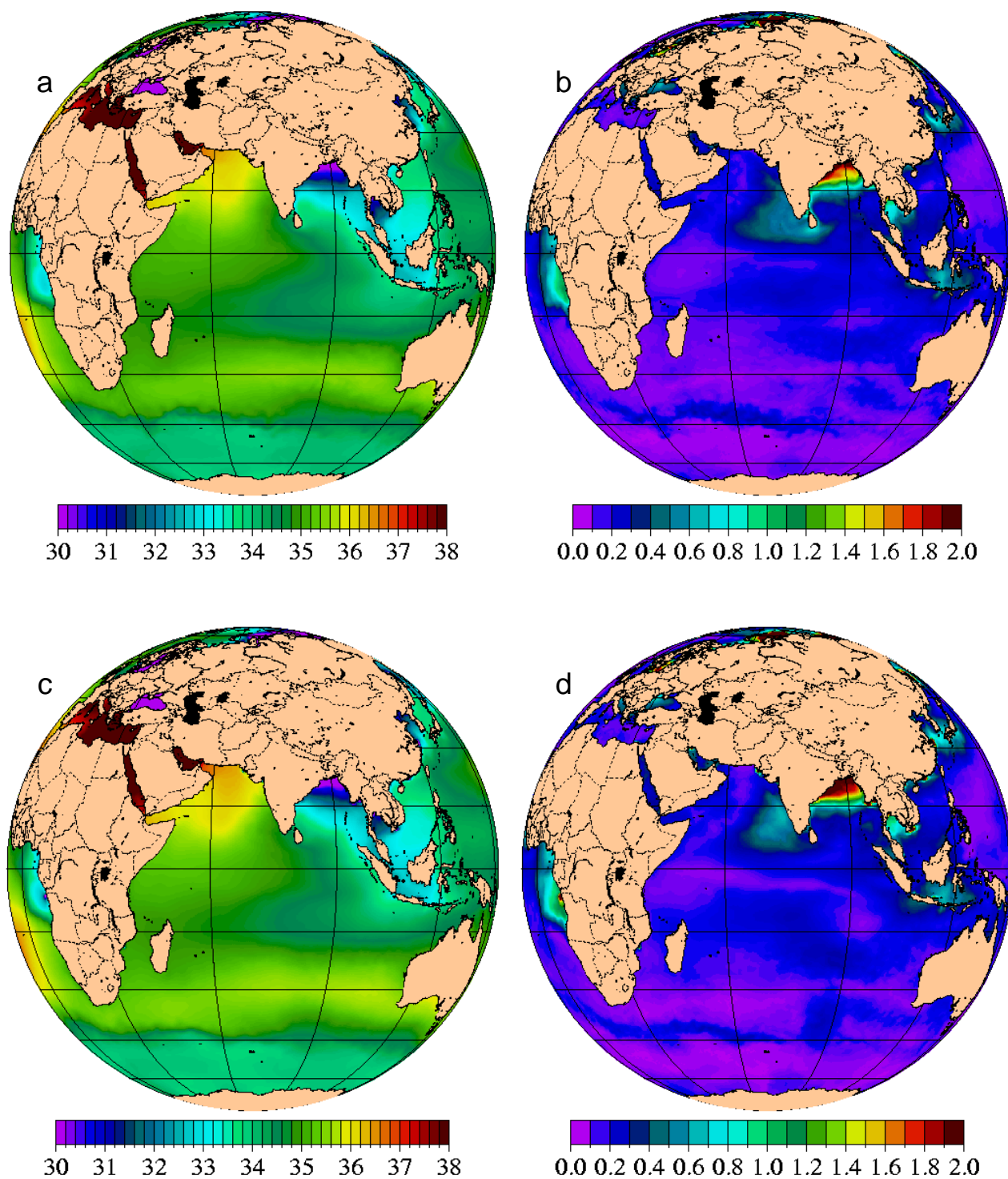


Fig. 12 – Indian hemispheric view of mean 1998-2000 SSS (left;a,c) and SSS standard deviation (right;b,d) for free-running (top;a,b) and assimilative (bottom;c,d)  $1/8^\circ$  global NCOM. NCOM is forced with NOGAPS wind and thermal forcing. The assimilative case relaxes to MODAS synthetic temperature and salinity derived from  $1/8^\circ$  MODAS2D SST and  $1/16^\circ$  NLOM SSH.

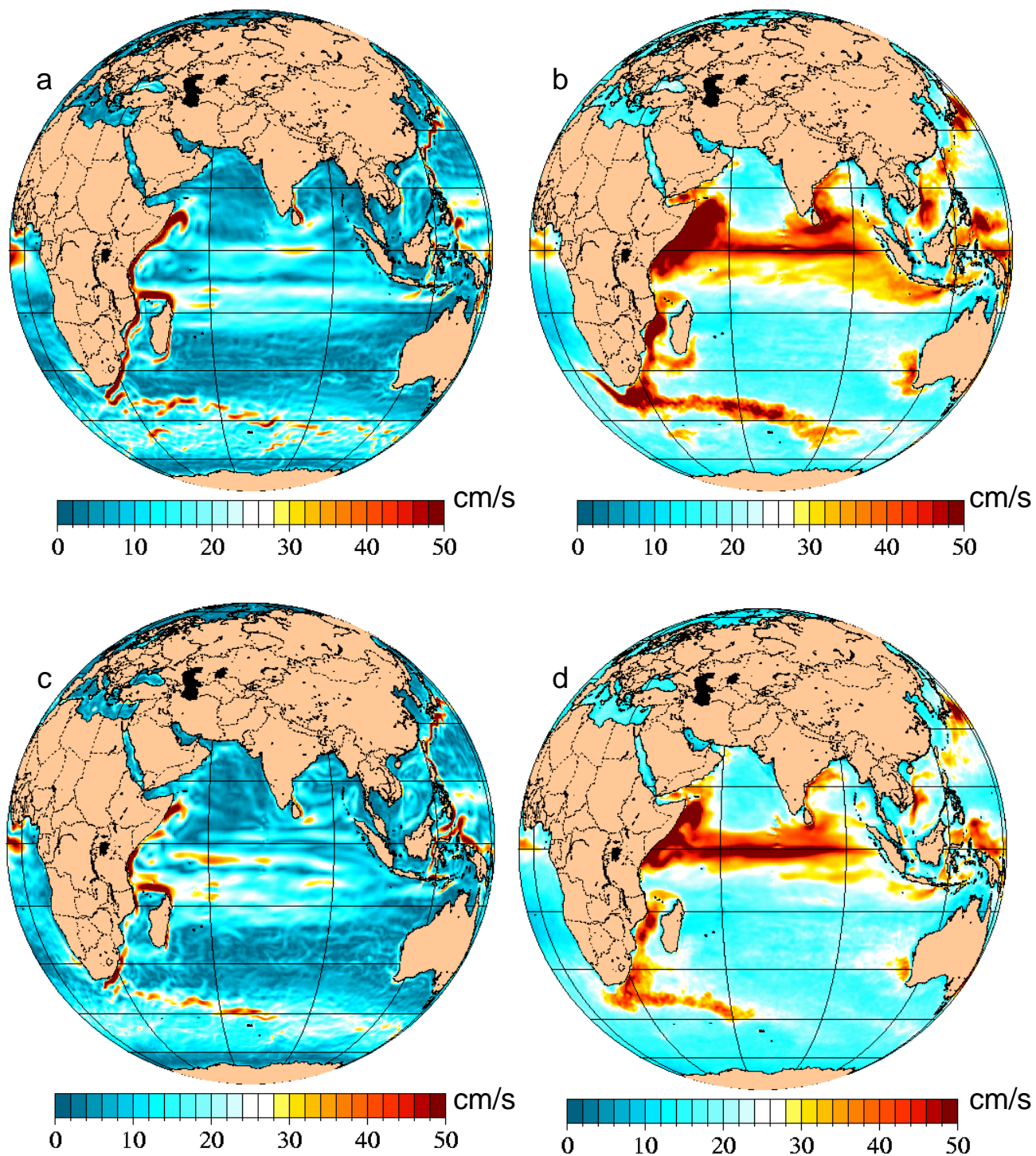


Fig. 13 – Indian hemispheric view of mean 1998-2000 surface speed (left; a,c) and surface speed standard deviation (right; b,d) for free-running (top; a,b) and assimilative (bottom; c,d)  $1/8^\circ$  global NCOM. NCOM is forced with NOGAPS wind and thermal forcing. The assimilative case relaxes to MODAS synthetic temperature and salinity derived from  $1/8^\circ$  MODAS2D SST and  $1/16^\circ$  NLOM SSH.

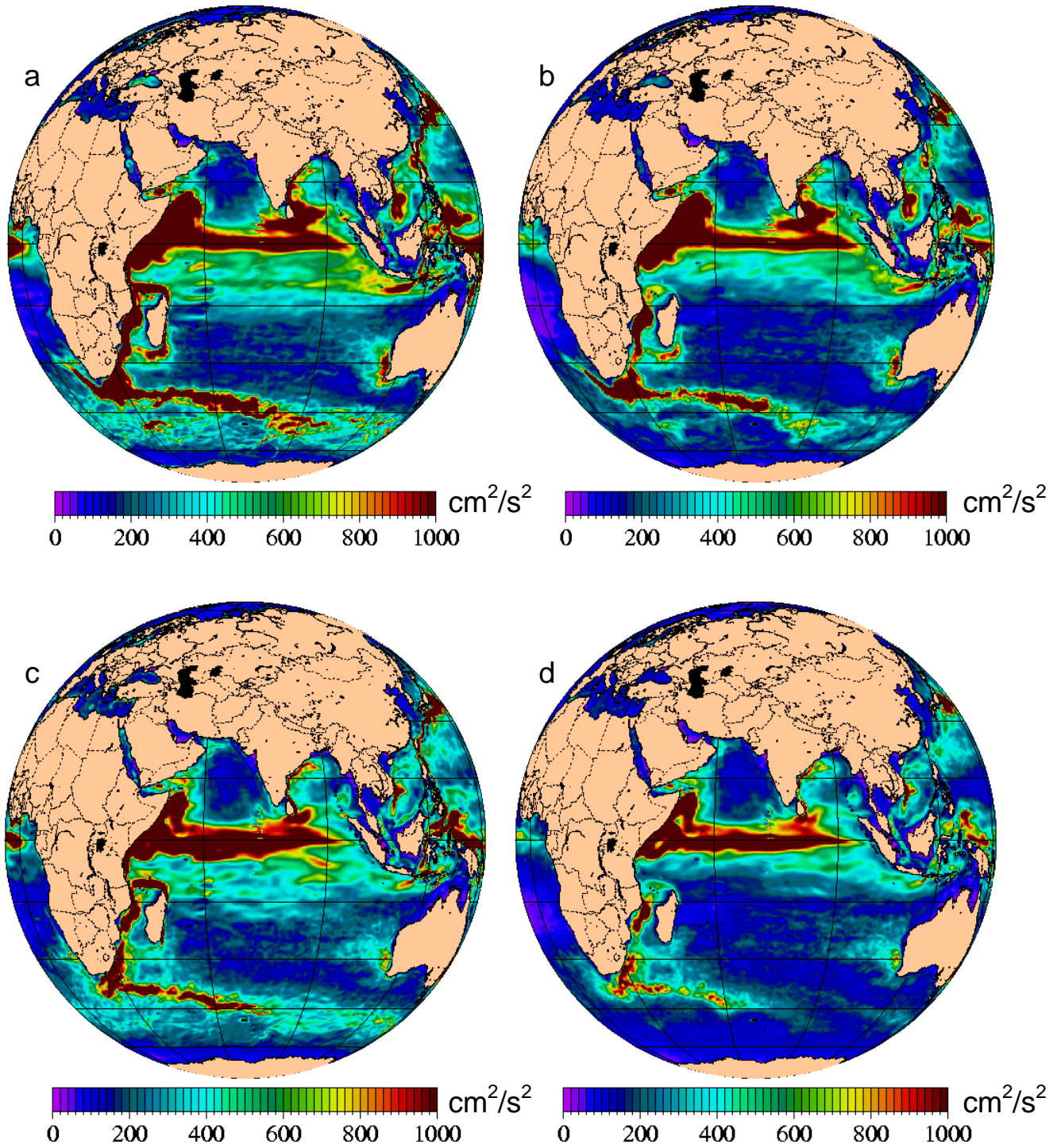


Fig. 14 – Indian hemispheric view of mean 1998-2000 surface kinetic energy (left; a, c) and surface EKE (right; b, d) for free-running (top; a, b) and assimilative (bottom; c, d)  $1/8^\circ$  global NCOM. NCOM is forced with NOGAPS wind and thermal forcing. The assimilative case relaxes to MODAS synthetic temperature and salinity derived from  $1/8^\circ$  MODAS2D SST and  $1/16^\circ$  NLOM SSH.

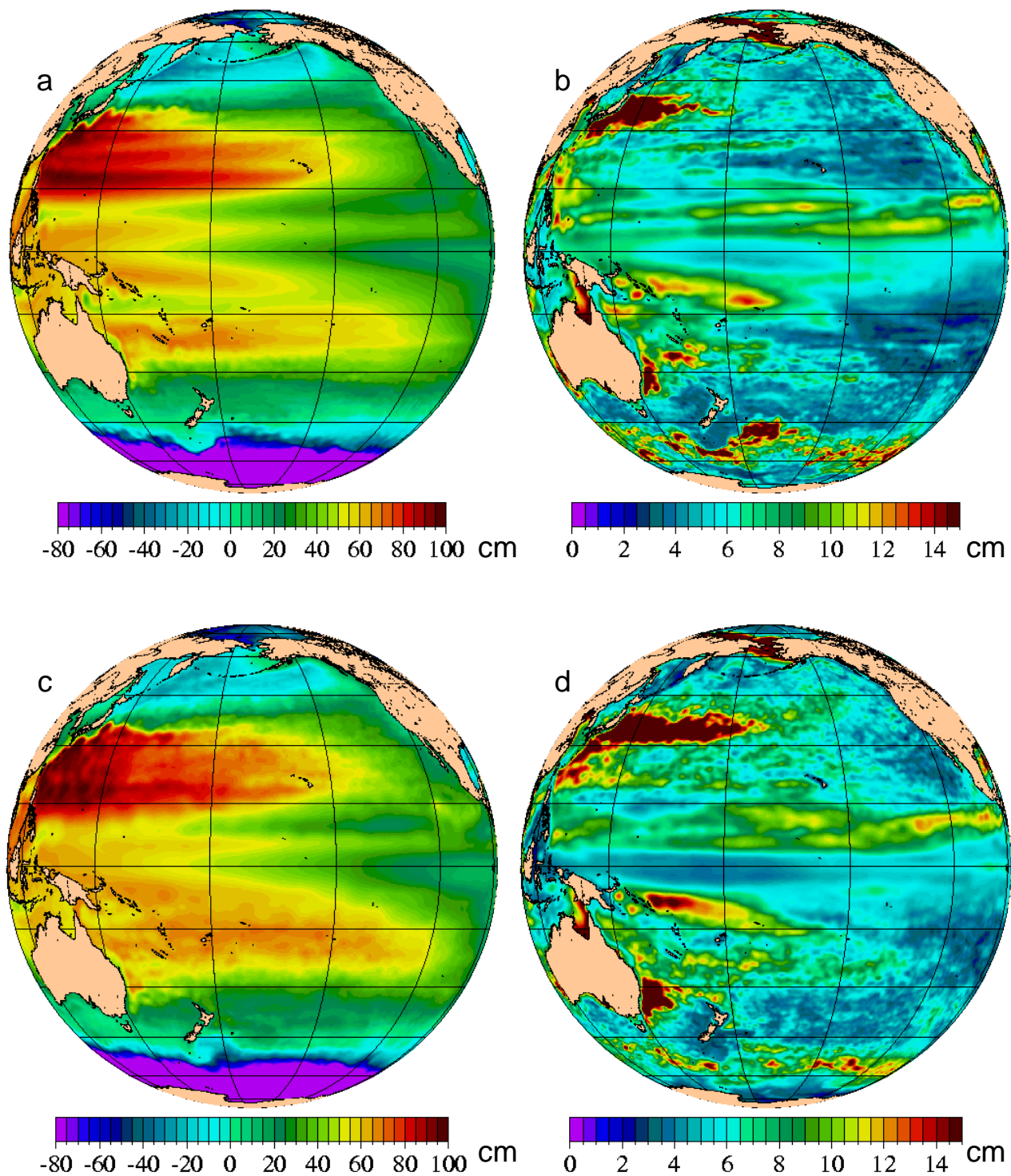


Fig. 15 – Pacific hemispheric view of mean 1998-2000 SSH (left;a,c) and SSH standard deviation (right;b,d) for free-running (top;a,b) and assimilative (bottom;c,d)  $1/8^\circ$  global NCOM. NCOM is forced with NOGAPS wind and thermalforcing. The assimilative case relaxes to MODAS synthetic temperature and salinity derived from  $1/8^\circ$  MODAS2D SST and  $1/16^\circ$  NLOM SSH.

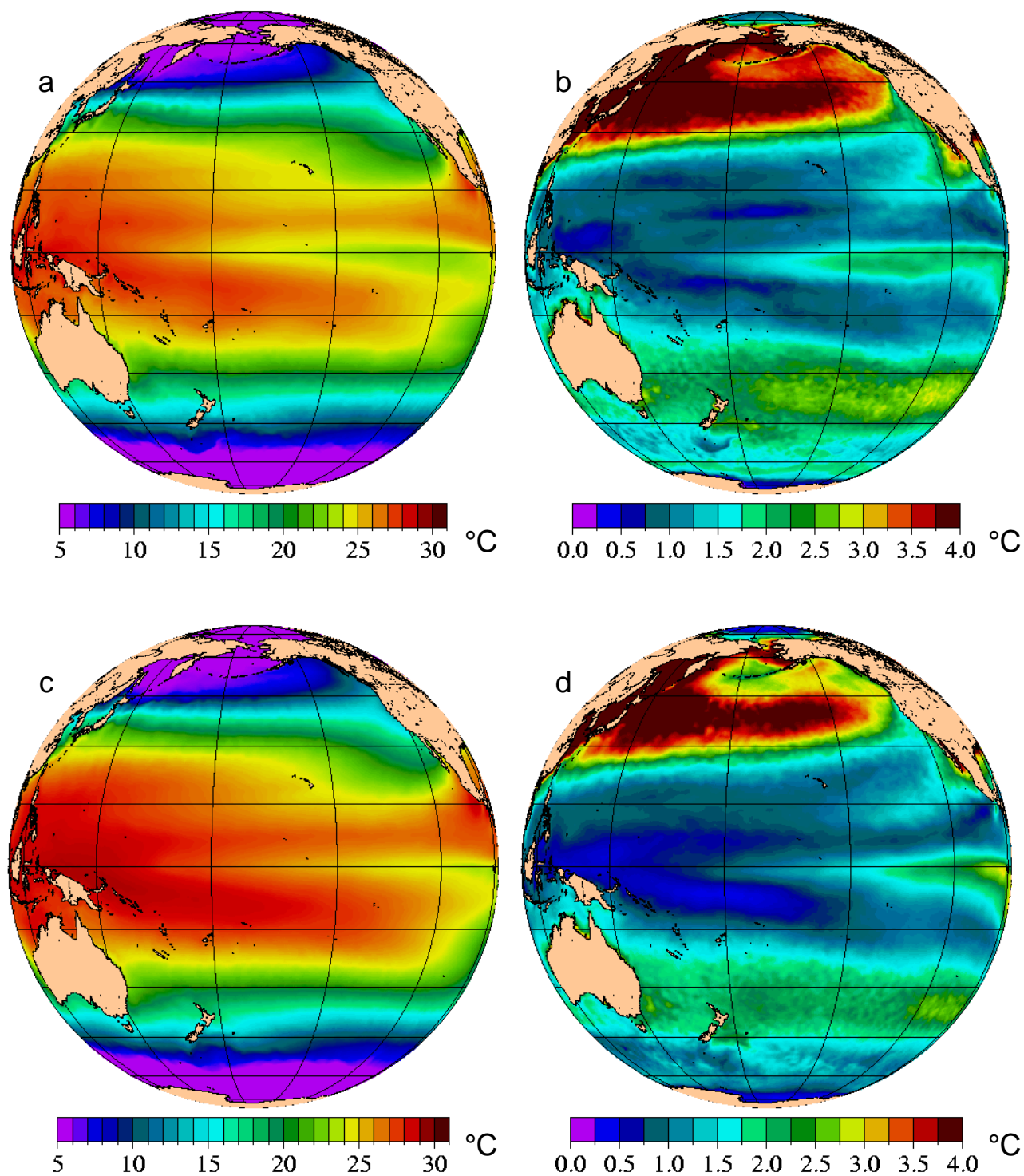


Fig. 16 – Pacific hemispheric view of mean 1998-2000 SST (left;a,c) and SST standard deviation (right;b,d) for free-running (top;a,b) and assimilative (bottom;c,d)  $1/8^\circ$  global NCOM. NCOM is forced with NOGAPS wind and thermal forcing. The assimilative case relaxes to MODAS synthetic temperature and salinity derived from  $1/8^\circ$  MODAS2D SST and  $1/16^\circ$  NLOM SSH.

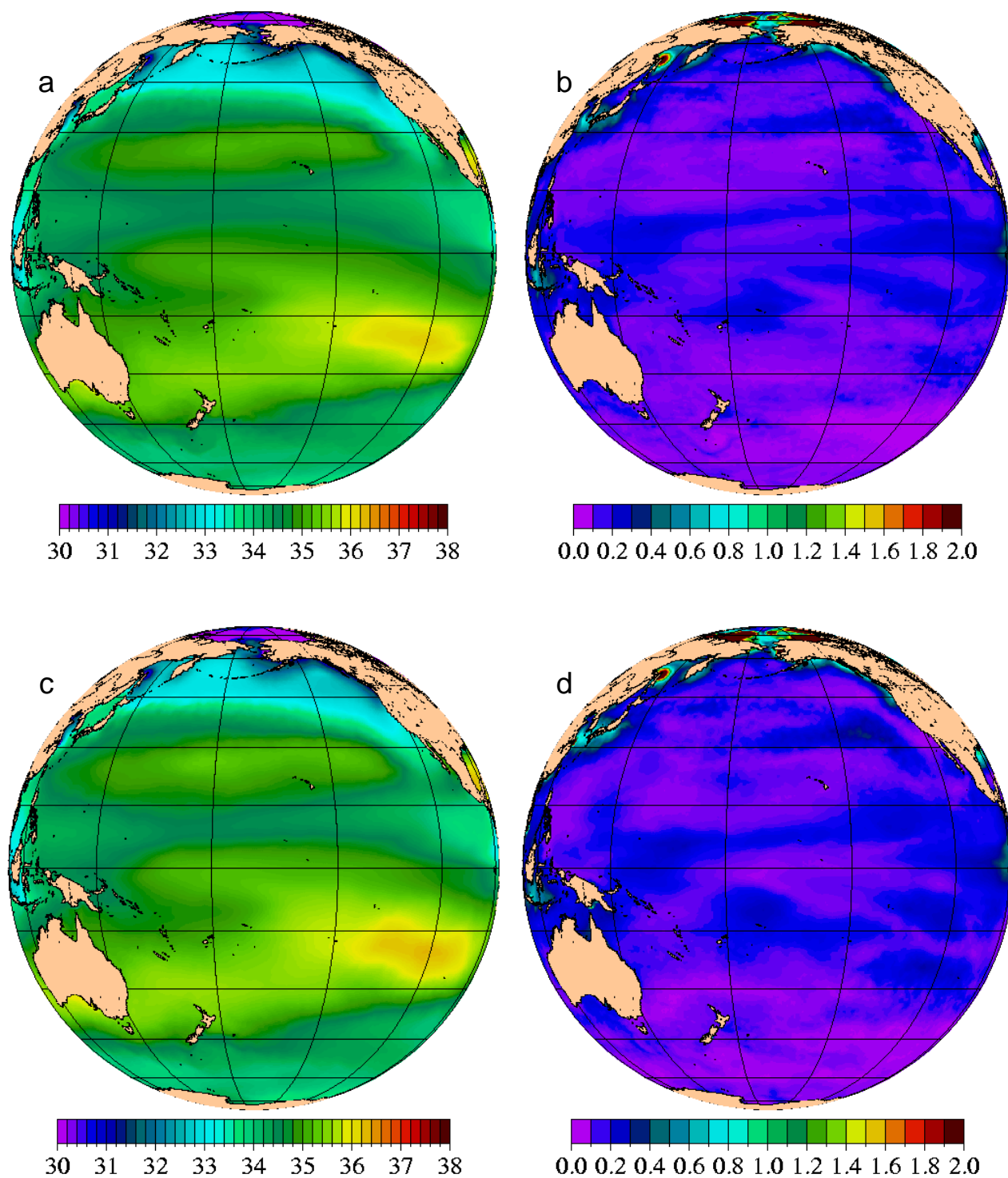


Fig. 17 – Pacific hemispheric view of mean 1998-2000 SSS (left;a,c) and SSS standard deviation (right;b,d) for free-running (top;a,b) and assimilative (bottom;c,d)  $1/8^\circ$  global NCOM. NCOM is forced with NOGAPS wind and thermal forcing. The assimilative case relaxes to MODAS synthetic temperature and salinity derived from  $1/8^\circ$  MODAS2D SST and  $1/16^\circ$  NLOM SSH.

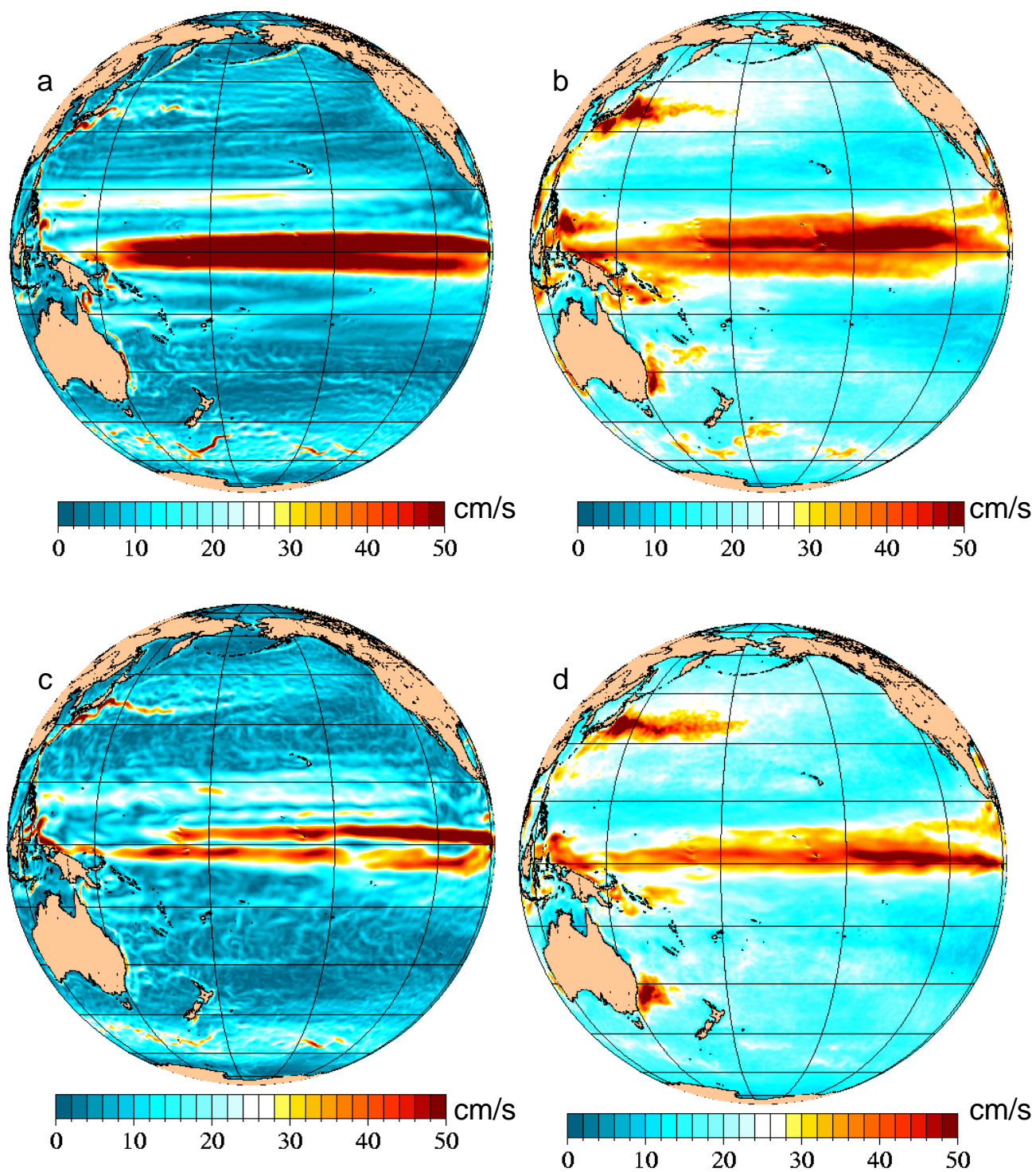


Fig. 18 – Pacific hemispheric view of mean 1998-2000 surface speed (left;a,c) and surface speed standard deviation (right;b,d) for free-running (top;a,b) and assimilative (bottom;c,d)  $1/8^\circ$  global NCOM. NCOM is forced with NOGAPS wind and thermal forcing. The assimilative case relaxes to MODAS synthetic temperature and salinity derived from  $1/8^\circ$  MODAS2D SST and  $1/16^\circ$  NLOM SSH.

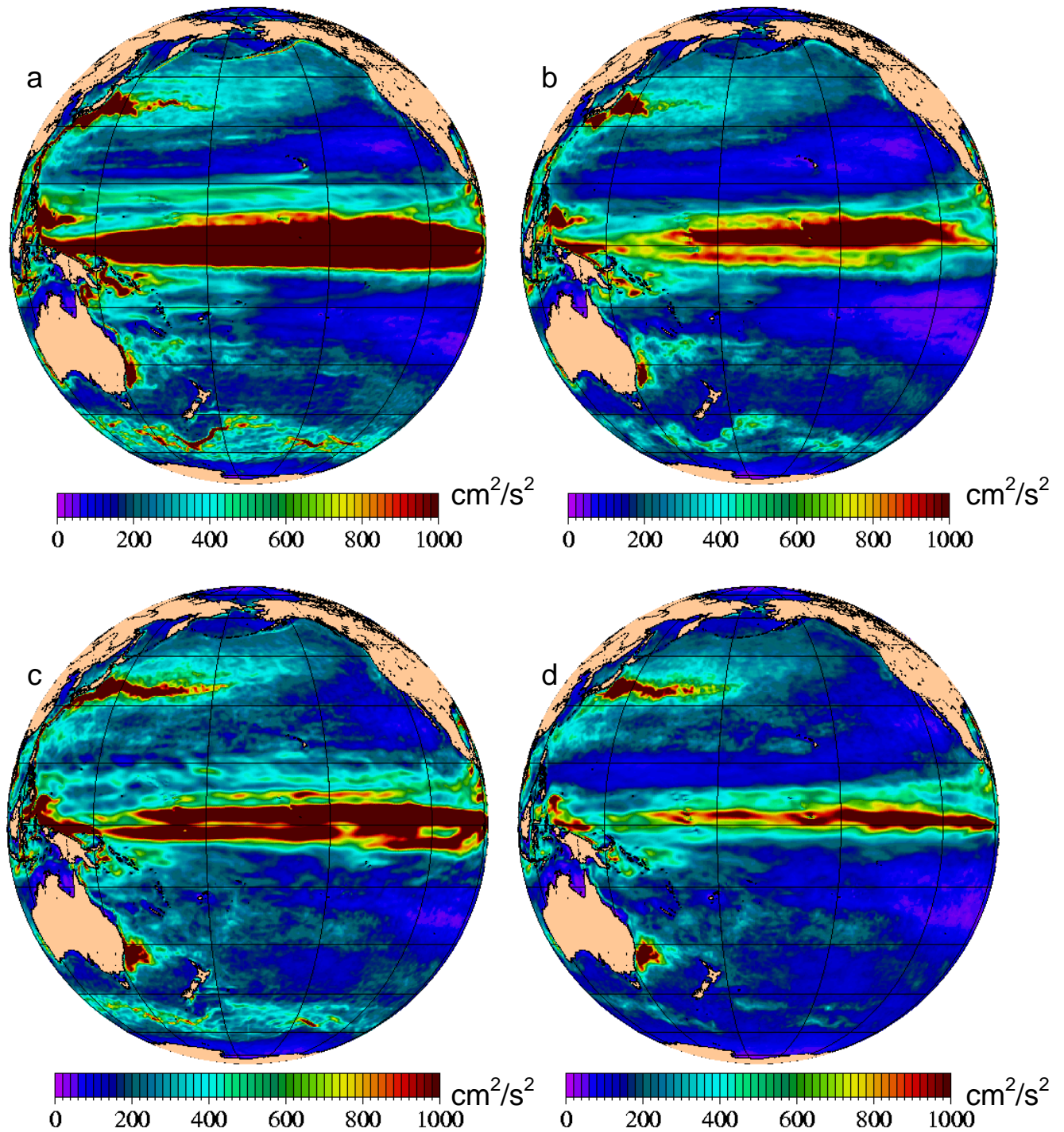


Fig. 19 – Pacific hemispheric view of mean 1998-2000 surface kinetic energy (left; a,c) and surface EKE (right; b,d) for free-running (top; a,b) and assimilative (bottom; c,d)  $1/8^\circ$  global NCOM. NCOM is forced with NOGAPS wind and thermal forcing. The assimilative case relaxes to MODAS synthetic temperature and salinity derived from  $1/8^\circ$  MODAS2D SST and  $1/16^\circ$  NLOM SSH.

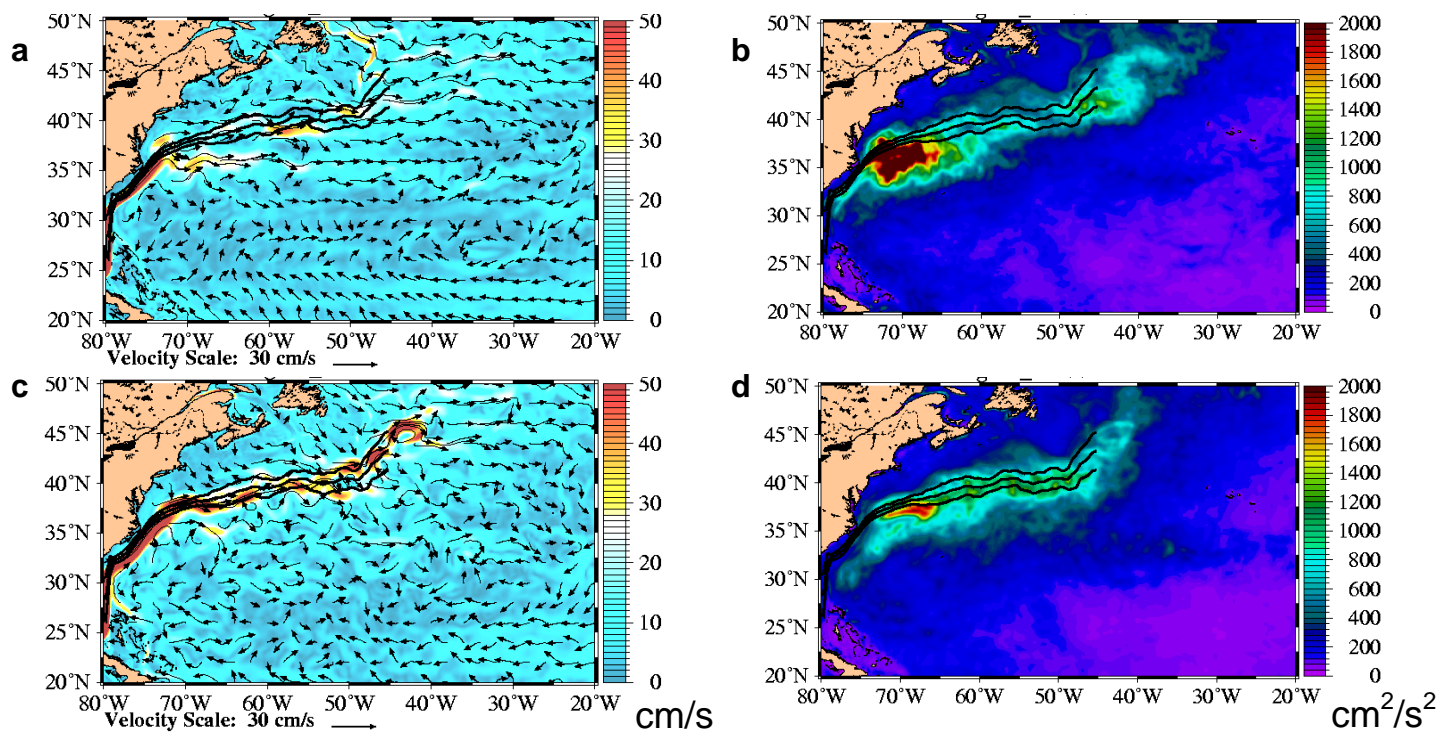


Fig. 20 – Gulf Stream zoom of mean 1998-2000 surface speed with superimposed currents (left;a,c) and surface EKE (right;b,d) for free-running (top;a,b) and assimilative (bottom;c,d)  $1/8^\circ$  global NCOM. Superimposed black curves are the mean and mean  $\pm 1$  standard deviation fronts from the NAVOCEANO Gulf Stream north wall bogues from archives over the same time period.

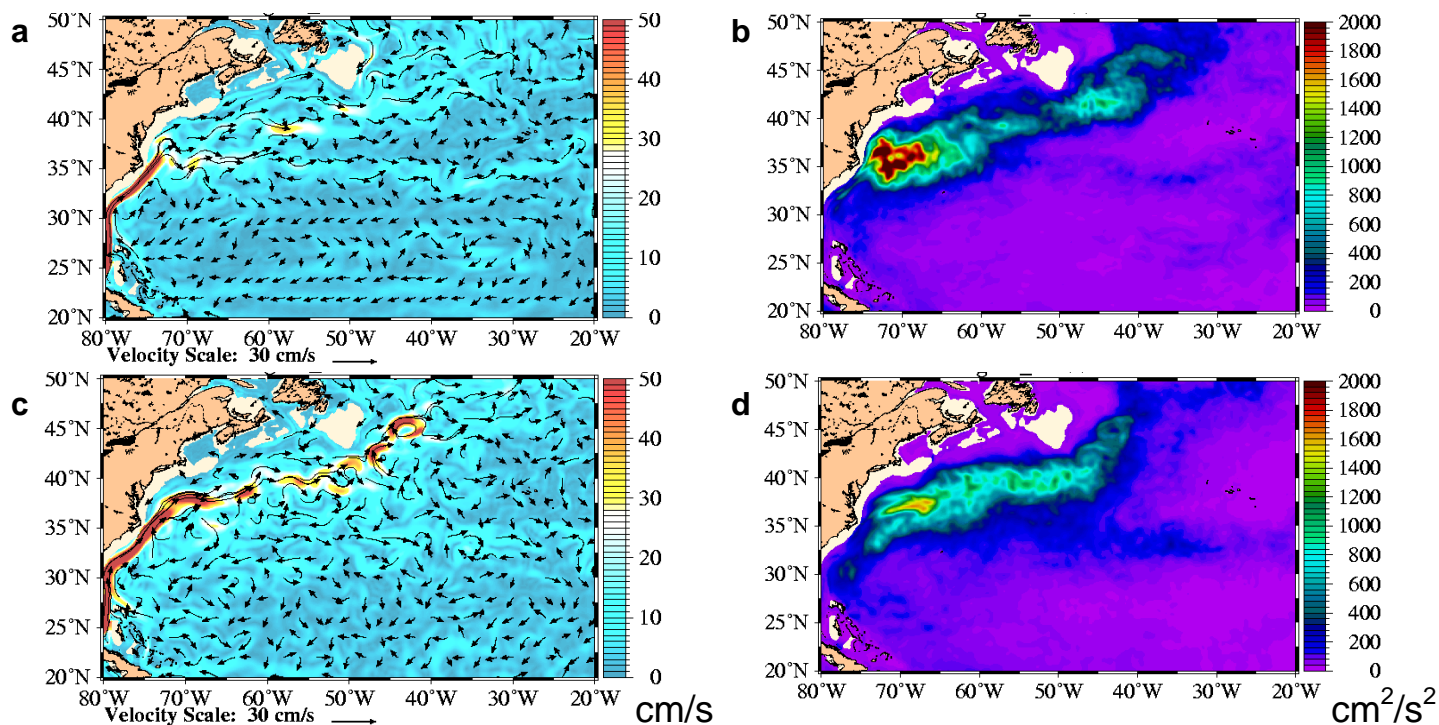


Fig. 21 – Gulf Stream zoom of mean 1998-2000 100m speed with superimposed currents (left;a,c) and 100m EKE (right;b,d) for free-running (top;a,b) and assimilative (bottom;c,d)  $1/8^\circ$  global NCOM.

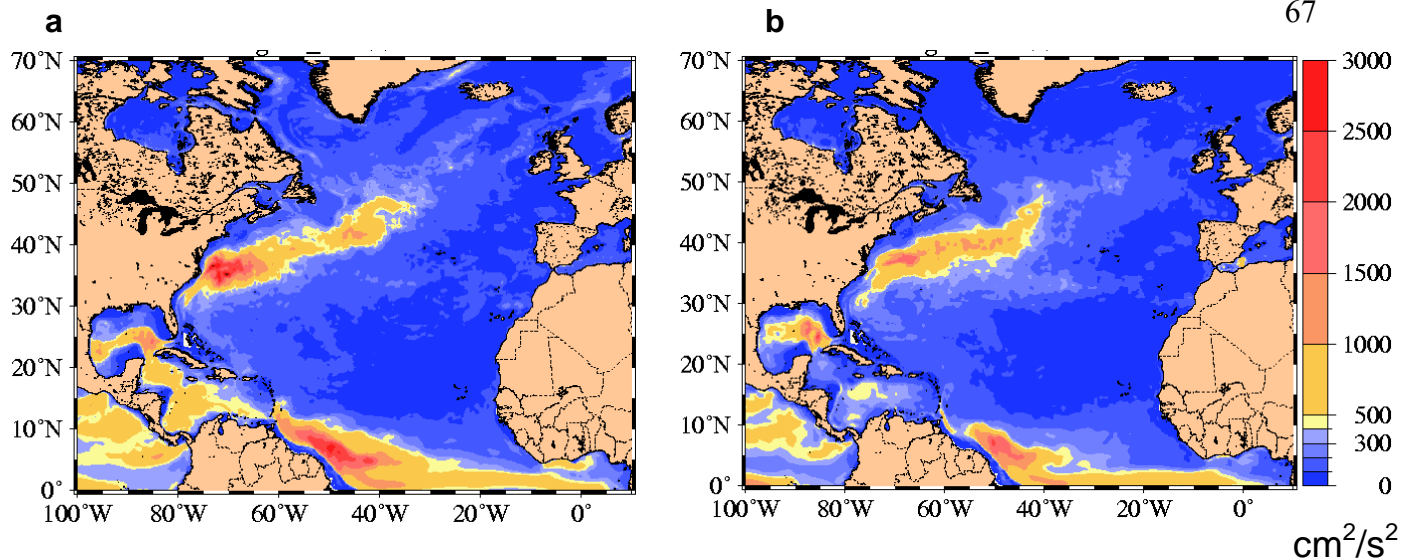


Fig. 22 – North Atlantic zoom of mean 1998-2000 5m EKE for free-running (a) and assimilative (b)  $1/8^\circ$  global NCOM. While similar to the assimilative case in most respects, the free-running case in the Caribbean Sea and north of  $60^\circ\text{N}$  has higher surface EKE, in better agreement with observations (below).

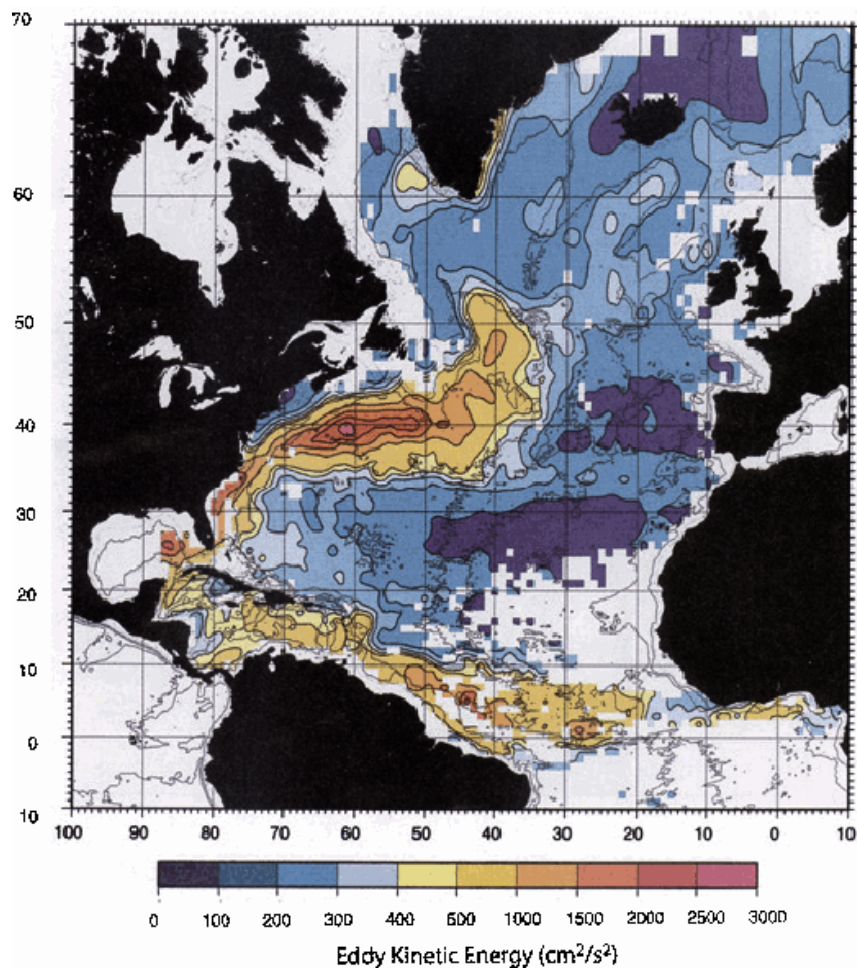


Fig. 23 – North Atlantic surface EKE calculated using Lagrangian velocities derived from satellite drifter observations during the 1990s. Taken from Fratantoni (2001).

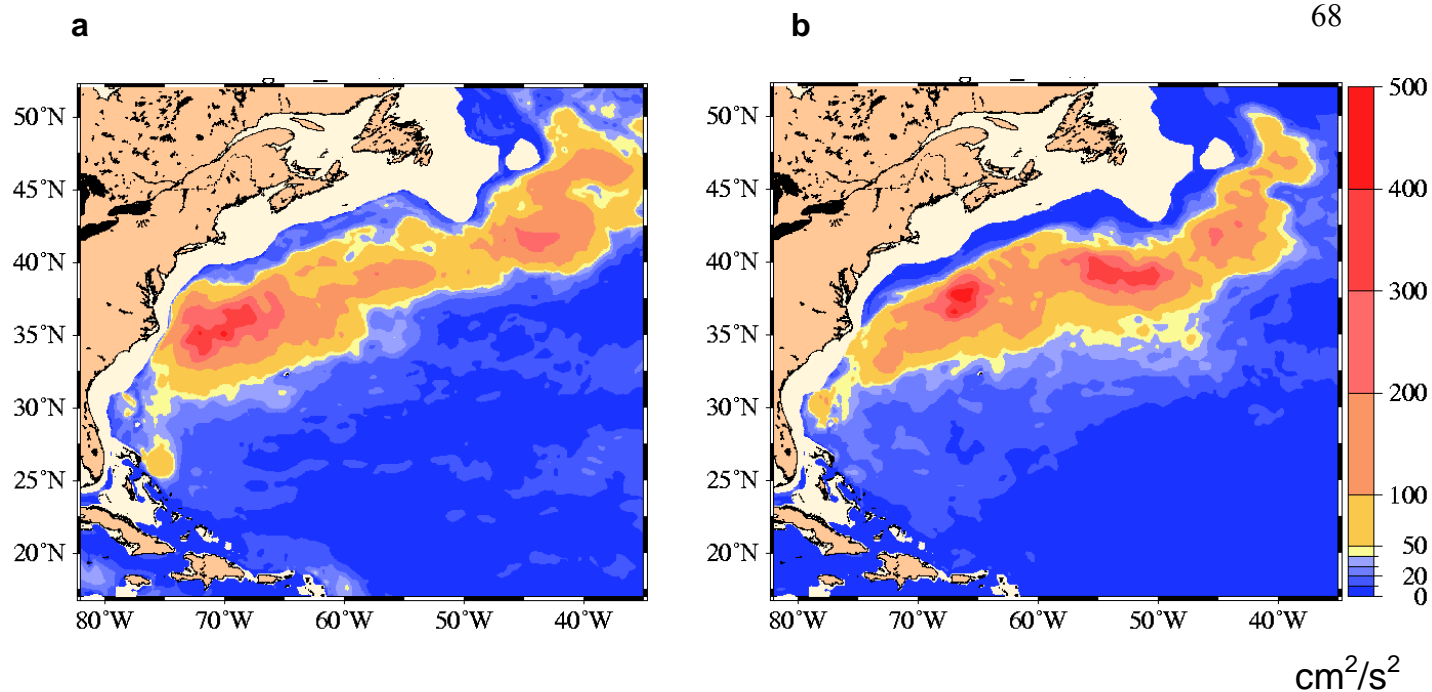


Fig. 24 – Gulf Stream zoom of mean 1998-2000 EKE at 700m from free-running (a) and assimilative (b)  $1/8^\circ$  global NCOM. In comparison to the free-running case, EKE at 700m in the assimilative case is generally higher and in closer agreement to historical observations (below), showing the two regions of relatively high EKE south of Nova Scotia and Newfoundland.

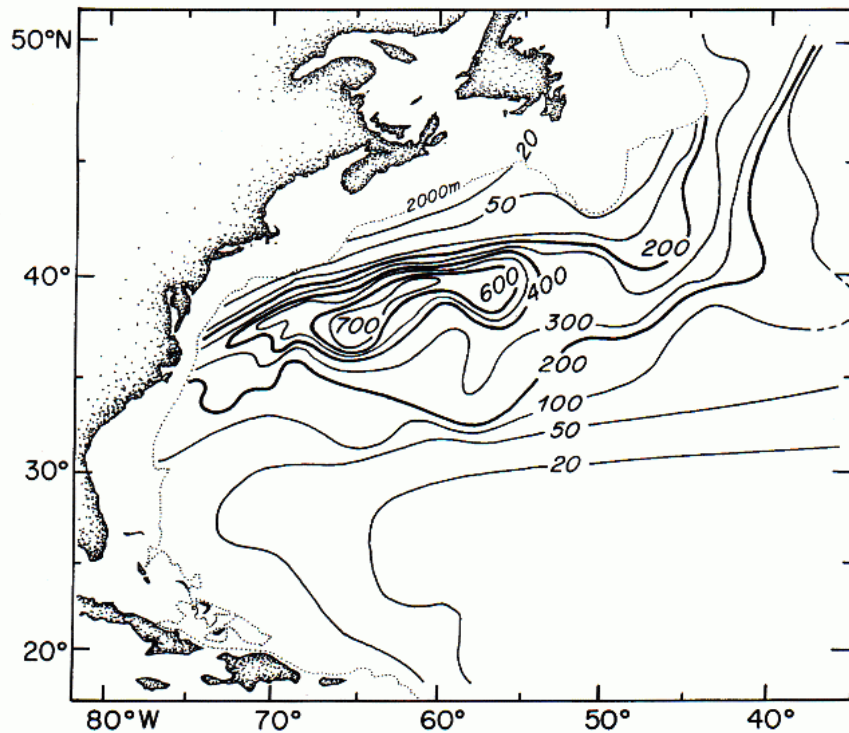


Fig. 25 – Climatological EKE near 700m depth in the western North Atlantic. Taken from Schmitz (1996) which adapted the data from Owens (1984,1991) and Richardson (1993).

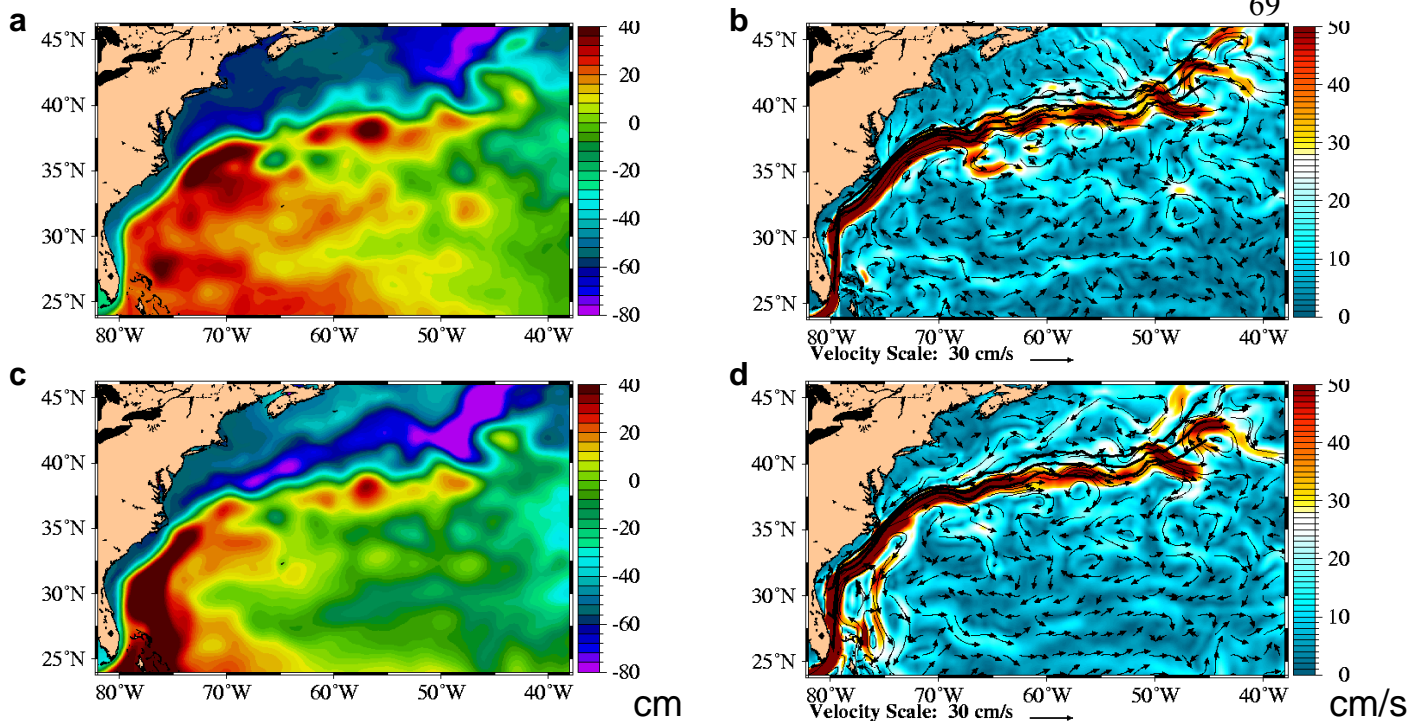


Fig. 26 – Gulf Stream zoom of mean SSH (left;a,c) and surface speed with superimposed currents (right;b,d) for assimilative  $1/8^\circ$  global NCOM (top;a,b) and assimilative  $1/4^\circ$  SWAFS Northworld (bottom;c,d). Superimposed black curves are the mean and mean  $\pm 1$  standard deviation fronts from the NAVOCEANO Gulf Stream north wall boguses from archives over the same time period. Mean is over period of available SWAFS surface data, 9/1/2002-5/31/2003. To enable the same color bar and ranges to be used, mean SWAFS SSH is offset to equal mean NCOM SSH over this domain.

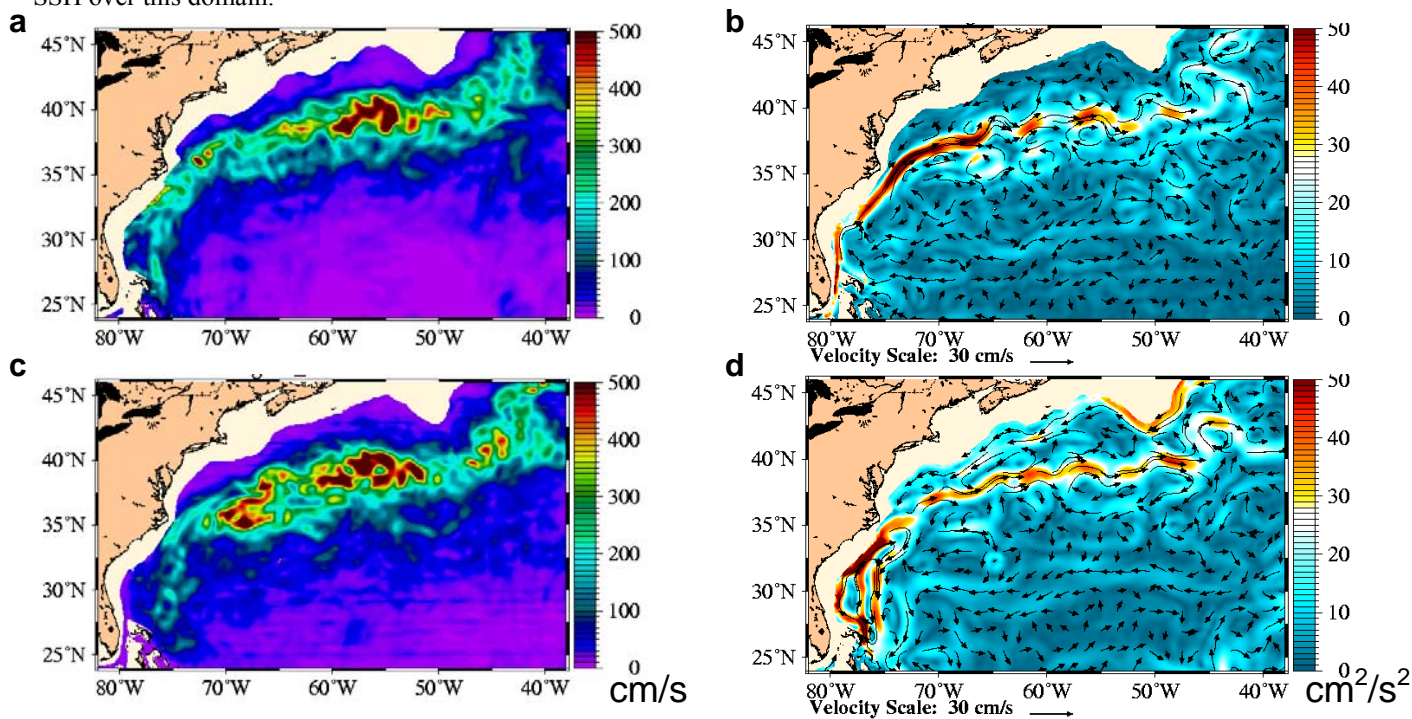


Fig. 27 – Gulf Stream zoom of mean 500m speed with superimposed currents (left;a,c) and 500m EKE (right;b,d) for assimilative  $1/8^\circ$  global NCOM (top;a,b) and assimilative  $1/4^\circ$  SWAFS Northworld (bottom;c,d). Mean is over period of available SWAFS subsurface data, 11/15/2002 – 5/15/2003.

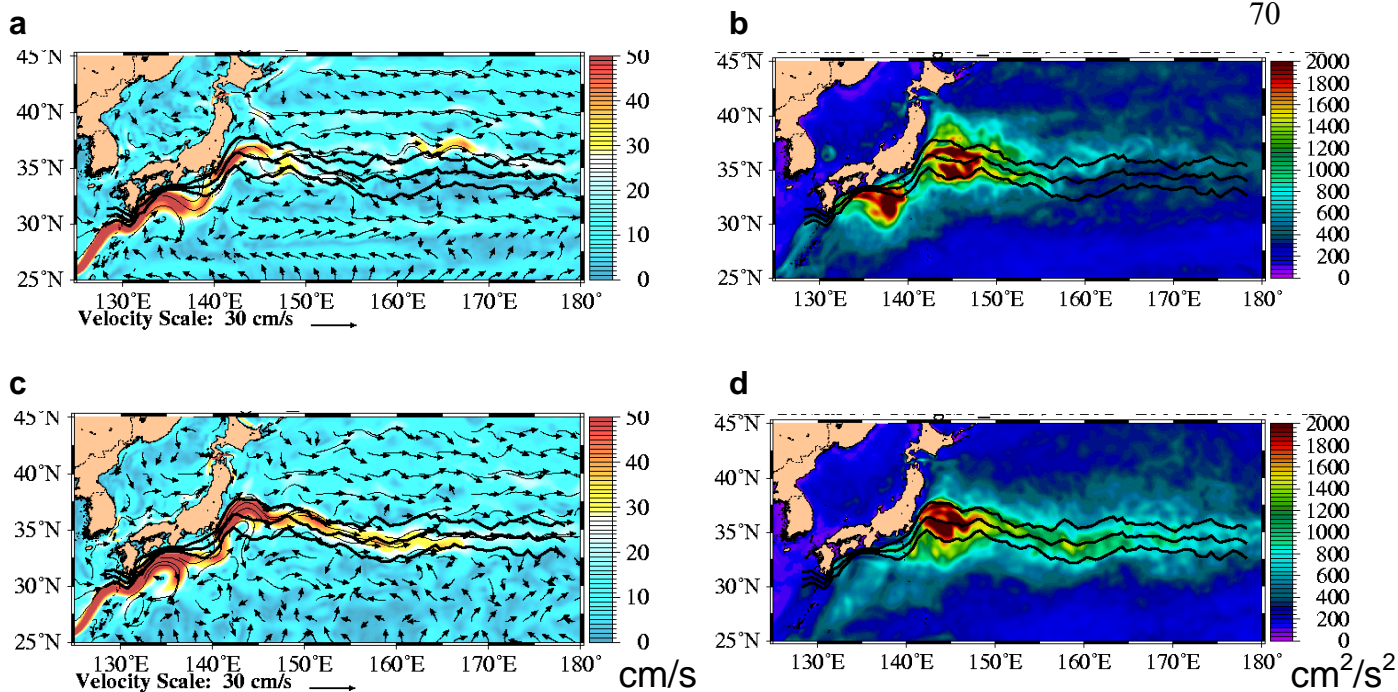


Fig. 28 – Kuroshio zoom of mean 1998-2000 surface speed with superimposed currents (left;a,c) and surface EKE (right;b,d) for free-running (top;a,b) and assimilative (bottom;c,d) 1/8° global NCOM. Superimposed black curves are the mean and mean  $\pm 1$  standard deviation fronts from the NAVOCEANO Kuroshio north wall boguses from archives over the same time period.

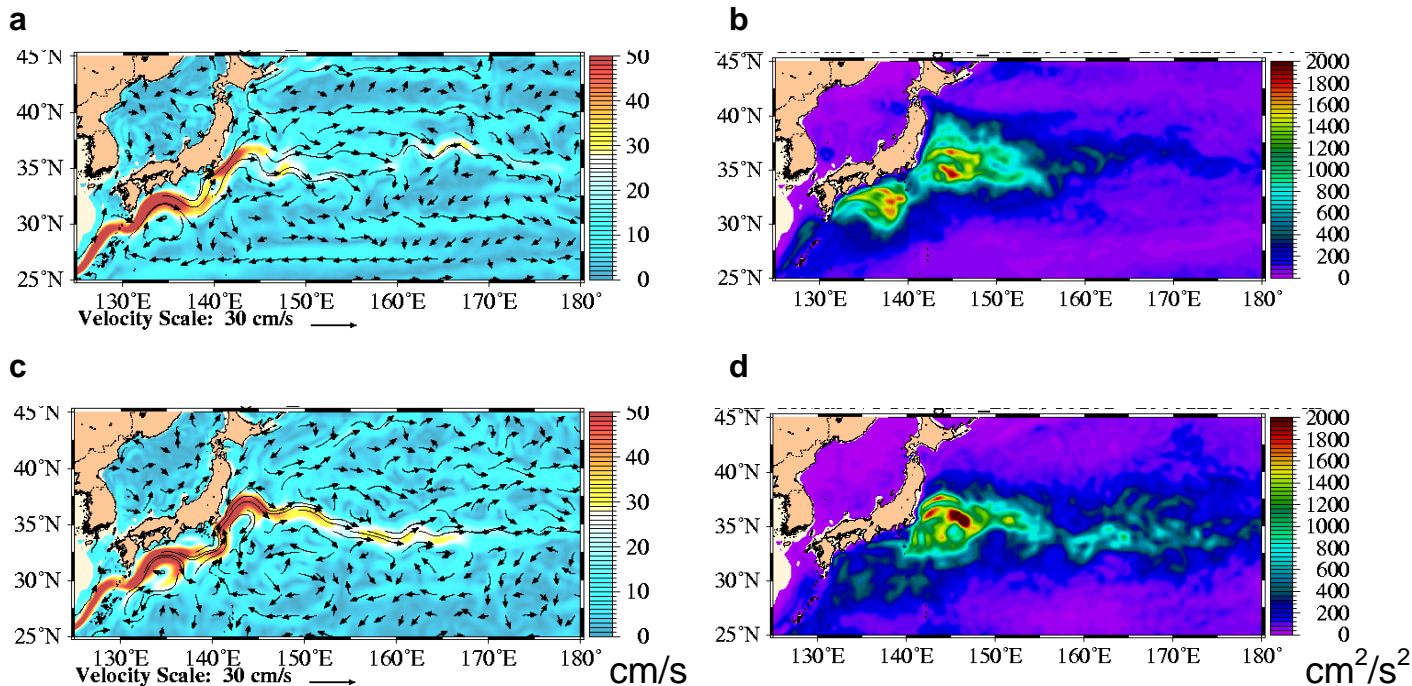


Fig. 29 – Kuroshio zoom of mean 1998-2000 100m speed with superimposed currents (left;a,c) and 100m EKE (right;b,d) for free-running (top;a,b) and assimilative (bottom;c,d) 1/8° global NCOM.

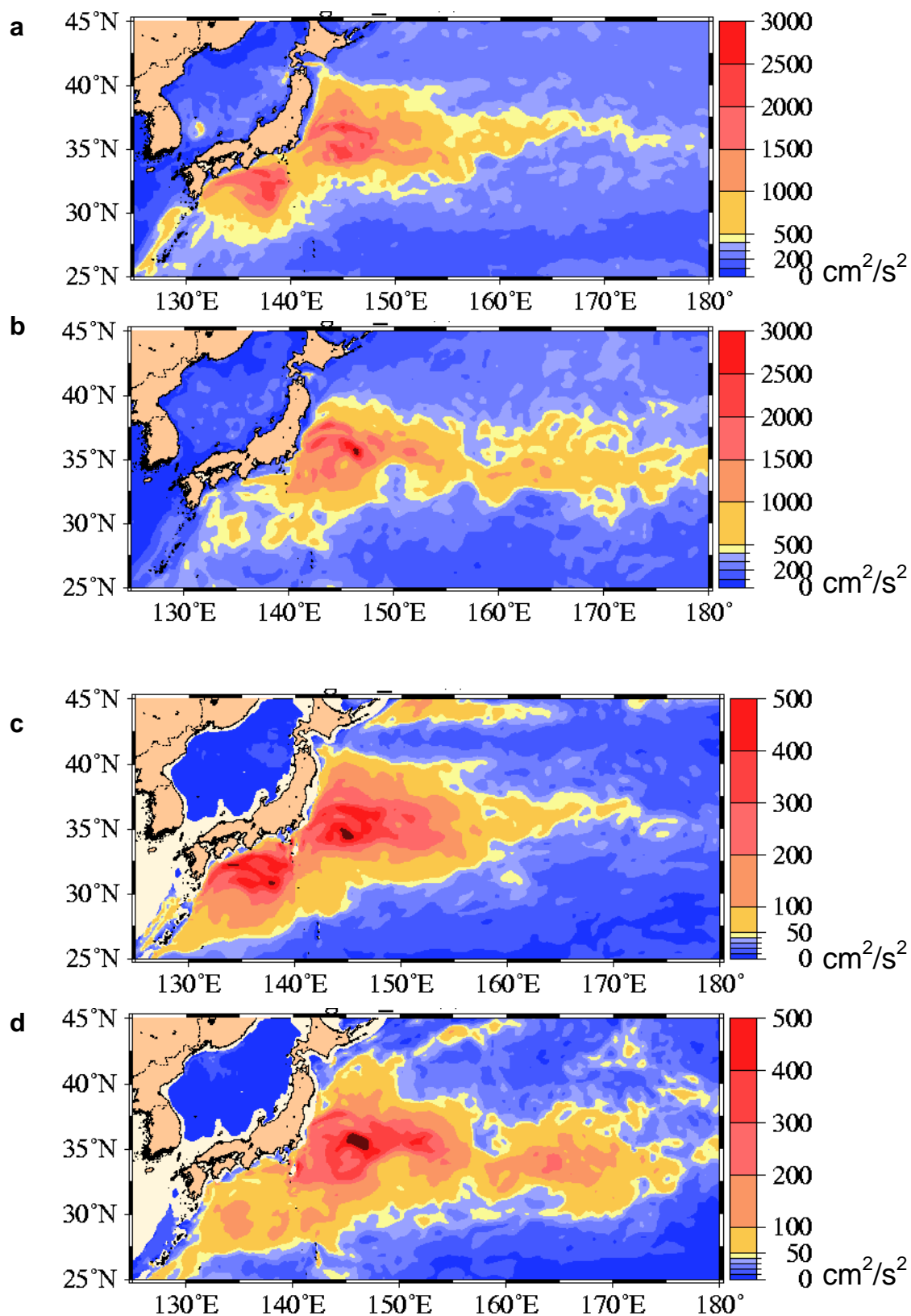


Fig. 30 – Kuroshio zoom of mean 1998-2000 EKE at 5m (a,b) and 500m (c,d) from free-running (a,c) and assimilative (b,d)  $1/8^\circ$  global NCOM. Assimilation produces a more realistic eastward extension of the Kuroshio and more tightly constrains the current east of  $140^\circ\text{E}$ .

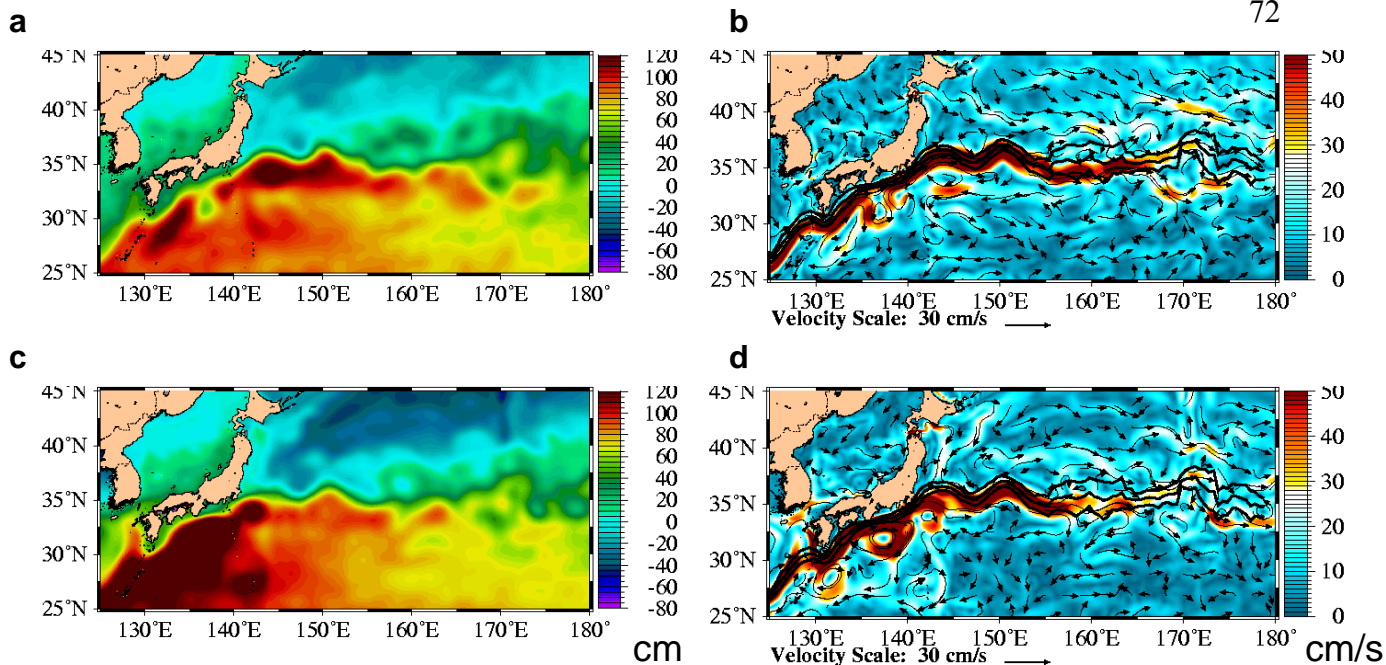


Fig. 31 – Kuroshio zoom of mean SSH (left;a,c) and surface speed with superimposed currents (right;b,d) for assimilative 1/8° global NCOM (top;a,b) and assimilative 1/4° SWAFS Northworld (bottom;c,d). Superimposed black curves are the mean and mean  $\pm 1$  standard deviation fronts from the NAVOCEANO Kuroshio north wall boguses from archives over the same time period. Mean is over period of available SWAFS surface data, 9/1/2002 – 5/31/2003. To enable the same color bar and ranges to be used, the mean SWAFS SSH is offset to equal the mean NCOM SSH over this domain. NCOM has a more realistic eastward extension of the Kuroshio.

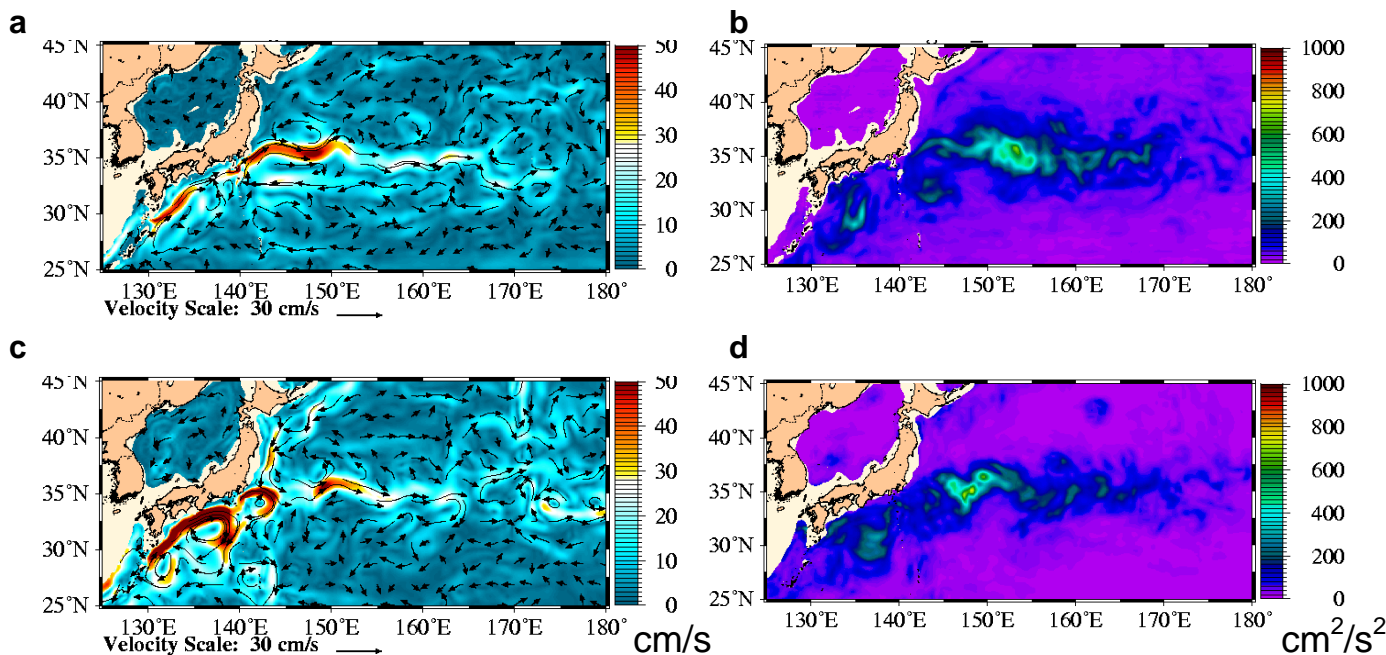


Fig. 32 – Kuroshio zoom of mean 500m speed with superimposed currents (left;a,c) and 500m EKE (right;b,d) for assimilative 1/8° global NCOM (top;a,b) and assimilative 1/4° SWAFS Northworld (bottom; c,d). Mean is over period of available SWAFS subsurface data, 11/15/2002 – 5/15/2003.

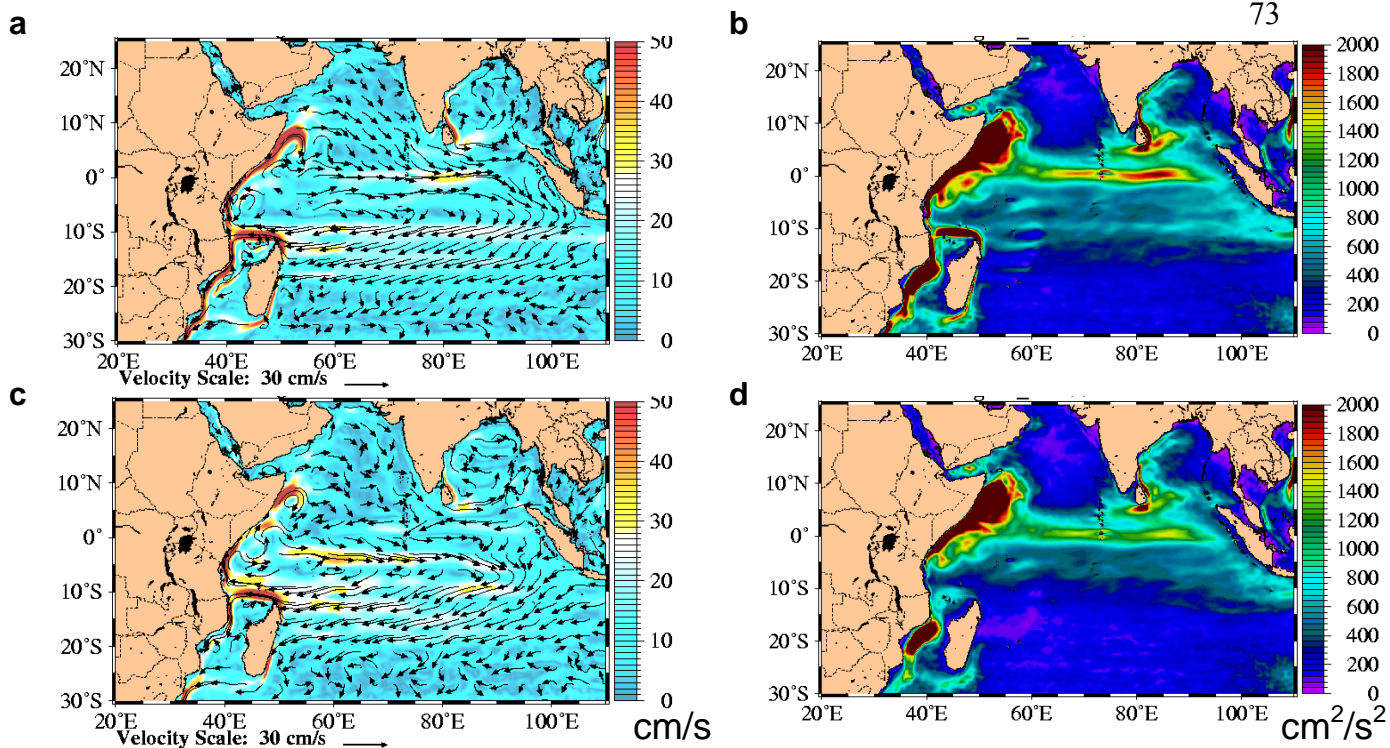


Fig. 33 – Indian Ocean zoom of mean 1998-2000 surface speed with superimposed currents (left;a,c) and surface EKE (right;b,d) for free-running (top;a,b) and assimilative (bottom;c,d) 1/8° global NCOM.

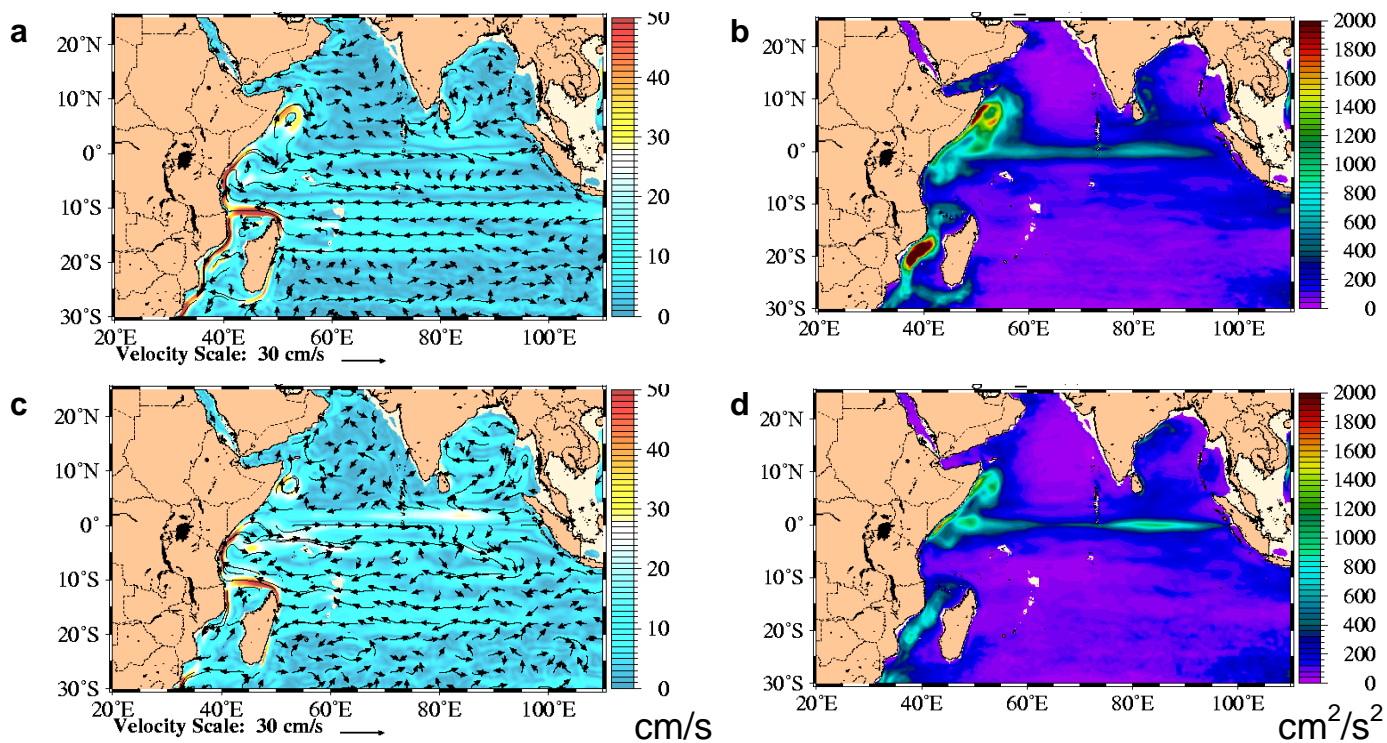


Fig. 34 – Indian Ocean zoom of mean 1998-2000 100m speed with superimposed currents (left;a,c) and 100m EKE (right;b,d) for free-running (top;a,b) and assimilative (bottom;c,d).

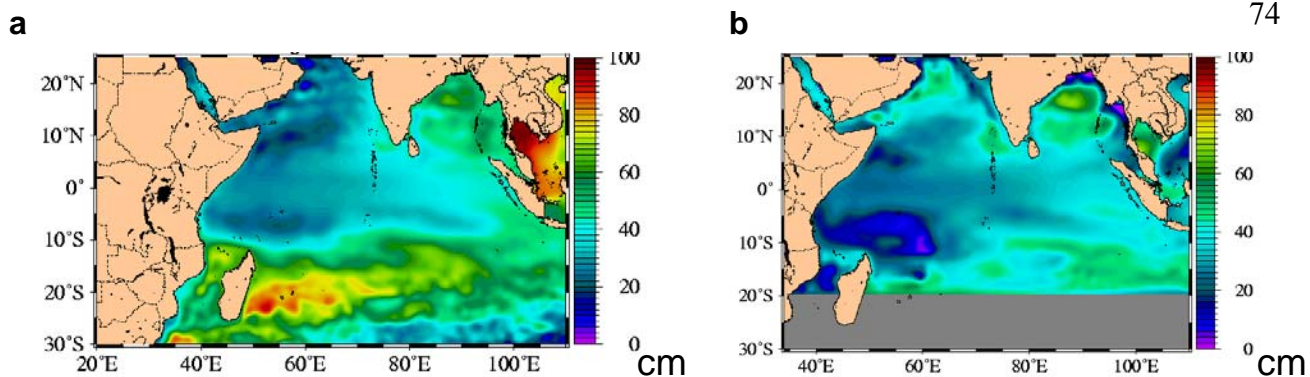


Fig. 35 – Indian Ocean zoom of mean SSH for assimilative 1/8° global NCOM (a) and assimilative 1/4° SWAFS Northworld (b). Mean is over winter monsoon period, 11/15/2002 – 3/15/2003. To enable the same color bar and ranges to be used, the mean SWAFS SSH is offset to equal the mean NCOM SSH over this domain.

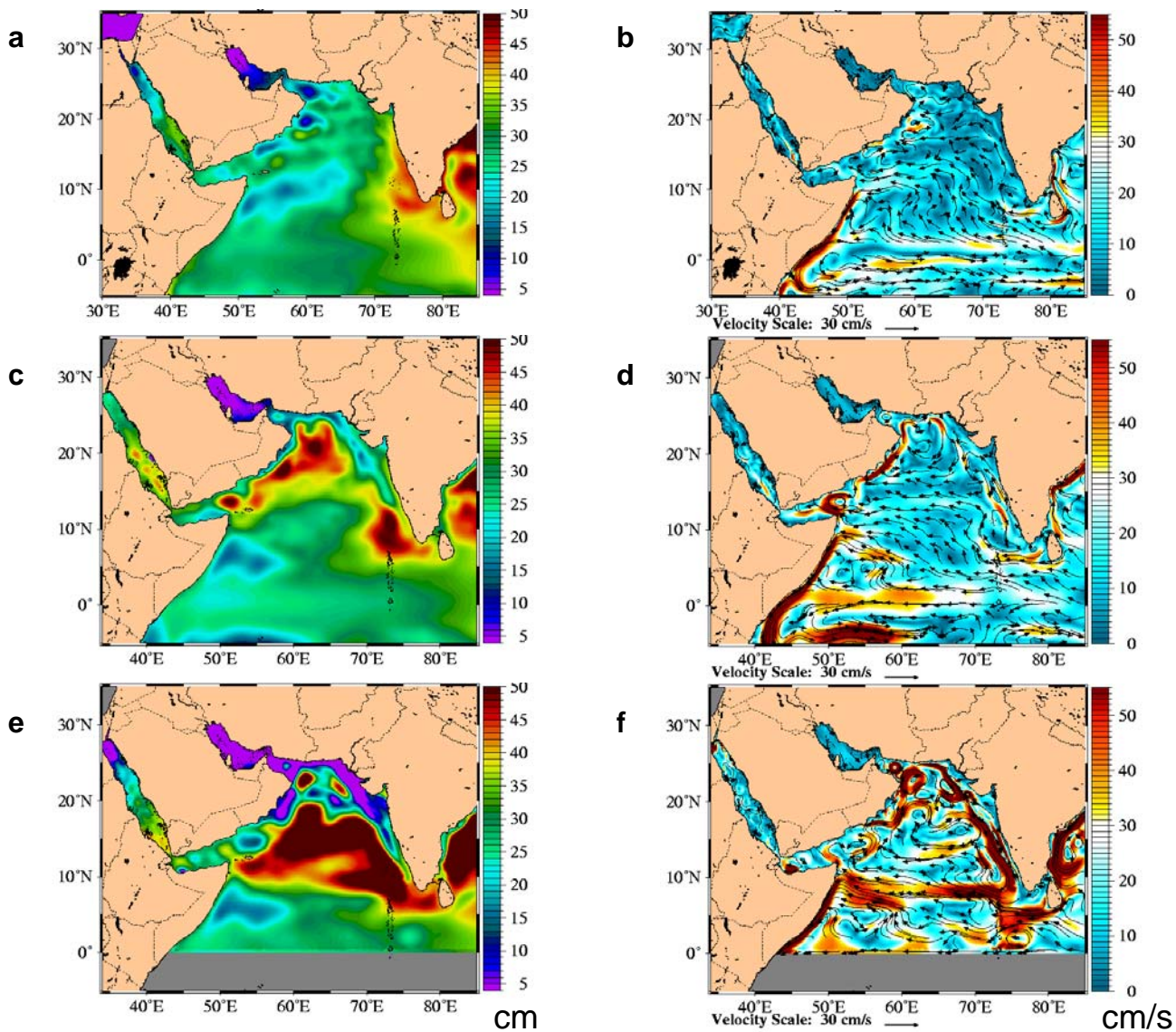


Fig. 36 – Arabian Sea zoom of SSH (left; a,c,e) and speed with superimposed currents (right; b,d,f) for assimilative 1/8° global NCOM (a,b), 1/4° SWAFS Northworld (c,d) and SWAFS IO nest (e,f). Mean is over winter monsoon period, 11/15/2002 – 3/15/2003. SSH mean is offset in SWAFS to equal NCOM SSH mean over the plot area.

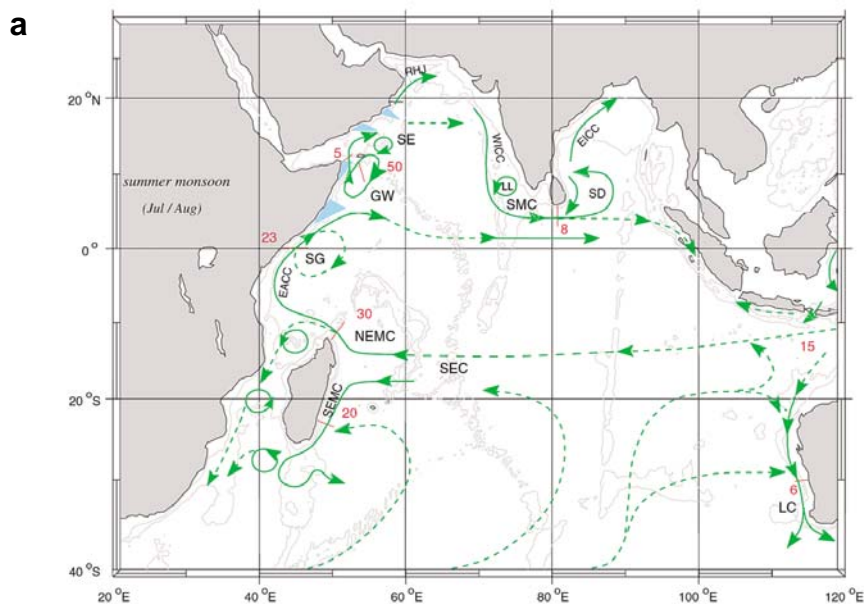


Fig. 8. A schematic representation of identified current branches during the Southwest Monsoon, including some choke point transport numbers ( $Sv=10^6 m^3 s^{-1}$ ). Current branches indicated (see also Fig. 9) are the South Equatorial Current (SEC), South Equatorial Countercurrent (SECC), Northeast and Southeast Madagascar Current (NEMC and SEMC), East African Coast Current (EACC), Somali Current (SC), Southern Gyre (SG) and Great Whirl (GW) and associated upwelling wedges, Socotra Eddy (SE), Ras al Hadd Jet (RHJ) and upwelling wedges off Oman, West Indian Coast Current (WICC), Laccadive High and Low (LH and LL), East Indian Coast Current (EICC), Southwest and Northeast Monsoon Current (SMC and NMC), South Java Current (JC) and Leeuwin Current (LC). See text for details.

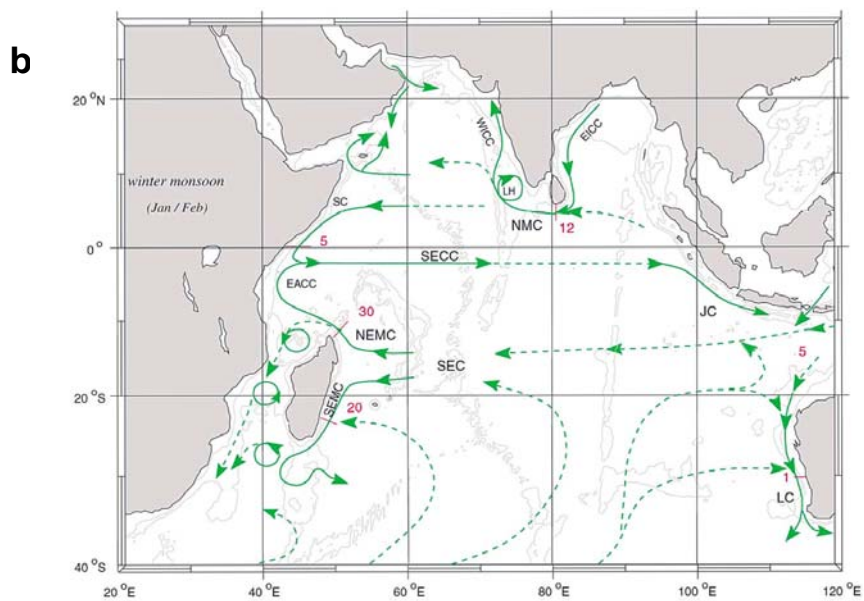


Fig. 9. As in Fig. 8, but for the Northeast Monsoon.

Fig. 37 – Depiction of prevalent circulation patterns in the Indian Ocean during the (a) Southwest Monsoon and (b) Northeast Monsoon from Schott and McCreary, 2001. Reprinted from *Progress in Oceanography*, vol. 51, Schott, F.A. and J.P. McCreary Jr., 1-123, copyright 2001, with permission from Elsevier.

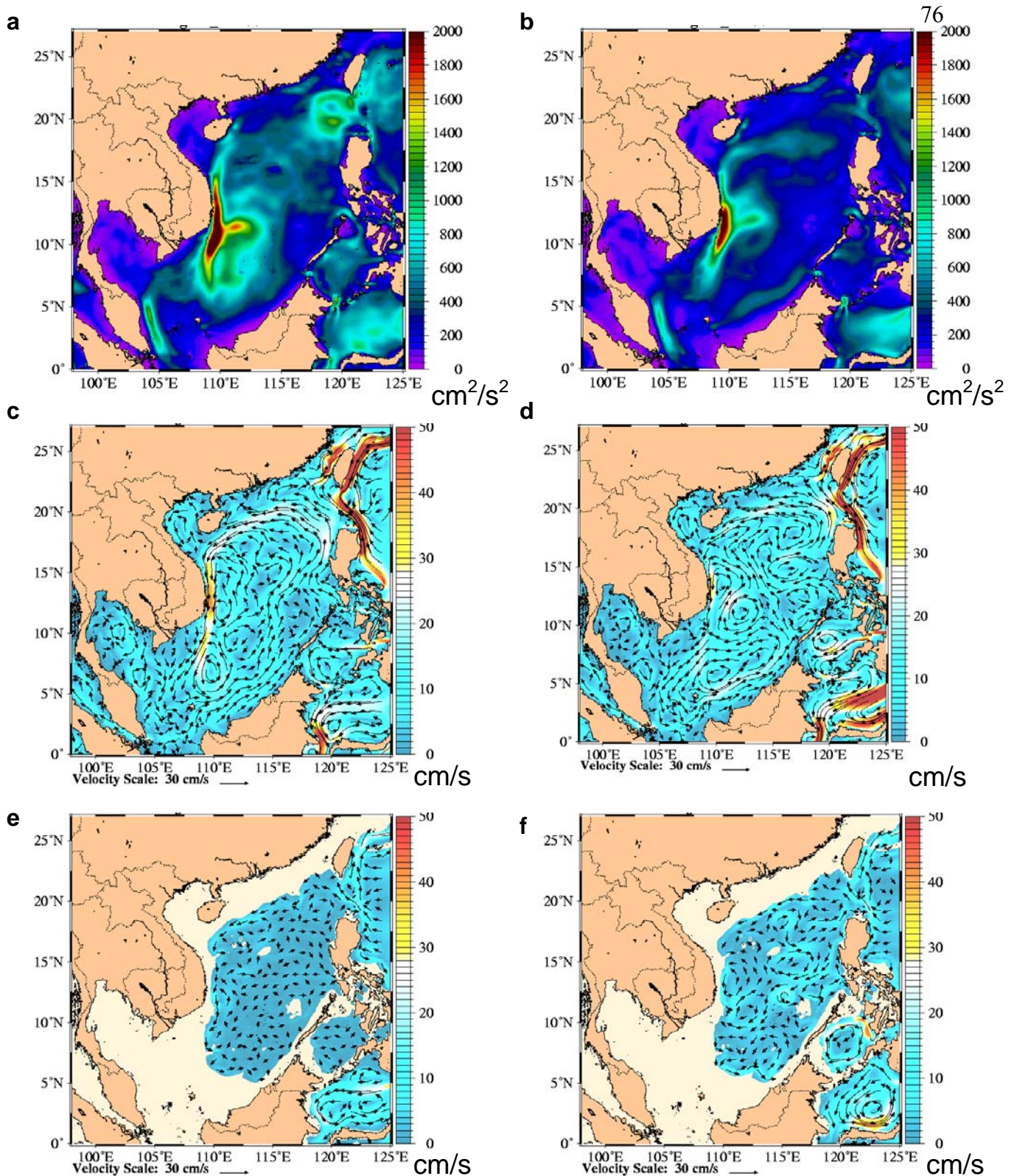


Fig. 38 – South China Sea zoom of mean 1998-2000 surface EKE (a,b) and surface (c,d) and 500m (e,f) speed with superimposed currents for free-running (left;a,c,e) and assimilative (right;b,d,f) 1/8° global NCOM. Assimilation reduces surface EKE south of Taiwan and increases surface current penetration into the Suluwesi Sea. At 500m, assimilation introduces anticyclonic circulation in the Sulu Sea and strengthens cyclonic circulation in the Suluwesi Sea.

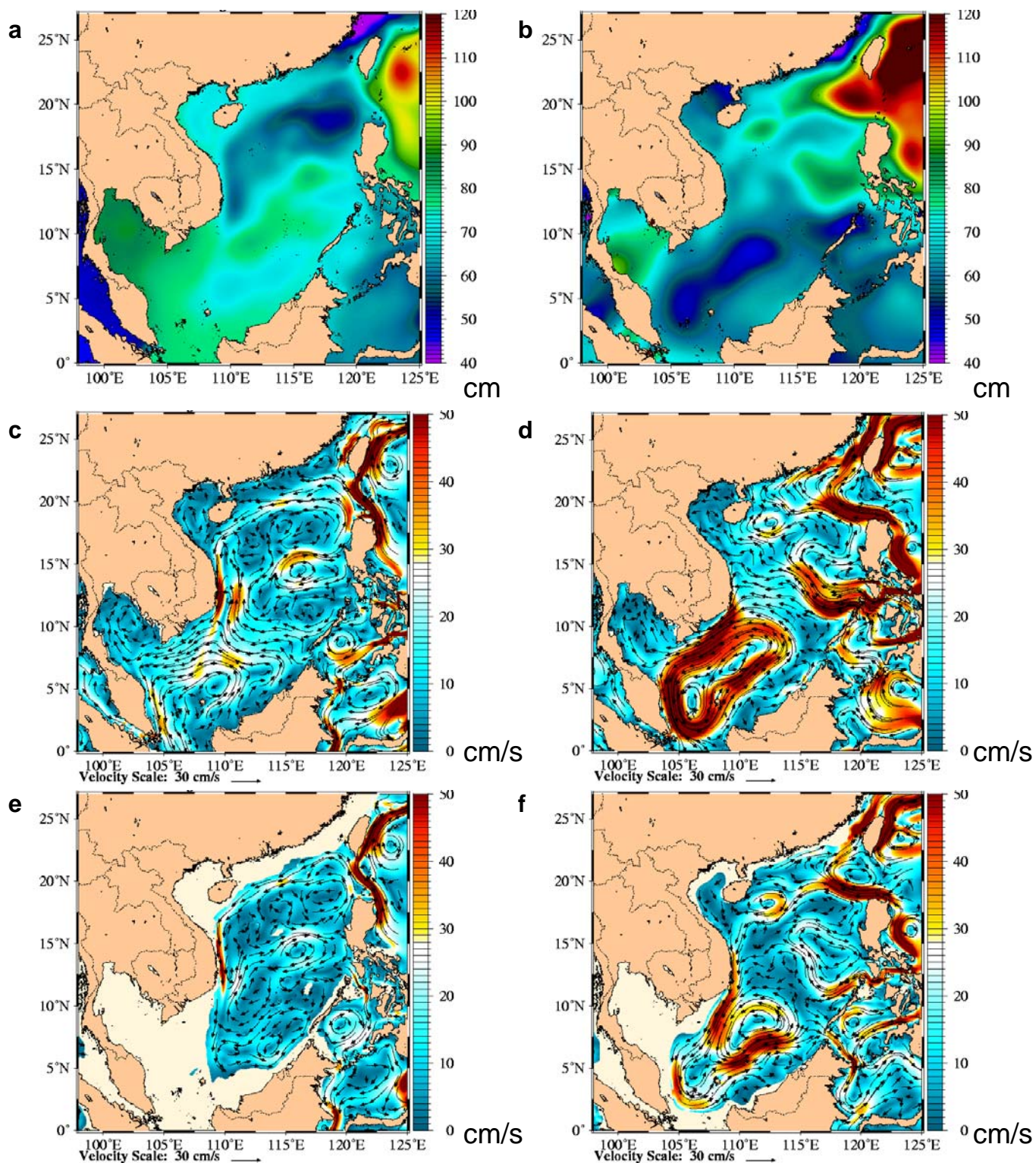


Fig. 39 – South China Sea zoom of SSH (a,b) and mean speed with superimposed currents at 5m (c,d) and 100m (e,f) for assimilative 1/8° global NCOM (right;a,c,e) and assimilative 1/4° SWAFS Northworld (left;b,d,f). Mean is over period of available SWAFS data, 9/1/2002 – 5/31/2003 for SSH and 11/15/2002-5/15/2003 for subsurface data. To enable the same color bar and ranges to be used, mean SWAFS SSH is offset to equal mean NCOM SSH over this domain.

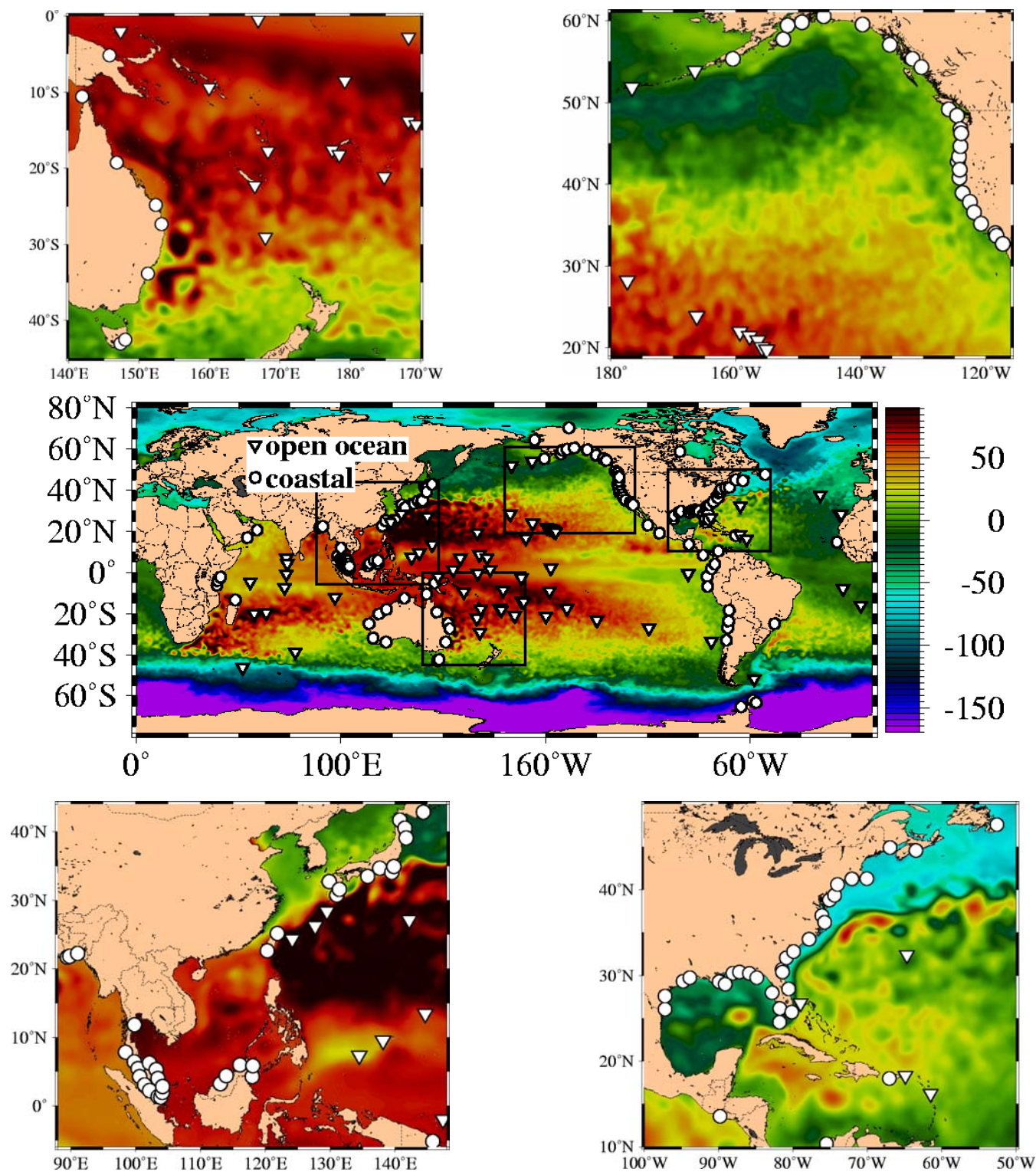


Fig. 40 – Tide gauge locations superimposed on a snapshot of SSH from the data-assimilative  $1/8^\circ$  global NCOM. All the tide gauges are maintained by the University of Hawaii JASL center and are located in both coastal and open ocean island regions of the Atlantic, Pacific and Indian Oceans. The tide gauges are separated into two categories located at (circles) coastal regions and (triangles) islands in the open ocean.

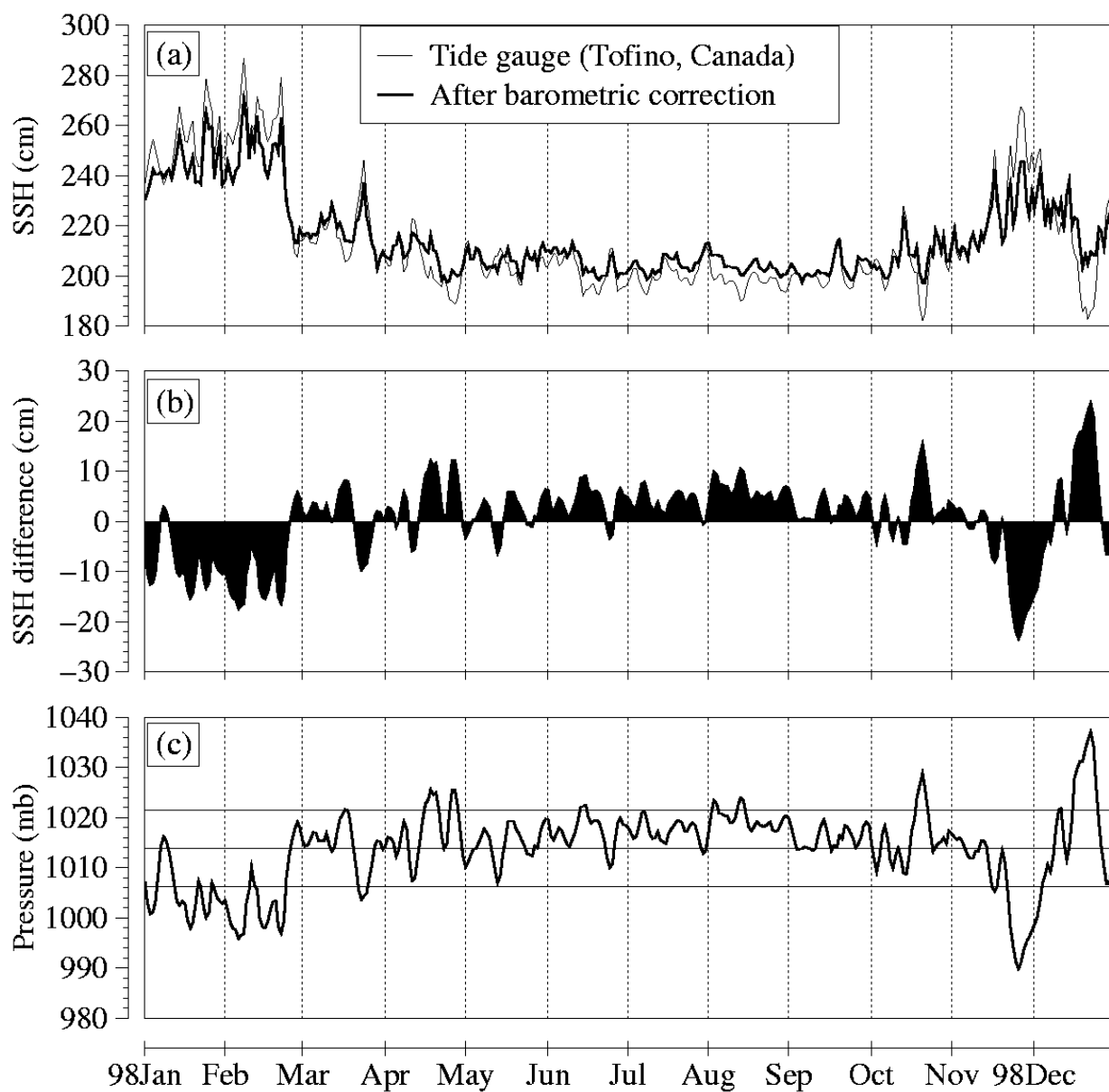


Fig. 41 – A sample application of the inverse barometer correction to a tide gauge time series at Tofino, Canada ( $49^{\circ}\text{N}, 126^{\circ}\text{W}$ ) in 1998: (a) Daily SSH time series directly obtained from JASL tide gauge data and the one obtained after applying the barometer correction, (b) daily difference between original tide gauge values and corrected ones, and (c) daily mean sea level atmospheric pressure values obtained from the Navy Operational Global Atmospheric Prediction System~(NOGAPS) and mean pressure  $\pm$  standard deviations shown with horizontal lines. An inverse barometer correction value of  $0.9955 \text{ cm mb}^{-1}$  is applied to SSH from tide gauges.

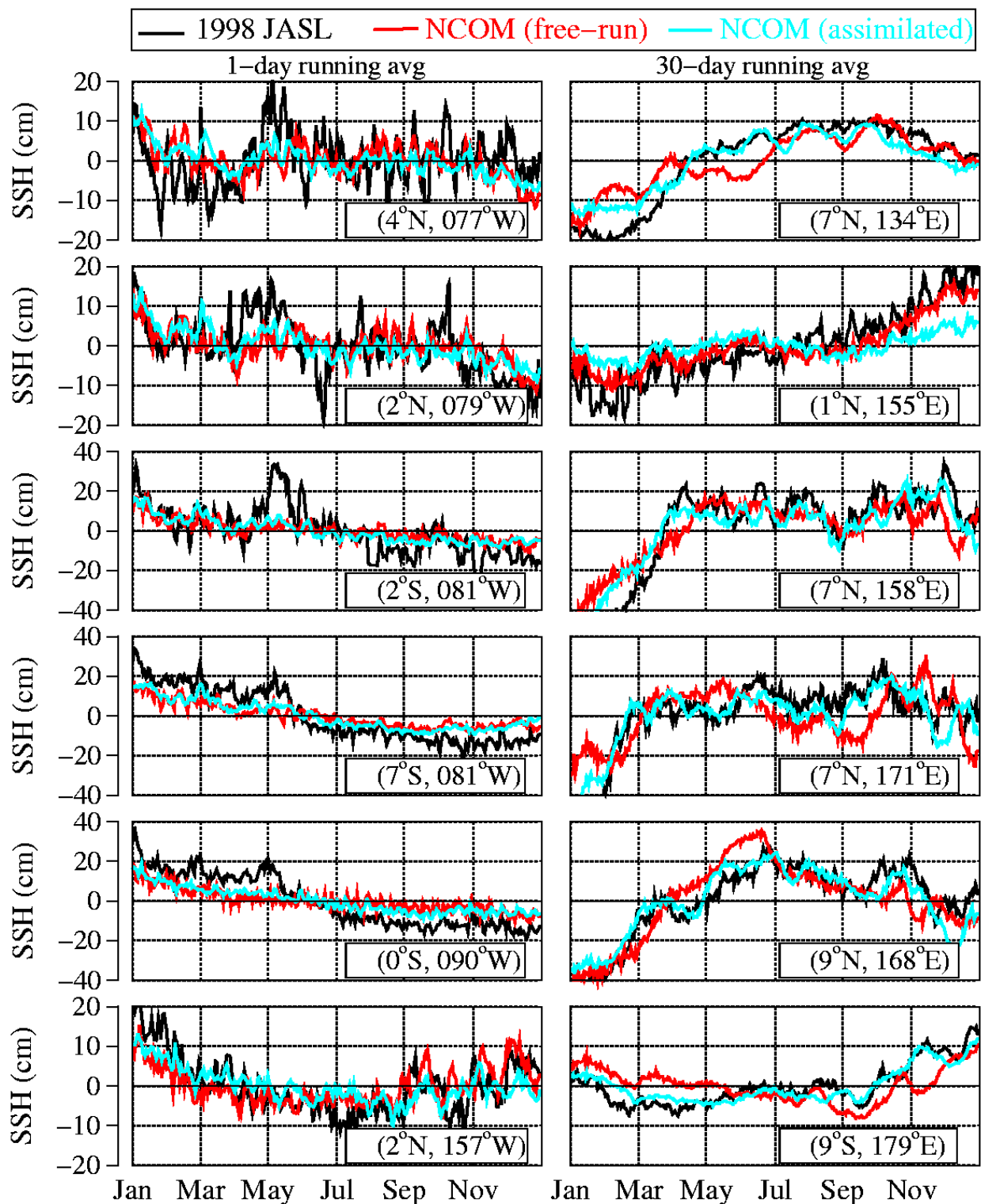


Fig. 42 – Daily SSH time series comparisons between the JASL and 1/8° NCOM values at various tide gauge locations in 1998. Note that the inverse barometer correction is already applied to SSH at each tide gauge. Model results are shown from free-running and data-assimilative NCOM simulations, separately. The right panels show results with a 30-day running average applied to daily SSH from tide gauges and NCOM simulations.

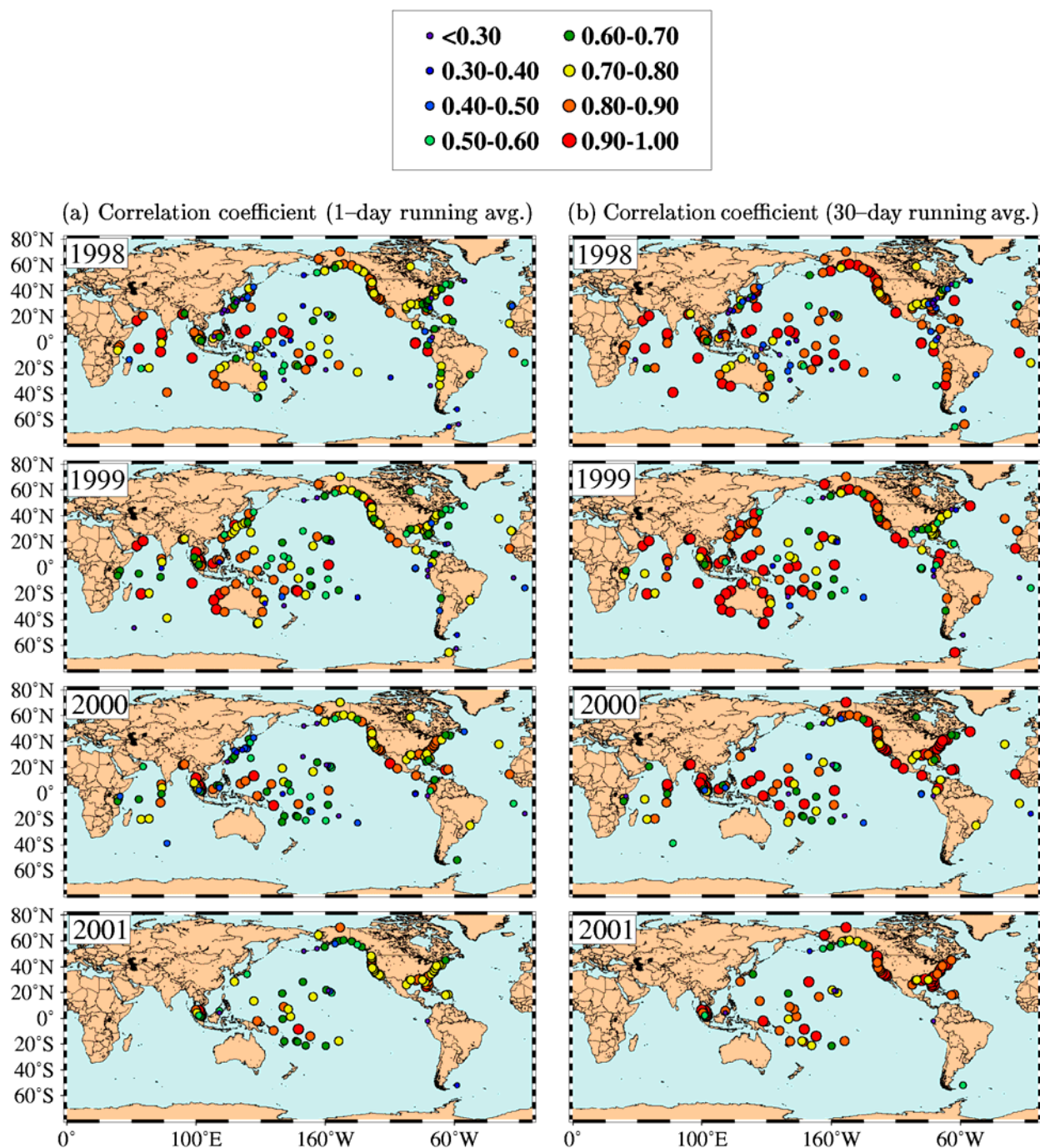


Fig. 43 – Correlation coefficients calculated using SSH time series from the JASL tide gauge data and the data-assimilative  $1/8^\circ$  NCOM simulation at all the tide gauge locations over the global ocean from 1998 to 2001. Correlation values are calculated based on (a) daily averaged SSH time series (left panels), and (b) 30-day running averages of SSH time series (right panels).

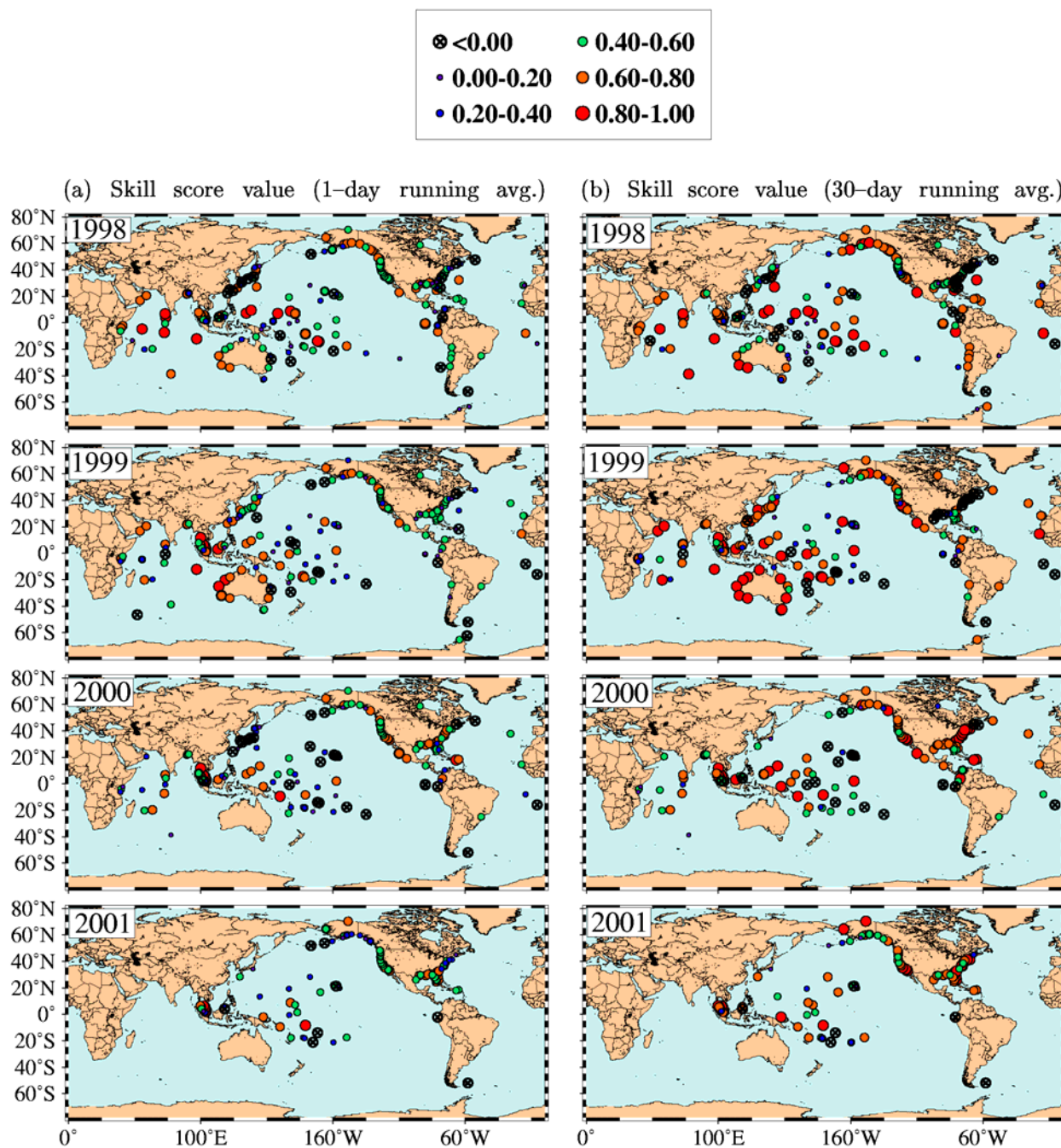


Fig. 44 – Skill Score calculated using SSH time series from the JASL tide gauge data and the data-assimilative  $1/8^\circ$  NCOM simulation at all the tide gauge locations over the global ocean from 1998 to 2001. Correlation values are calculated based on (a) daily averaged SSH time series (left panels), and (b) 30-day running averages of SSH time series (right panels).

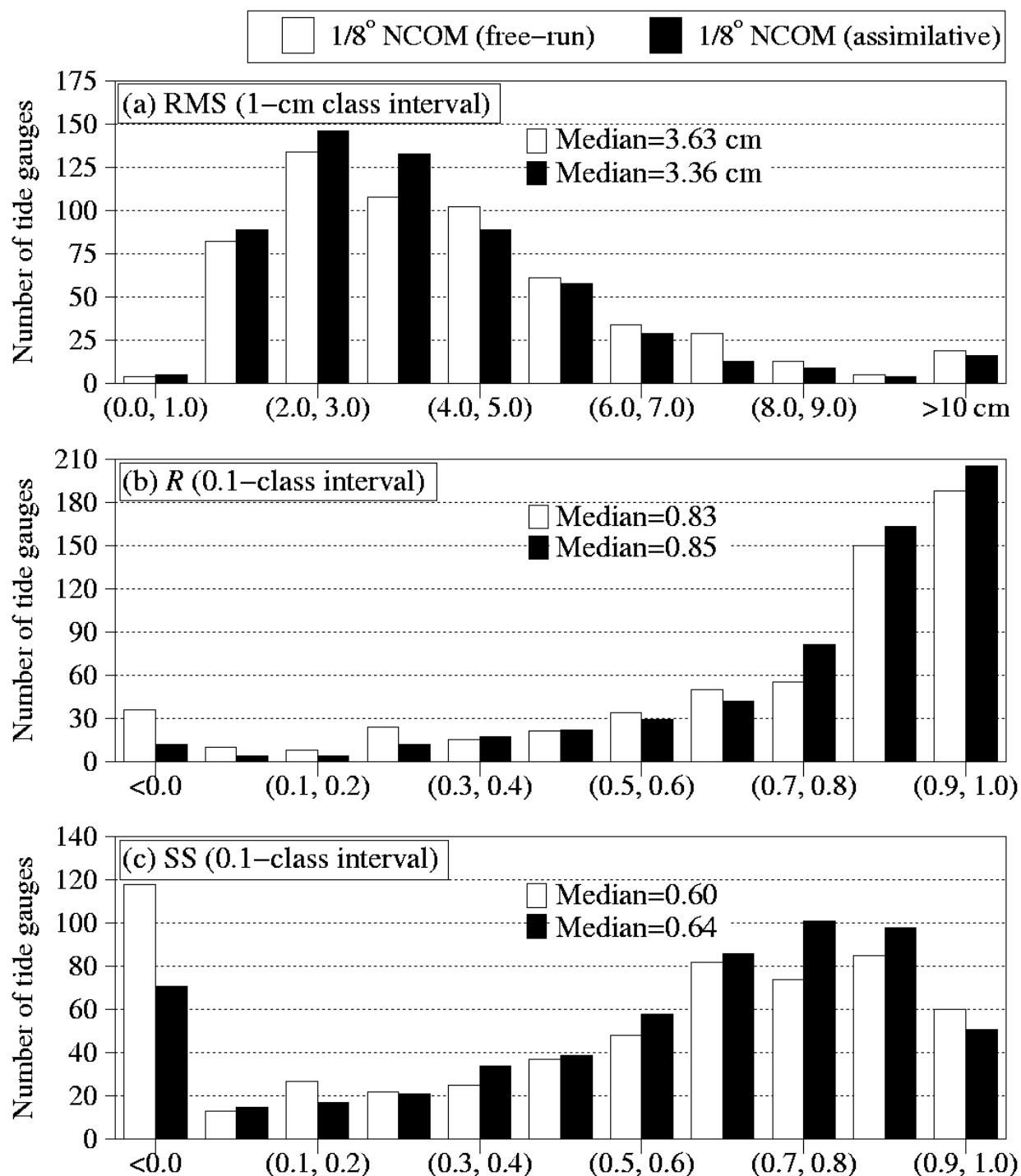


Fig. 45 – Histograms of root-mean-square (RMS) difference, correlation coefficient (R) and non-dimensional skill score (SS) used for verifying the free-running and data-assimilative 1/8° NCOM simulations during 1998-2001: (a) RMS values with 1-cm class interval, (b) R values with 0.1-class interval, and (c) SS values with 0.1-class interval. All results are based on 30-day running averages of SSH time series. The total number of year-long tide gauge time series used in the analysis is 591 for the 4-year time period. Note that a RMS class interval of, for example, (2.0, 3.0) on the x-axis represents the RMS values  $\geq 2.0$  cm but  $< 3.0$  cm, similarly for R and SS class intervals.

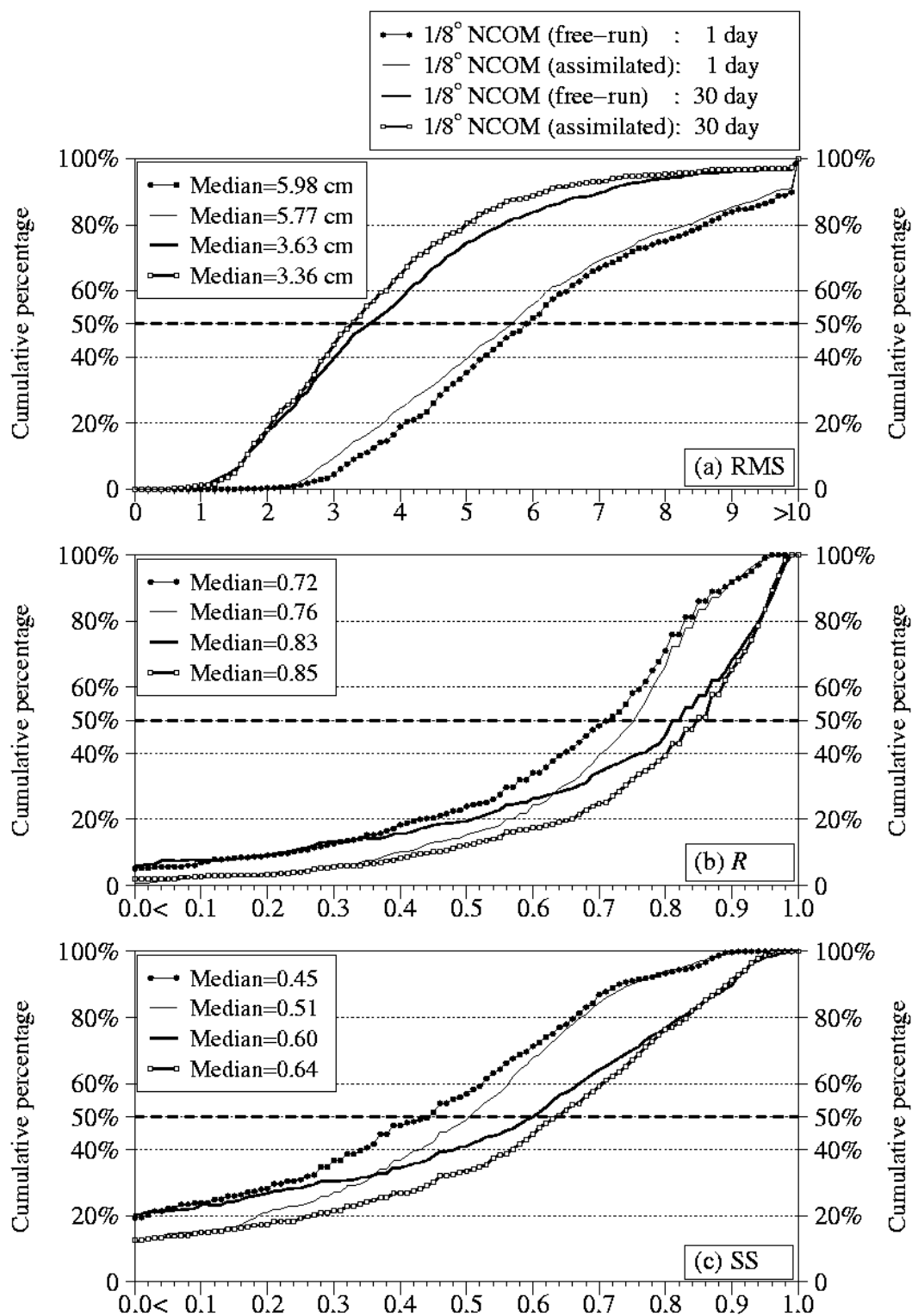


Fig. 46 – Cumulative percentage of RMS, R and SS values calculated using year-long SSH time series from all the tide gauges and 1/8° NCOM over the global ocean during 1998-2001. The results are shown for both free-running and data-assimilative 1/8° NCOM simulations when applying 1-day and 30-day running averages on the time series. Note that an inverse barometer correction has been applied to the tide gauge data before the statistical analysis.

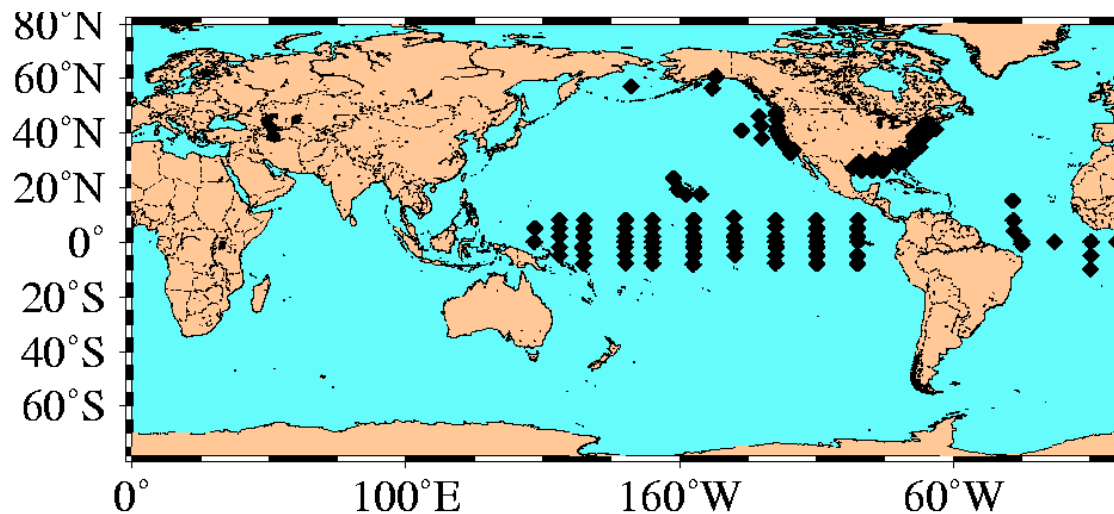


Fig. 47 – Locations of TAO, PIRATA and NDBC buoys providing 219 unassimilated, year-long buoy temperature profiles used for validation of NCOM SST 1998-2000.

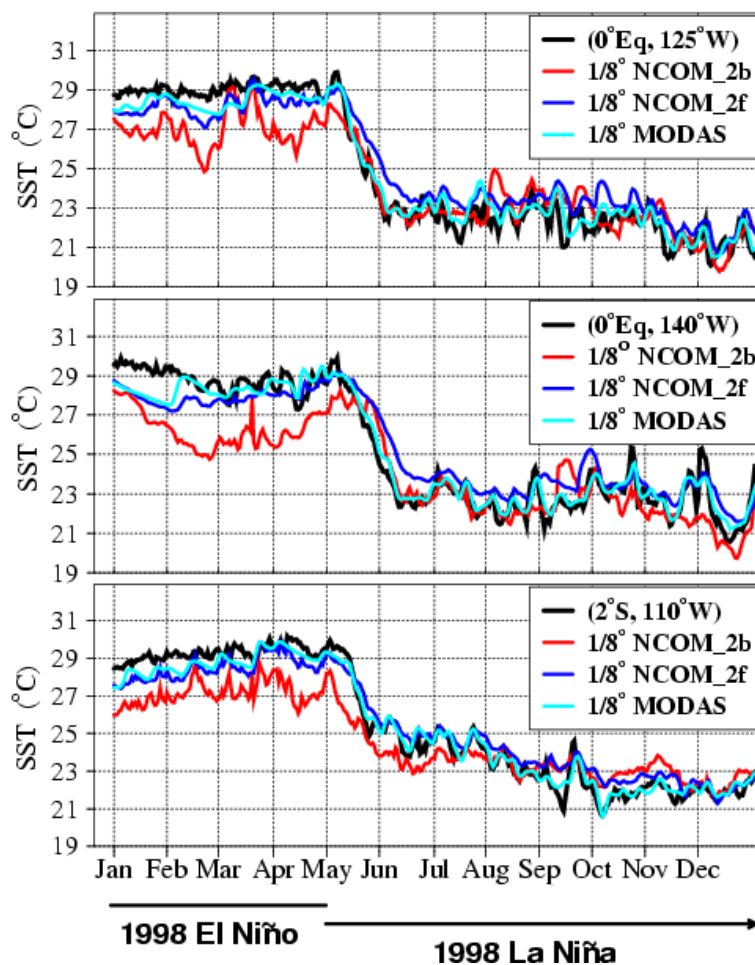


Fig. 48 – Comparison between observed (black), free-running NCOM (red), assimilative NCOM (blue) and MODAS analyses (SST) at three TAO equatorial Pacific stations during the 1998 El Niño to La Niña transition.

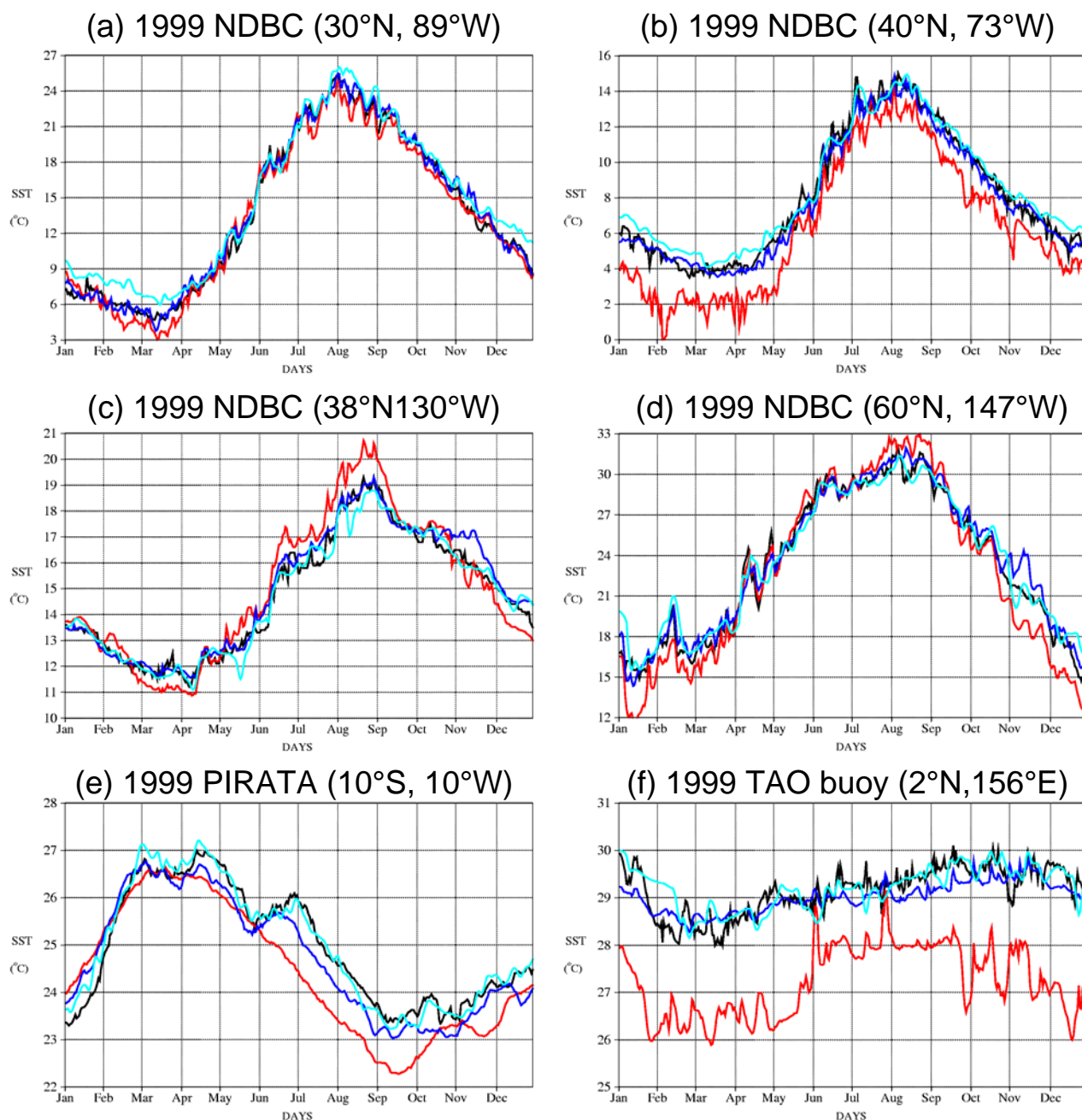
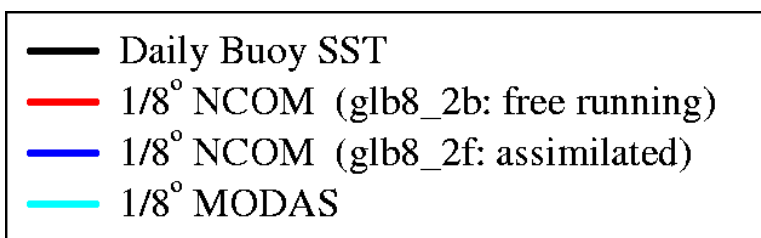


Fig. 49 – Comparison between observed (black), free-running NCOM (red), assimilative NCOM (blue) and MODAS analyses (SST) at a sample of observing buoy stations for 1999. (a) NDBC buoy along the U.S. Gulf coast (30°N, 89°W); (b) NDBC buoy along the U.S. east coast (40°N, 73°W); (c) NDBC buoy along the U.S. west Coast (38°N, 130°W); (d) NDBC off the coast of Alaska (60°N, 147°W); (e) PIRATA buoy in the equatorial Atlantic (10°S, 10°W); (f) TAO buoy in equatorial Pacific warm pool (2°N, 156°E)

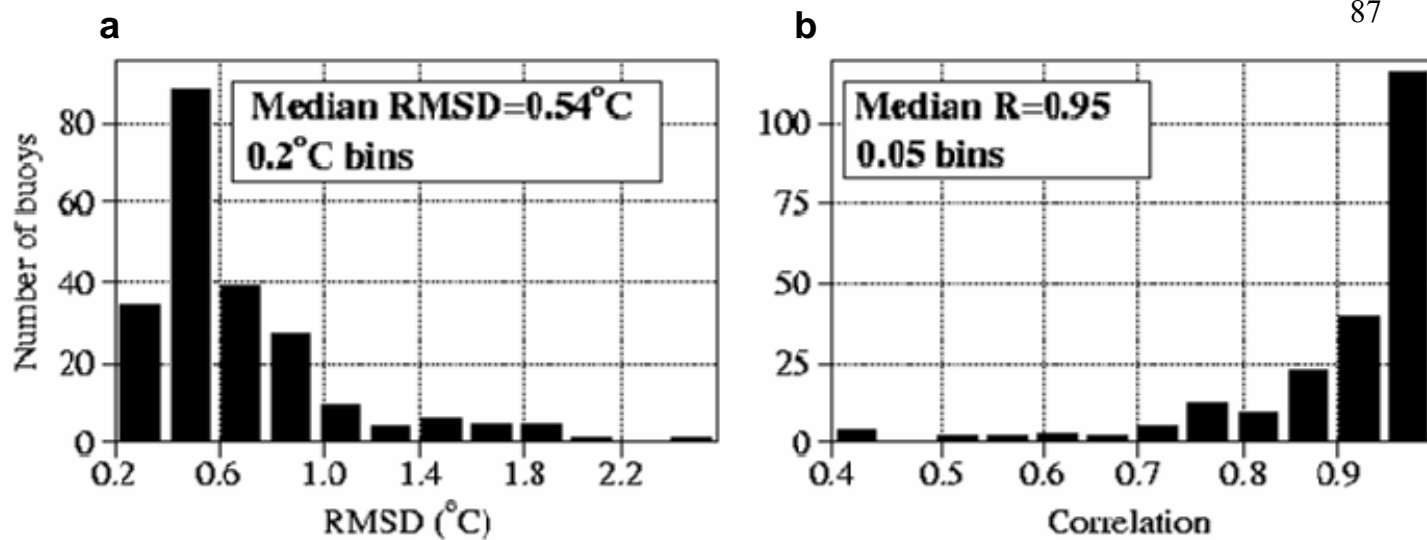


Fig. 50 – Histograms of (a) root-mean-squared difference and (b) correlation between buoy observed and assimilative 1/8° global NCOM SST over 219 unassimilated year-long time series over 1998-2000.

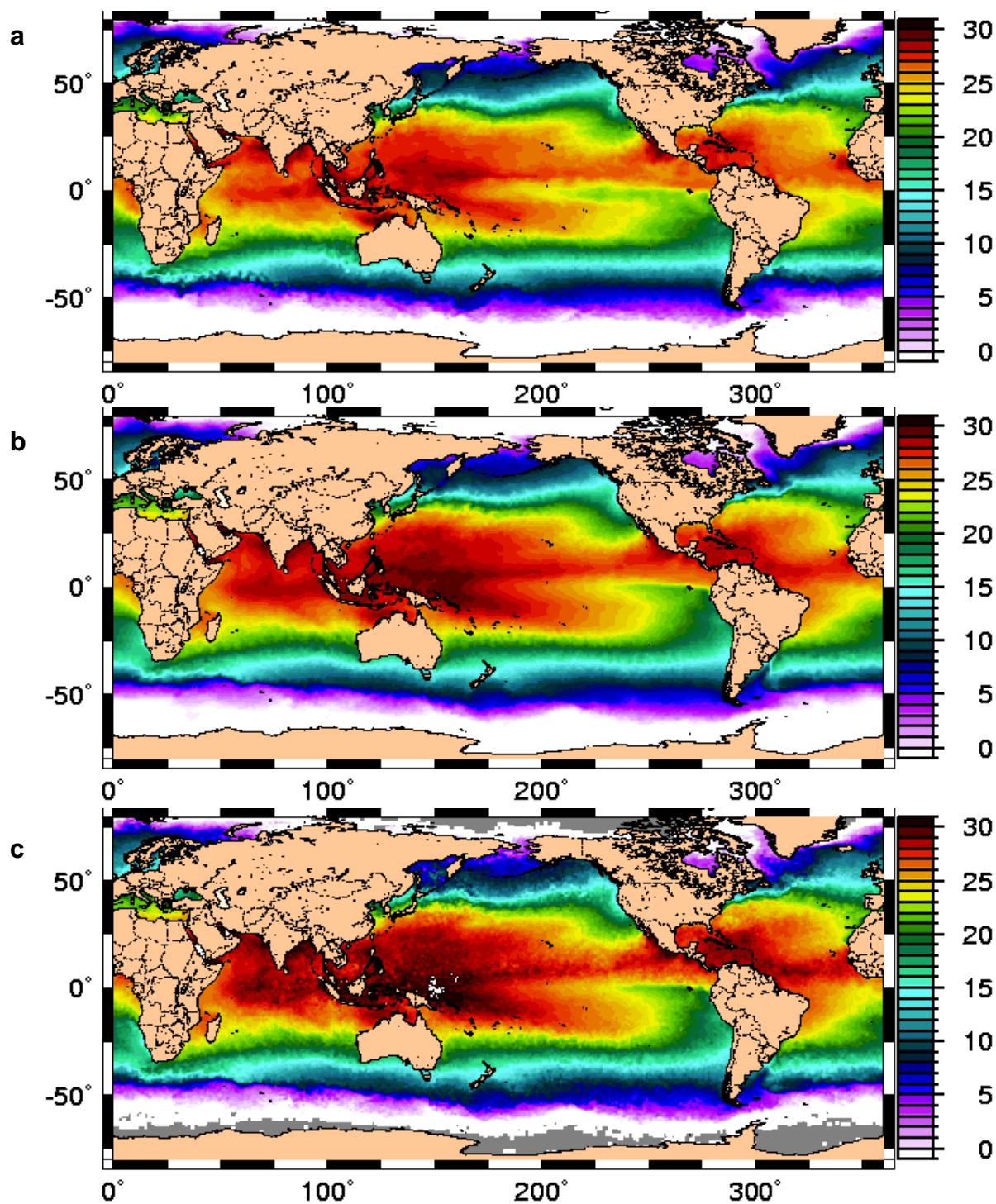


Fig. 51 – Global plots of mean SST for October 2000: (a) free-running  $1/8^\circ$  global NCOM, (b) assimilative  $1/8^\circ$  global NCOM, and (c) 9km Pathfinder. The NCOM means are calculated from daily snapshots, while the Pathfinder mean is a mean in each cell of the observations during the month in that cell. Grey areas have no observations during the month and are excluded further statistical analyses. Note that the NCOM means are noticeably smoother than the Pathfinder composite mean. Free running NCOM is noticeably cooler than the others.

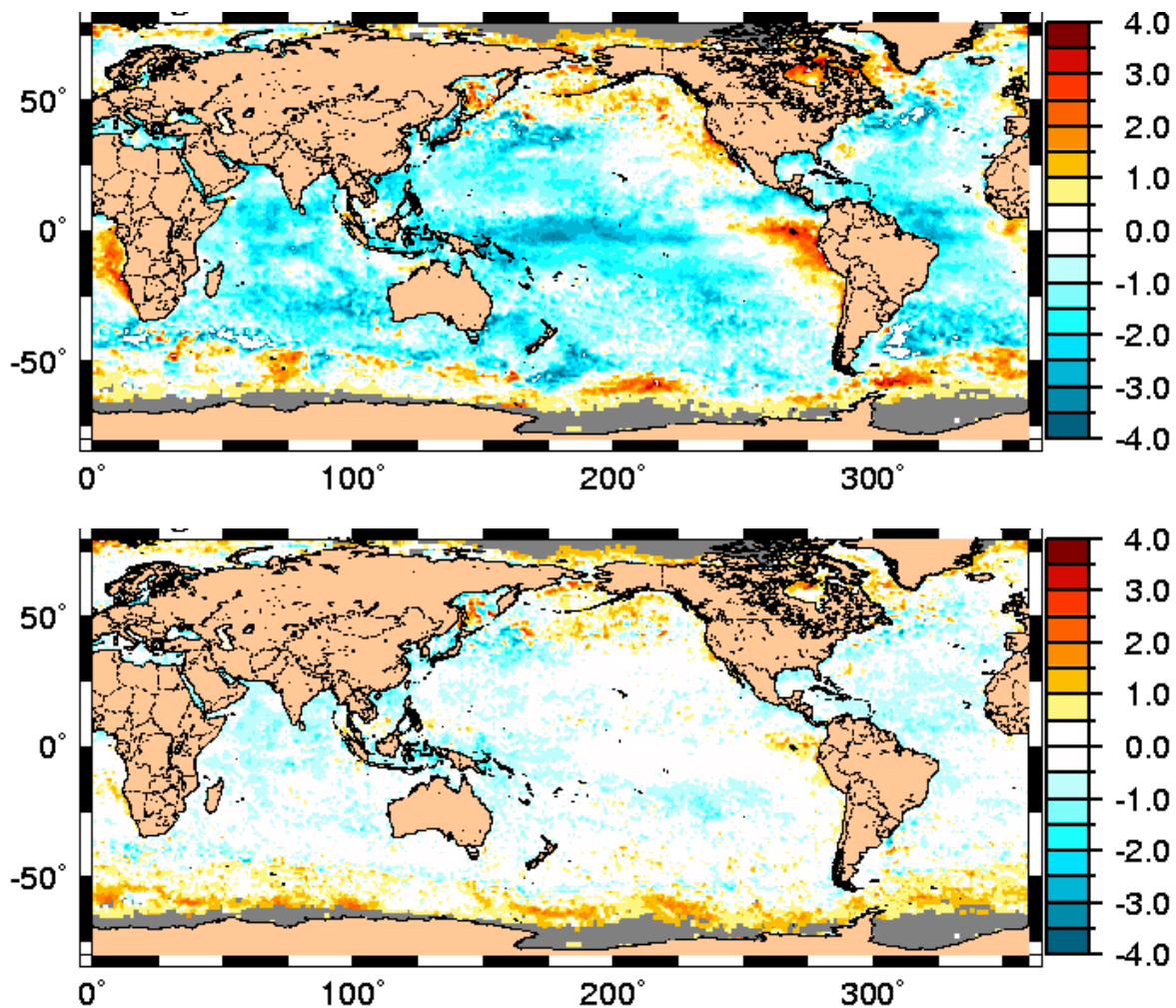


Fig. 52 – Global plots of differences between mean monthly SST for October 2000: (a) free-running  $1/8^\circ$  global NCOM – 9km Pathfinder, and (b) assimilative  $1/8^\circ$  global NCOM - 9km Pathfinder. NCOM tends to be warmer at high latitudes and along the eastern boundaries, and cooler over most of the central ocean. The deviations are much larger in the free-running case with similar distribution of the trends.

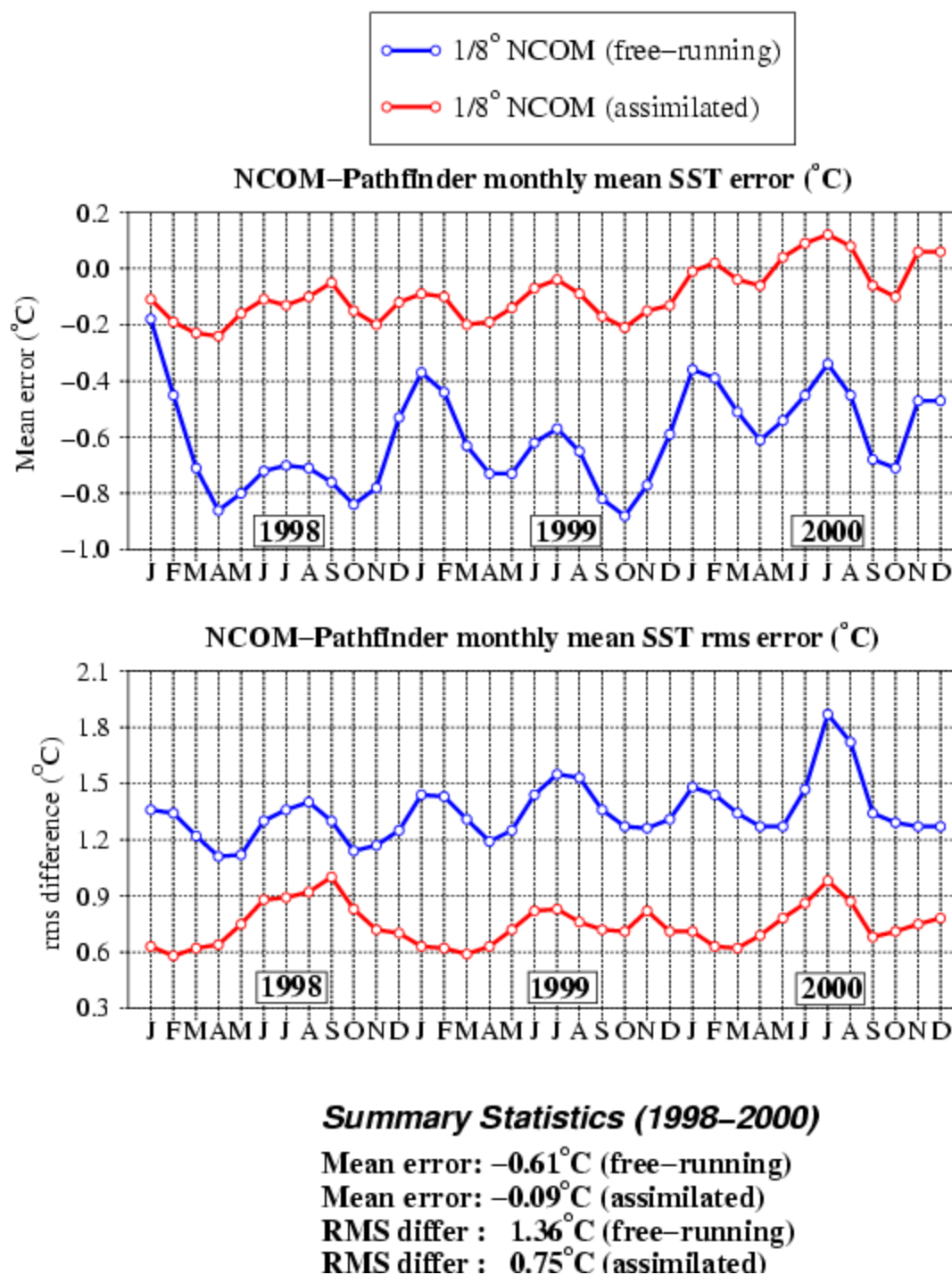


Fig. 53 – Summary time series and statistics for differences between monthly mean NCOM and 9km Pathfinder data during 1998-2000. Results using free-running 1/8° global NCOM are shown in blue, while results using the assimilative model are shown in red. The free running model shows a mean cold bias of -0.61°C, while the assimilative model has a -0.09°C bias relative to Pathfinder. The cold bias is significantly reduced in 2000 relative to 1998-1999, with the assimilative model showing little annual bias for 2000.

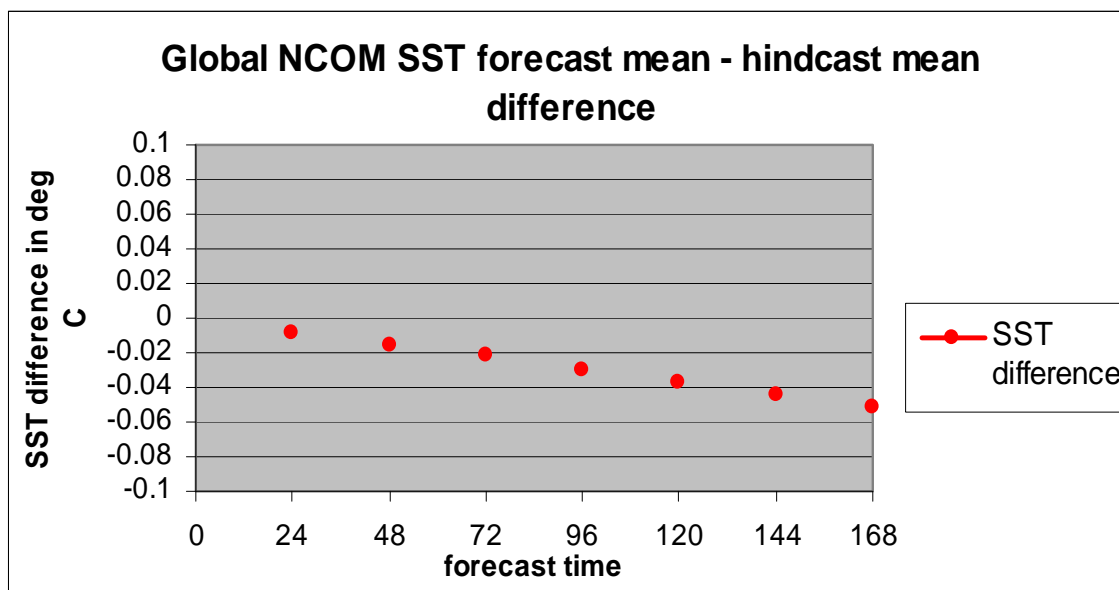


Fig. 54 – Analysis of global forecast bias in global NCOM SST. Mean SST files were calculated for each 24-hour forecast increment over 1998-2002. For example, we calculated a mean of 48-hour forecasts. SST means were calculated for the corresponding SST nowcast analyses and subtracted from the forecast means. The analyses indicate a slight global SST bias of  $-0.009^{\circ}\text{C}$  for 24 hour forecasts and  $-0.05^{\circ}\text{C}$  for 7-day forecasts.

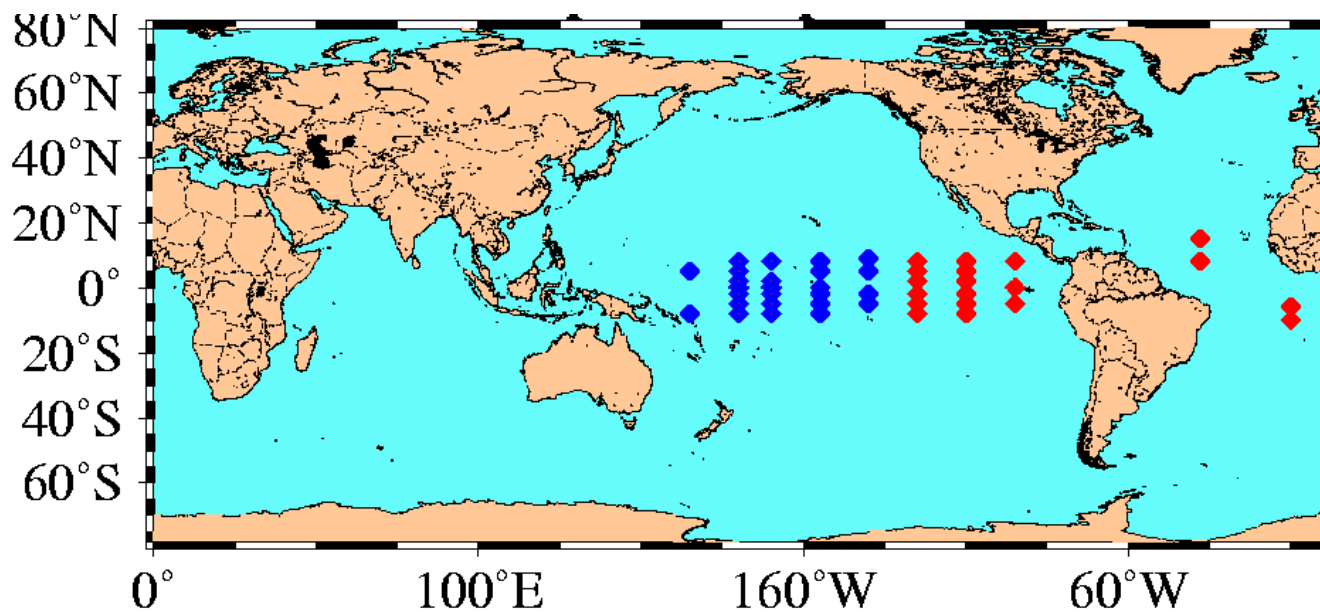


Fig. 55 – Locations of buoys providing 95 unassimilated, year-long time series of buoy temperature profiles used for validation of NCOM temperature profiles for 1998-2001. Stations are of two types, distinguished by the set of standard depths for placement of temperature measurements. Type I is shown in red; type II is shown in blue.

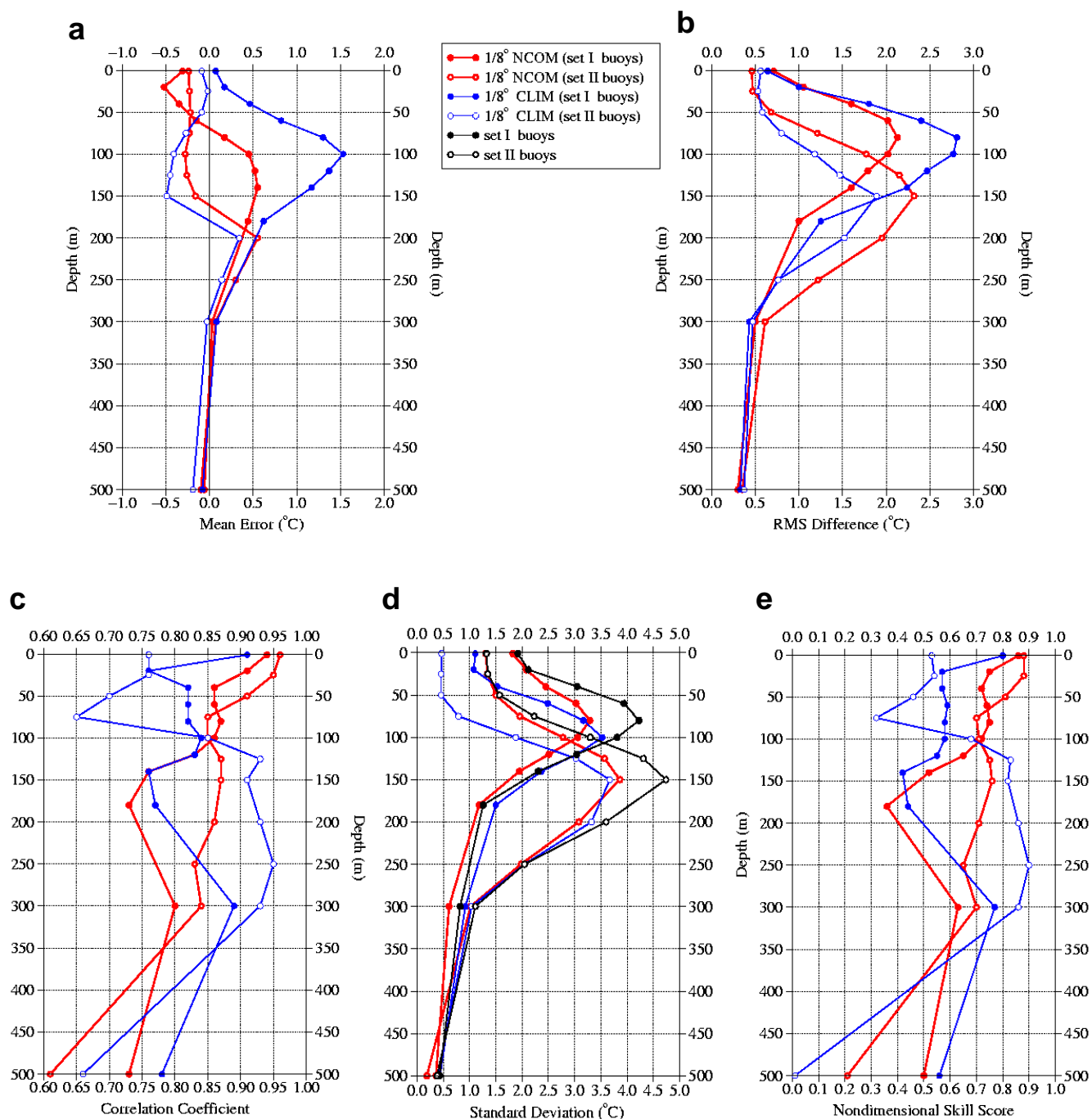


Fig. 56 – Comparison statistics for 95 unassimilated, year-long buoy temperature profiles (over 34000 profiles) used for validation of NCOM temperature profiles for 1998-2001. Stations are of two types, distinguished by the set of standard depths for placement of temperature measurements. Type I is shown in red; type II is shown in blue. (a) mean error; (b) RMS difference; (c) correlation coefficient; (d) standard deviation; (e) nondimensional skill score.

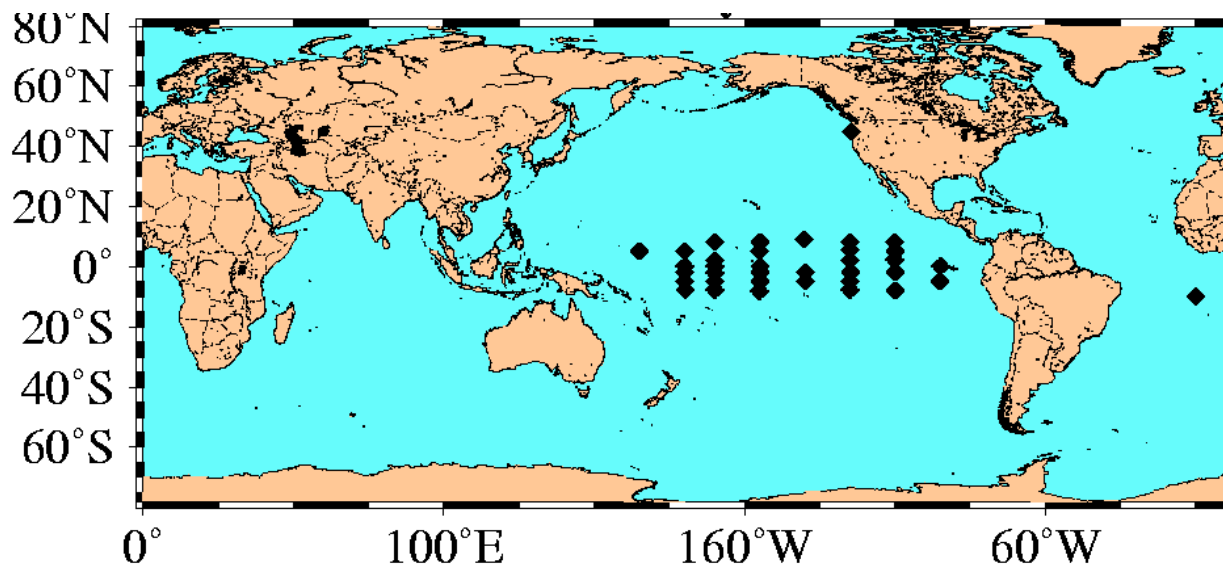
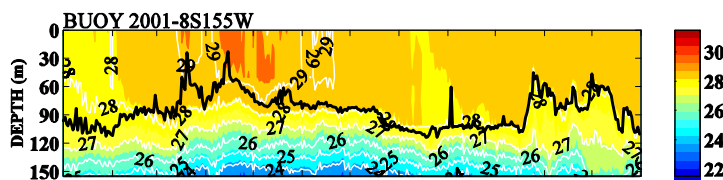
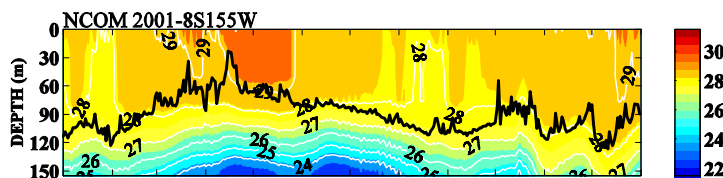


Fig. 57 – Locations of buoys providing 71 unassimilated, year-long buoy temperature profiles used for validation of NCOM mixed layer 1998-2000.

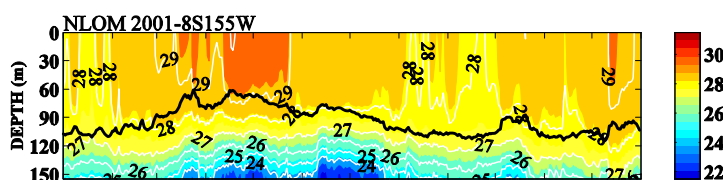
**Daily temperature  
(8°S, 155°W)  
TAO buoy**



**1/8° Global NCOM**



**1/8° MODAS  
dynamic climatology  
with NLOM SSH**



**1/8° MODAS  
climatology**

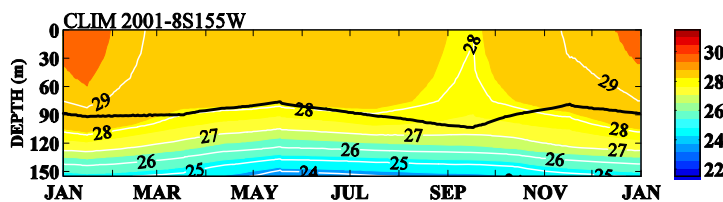


Fig. 58 – Time-series from 2001 at a TAO buoy location in the equatorial Pacific (8°S, 155°W). The bottom series indicates the MODAS climatological background. Using real-time MODAS SST and NLOM SSH, the MODAS dynamic climatology produces a field which is assimilated into global NCOM. The ability of global NCOM to resolve the mixed-layer dynamics allows it to produce a mixed-layer depth (black line on each series) in closer agreement with the variability measured in the observations.

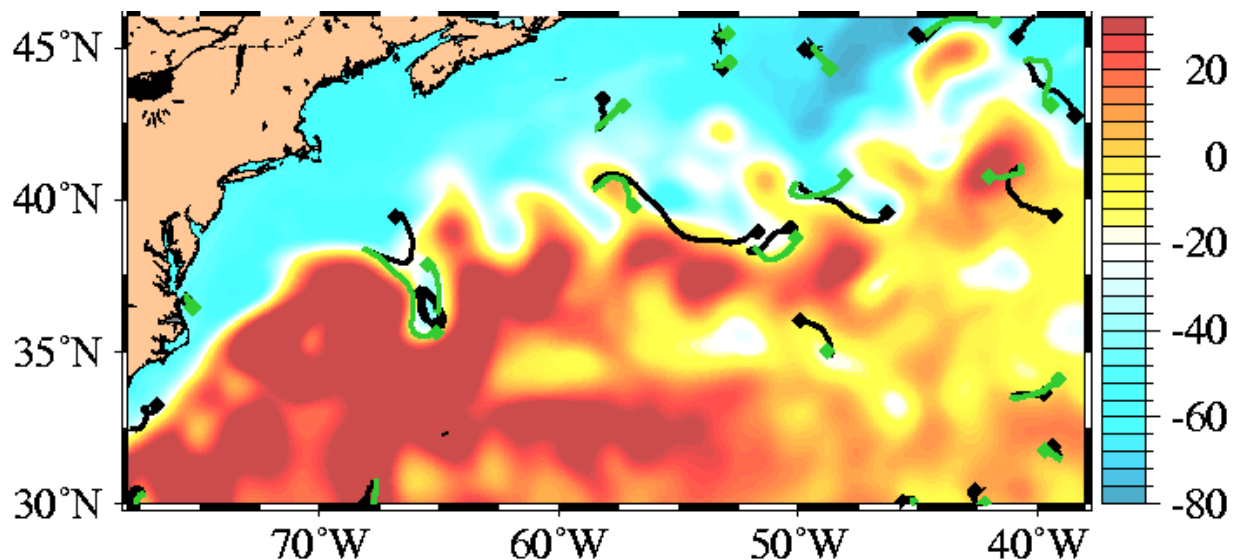


Fig. 59 – Comparison between observed WOCE drifter trajectories (black) and trajectories simulated using data-assimilative  $1/8^\circ$  global NCOM (green). The trajectories start at the same location and time, 31 July 2002. All trajectories are seven days long. The trajectories are superimposed on NCOM SSH for the start date.

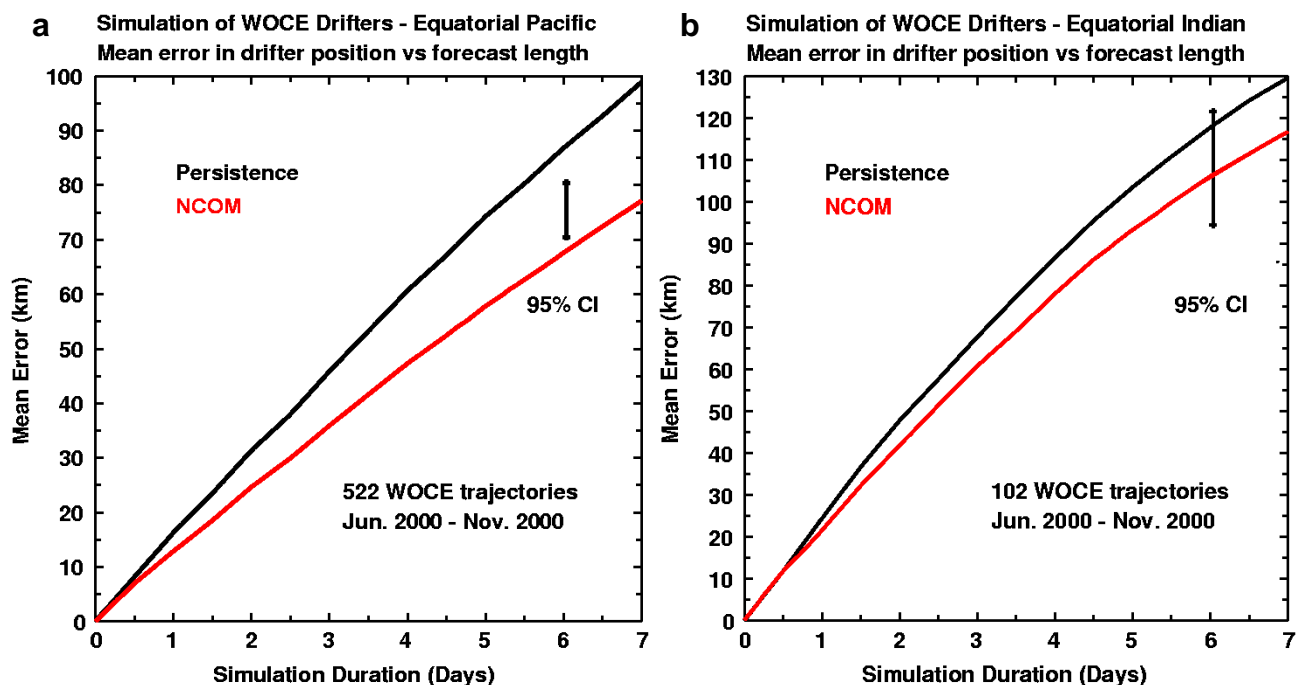


Fig. 60 – Summary of assimilative  $1/8^\circ$  global NCOM validation using seven-day segments of WOCE drifter trajectories. The axes show mean separation between WOCE and NCOM drifters versus number of days of trajectory integration. These results are derived over (a) 522 drifter pairs in the equatorial Pacific and (b) 102 drifter pairs in the equatorial Indian Ocean. A 95% confidence interval for these statistics is indicated.

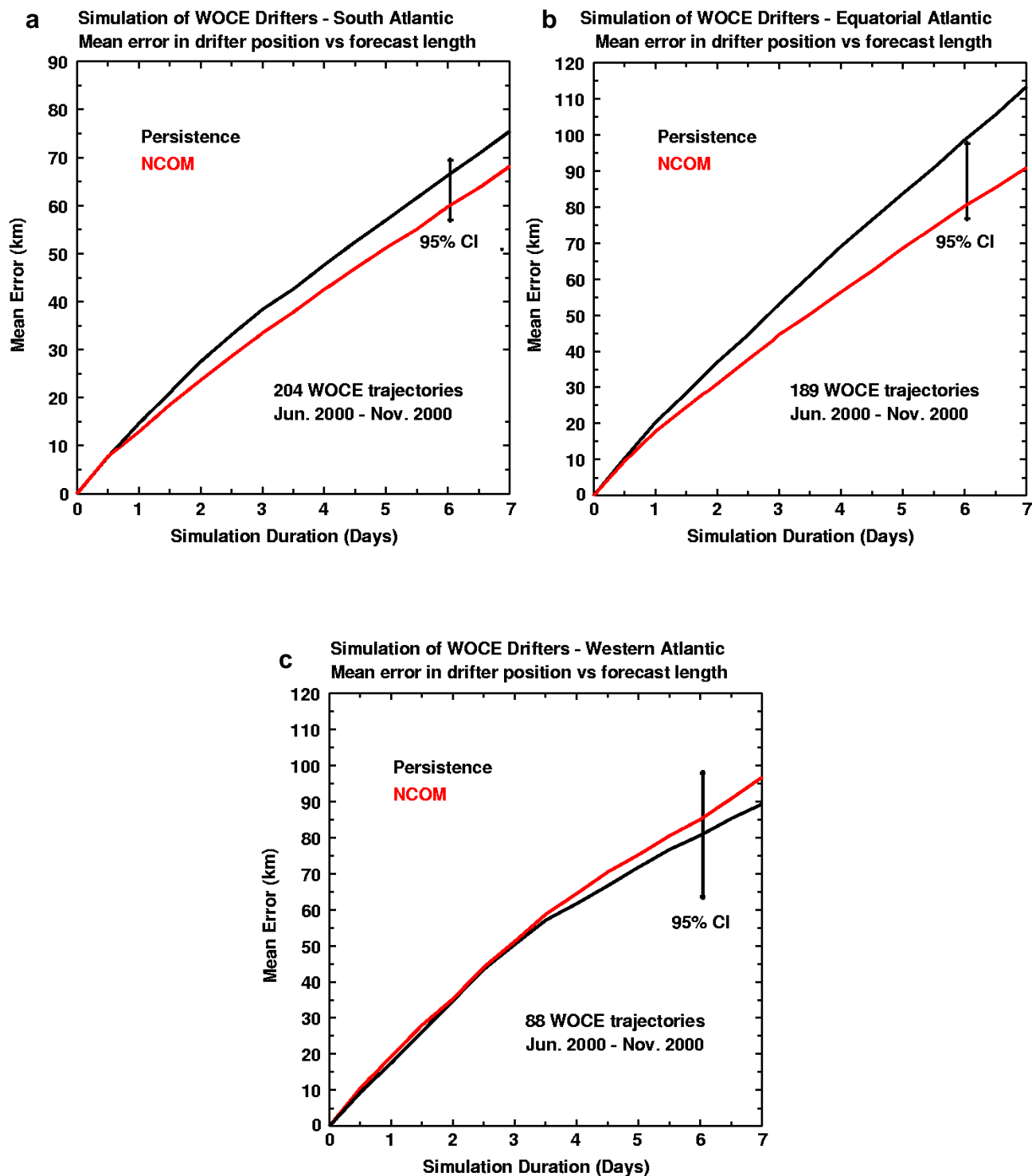


Fig. 61 – Summary of assimilative  $1/8^\circ$  global NCOM validation using seven-day segments of WOCE drifter trajectories. The axes show mean separation between WOCE and NCOM drifters versus number of days of trajectory integration. These results are derived over (a) 204 drifter pairs in the South Atlantic, (b) 189 drifter pairs in the equatorial Atlantic, and (c) 88 drifter pairs in the western Atlantic. A 95% confidence interval for these statistics is indicated.

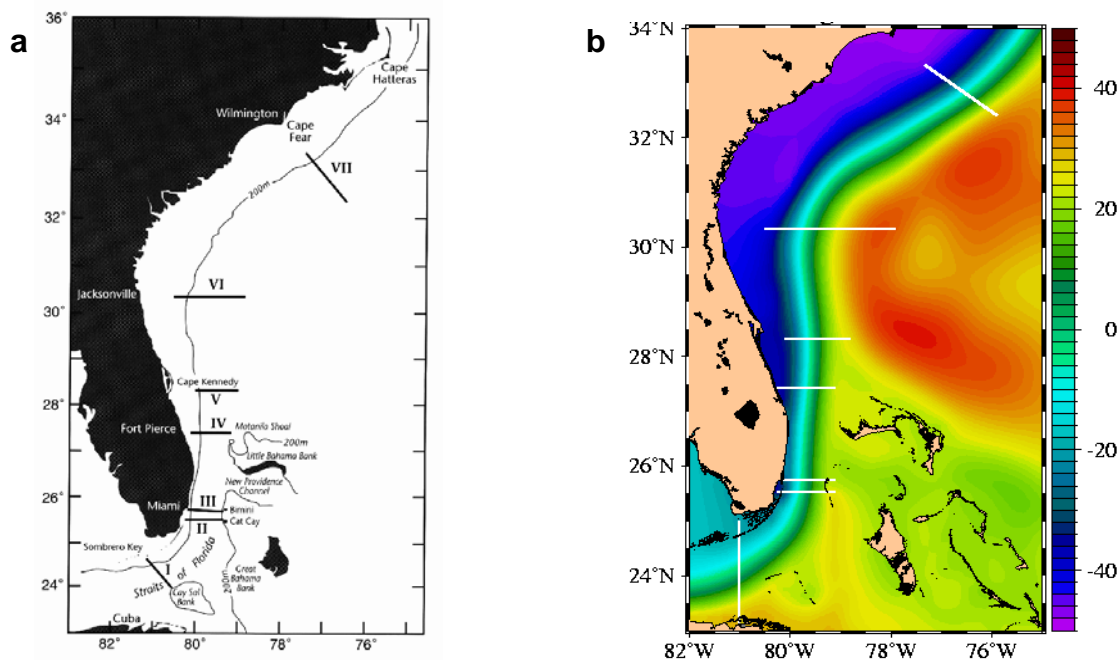


Fig. 62 – Locations of sections of downstream speed contours across the Florida Current. (a) Illustration from Schmitz (1996) based on dropsonde data and adapted from Richardson *et al.* (1969). (b) Global NCOM 1998-2000 SSH mean with several sections. Superimposed white lines locate vertical sections extracted from NCOM for validation.

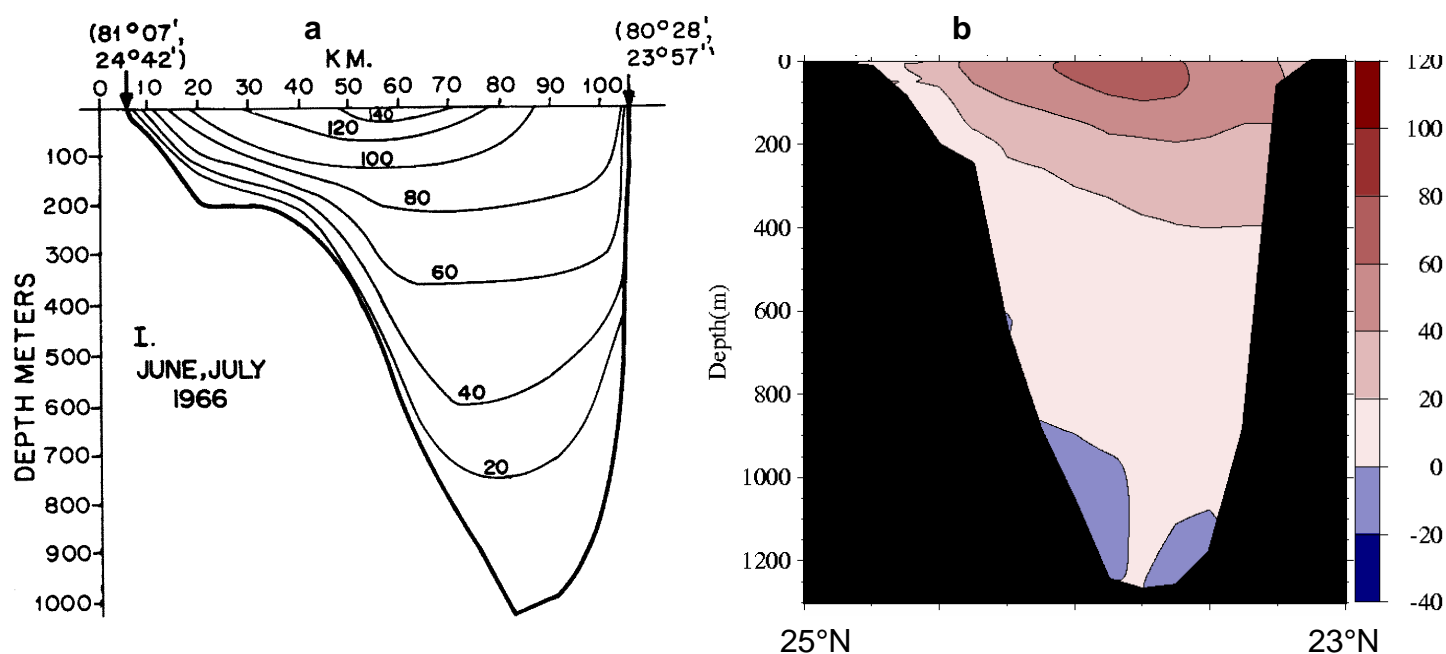


Fig. 63 – Comparison of mean currents through Florida Current section I. (a) downstream speed contours from Schmitz (1996) with observations from June-July 1966 and (b) eastward speed contours from assimilative  $1/8^\circ$  global NCOM 1998-2000 mean section at  $81^\circ\text{W}$ ,  $23^\circ\text{N}$ - $25^\circ\text{N}$ .

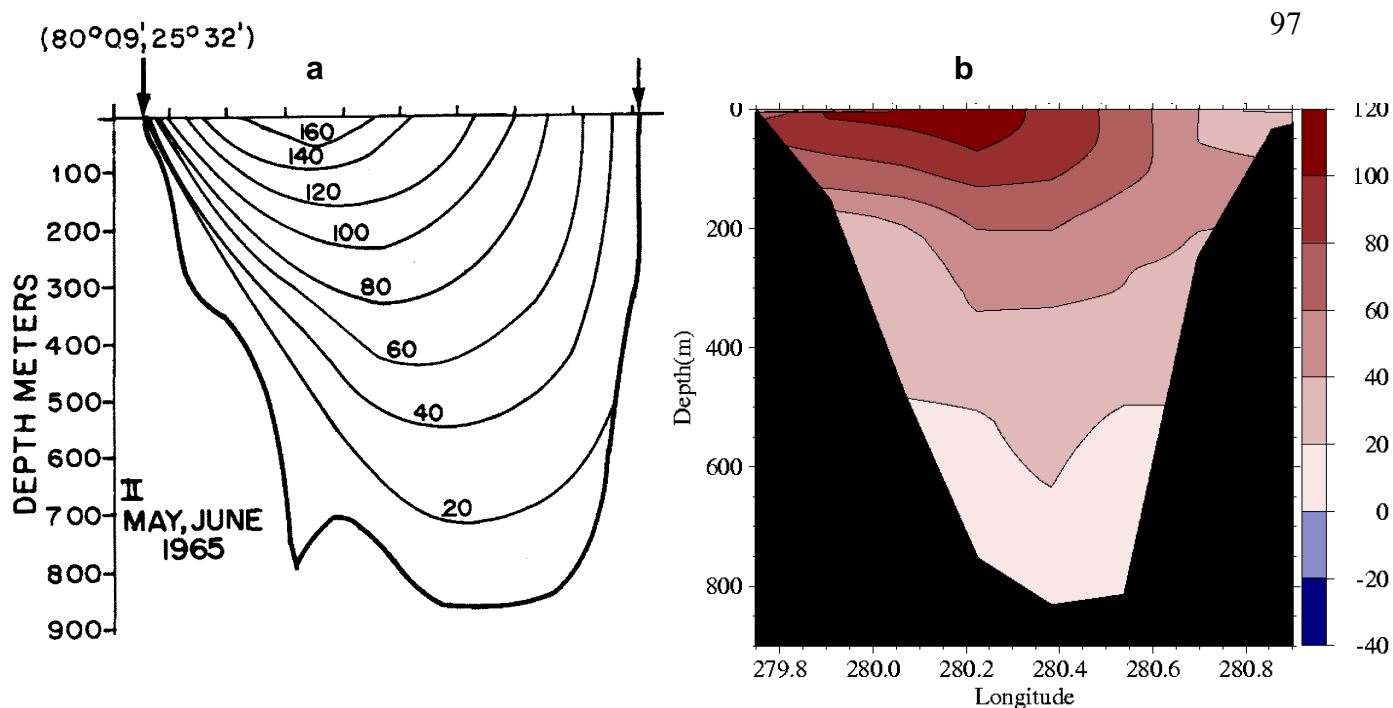


Fig. 64 – Comparison of mean currents through Florida Current section II. (a) downstream speed contours from Schmitz (1996) with observations from May-June 1965 and (b) northward speed contours from assimilative  $1/8^\circ$  global NCOM 1998-2000 mean section at  $25.5^\circ\text{N}$ ,  $80.0^\circ\text{W}$ - $79.1^\circ\text{W}$ .

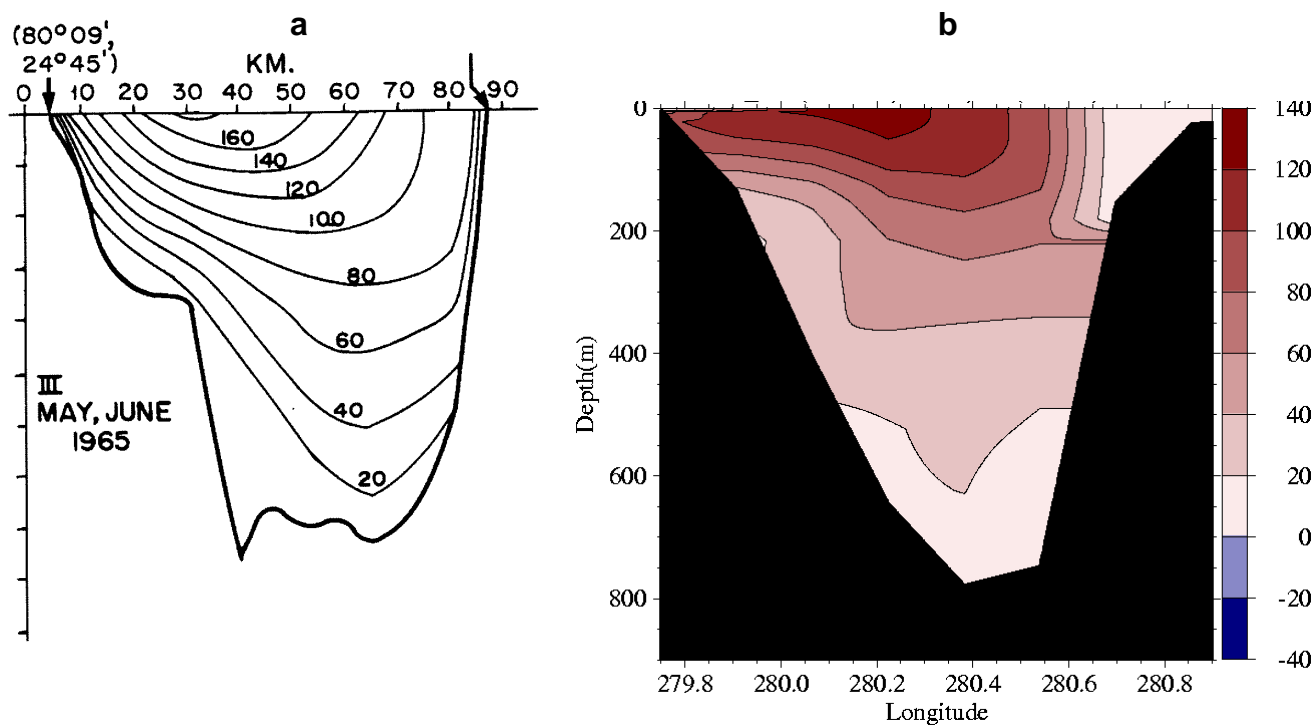


Fig. 65 – Comparison of mean currents through Florida Current section III. (a) downstream speed contours from Schmitz (1996) with observations from May-June 1965 and (b) northward speed contours from assimilative  $1/8^\circ$  global NCOM 1998-2000 mean section at  $25.75^\circ\text{N}$ ,  $80.0^\circ\text{W}$ - $79.1^\circ\text{W}$ .

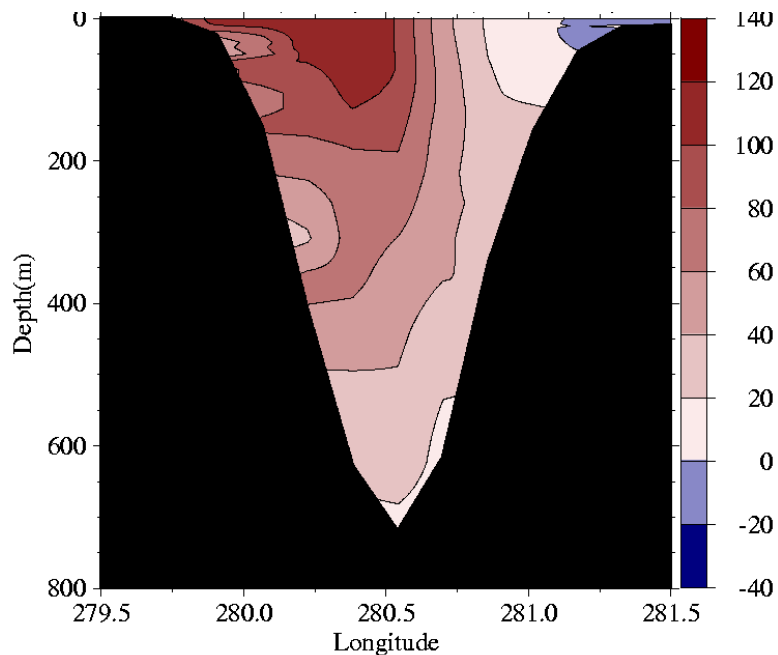


Fig. 66 – Mean currents through Florida Current at 27°N, 80.5°W-78.5°W from assimilative 1/8° global NCOM 1998-2000.

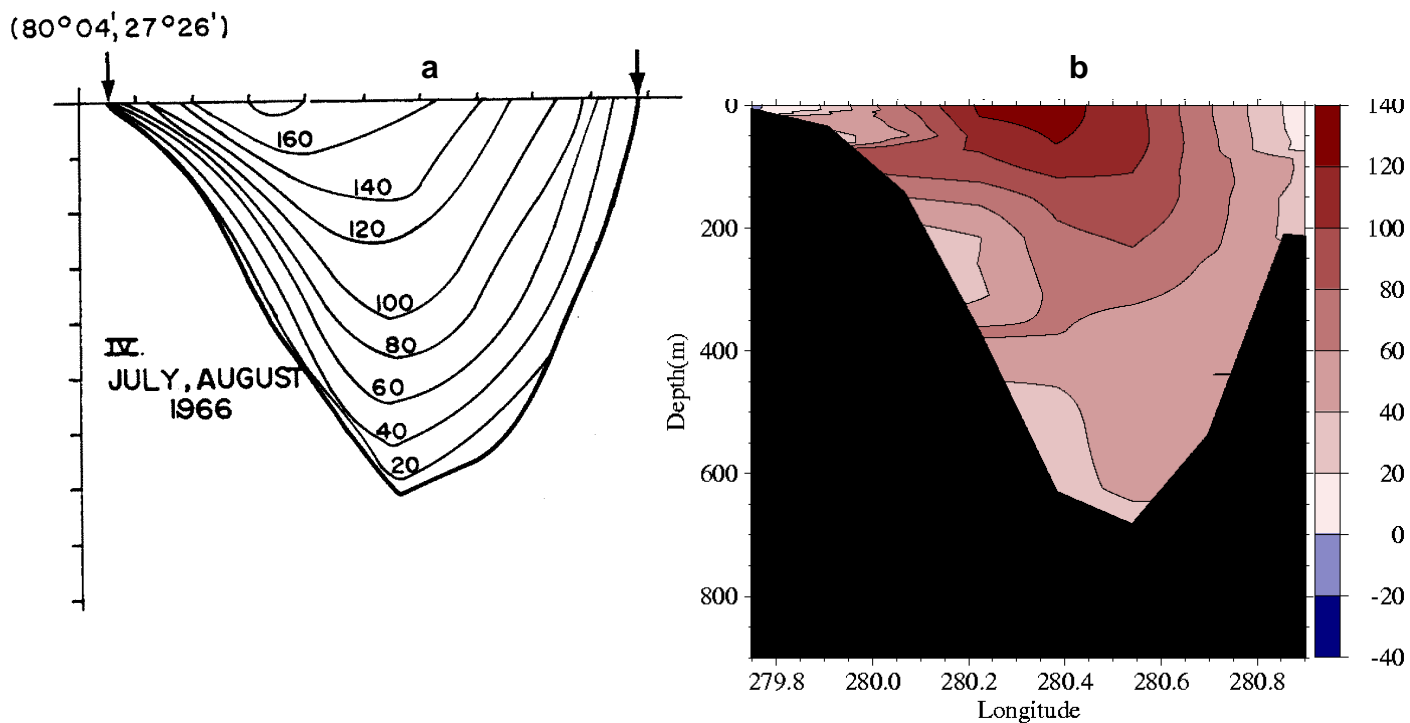


Fig. 67 – Comparison of mean currents through Florida Current section IV. (a) downstream speed contours from Schmitz (1996) with observations from July-August 1966 and (b) northward speed contours from assimilative 1/8° global NCOM 1998-2000 mean section at 27.43°N, 80.25°W-79.1°W.

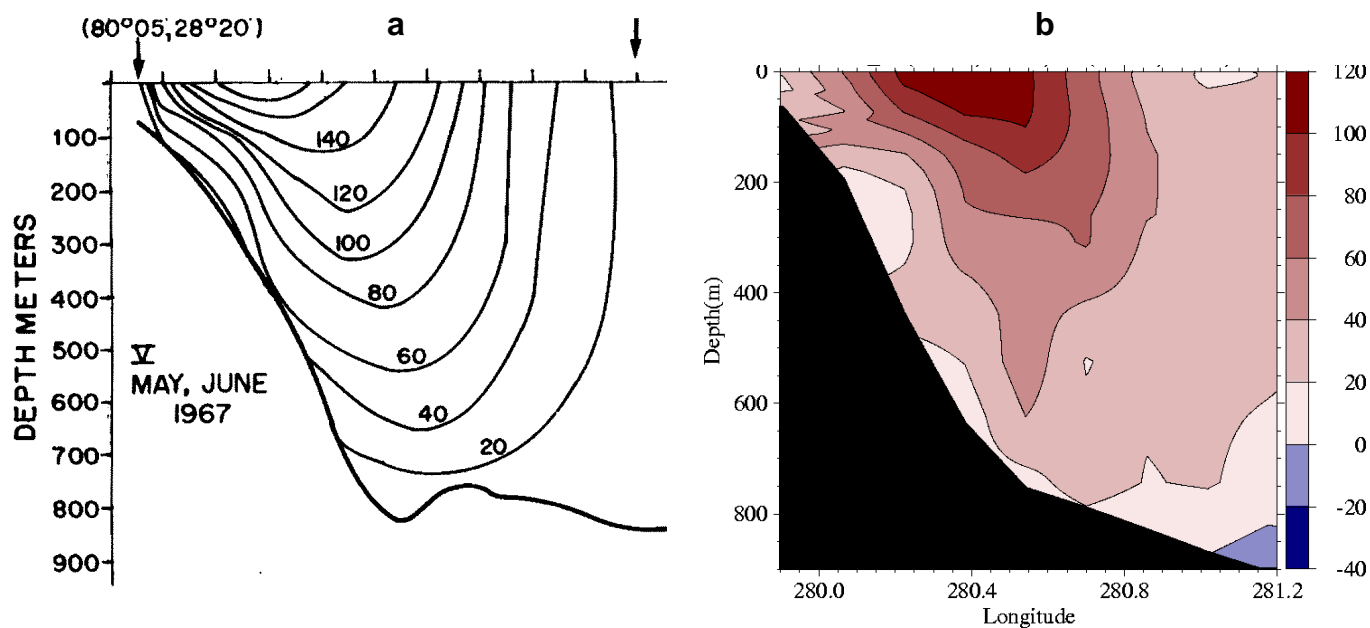


Fig. 68 – Comparison of mean currents through Florida Current section V. (a) downstream speed contours from Schmitz (1996) with observations from May-June 1967 and (b) northward speed contours from assimilative  $1/8^{\circ}$  global NCOM 1998-2000 mean section at  $28^{\circ}20'N$ ,  $80^{\circ}06'W$ - $78^{\circ}48'W$ .

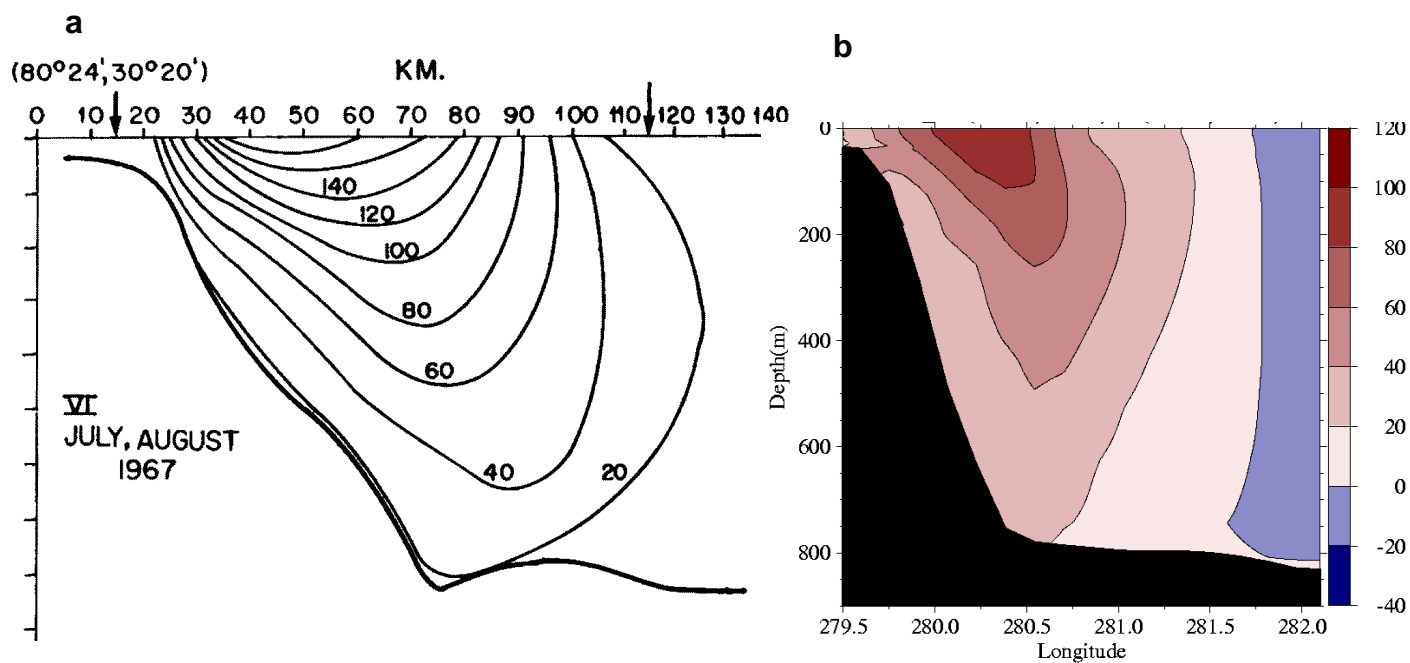


Fig. 69 – Comparison of mean currents through Florida Current section VI. (a) downstream speed contours from Schmitz (1996) with observations from July-August 1967 and (b) northward speed contours from assimilative  $1/8^{\circ}$  global NCOM 1998-2000 mean section at  $30^{\circ}20'N$ ,  $80^{\circ}30'W$ - $77^{\circ}54'W$ .

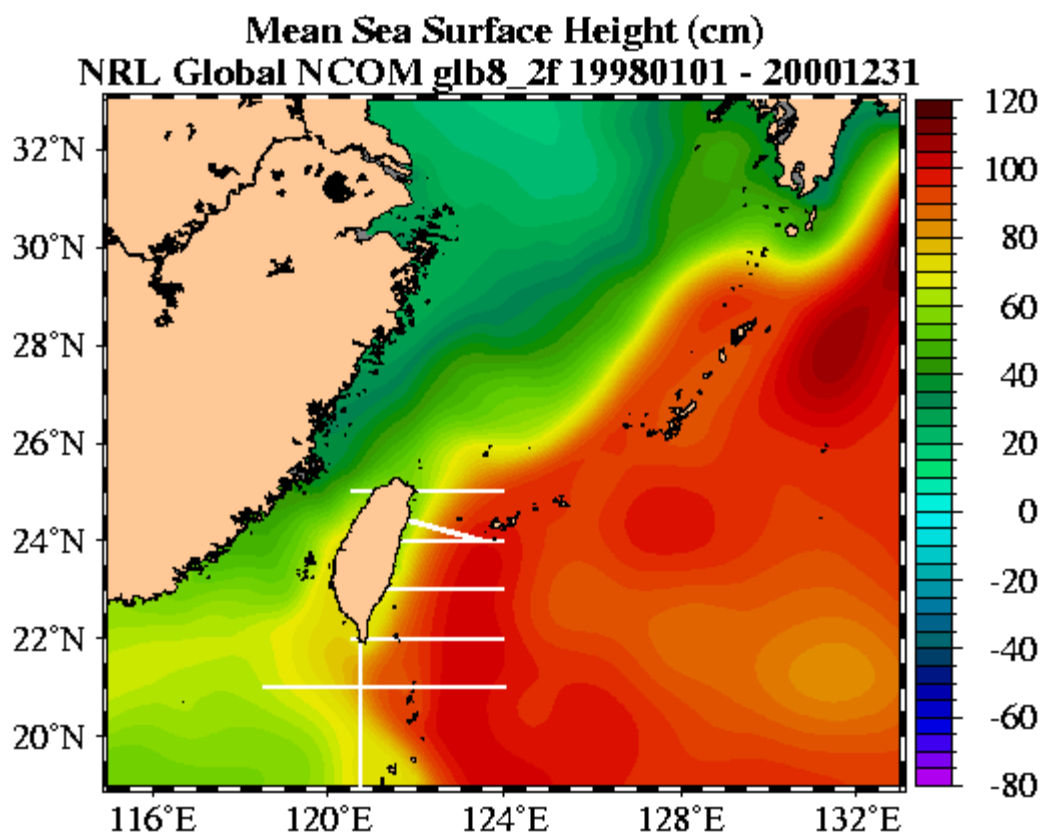


Fig. 70 – Global NCOM 1998-2000 SSH mean in the Taiwan area. Superimposed white lines locate vertical sections extracted from NCOM for comparison with sections of mean currents from historical observations.

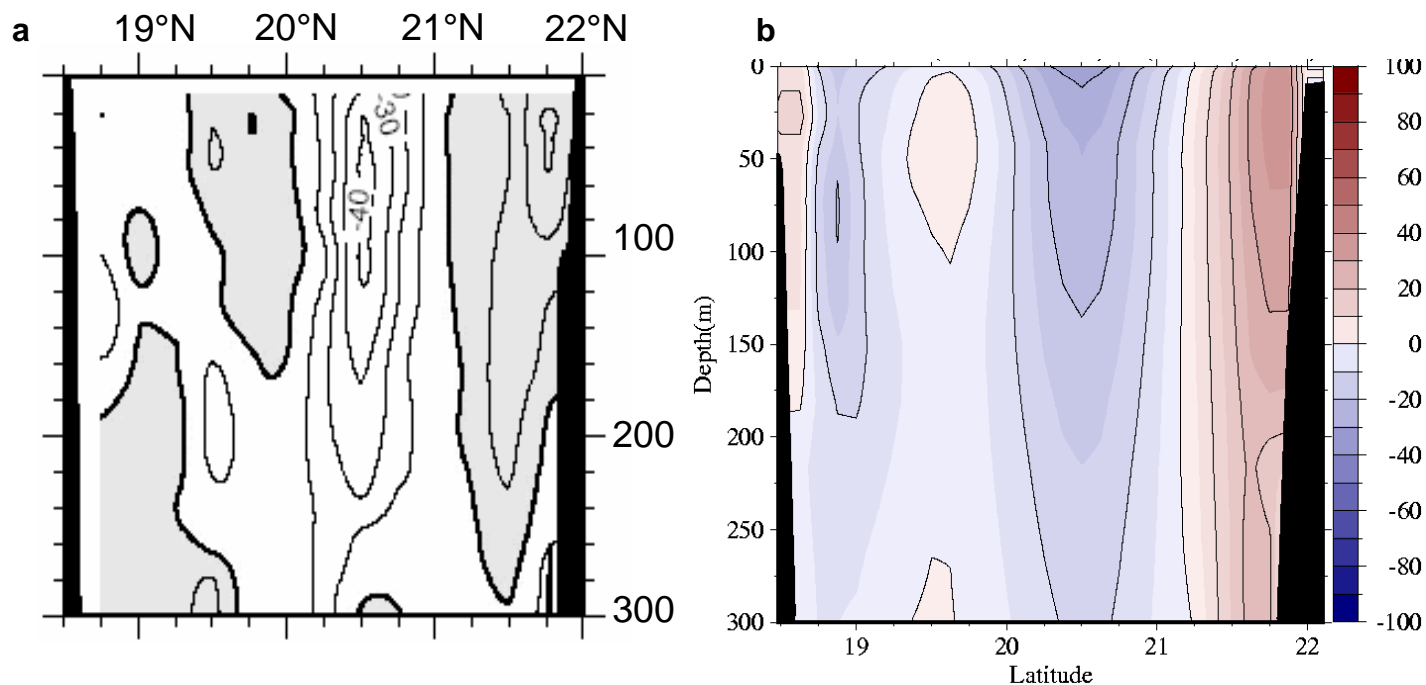


Fig. 71 – Velocity section across the upper 300m of the Luzon Strait,  $120^{\circ}75'E$  between Taiwan and Luzon. (a) Contours of eastward speed from Sb-ADCP observations from Liang *et al.* (2003) and (b) contours of eastward speed from assimilative  $1/8^{\circ}$  global NCOM 1998-2000 mean.

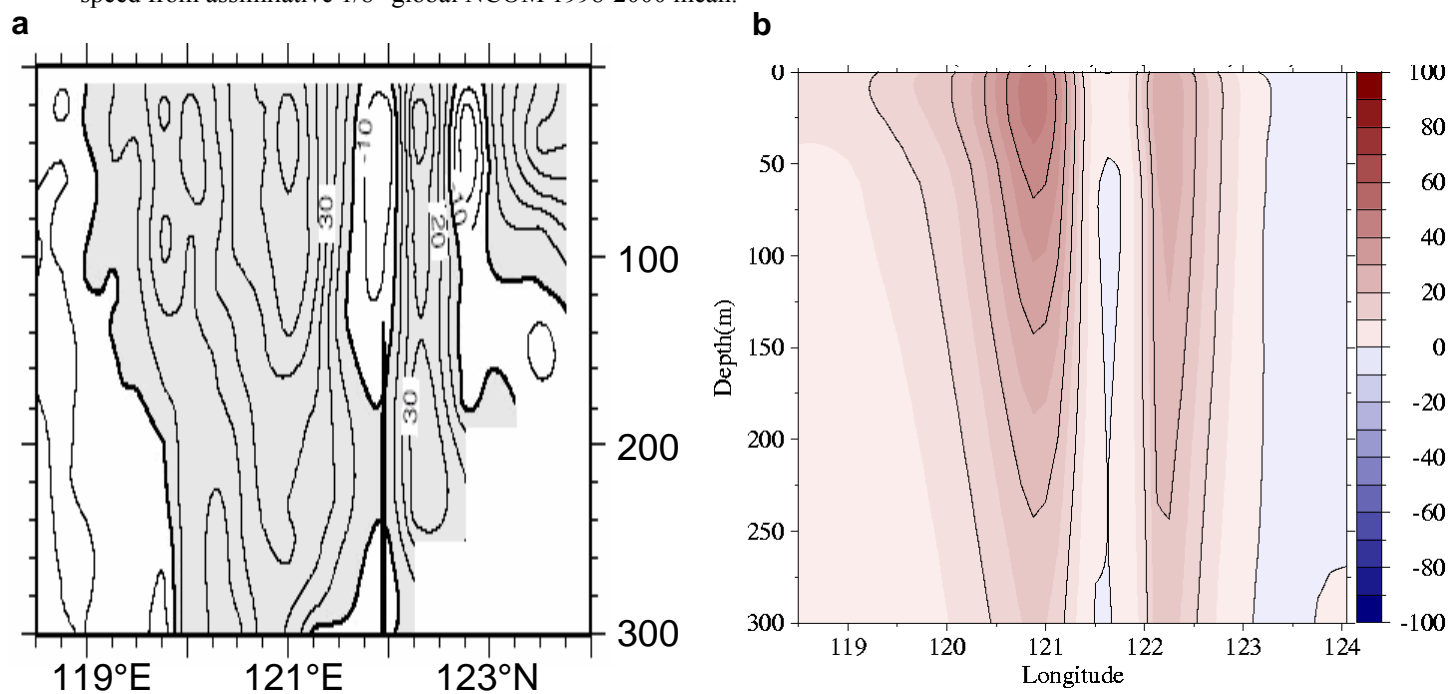


Fig. 72 – Velocity section in the upper 300m of the Luzon Strait,  $21^{\circ}N$  between  $118^{\circ}30'E$  and  $124^{\circ}E$ . (a) Contours of northward speed from Sb-ADCP observations from Liang *et al.* (2003) and (b) contours of northward speed from assimilative  $1/8^{\circ}$  global NCOM 1998-2000 mean.

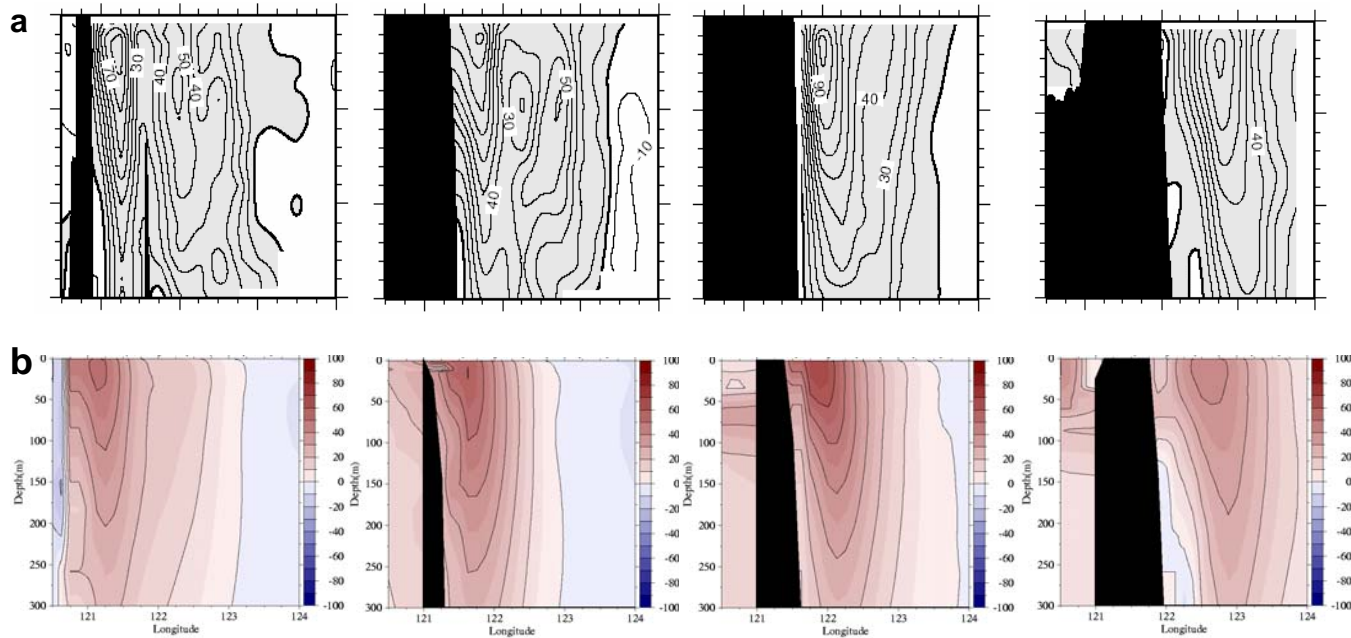


Fig. 73 – Four velocity sections across the upper 300m east of Taiwan, 120°30'E-124°00'E, at 22°N, 23°N, 24°N and 25°N. (a) contours of northward speed from ADCP observations from (Liang *et al.*, 2003) and (b) contours of northward speed from assimilative 1/8° global NCOM 1998-2000 mean.

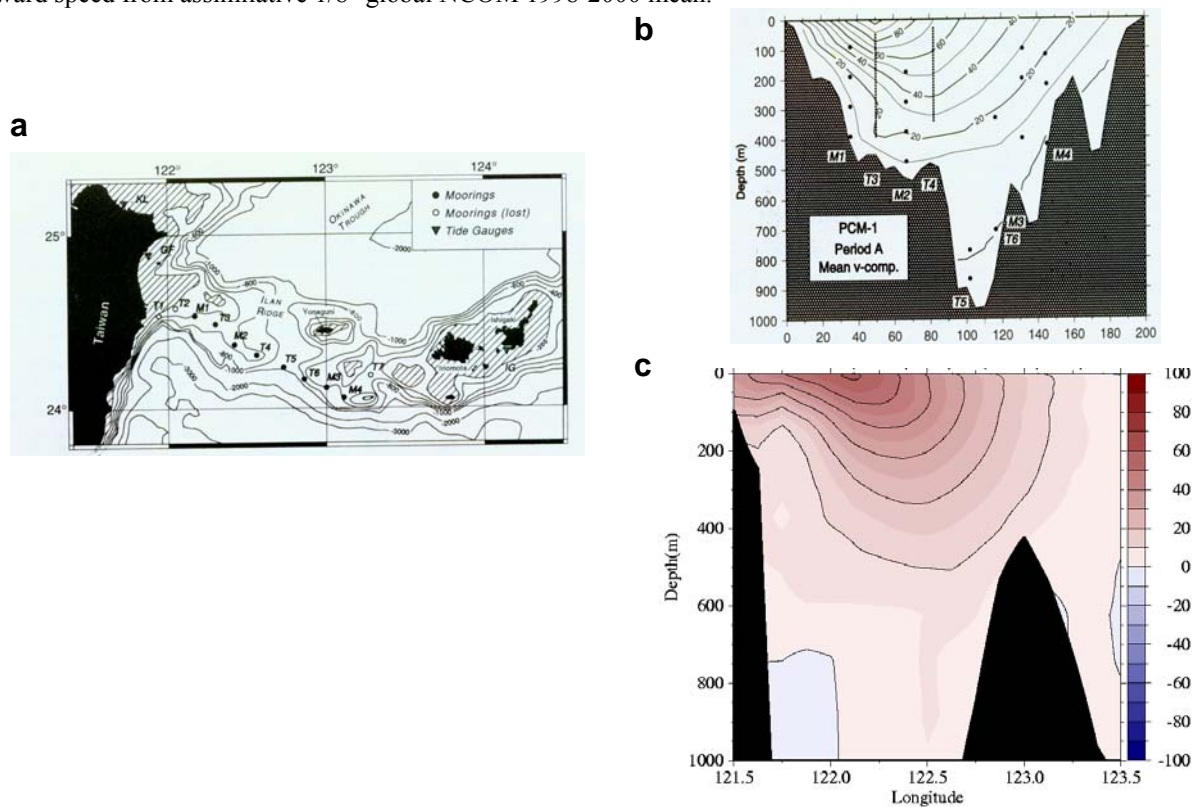


Fig. 74 – Velocity section along the WOCE PCM\_1 line east of Taiwan. (a) Locations of the PCM-1 current meters. (b) Contours of northward speed from PCM-1 data September 1995 to May 1996. (c) Contours of northward speed from assimilative 1/8° global NCOM 1998-2000 mean. (a) and (b) are from Lee *et al.* (2001).

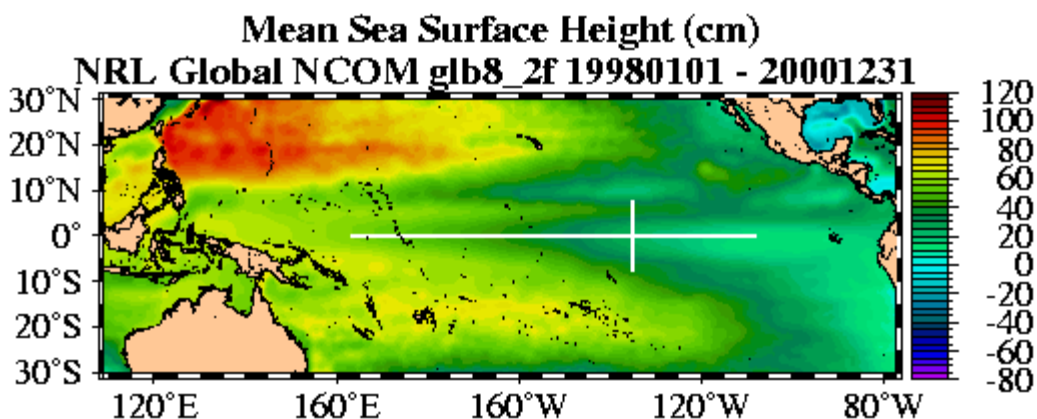


Fig. 75 – Global NCOM 1998-2000 SSH mean in the equatorial Pacific. White lines locate vertical current sections extracted from NCOM for comparison with historical observation means.

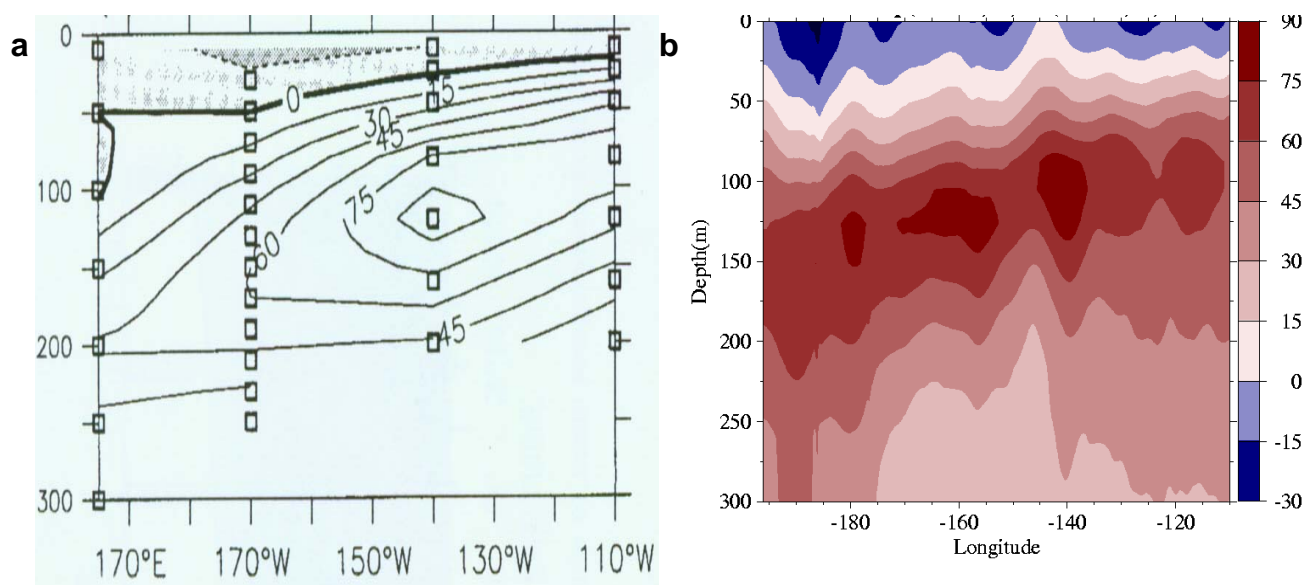


Fig. 76 – Velocity section along the equator ( $0^{\circ}\text{N}$ ) between  $165^{\circ}\text{E}$  and  $110^{\circ}\text{W}$ . (a) Contours of eastward speed derived from 1991-1999 shipboard observations (Yu and McPhaden, 1999) and (b) contours of eastward speed from assimilative  $1/8^{\circ}$  global NCOM 1998-2000 mean.

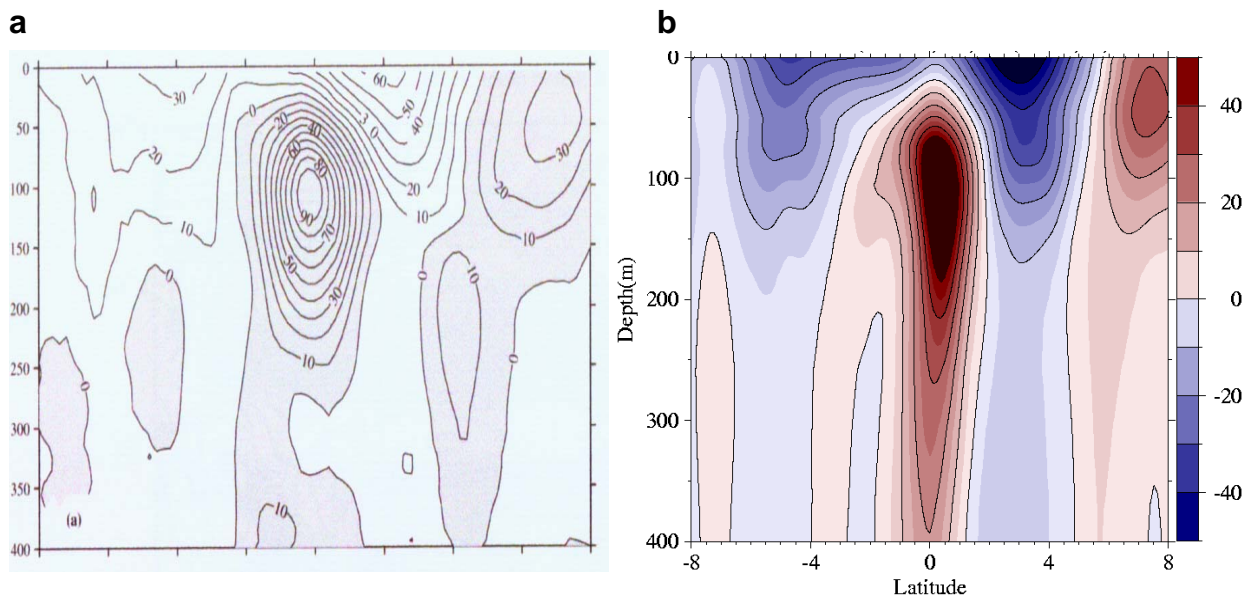


Fig. 77 – Velocity section across the equator at 135°W between 8°S and 8°N. (a) Contours of eastward speed derived from ADCP observations (Johnson *et al.*, 2001) and (b) contours of eastward speed from assimilative 1/8° global NCOM 1998-2000 mean.

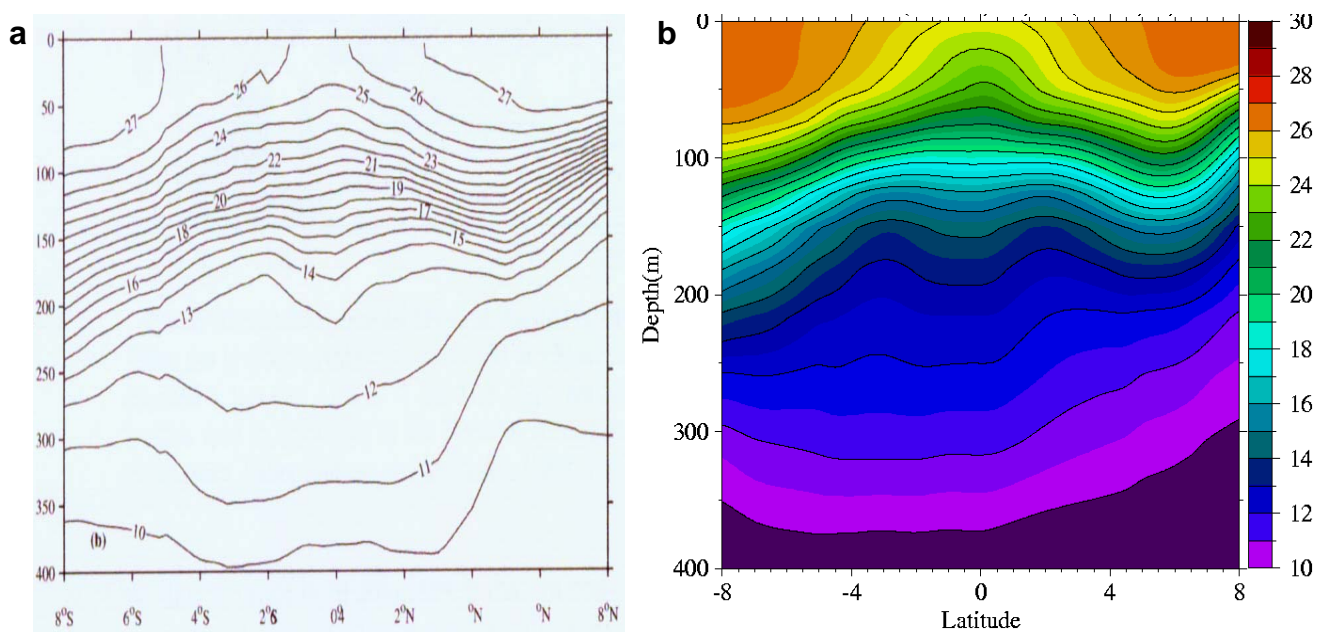


Fig. 78 – Temperature section across the equator at 135°W between 8°S and 8°N (a) derived from CTD observations (Johnson *et al.*, 2001) and (b) from assimilative 1/8° global NCOM 1998-2000 mean.

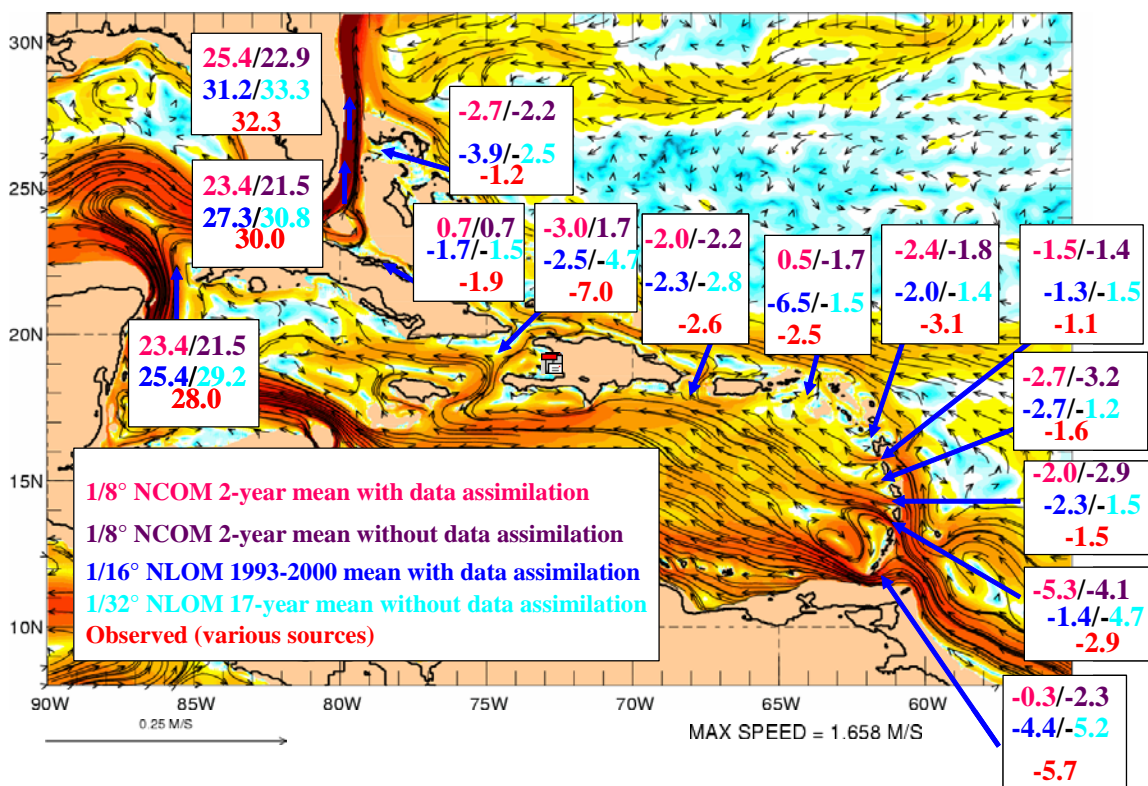


Fig. 79 – Annual mean Caribbean and Bahamas passage transports from the 1/8 ° NCOM, 1/16 ° (blue) and 1/32 ° (cyan) global NLOM compared to observations. Background plot shows the 1/32 ° NLOM annual mean upper layer current vectors superimposed on their strength (log of the kinetic energy of the mean flow) in color. Major currents are indicated relatively long vectors that are collocated with areas of high kinetic energy (red and yellow).

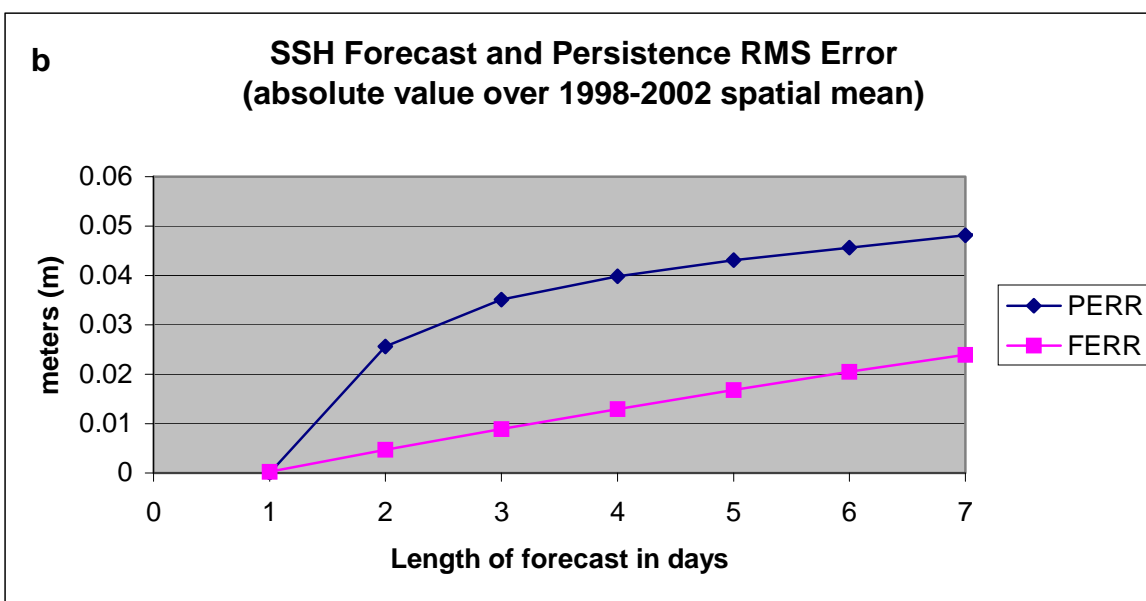
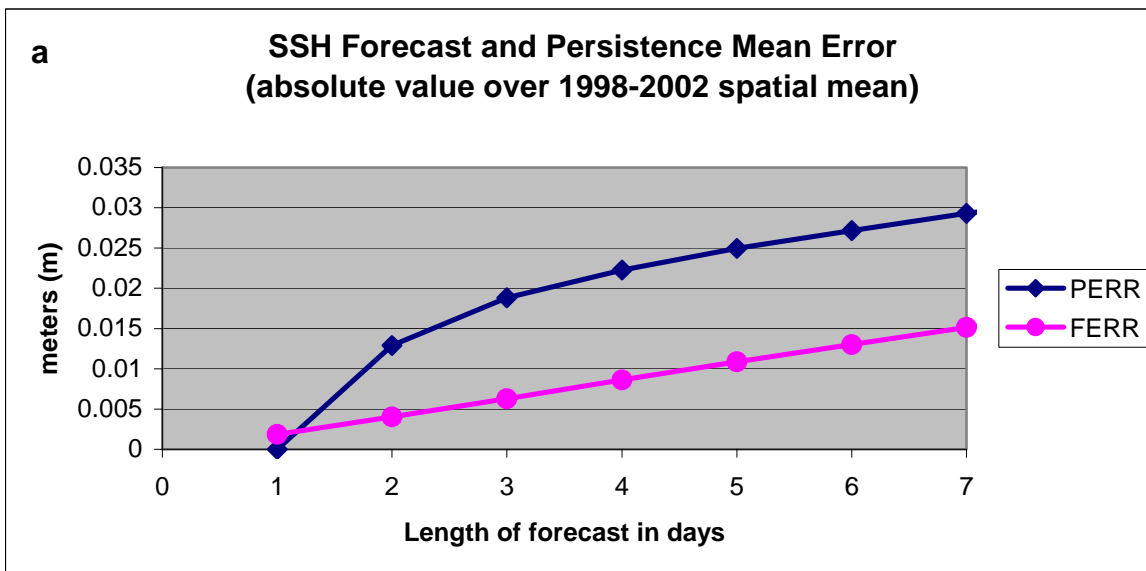


Fig. 80 – SSH forecast and persistence error comparisons versus forecast length up to seven days for  $1/8^\circ$  global NCOM. Calculated from bimonthly 7-day forecasts from 1998-2002. (a) mean absolute error in SSH and (b) square root of mean squared error in SSH. Means are calculated in space over the global ocean and in time over 1998-2002. Error is relative to the NCOM analysis valid on zero hours of each forecasted day. Forecast error is consistently smaller than persistence. The forecast is particularly better in shallow water.

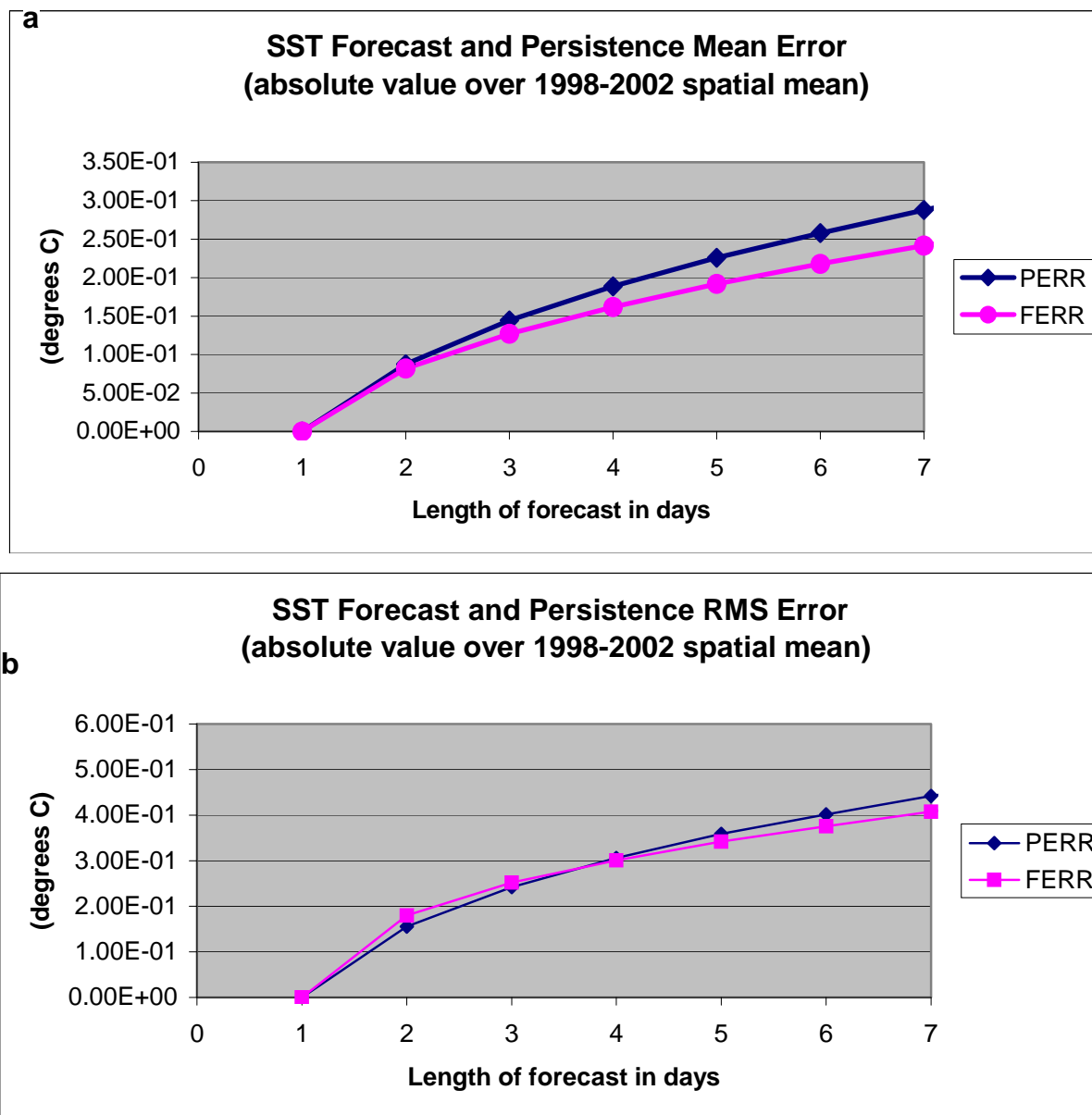


Fig. 81 – SST forecast and persistence error comparisons versus forecast length up to seven days for  $1/8^\circ$  global NCOM. Calculated from bimonthly 7-day forecasts from 1998-2002. (a) mean absolute error in SST and (b) square root of mean squared error in SST. Means are calculated in space over the global ocean and in time over 1998-2002. Error is relative to the NCOM analysis valid on zero hours of each forecasted day. Forecast error is consistently smaller than persistence, but less so than for SSH. Relatively large forecasts errors adjacent to the coast and cold forecasts biases degrade the overall forecast performance.

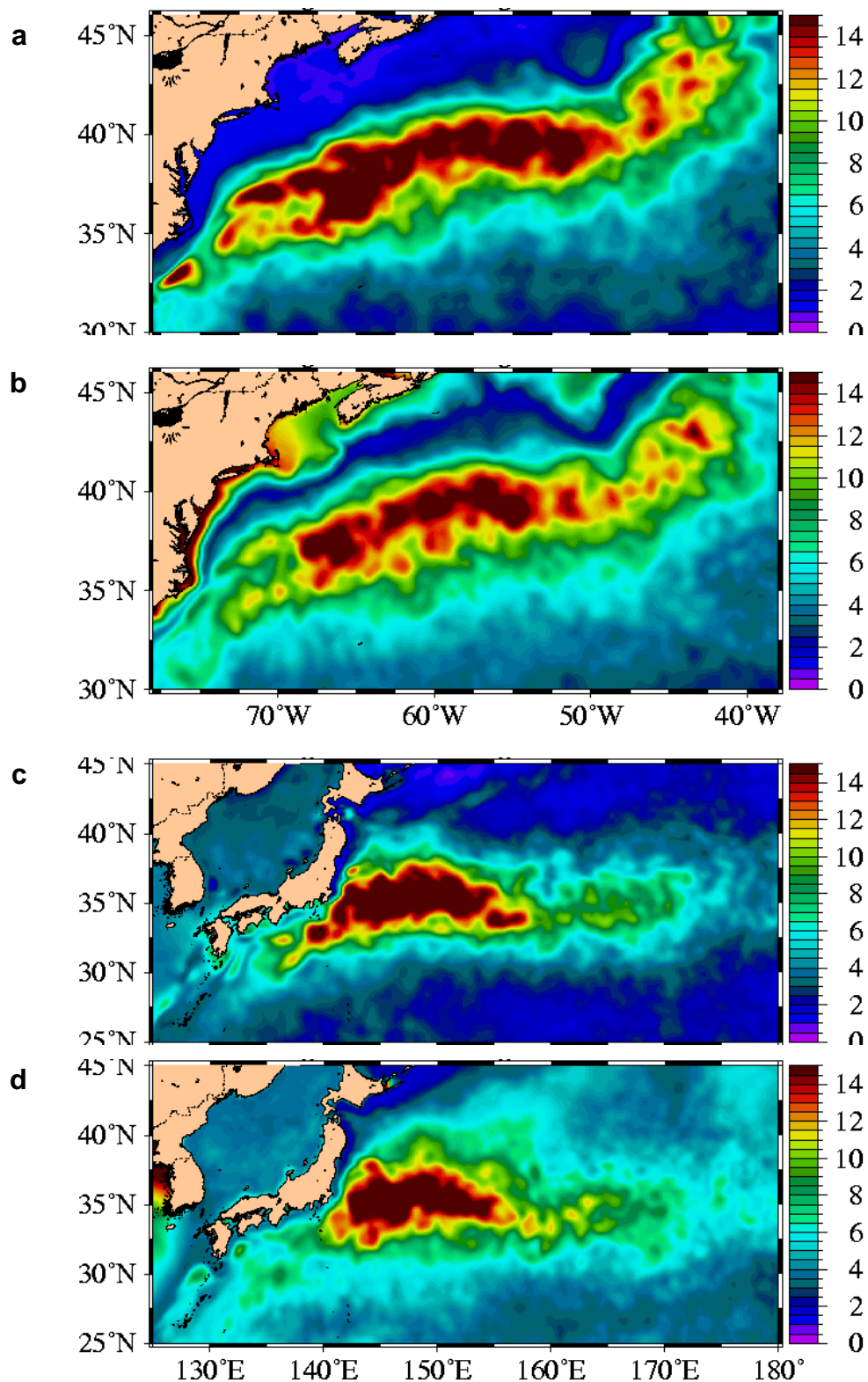


Fig. 82 – Mean 7-day  $1/8^\circ$  global NCOM (a,c) forecast and (b,d) persistence error in SSH (cm) relative to subsequent global NCOM nowcasts for forecasts from 1998-2002 in the (a,b) Gulf Stream and (c,d) Kuroshio regions. Relative forecast errors are particularly good on the continental shelves. Relative forecast skill is lower along the main fronts, reflecting the free-running difficulty in representing these frontal dynamics at  $1/8^\circ$  resolution.

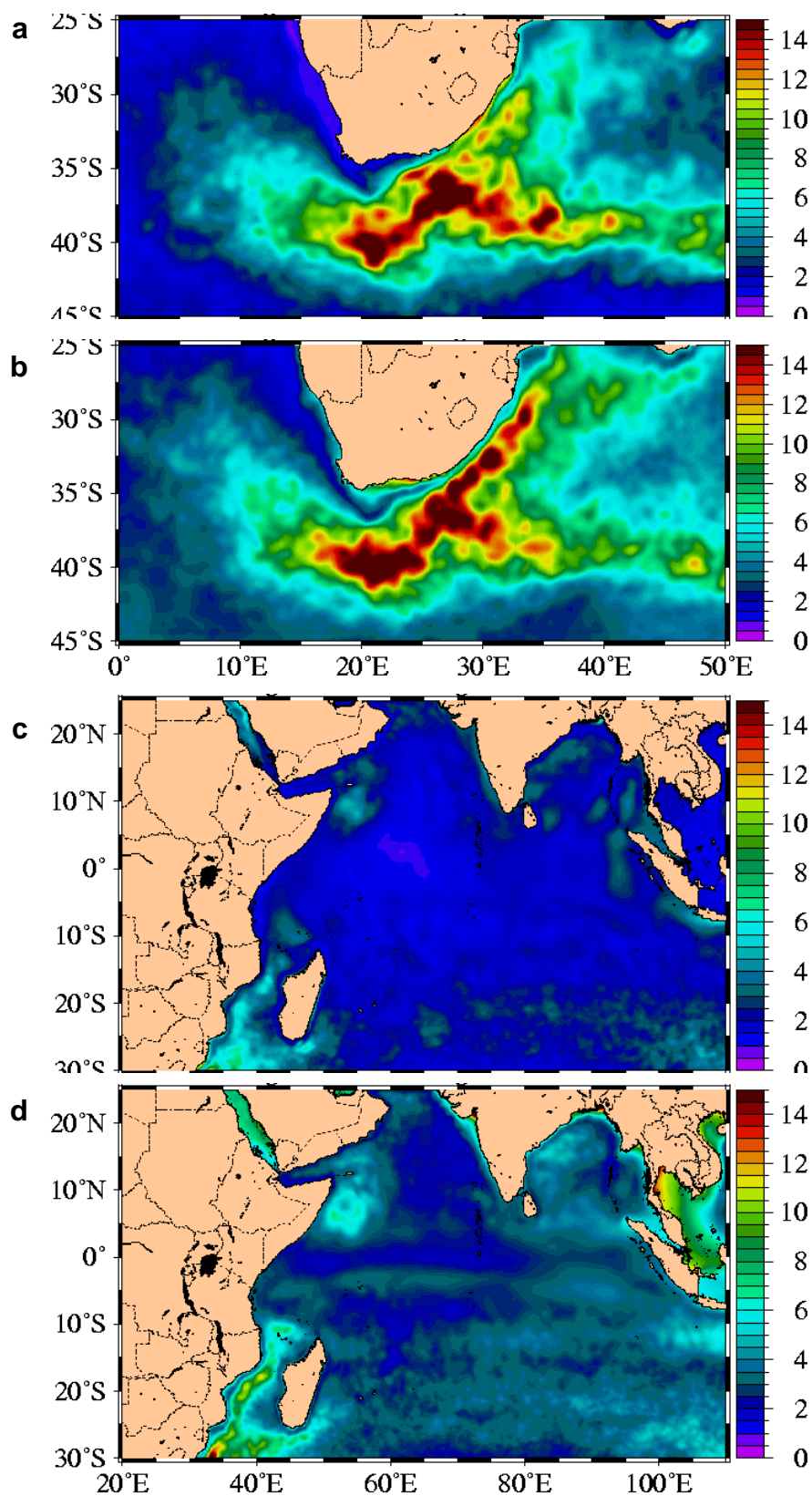


Fig. 83 – Mean 7-day  $1/8^\circ$  global NCOM (a,c) forecast and (b,d) persistence error in SSH (cm) relative to subsequent global NCOM nowcasts for forecasts from 1998-2002 in the (a,b) Agulhas and (c,d) Indian Ocean regions. Relative forecast errors are generally low and better than persistence. Skill is lower in the Agulhas Retroflection, reflecting the free-running difficulty in representing these frontal dynamics at  $1/8^\circ$  resolution.

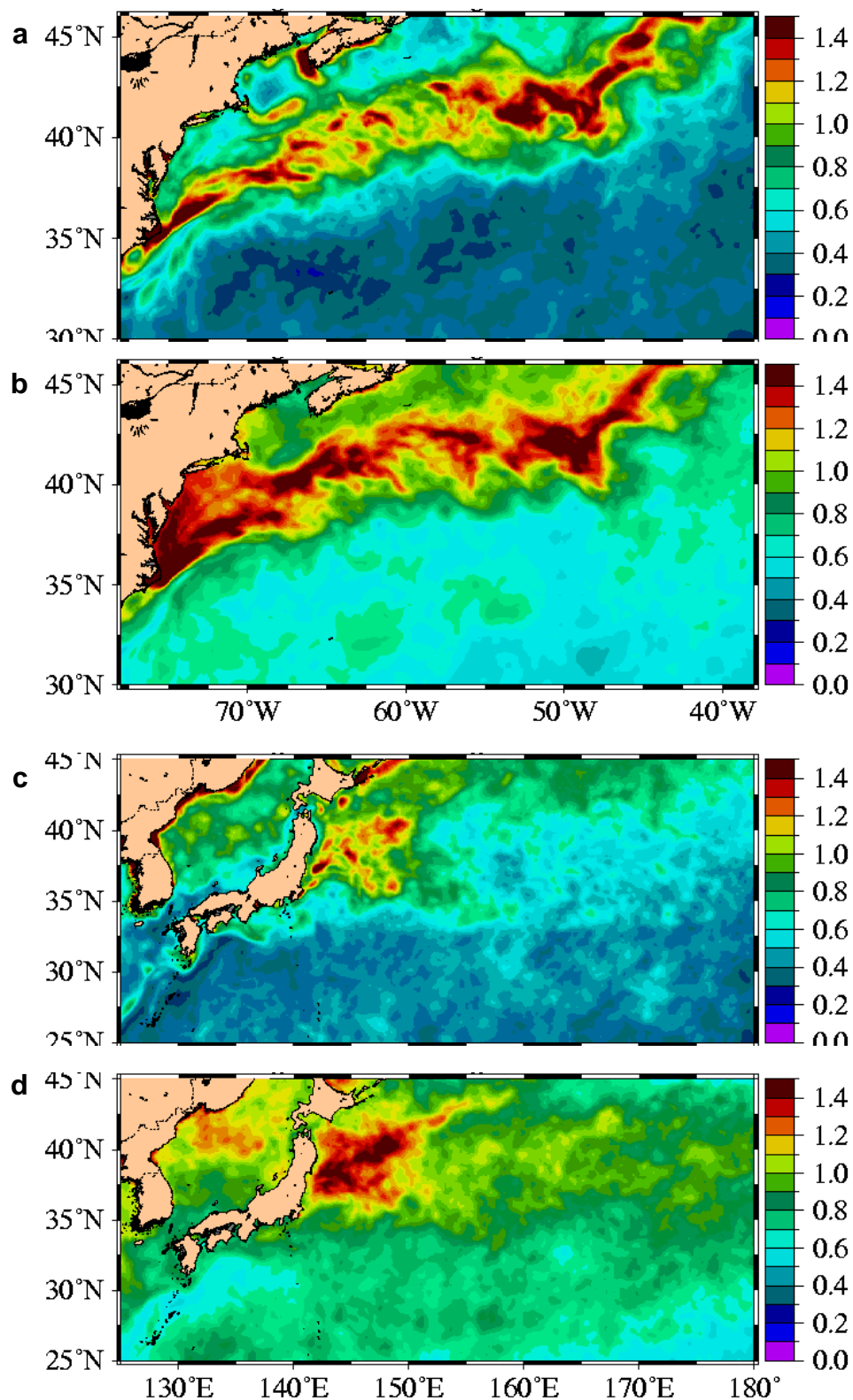


Fig. 84 – Mean 7-day 1/8° global NCOM (a,c) forecast and (b,d) persistence error in SST (°C) relative to subsequent global NCOM nowcasts for forecasts from 1998-2002 in the (a,b) Gulf Stream and (c,d) Kuroshio regions. The forecast has generally smaller errors than persistence except in narrow bands immediately adjacent to the coast, where forecast errors are quite high. We attribute these errors to inadequate land masking in the global atmospheric forcing, resulting in application of flux values appropriate for land areas near the land-sea boundary.

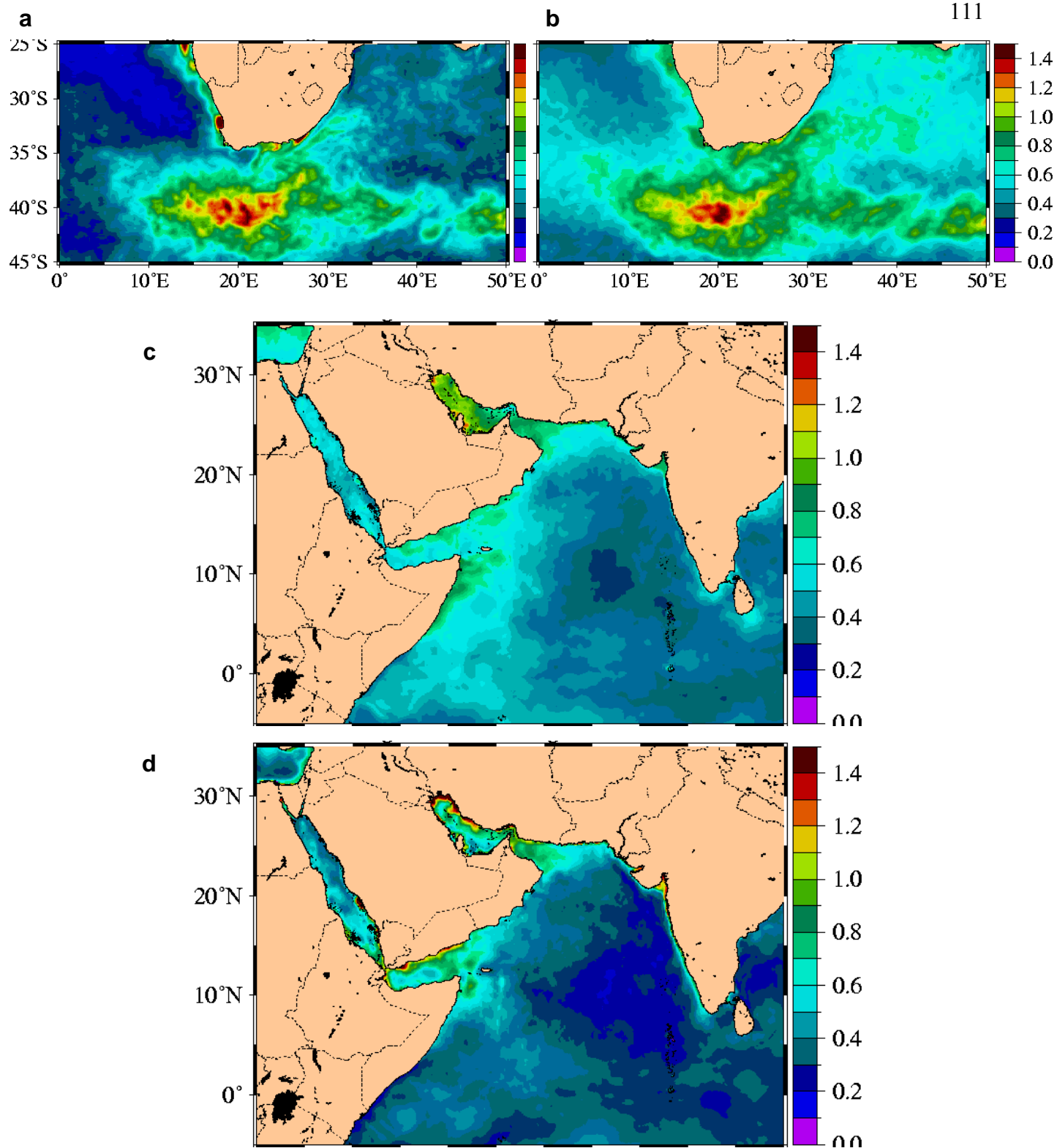


Fig. 85 – Mean 7-day  $1/8^\circ$  global NCOM (a,c) forecast and (b,d) persistence error in SST ( $^\circ\text{C}$ ) relative to subsequent global NCOM nowcasts for forecasts from 1998-2002 in the (a,b) Agulhas and (c,d) Arabian Sea regions. The forecast has generally smaller errors than persistence except in narrow bands immediately adjacent to the coast, where forecast errors are quite high. We attribute these errors to inadequate land masking in the global atmospheric forcing, resulting in application of flux values appropriate for land areas near the land-sea boundary.

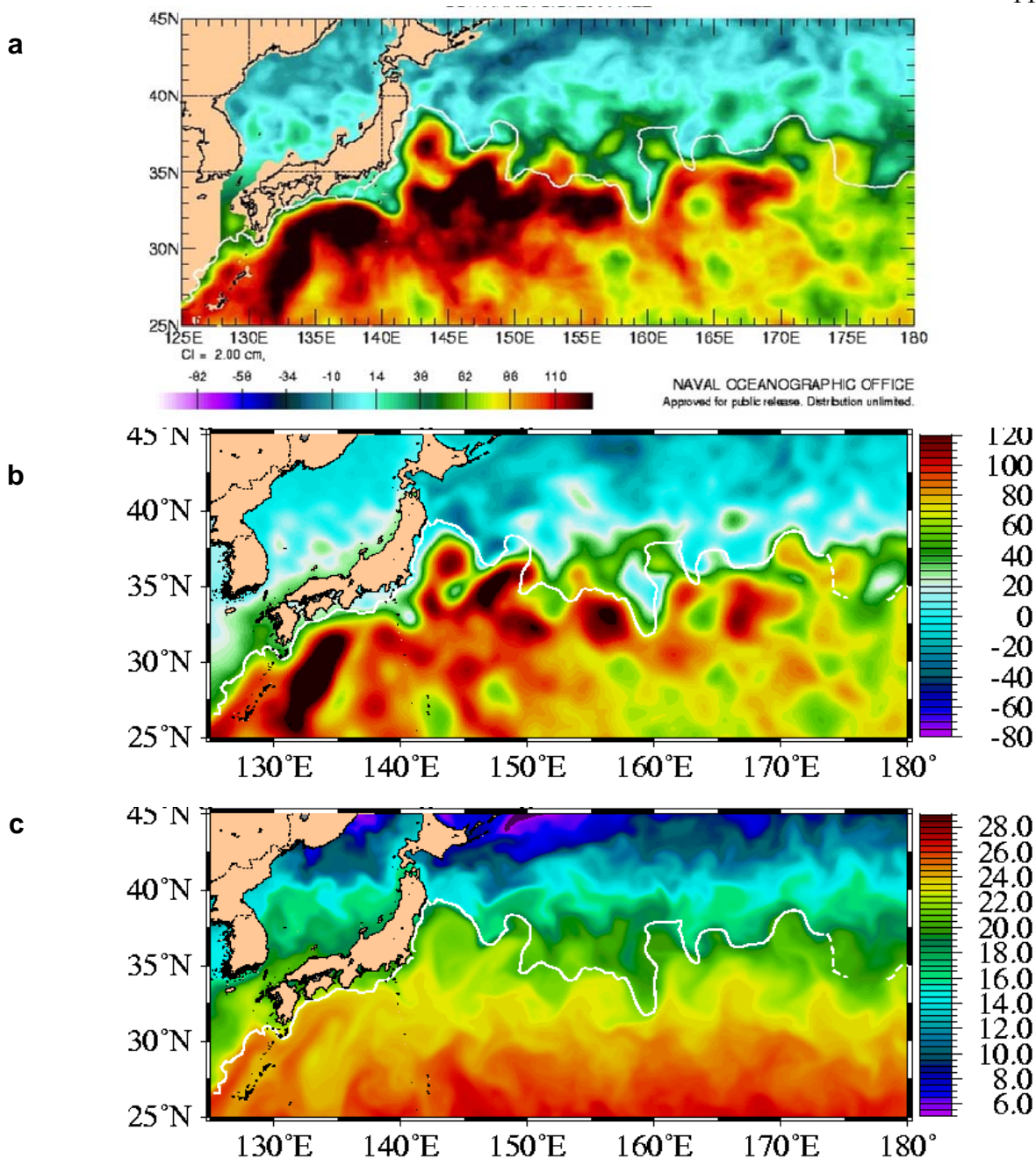


Fig. 86 – Surface plots from the Kuroshio region east of Japan for 22 November 2001. (a) SSH from operational 1/16° global NLOM, (b) SSH from assimilative 1/8° global NCOM, and (c) SST from assimilative 1/8° global NCOM. Superimposed on each plot in white is the NAVOCEANO IR frontal analysis of the Kuroshio north wall for the same date. Since the horizontal resolution of global NCOM is insufficient in some regions for skill in lengthy SSH forecasts, global NLOM depends on data assimilation to improve placement of fronts and eddies in regions such as the Kuroshio and Gulf Stream. Comparison between the front location and NCOM shows that the assimilation of synthetic T and S successfully transmits information from global NLOM necessary for global NCOM to accurately locate and forecast front and eddy location.

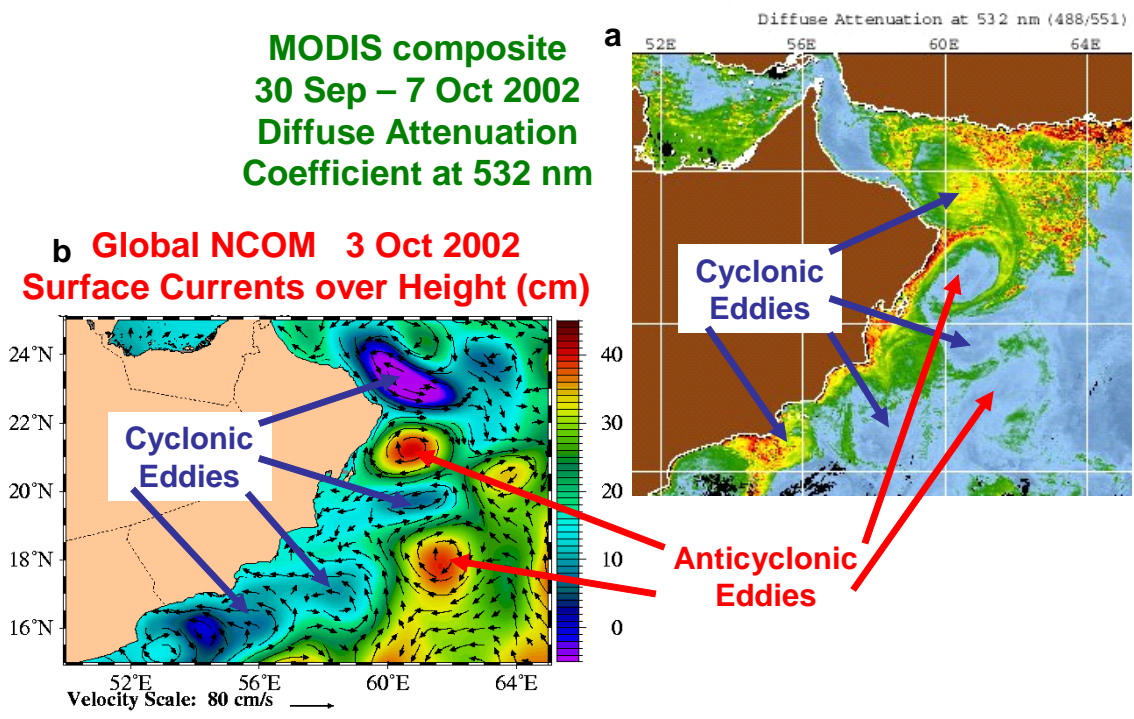


Fig. 87 – Comparison between ocean color composite image and assimilative 1/8° global NCOM results for the northwest Arabian Sea. (a) MODIS composite of the diffuse attenuation coefficient at 532 nm for the week of 30 September – 7 October 2002, and (b) snapshot of NCOM surface currents superimposed on SSH for 3 October 2003. In a comparison of features, a series of eddies delineated by gradients of attenuation coefficient during this relatively cloud-free period are independently replicated in global NCOM.

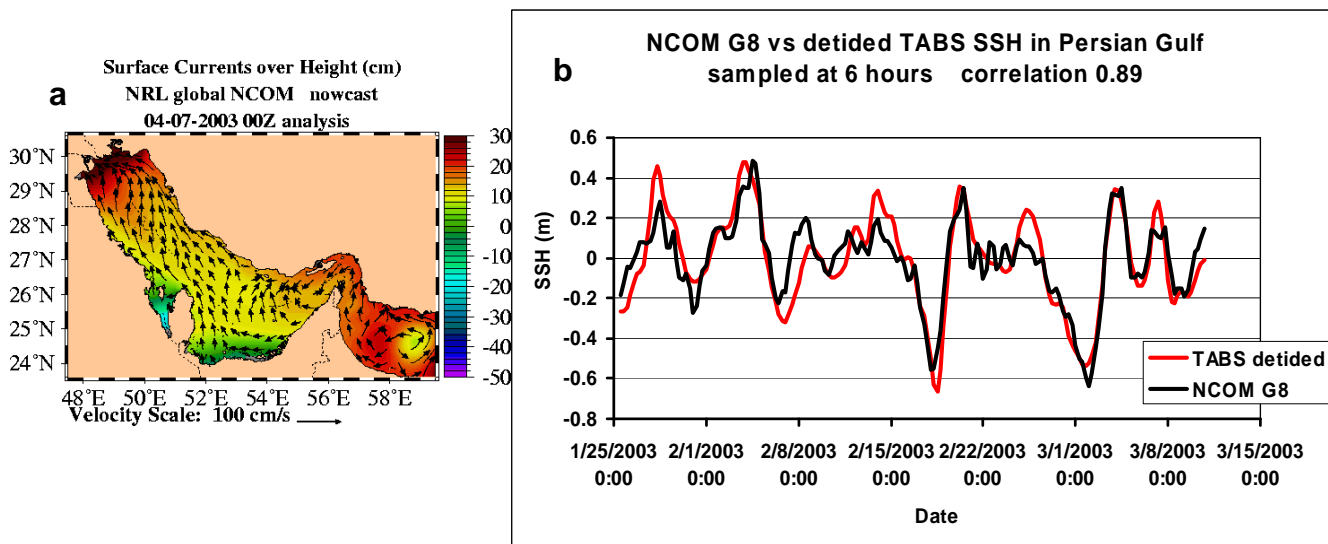


Fig. 88 – (a) Snapshot of global NCOM SSH and surface currents for 7 March 2003 (b) Comparison between detided SSH in the northwestern Persian Gulf measured by a TABS buoy and simulated by 1/8° global NCOM from mid-January to mid-March 2003, shortly before the official start of Operation Iraqi Freedom. Comparison of the independent buoy observations with NCOM referenced to the same mean demonstrates the accuracy NCOM results.

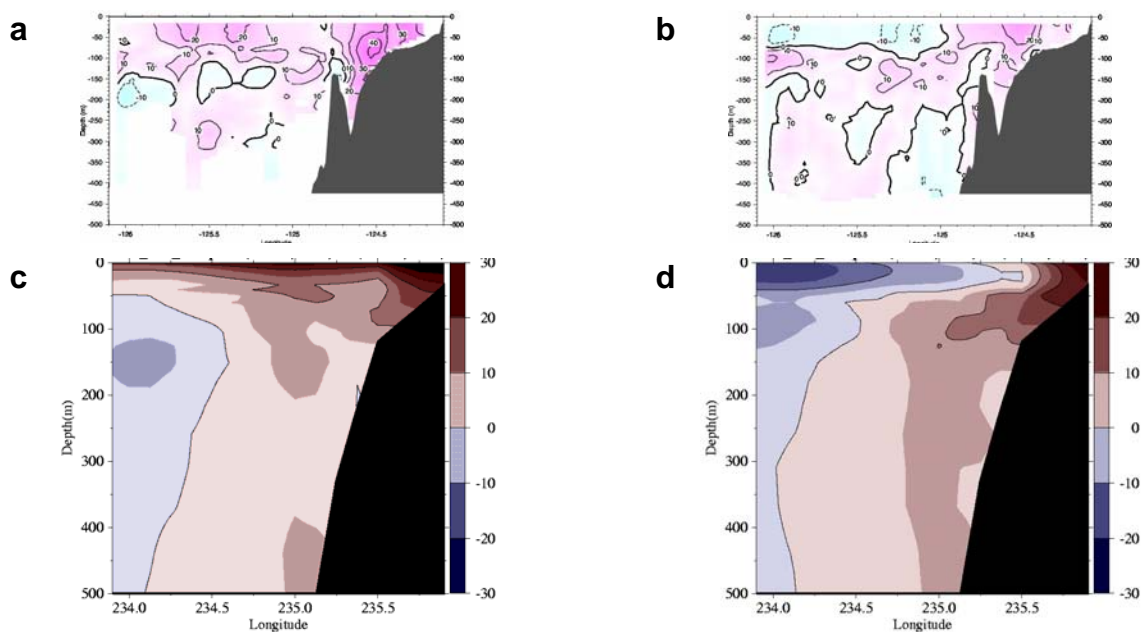


Fig. 89 – A Feb. 2000 comparison of northward velocity (cm/s) through a section at  $44.6^{\circ}\text{N}$  near Newport, Oregon. Sections from (a,b) ADCP surveys conducted as a part of the Northeast Pacific Long Term Observation Program at Oregon State University and (c,d) snapshots from the assimilative  $1/8^{\circ}$  global NCOM. Comparison of the ADCP surveys reveals a reversal in the offshore surface current between the (a) Feb. 1-2 section and (b) Feb. 2-3 section. A similar reversal is seen between the NCOM snapshots on (a) Feb 1 and (b) Feb 2. Note that the fine scale details of the bathymetry and currents are not resolved in the source bathymetry, the NOGAPS atmospheric forcing, or the 14-km grid spacing of global NCOM in this region.

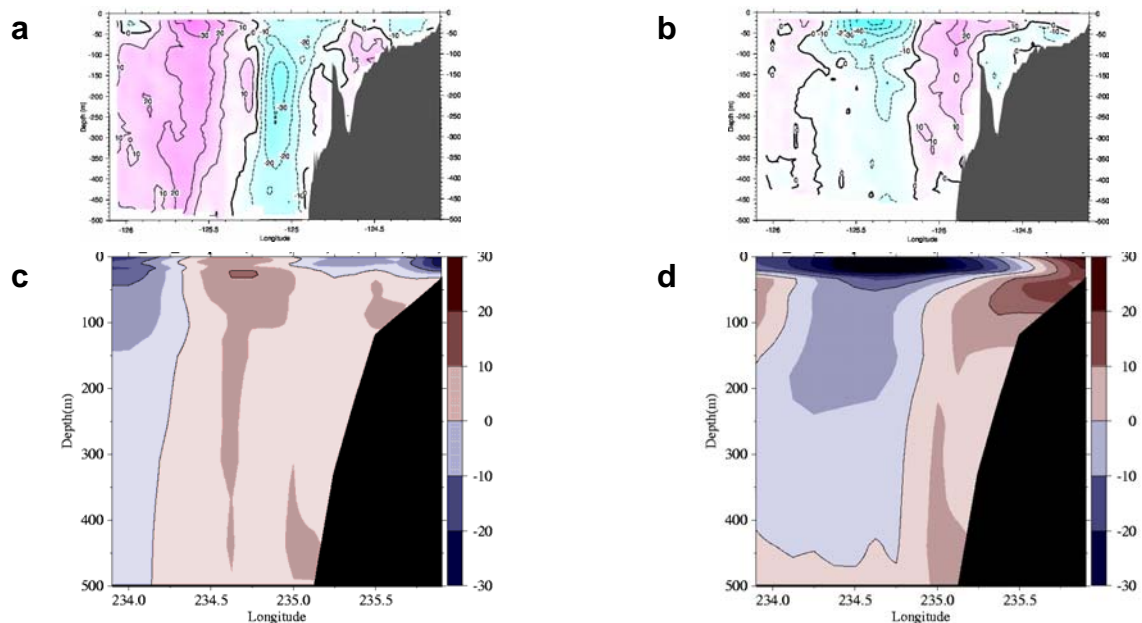


Fig. 90 – Comparison of northward velocity (cm/s) through a section at  $44.6^{\circ}\text{N}$  near Newport, Oregon. Sections from (a,b) ADCP surveys conducted as a part of the Northeast Pacific Long Term Observation Program at Oregon State University and (c,d) snapshots from the assimilative  $1/8^{\circ}$  global NCOM. The (a) Sep. 22-23 1999 survey and the (c) 22 Sep. 1999 snapshot present currents that are almost opposites. Better agreement is found between (b) the 4-5 Nov. 1999 survey and (d) 4 Nov. 1999 snapshot, although the model surface current is too broad.

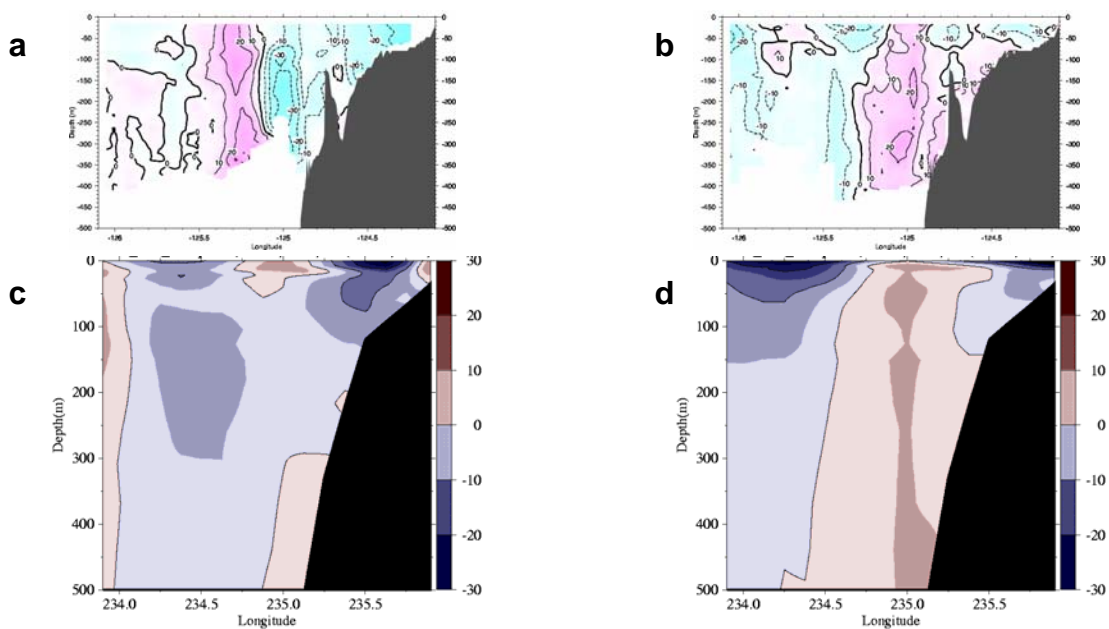


Fig. 91 – 2001 comparisons of northward velocity (cm/s) through a section at  $44.6^{\circ}\text{N}$  near Newport, Oregon. Sections from (a,b) ADCP surveys conducted as a part of the Northeast Pacific Long Term Observation Program and (c,d) snapshots from the assimilative  $1/8^{\circ}$  global NCOM. The midsection eddy in (a) the 20-21 Mar. ADCP line is missing at depth and misplaced at the surface in (b) the 20 Mar. NCOM results. In contrast, the 5 Sep. NCOM section (d) is in good agreement with the larger scale features in the (b) 4-6 Sep. survey, although there is more observed variation in the offshore southward surface jet.

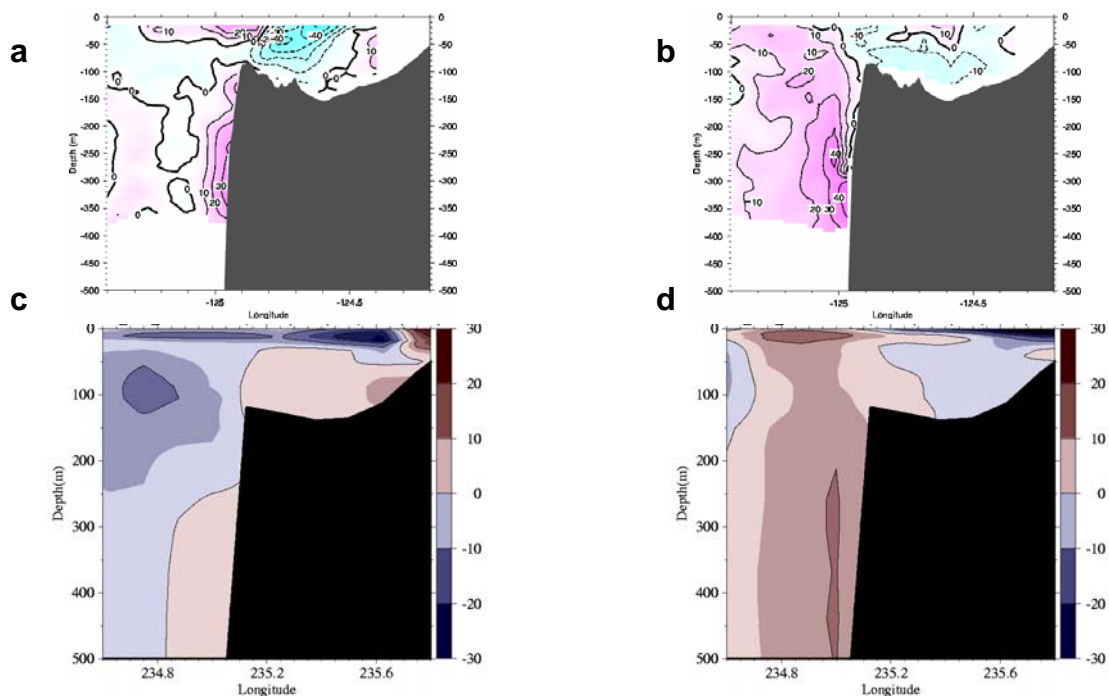


Fig. 92 – 2002 comparisons of northward velocity (cm/s) through a section at  $44.0^{\circ}\text{N}$  near Heceta Head, Oregon. Sections from (a,b) ADCP surveys conducted as a part of the Northeast Pacific Long Term Observation Program and (c,d) snapshots from the assimilative  $1/8^{\circ}$  global NCOM. The 9-10 Apr. observations (a) show a midsection eddy and a strong northward boundary layer *jet* along the slope are not present in the (c) 10 Mar. model results. The (b) 14-15 July observations and (d) 14 July NCOM snapshot are quite similar, but again the intense northward boundary layer *jet* along the slope is present in the observations but not resolved by the model.

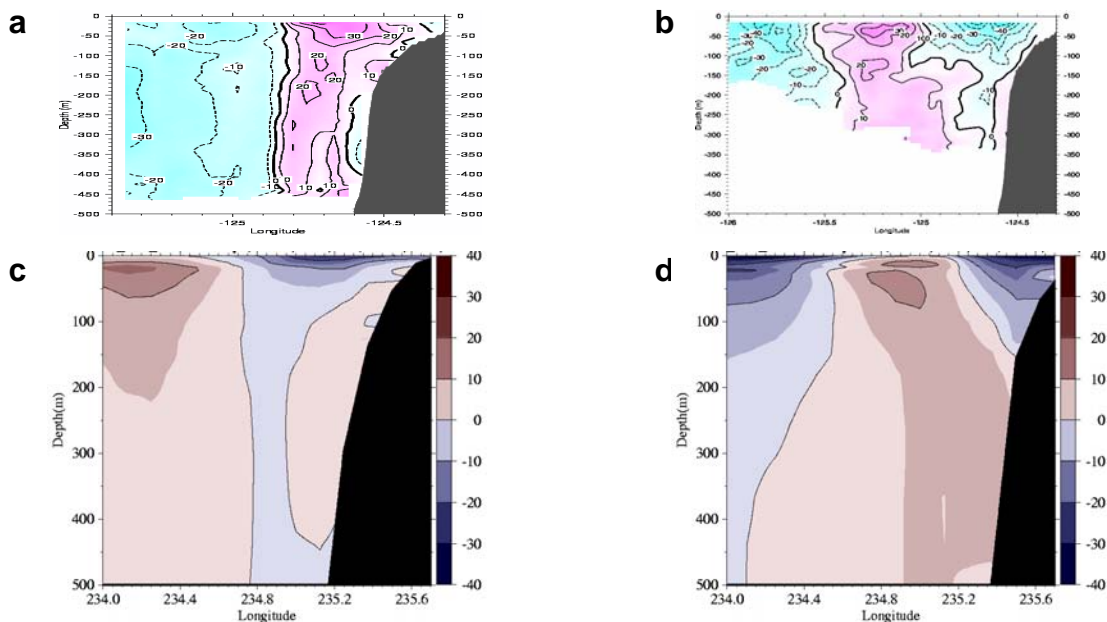


Fig. 93 – Northward velocity (cm/s) through Oregon coast sections from (a,b) ADCP surveys conducted as a part of the Northeast Pacific Long Term Observation Program and (c,d) snapshots from the (b) assimilative  $1/8^\circ$  global NCOM. At  $43.2^\circ\text{N}$ , the (a) 24-25 Sep. 1999 ADCP survey shows currents opposite to those seen in the (c) 24 Sep. 1999 NCOM snapshot. Good agreement is found on 13 Jul. 2002 at  $41.9^\circ\text{N}$ , when both the (b) observations and (d) model indicate a deep, surface-intensified northward flow flanked by surface intensified southward currents.

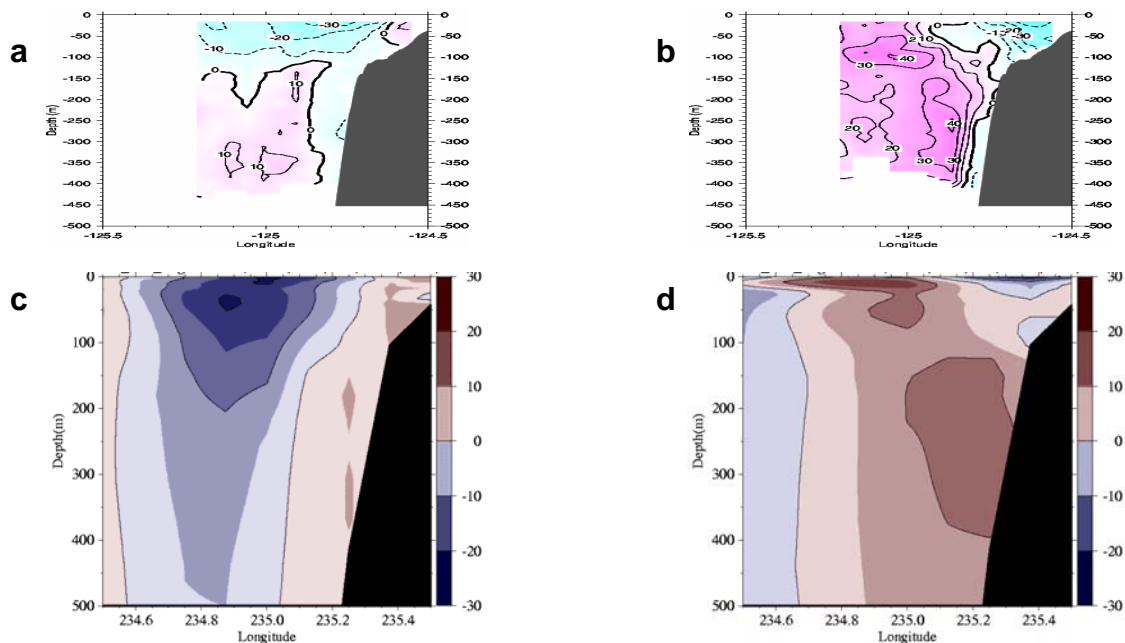


Fig. 94 – Comparisons of northward velocity (cm/s) through a sections near the Rogue River, Oregon. Sections from (a,b) ADCP surveys conducted as a part of the Northeast Pacific Long Term Observation Program and (c,d) snapshots from the assimilative  $1/8^\circ$  global NCOM. The (a) 15-16 Apr. 2000 observations and (c) 16 Apr. 2000 NCOM snapshot both show northward flow in the upper 100m but opposite flow at depth. Agreement is close between the (b) 13-14 July 2002 survey and (d) 14 July 2002 model results, although the model structure shows less detail and lower extrema.

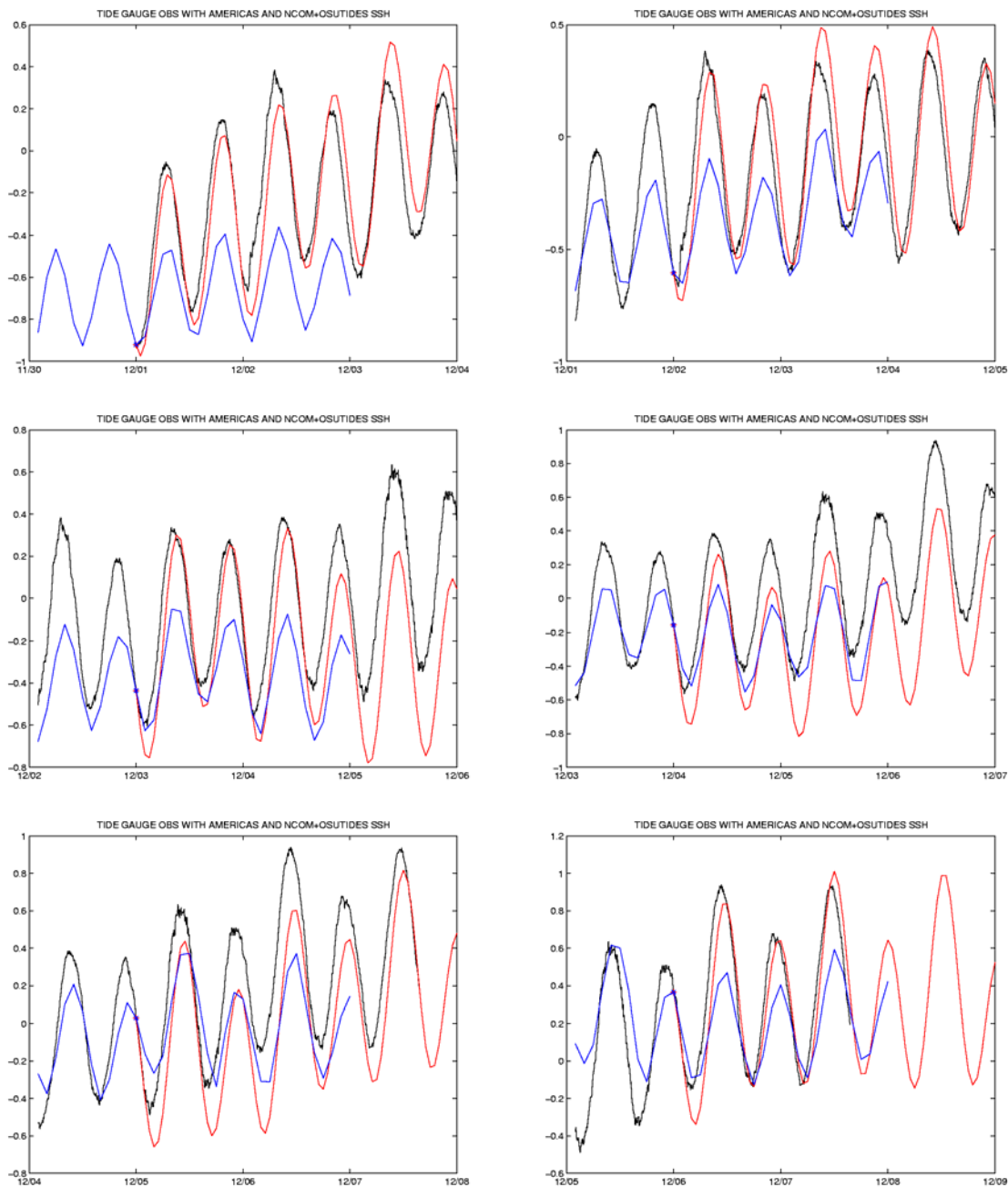


Fig. 95 – Sea surface elevation time series at Duck, NC from SWAFS Americas grid (blue), global NCOM with the OSU tide model (red), and observed (black), for run days 20031201 to 20031206. The time series of observed levels is de-meant. NCOM/OSU output (0 to 48 h) is referenced to the observed level at the beginning of the daily time series (red x). SWAFS output (-24 to 48h) is referenced to the observed level at the daily nowcast time (blue +).

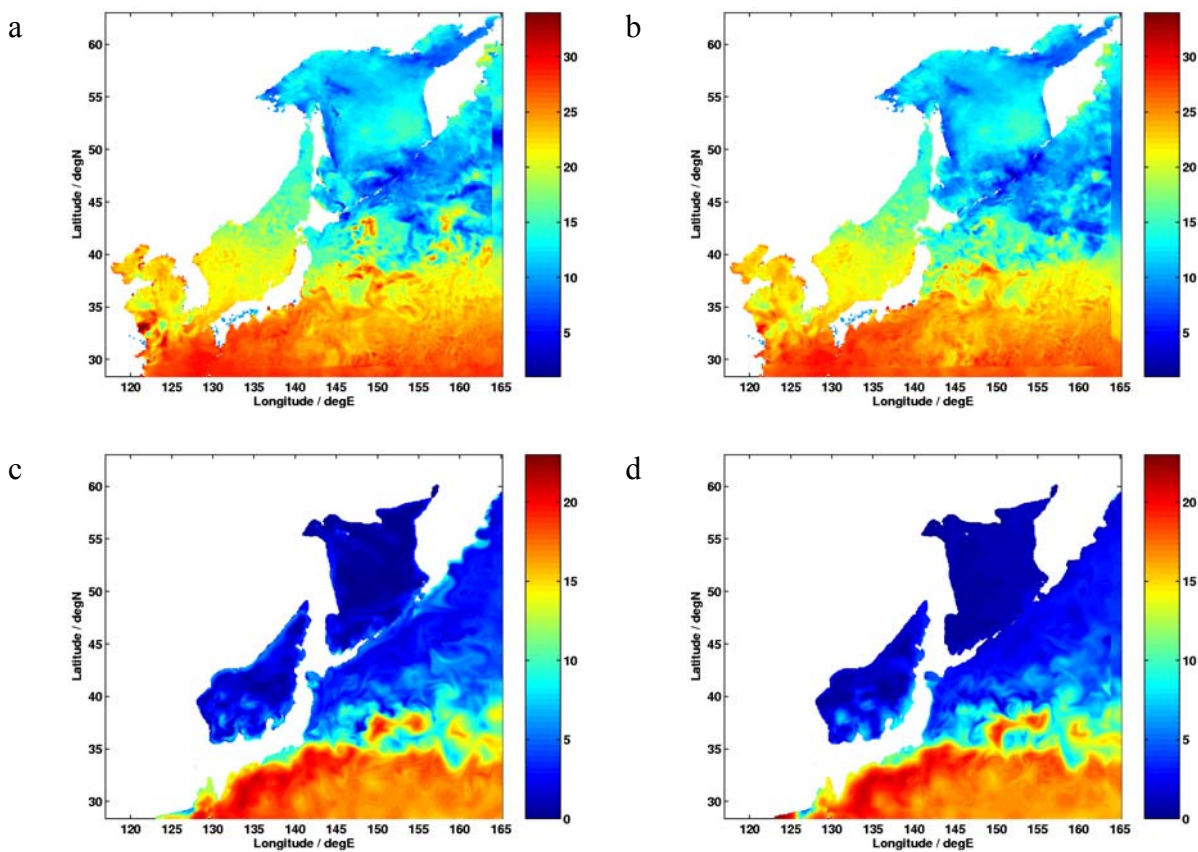


Fig. 96 – Temperature ( $^{\circ}\text{C}$ ) from SWAFS pacnest restart files valid 19 July 2003 using SWAFS northworld boundary conditions (a,c) and NCOM/OSU boundary conditions (b,d) at the surface (a,b) and 200m (c,d).

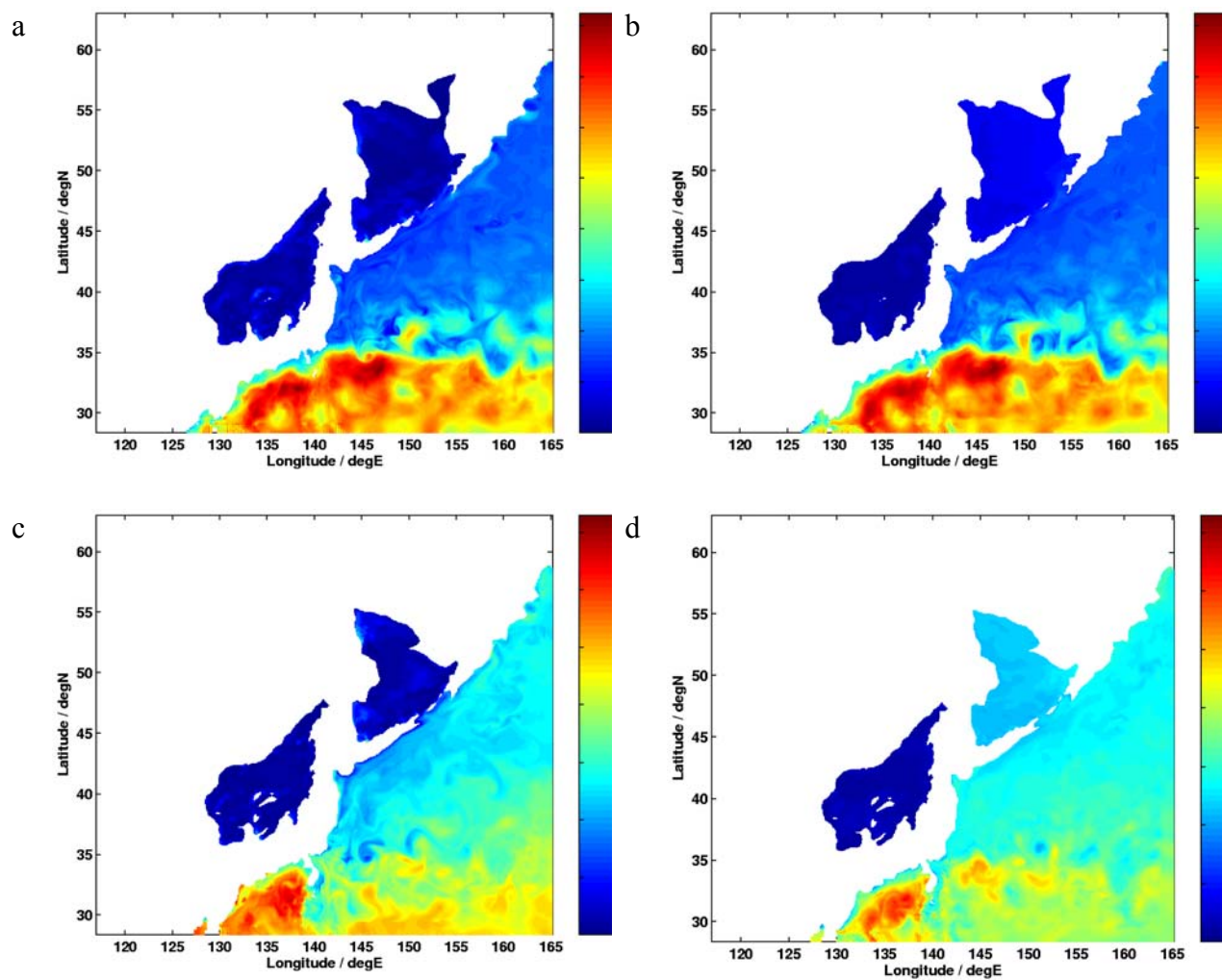


Fig. 97 – Temperature ( $^{\circ}\text{C}$ ) from SWAFS pacnest restart files valid 19 July 2003 using SWAFS northworld boundary conditions (a,c) and NCOM/OSU boundary conditions (b,d) at 500m (a,b) and 1000m (c,d).

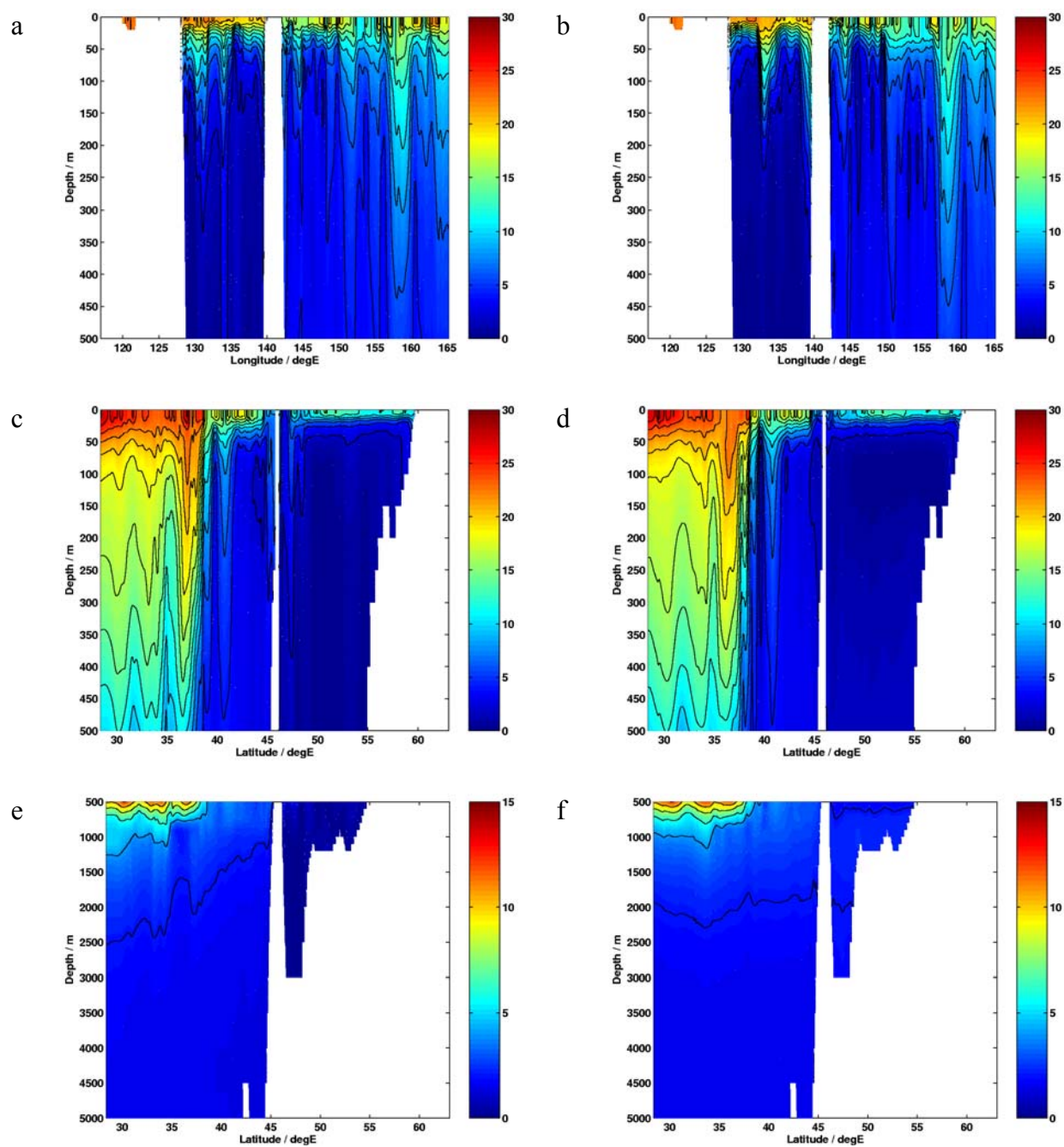


Fig. 98 –Temperature ( $^{\circ}\text{C}$ ) from SWAFS pacnest restart files valid 19 July 2003 using SWAFS northworld boundary conditions (a,c,e) and NCOM/OSU boundary conditions (b,d,f) from the surface to 500m along 40N (a,b) and 150E (c,d), and from 500m to 5000m along 150E (e,f).

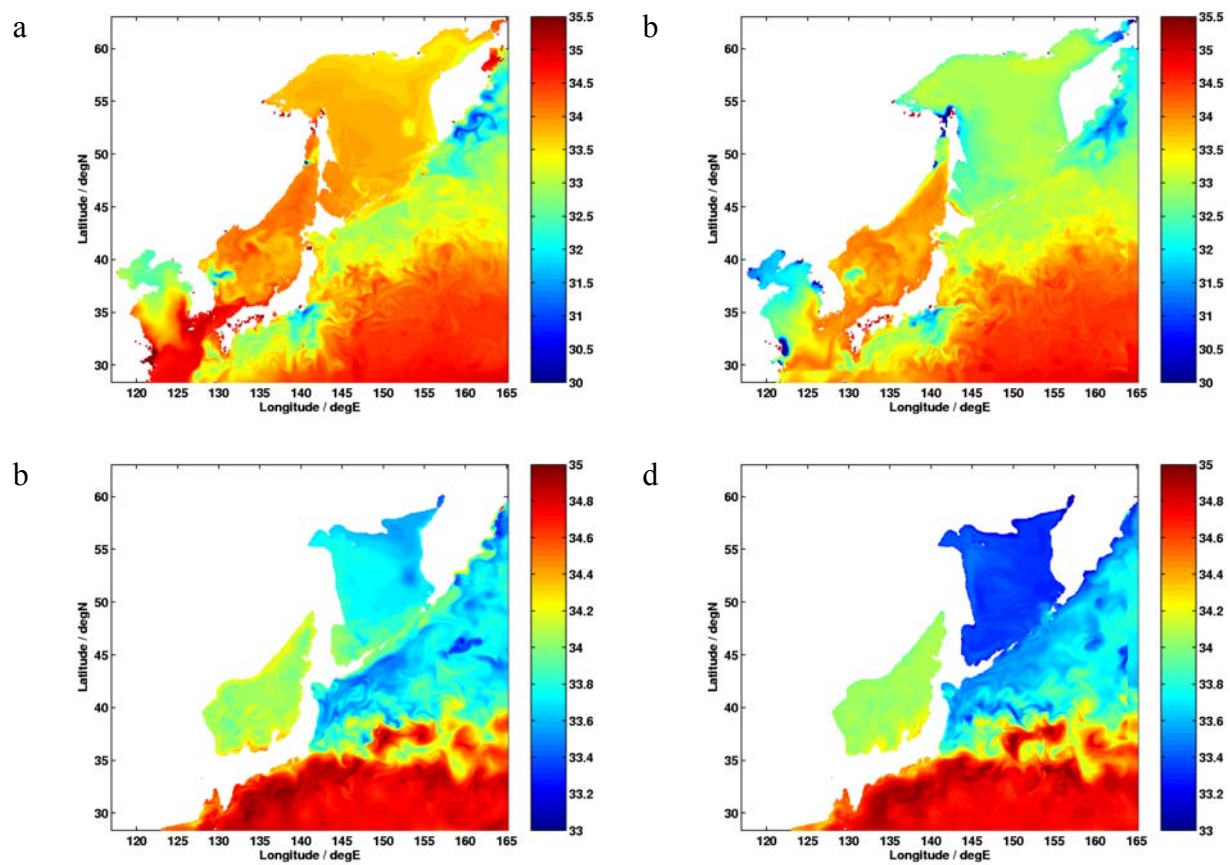


Fig. 99 – Salinity from SWAFS pacnest restart files valid 19 July 2003 using SWAFS northworld boundary conditions (a,c) and NCOM/OSU boundary conditions (b,d) at the surface (a,b) and 200m (c,d).

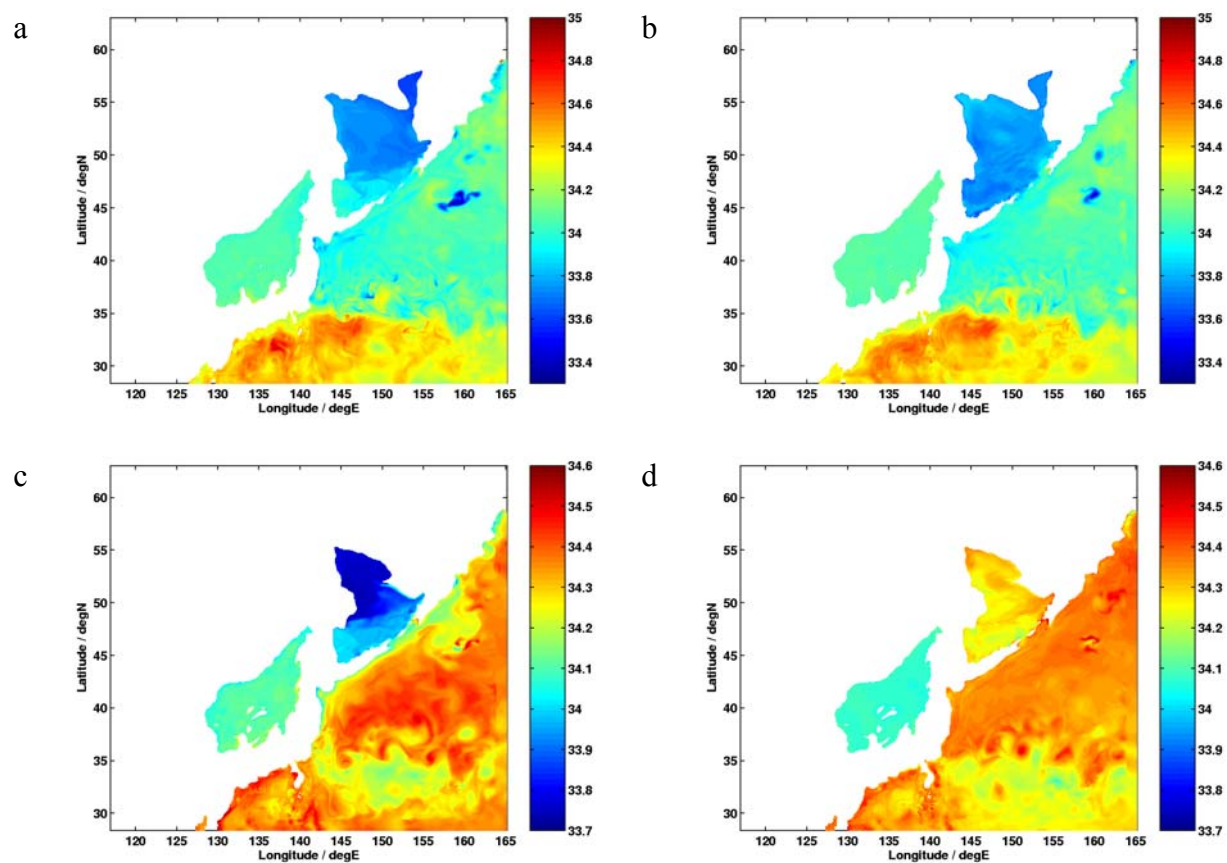


Fig. 100 - Salinity from SWAFS pacnest restart files valid 19 July 2003 using SWAFS northworld boundary conditions (a,c) and NCOM/OSU boundary conditions (b,d) at 500m (a,b) and 1000m (c,d).

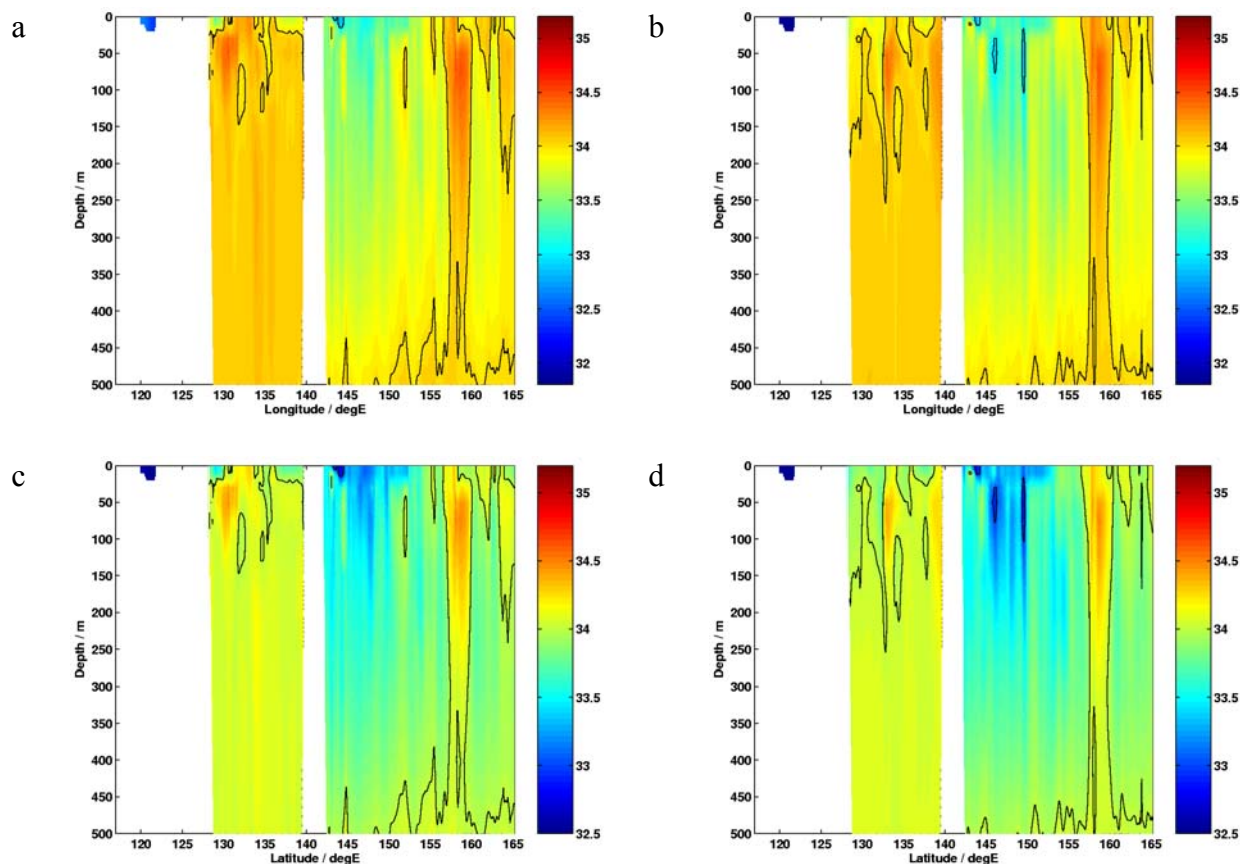


Fig. 101 Salinity from SWAFS pacnest restart files valid 19 July 2003 using SWAFS northworld boundary conditions (a,c) and NCOM/OSU boundary conditions (b,d) from the surface to 500m along 40N (a,b) and 150E (c,d).

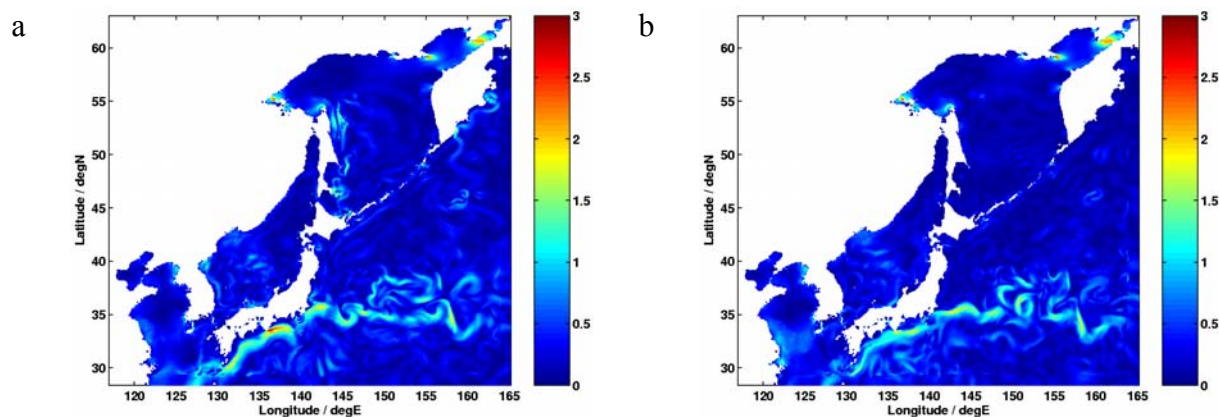


Fig. 102 – Surface speed (m/s) from the SWAFS pacnest restart files valid 19 July 2003 from the run using SWAFS northworld boundary conditions (a) and NCOM/OSU boundary conditions (b).

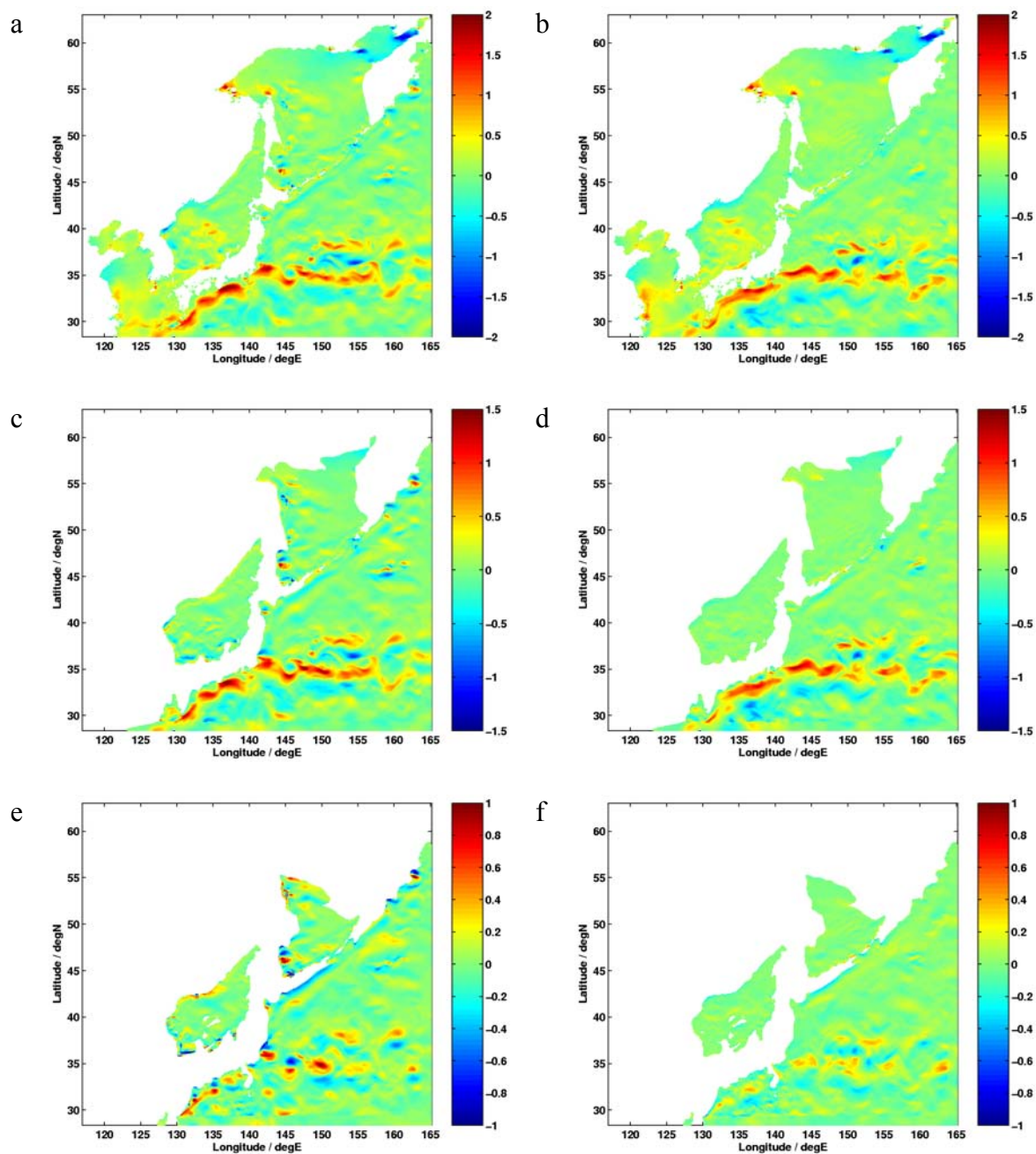


Fig. 103 –Zonal velocity (m/s) from the SWAFS pacnest restart files valid 19 July 2003 from the run using SWAFS northworld boundary conditions (a,c,e) and NCOM/OSU boundary conditions (b,d,f) at the surface (a,b), 200m (c,d), and 1000m (e,f).

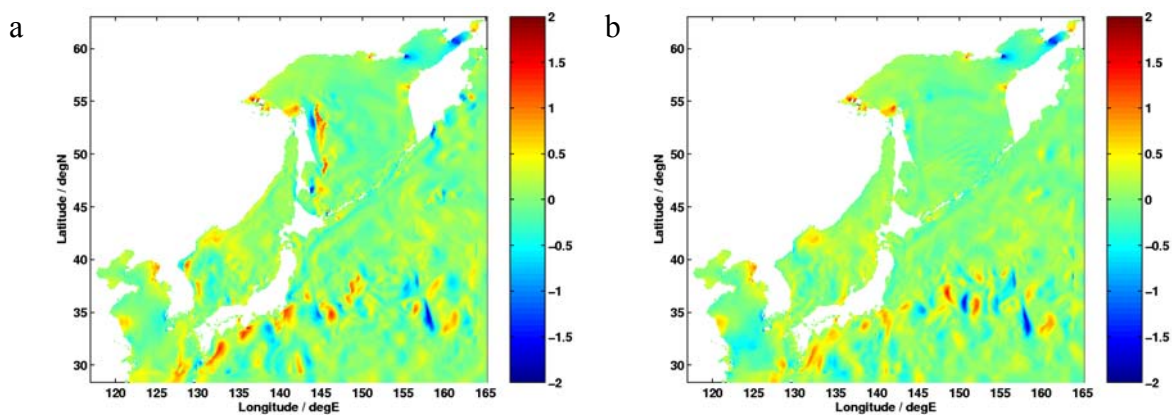


Fig. 104 – Meridional surface velocity (m/s) from the SWAFS pacnest restart files valid 19 July 2003 from the run using SWAFS northworld boundary conditions (a) and NCOM/OSU boundary conditions (b).

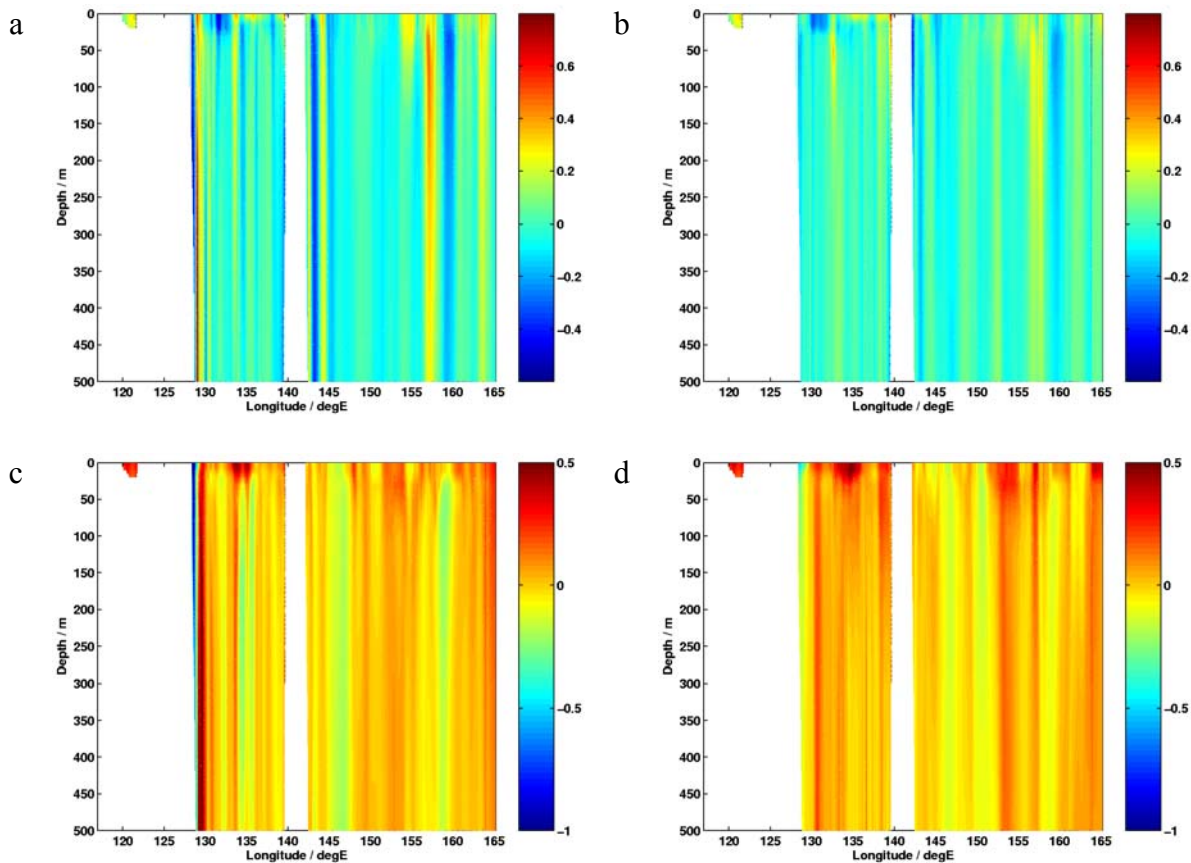


Fig. 105 – Velocity sections (m/s) along 40 N from the SWAFS pacnest restart files valid 19 July 2003 from the run using SWAFS northworld boundary conditions (a,c) and NCOM/OSU boundary conditions (b,d). The meridional (a,b) and zonal (c,d) velocities are shown separately.

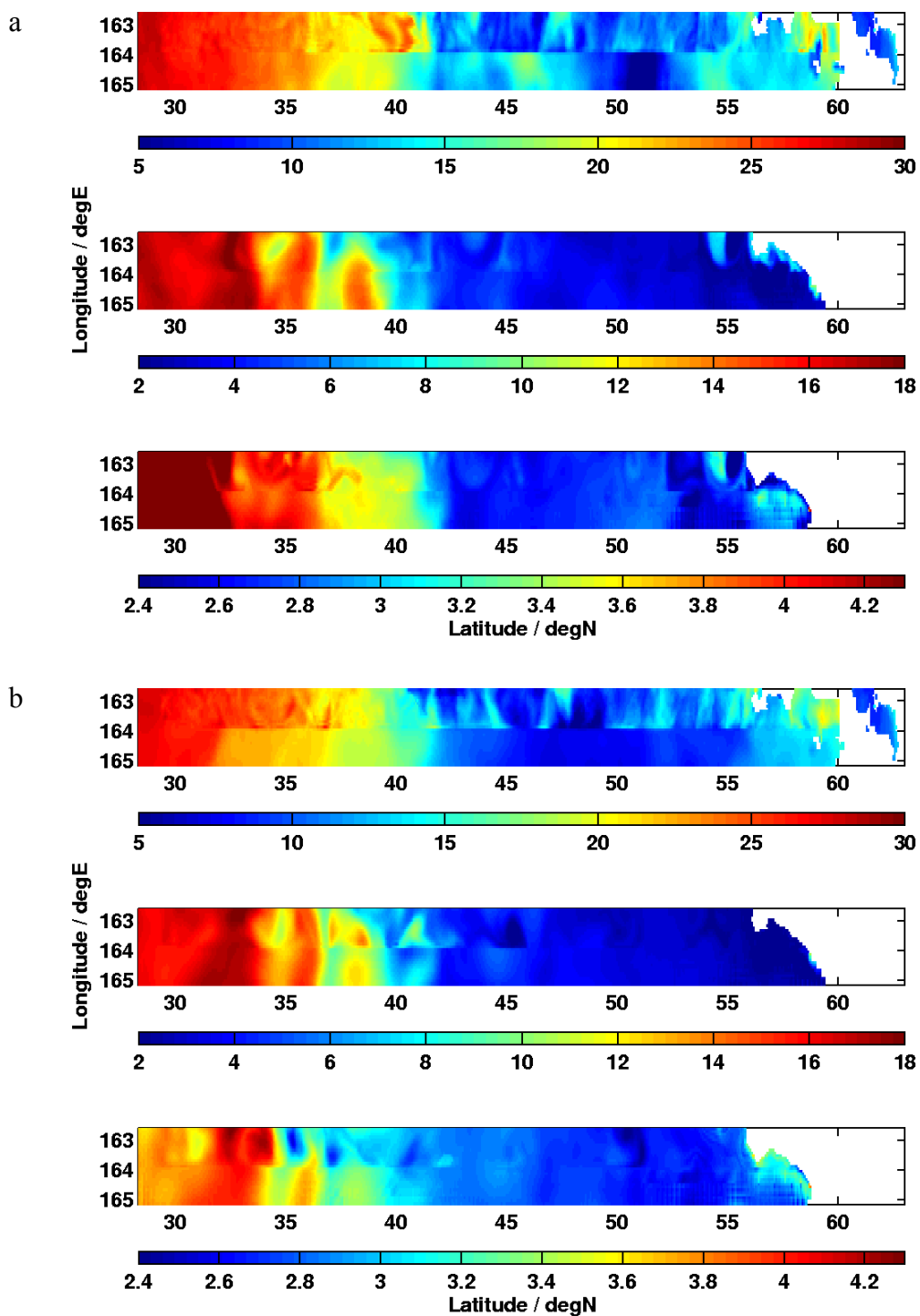


Fig. 106 – Temperature (°C) along the eastern boundary of the SWAFS pacnest domain restart files valid 17 July 2003 using the northworld (a) and NCOM/OSU (b) boundary conditions, each at 0 (top), 200 (middle), 1000 (bottom) m.

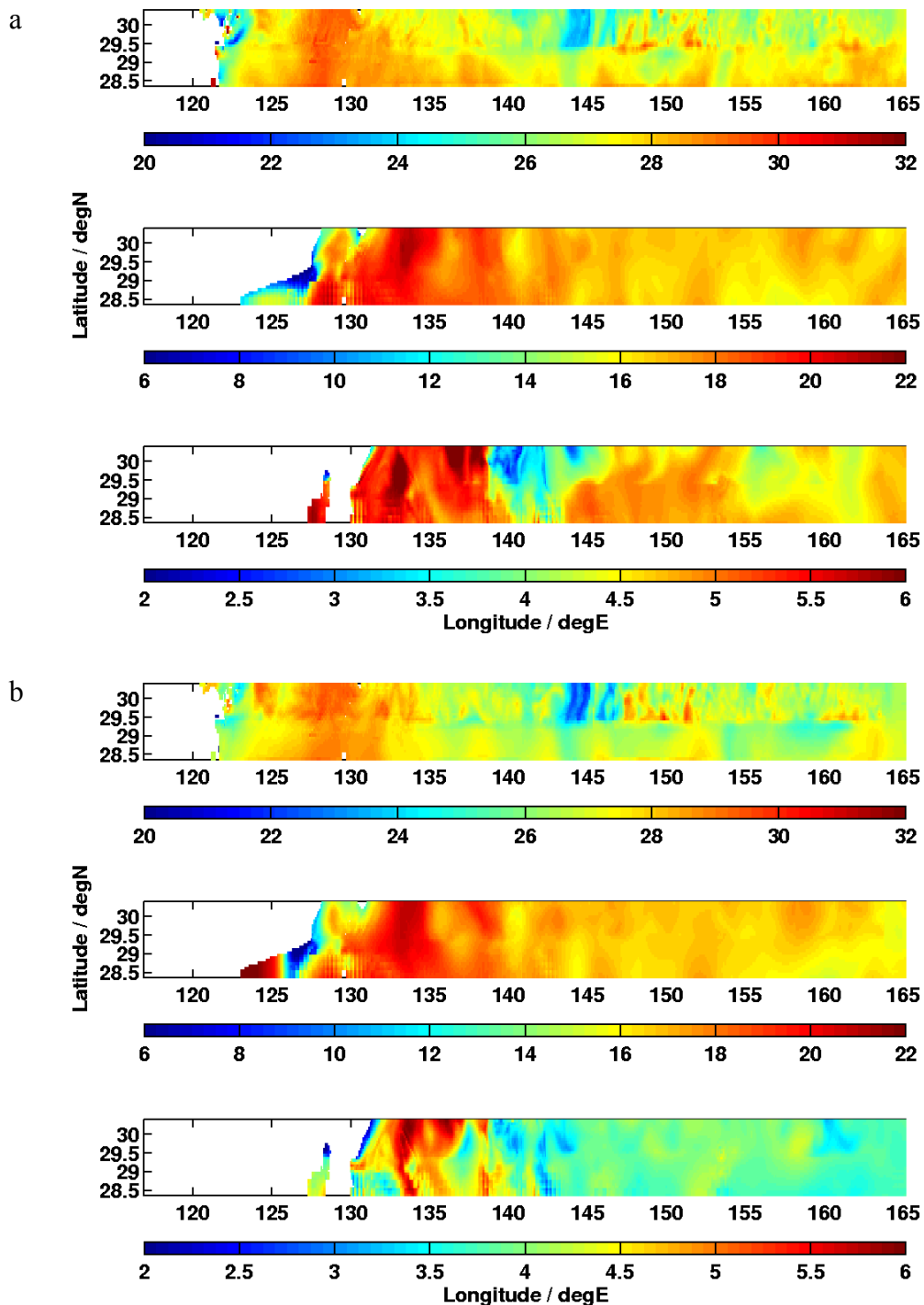


Fig. 107 – Temperature ( $^{\circ}\text{C}$ ) along the southern boundary of the SWAFS pacnest domain restart files valid 17 July 2003 using the northworld (a) and NCOM/OSU (b) boundary conditions, each at 0 (top), 200 (middle), 1000 (bottom) m.

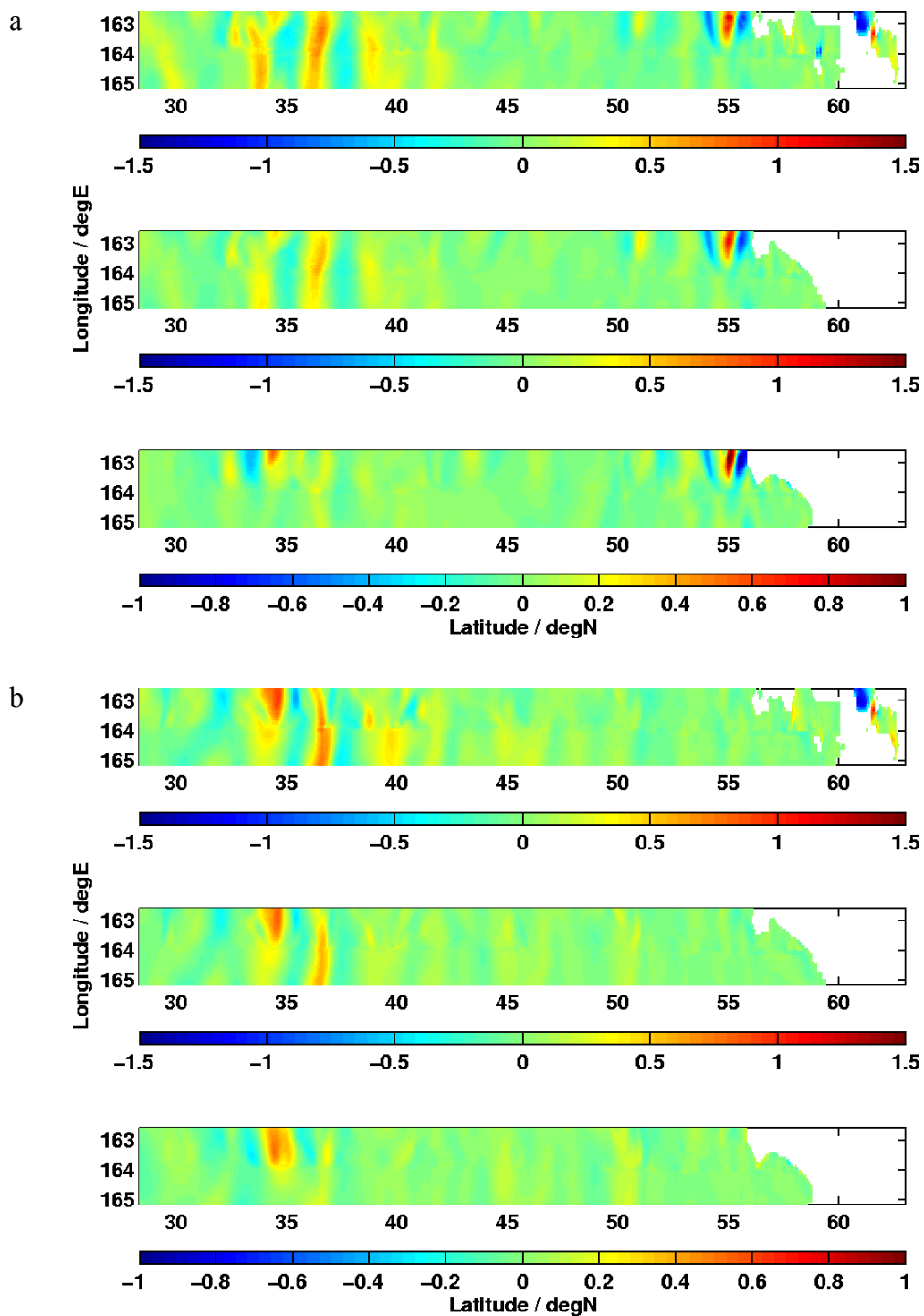


Fig. 108 – Zonal velocity (m/s) along the eastern boundary of the SWAFS pacnest domain restart files valid 17 July 2003 using the northworld (a) and NCOM/OSU (b) boundary conditions, each at 0 (top), 200 (middle), 1000 (bottom) m.

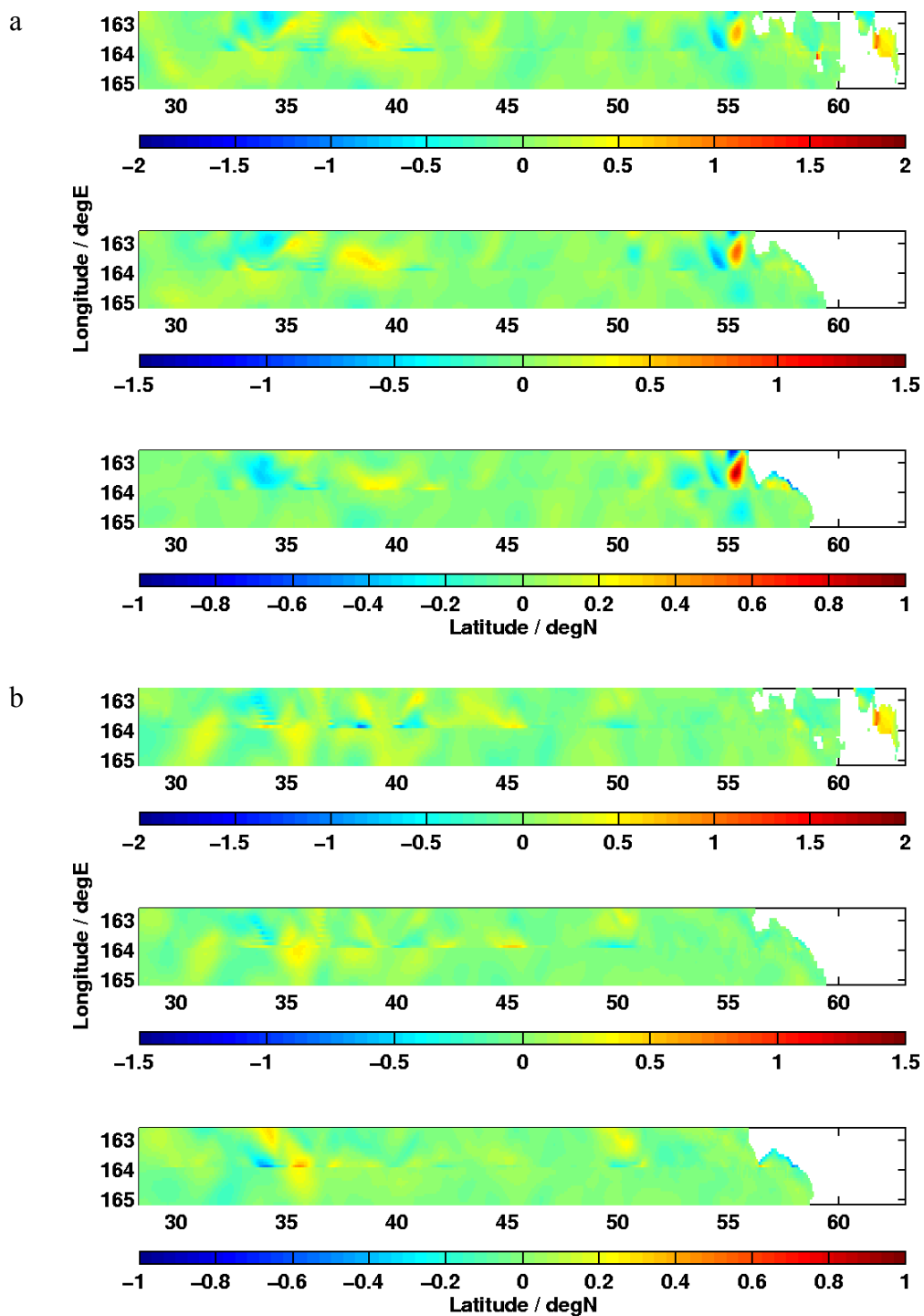


Fig. 109 – Meridional velocity (m/s) along the eastern boundary of the SWAFS pacnest domain restart files valid 17 July 2003 using the northworld (a) and NCOM/OSU (b) boundary conditions, each at 0 (top), 200 (middle), 1000 (bottom) m.

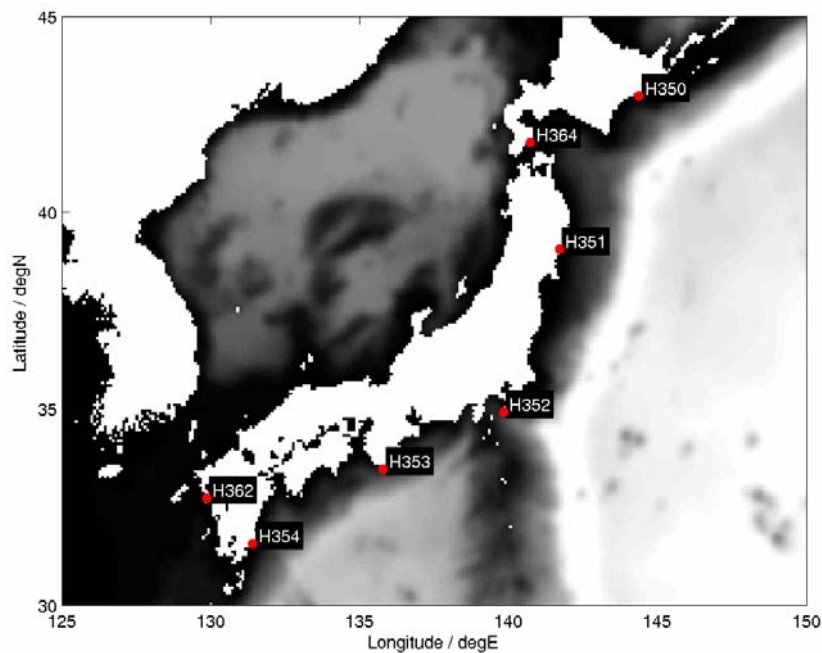


Fig. 110 Locations of the tide gauge stations used for NCOM/OSU validation. The ‘H’ in each id refers to the hourly data contained in the file, and the number is the GLOSS database station identifier.

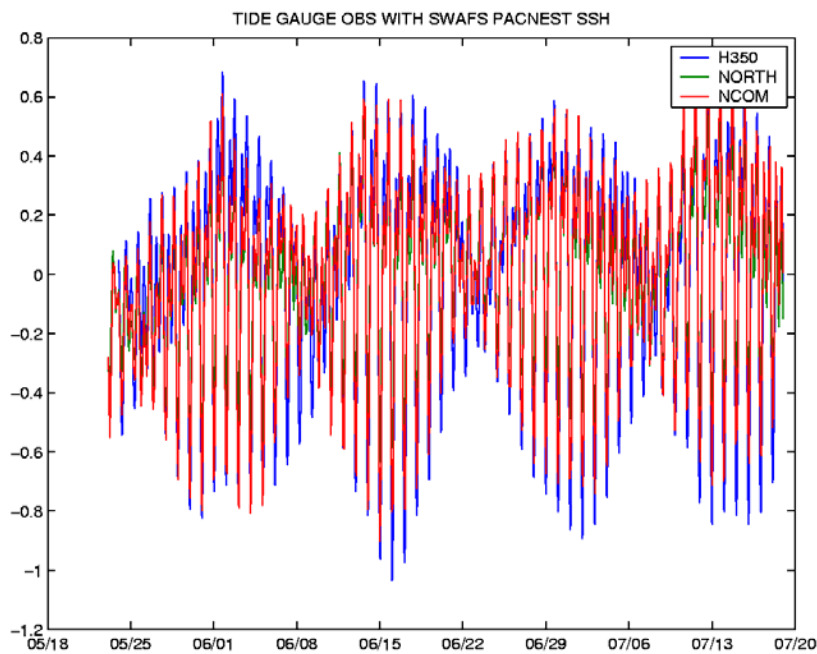


Fig. 111 – Example of the water level time series from station 350 (blue), with the corresponding time series from the SWAFS pacnest runs using SWAFS northworld boundary conditions (green) and NCOM/OSU boundary conditions (red), for the full time series 24 May to 19 July 2003. The time series have the means individually removed before plotting.

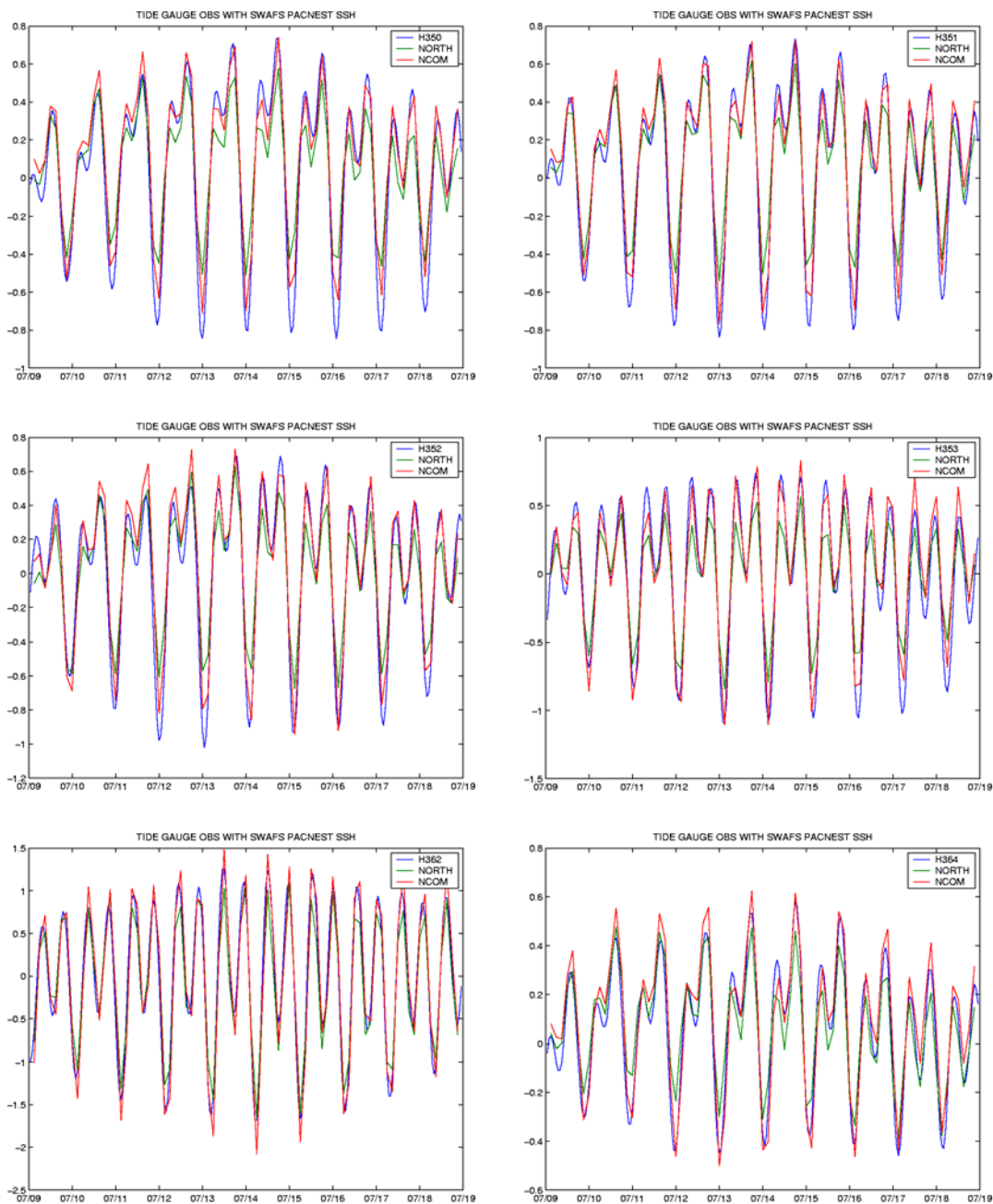


Fig. 112 – Water level time series from the six GLOSS stations used for this validation. For each station (a-f), the observed water level (blue), SWAFS pacnest run using SWAFS northworld boundary conditions (green), and SWAFS pacnest run using NCOM/OSU boundary conditions (red), are show for the last 10 d of the time series. The time series have the means individually removed before plotting.

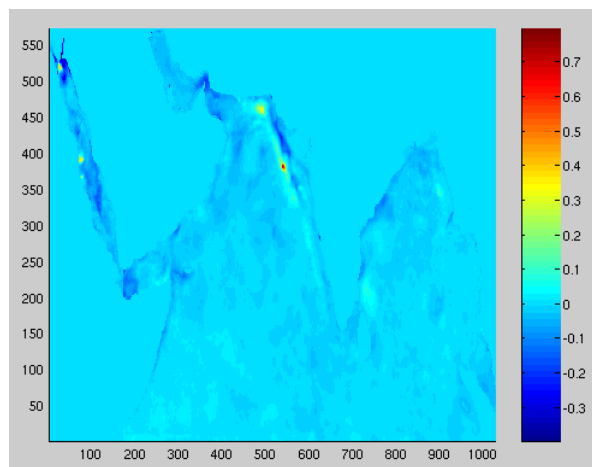


Fig. 113 – The heat flux adjustment parameter for the operational SWAFS ionest run 08 Dec 2003.

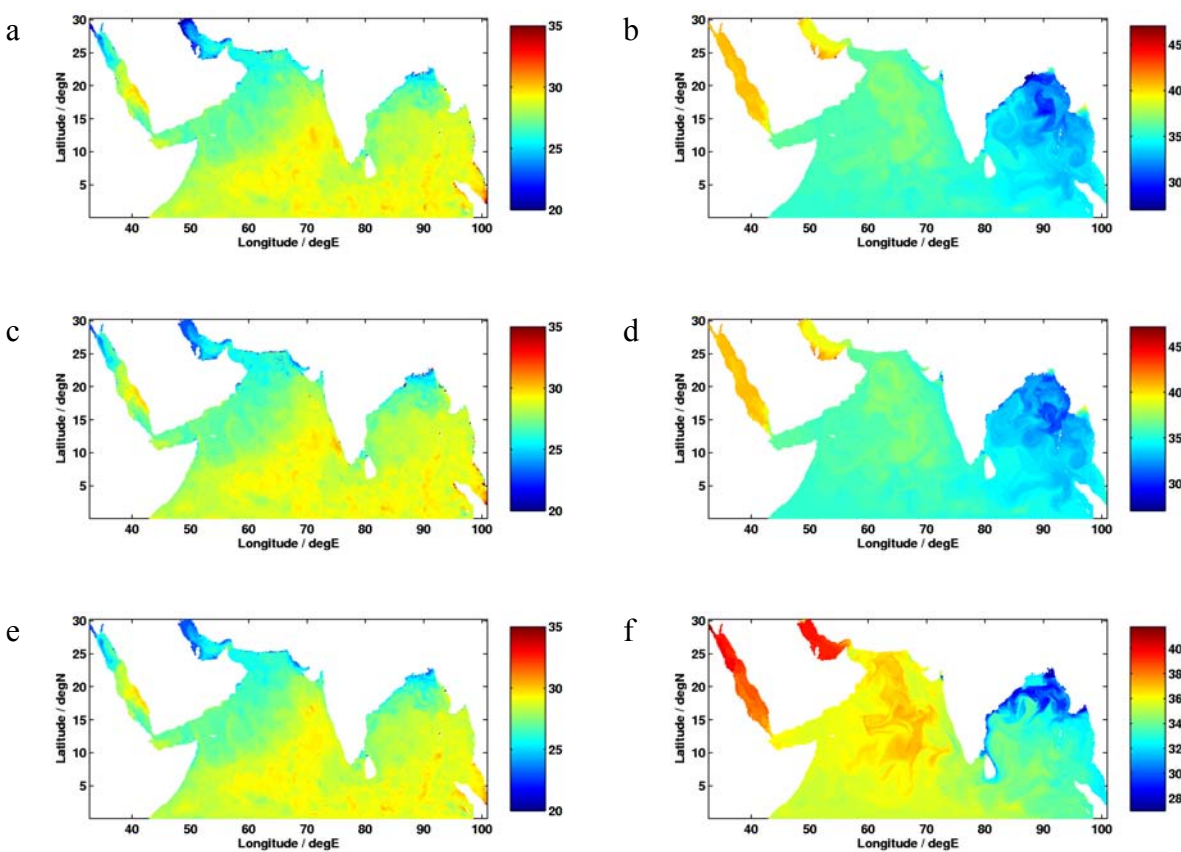


Fig. 114 – Surface temperature ( $^{\circ}\text{C}$ , a,c,e) and salinity (b,d,f) from the SWAFS ionest domain restart files valid 07 Dec 2003 from the SWAFS operational run (a,b), SWAFS test run with northworld boundary conditions (c,d), and test run with NCOM/OSU boundary conditions (e,f).

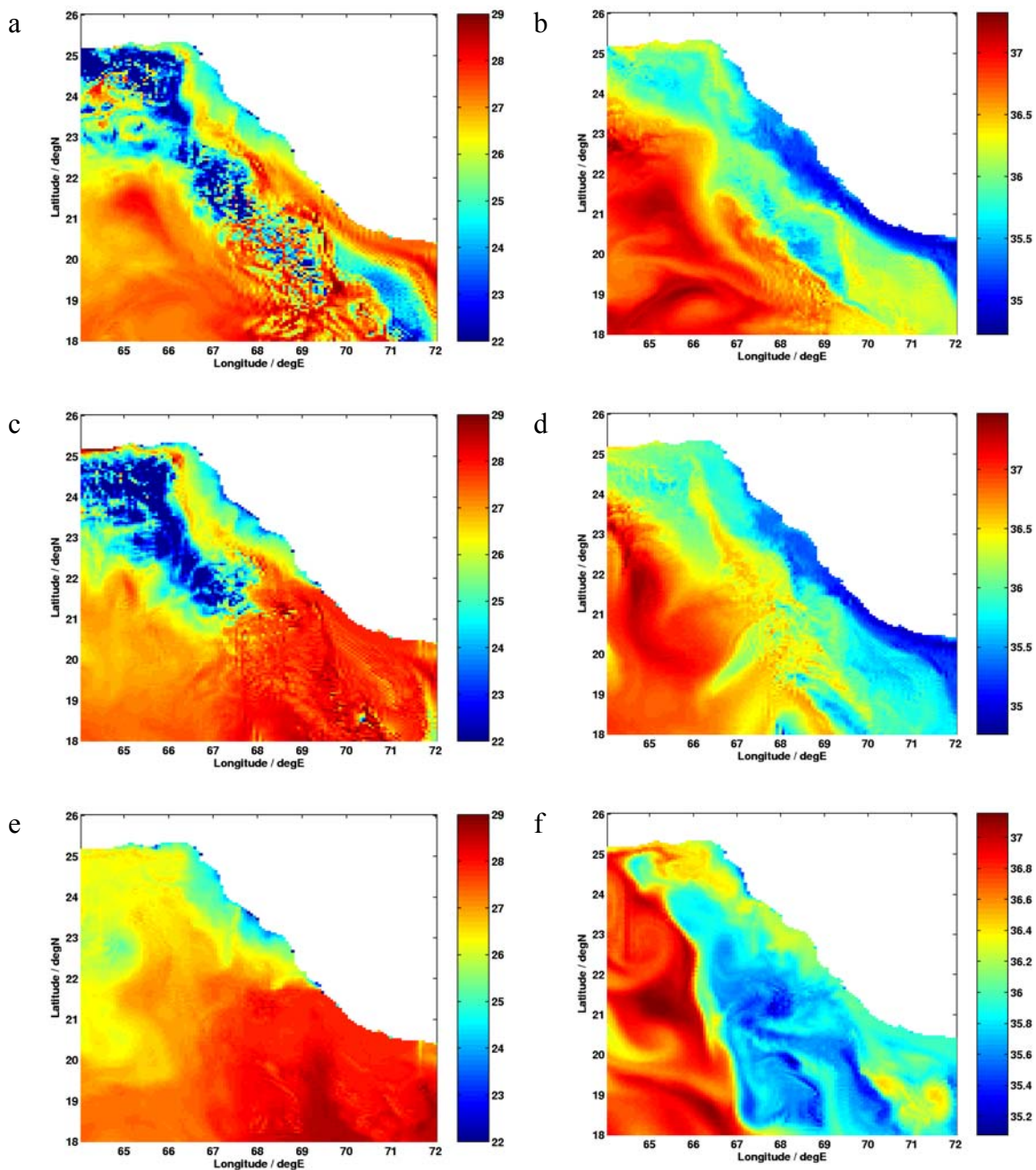


Fig. 115 – Temperature ( $^{\circ}\text{C}$ , a,c,e) and salinity (b,d,f) at 20m from the ionest restart files valid 07 Dec 2003 from the SWAFS operational run (a,b), SWAFS test run with northworld boundary conditions (c,d), and test run with NCOM/OSU boundary conditions (e,f).

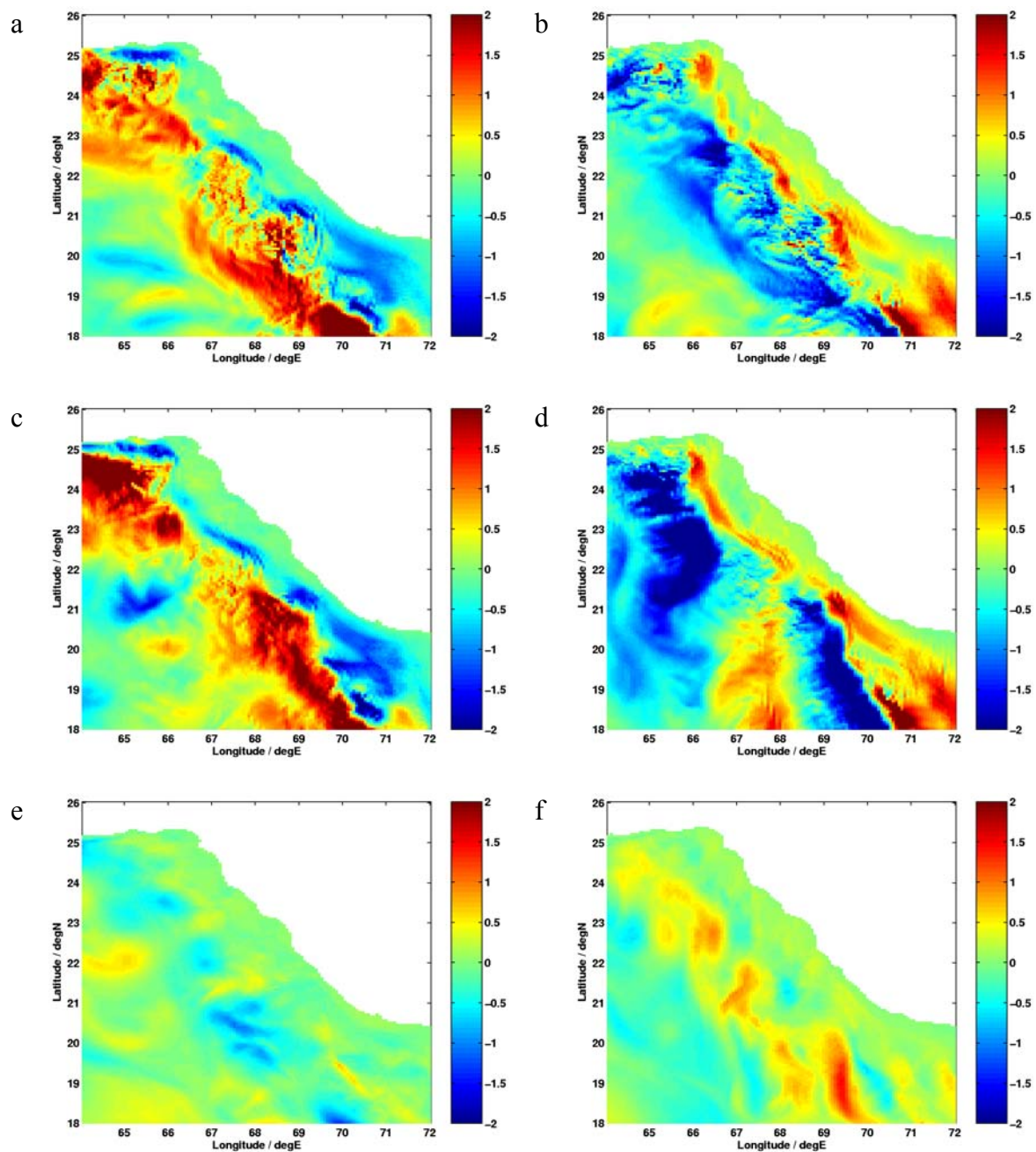


Fig. 116 – Zonal (a,c,e) and meridional (b,d,f) velocity (m/s) at 20m from the ionest restart files valid 07 Dec 2003 from the SWAFS operational run (a,b), SWAFS test run with northworld boundary conditions (c,d), and test run with NCOM/OSU boundary conditions (e,f).

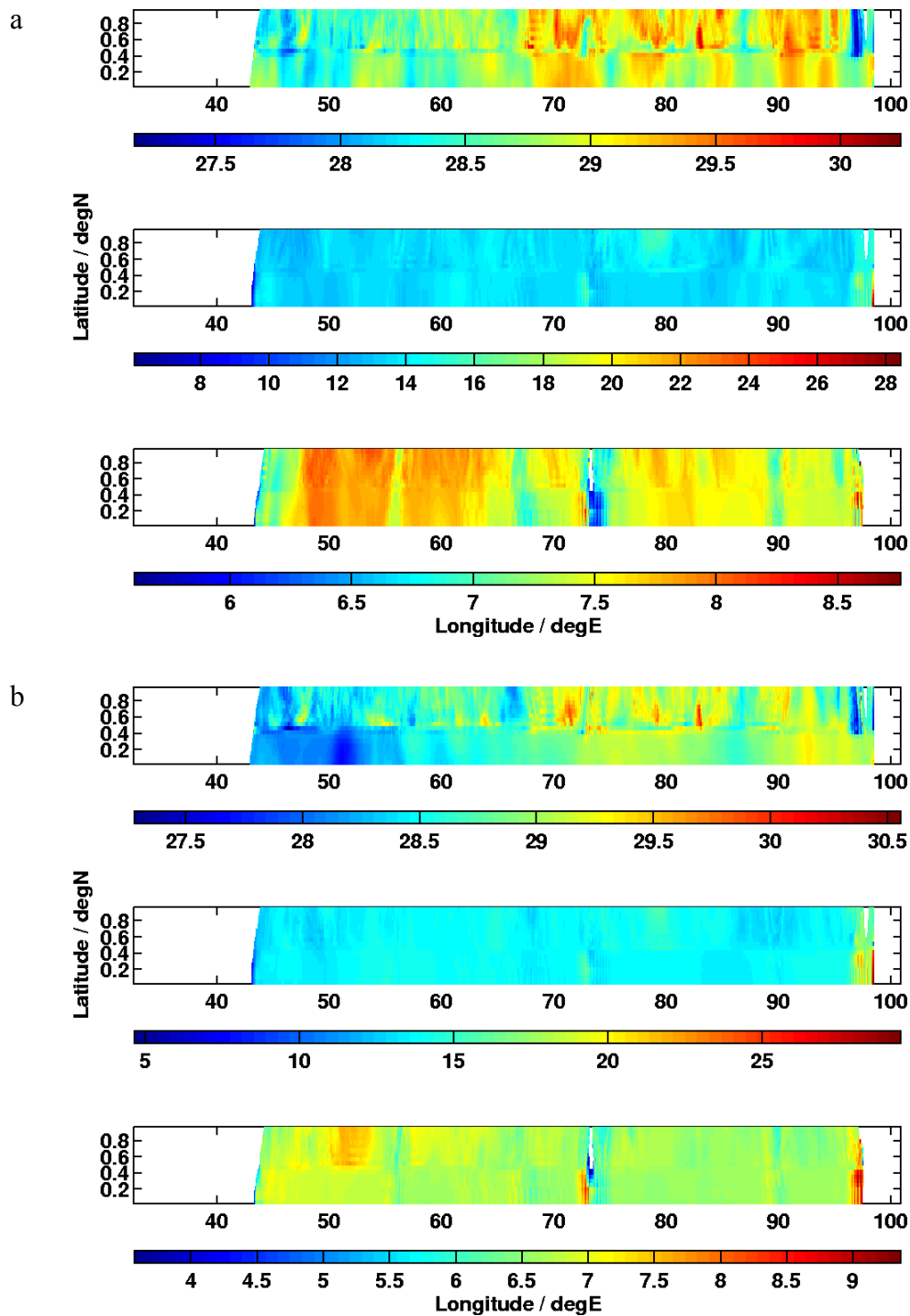


Fig. 117 – Temperature (°C) along the southern boundary of the SWAFS ionest domain restart files valid 07 Dec 2003 using the northworld (a) and NCOM/OSU (b) boundary conditions, each at 0 (top), 200 (middle), 1000 (bottom) m.

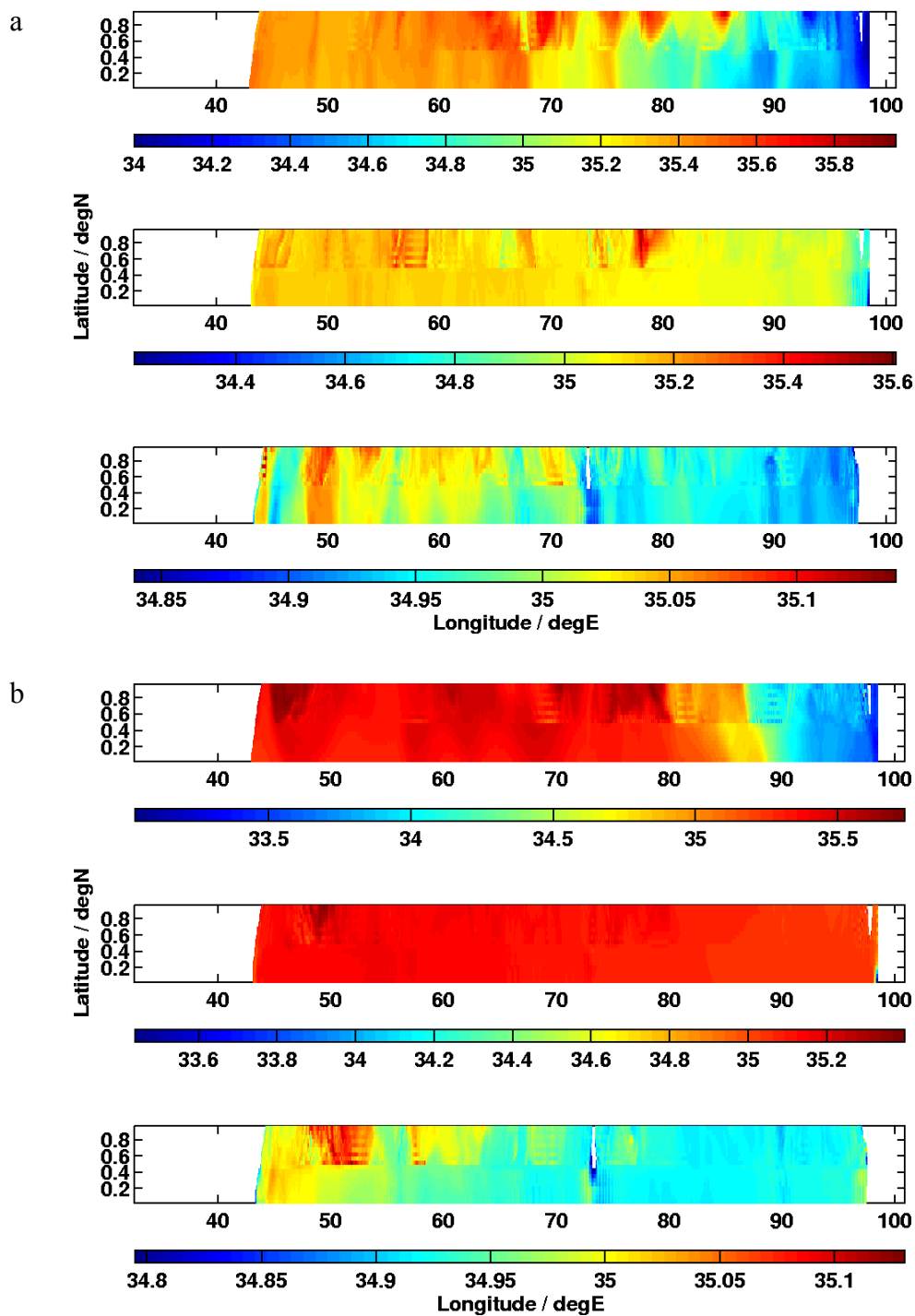


Fig. 118 – Salinity along the southern boundary of the SWAFS ionest domain restart files valid 07 Dec 2003 using the northworld (a) and NCOM/OSU (b) boundary conditions, each at 0 (top), 200 (middle), 1000 (bottom) m.

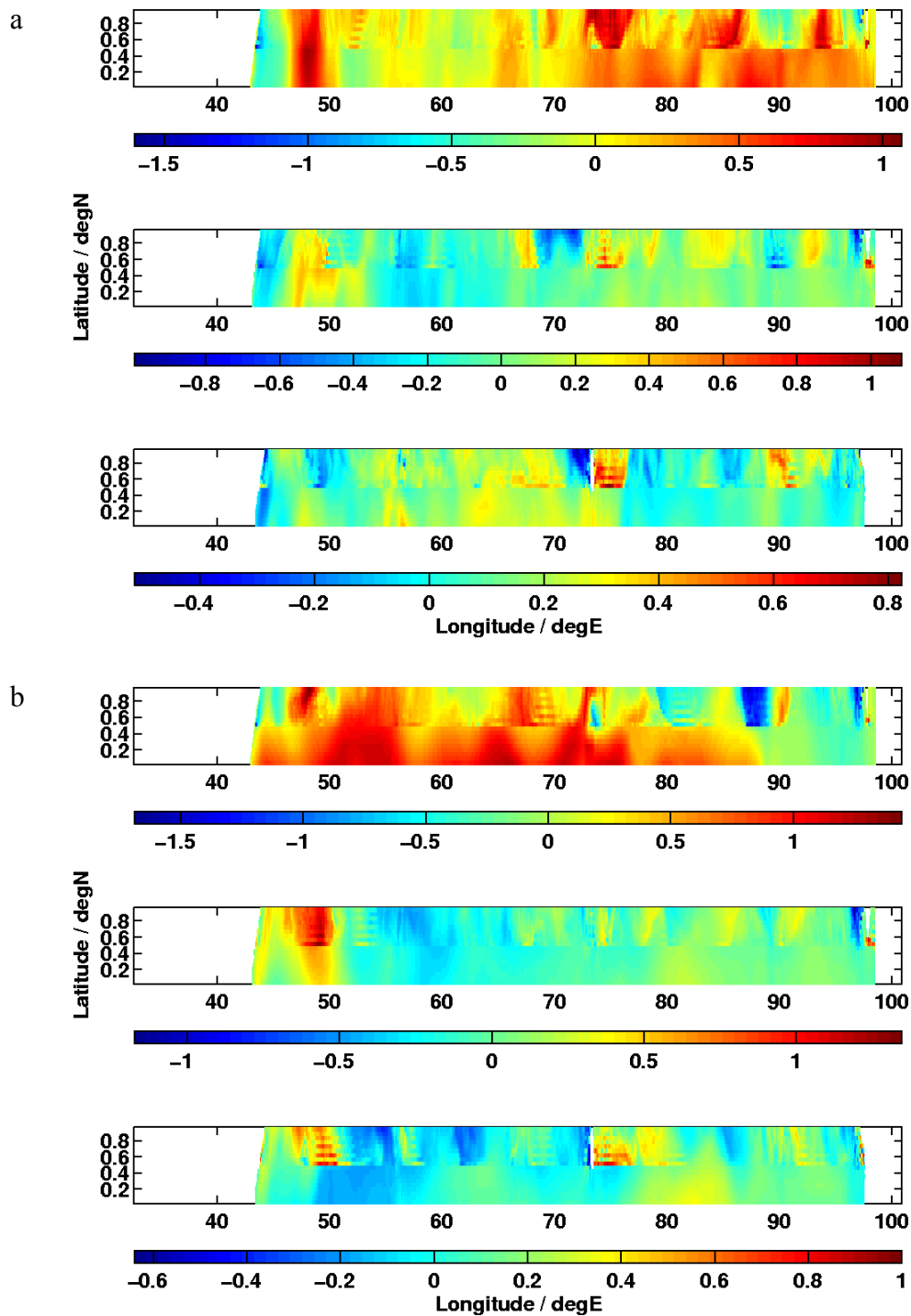


Fig. 119 – Zonal velocity (m/s) along the southern boundary of the SWAFS ionest domain restart files valid 07 Dec 2003 using the northworld (a) and NCOM/OSU (b) boundary conditions, each at 0 (top), 200 (middle), 1000 (bottom) m.

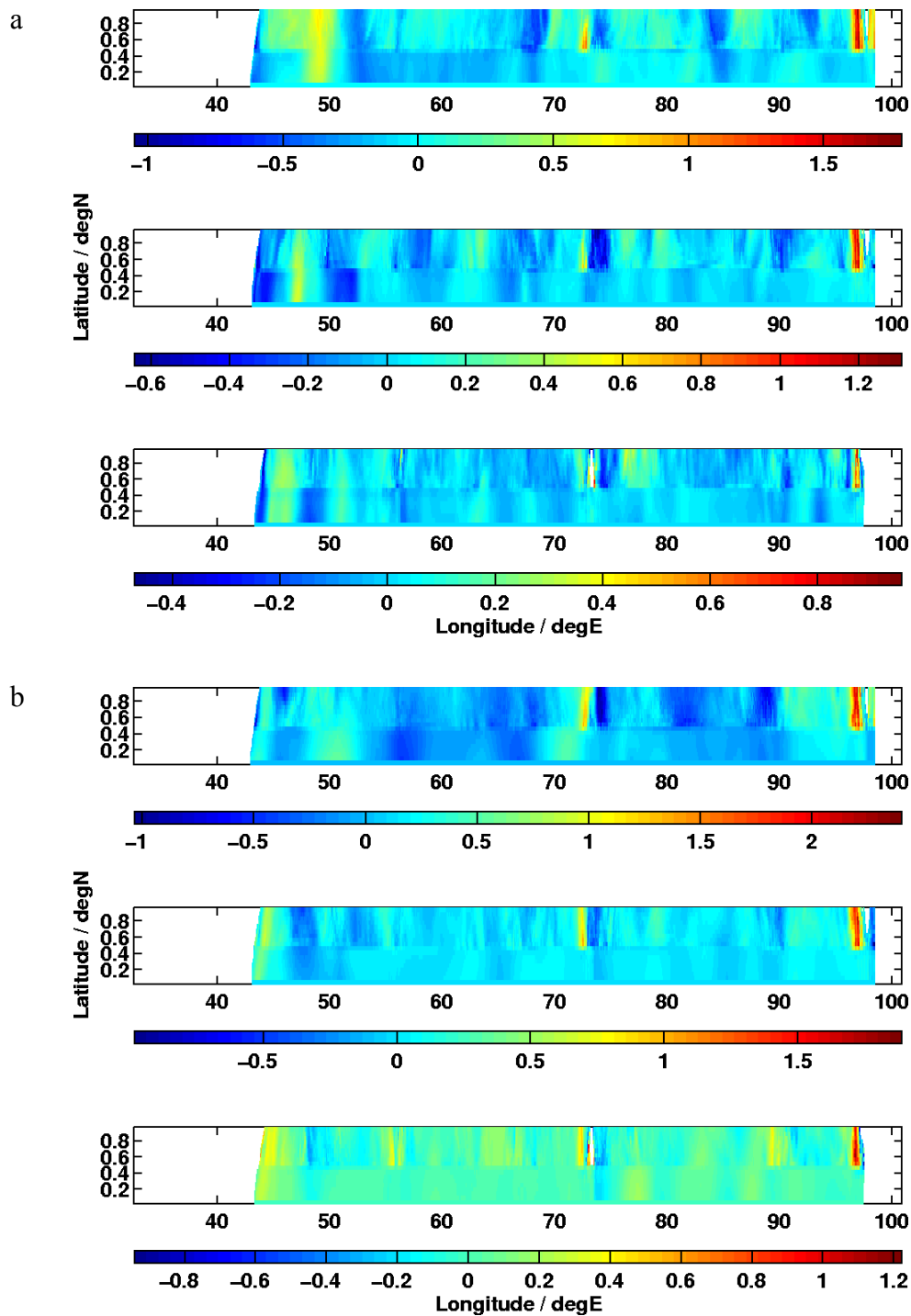


Fig. 120 – Meridional velocity (m/s) along the southern boundary of the SWAFS ionest domain restart files valid 07 Dec 2003 using the northworld (a) and NCOM/OSU (b) boundary conditions, each at 0 (top), 200 (middle), 1000 (bottom) m.

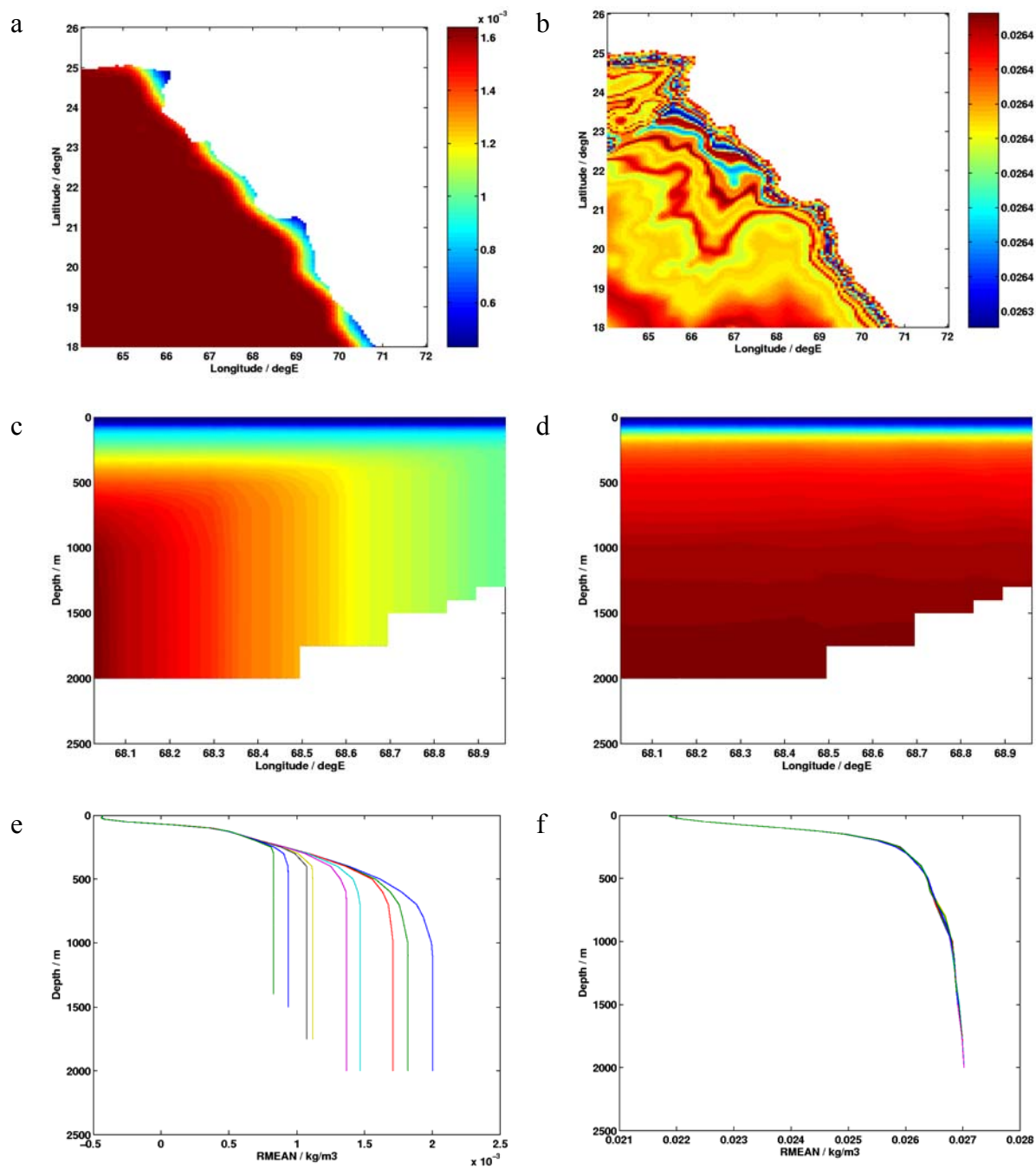


Fig. 121 – The background or reference density (kg/m<sup>3</sup>) in the east Arabian Sea from the SWAFS ionest grid (“unit 40”) files used for the test runs with the northworld (a,c,e) and NCOM/OSU (b,d,f) boundary conditions. The reference density was interpolated to uniform z levels from the model  $\sigma$  grid. The density on 500 m (a,b), along 21° N (c,d), and in profiles from 68.1-68.9° E (e,f) all display the horizontal variation in the operational file.

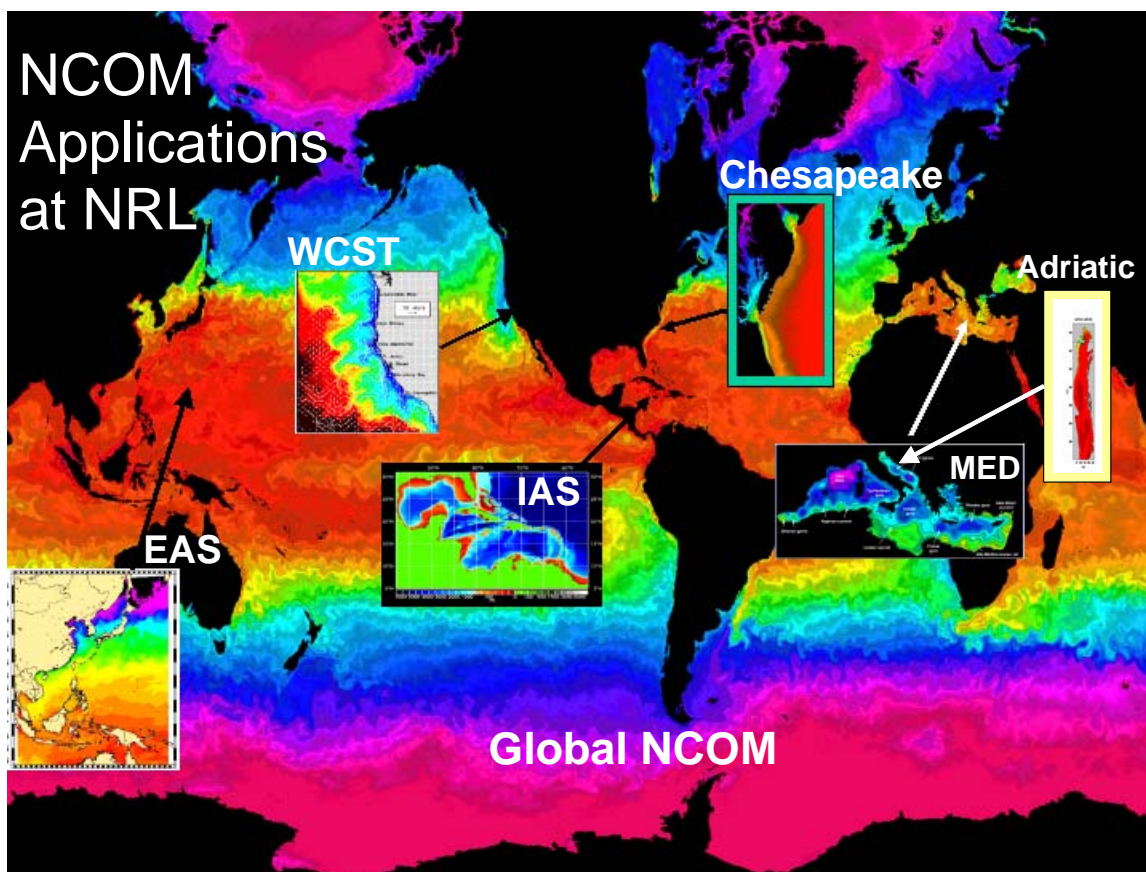


Fig. 122 – An example of some of the applications of NCOM at NRL. The EAS, IAS and WCST domains use boundary and/or initial condition information from global NCOM.

gauge location	NCOM simulation	RMS (cm)	$\sigma_x$ (cm)	$\sigma_y$ (cm)	R	SS	n (days)
27°N,142°E	free-run	9.36	11.57	4.70	0.63	0.34	365
	assimilative	5.65	11.57	8.30	0.89	0.76	365
39°N,074°W	free-run	9.95	13.22	15.85	0.78	0.43	365
	assimilative	10.04	13.22	16.05	0.78	0.42	365
49°N,126°W	free-run	8.61	16.00	9.17	0.91	0.71	365
	assimilative	9.40	16.00	8.29	0.89	0.65	365
12°S,097°E	free-run	9.38	11.54	12.01	0.68	0.34	365
	assimilative	4.99	11.54	8.62	0.92	0.81	365
70°N,149°W	free-run	11.06	15.95	19.29	0.82	0.52	365
	assimilative	10.92	15.95	18.77	0.81	0.53	365
01°S,090°W	free-run	5.99	11.17	6.22	0.92	0.71	365
	assimilative	4.37	11.17	7.68	0.96	0.85	365

Table 1 – Statistical verification of SSH between the JASL tide gauges and free--running and assimilative 1/8°NCOM simulations at a few tide gauge locations in 1998. The results are based on daily averages of SSH time series. Note that n is the number of days over which the statistics were calculated. An inverse barometer correction was applied to SSH time series from tide gauges. Standard deviations of SSH time series from the tide gauge and NCOM are denoted as  $\sigma_x$  and  $\sigma_y$ , respectively.

JASL (x) vs global NCOM (y): daily avg.							
Year	global NCOM simulation	RMS (cm)	$\sigma_x$ (cm)	$\sigma_y$ (cm)	R	SS	# of buoys
1998	free-run	6.33	8.92	6.71	0.73	0.47	189
	assimilative	6.25	8.92	6.79	0.76	0.51	189
1999	free-run	6.01	7.97	6.27	0.68	0.39	181
	assimilative	5.38	7.97	6.33	0.75	0.50	181
2000	free-run	5.39	7.19	5.81	0.70	0.35	151
	assimilative	5.21	7.19	5.69	0.74	0.51	151
2001	free-run	6.64	9.42	6.58	0.72	0.50	91
	assimilative	6.32	9.42	6.38	0.77	0.53	91
1998-2001	free-run	5.98	7.98	6.28	0.72	0.45	612
	assimilative	5.77	7.98	6.22	0.76	0.51	612

JASL (x) vs global NCOM (y): 30-day avg.							
Year	global NCOM simulation	RMS (cm)	$\sigma_x$ (cm)	$\sigma_y$ (cm)	R	SS	# of buoys
1998	free-run	3.91	5.96	5.37	0.82	0.61	187
	assimilative	4.19	5.96	4.93	0.85	0.61	187
1999	free-run	4.03	5.34	4.56	0.80	0.56	177
	assimilative	3.12	5.34	4.61	0.85	0.62	177
2000	free-run	3.15	4.96	5.06	0.85	0.53	137
	assimilative	2.82	4.96	4.48	0.88	0.65	137
2001	free-run	3.78	5.69	4.89	0.88	0.65	90
	assimilative	3.51	5.69	4.73	0.88	0.68	90
1998-2001	free-run	3.63	5.77	4.67	0.83	0.60	591
	assimilative	3.36	5.77	4.67	0.85	0.64	591

Table 2 – Median statistics based on 1- and 30-day running averages of SSH time series from NCOM and de-meaned tide gauge sea level data in 1998, 1999, 2000, 2001, separately. Median statistics are also given for the 4-year period during 1998-2001. Both data series have had the mean over coincident samples removed. Tide gauge time series have been corrected for the static inverse barometer effect. Results are shown for free-running and data-assimilative  $1/8^\circ$  NCOM simulations. Standard deviations of SSH time series from the tide gauge and NCOM are denoted as  $\sigma_x$  and  $\sigma_y$ , respectively.

Section	Location	Mean	std dev
Gulf Stream 26.6	26.6N, 78.9-80.2 W	25.7	2.2
East of Abaco	26.6N, 75.1-77.2 W	-24.2	11.9
Gulf Stream 29N	29N, 78.4 – 81 W	40.7	9.2
Gulf Stream 31N	31N, 76.7-80.5 W	46.7	11.5
GS-Cape Hatteras	36N,75.3W – 34.7N, 72.6 W	69.9	15.4
Gulf Stream 68W	35.8 – 40.5 N, 68W	61.8	22.5
Gulf Stream 55W	37.5 – 40N, 55 W	81.9	56.8
Florida St 81W	22.9 – 25.2N, 81W	22.2	2.0
NW Prov Chan	25.5 – 27 N, 78.6W	-3.7	1.7
Florida St 25.5N	25.5N, 78.6-80.7W	17.6	1.7
Old Bahama Chan	22 – 23.5 N, 78.6W	0.2	0.5
Yucatan Channel	21.3N,86.7W– 23.2 N, 80.7W	22.2	2.1
Windward Passage	20.3N, 79.4W – 19.5N, 74.4W	-1.2	2.6
Carib Haiti	12.5-18N, 71.6W	-21.0	3.0
Mona Passage	19.5N,68.8W – 18.5N, 67W	-0.9	1.1
Less Antilles PR	10.5-18N, 66W	-20.1	3.2
Leeward Islands	15.3 – 17.5N, 63W	-11.1	2.1
Anegada Passage	18N, 63.1 – 66W	-0.3	1.8
Lessr Antilles A	10.5-17N, 61.7W	-16.0	3.2
Antigua Passage	17N,61.9W – 16.8N,61.7W	-0.5	0.6
Guadeloupe Pass	16.6 – 16.8 N, 61.7W	-3.2	0.9
Dominica	15.7-15.8N, 61.5W	-1.8	0.4
Martinique Pass	15.3N,61.3W – 14.8N,61W	-4.0	1.0
Windward Islands	15.3N, 61W – 10.6N, 61.3W	-6.5	4.1
St. Lucia	14-14.8N, 61W	-1.6	1.2
St. Vincent Pass	13.7N,60.9W – 12.4N, 61.2W	-4.4	2.6
Grenada Passage	12.4N, 61.2W – 11N,61.7W	0.3	1.6
Str of Gibraltar	35.6-36.31N, 6W	0.0	0.2
Davis Strait	63.7N, 64.6W – 66.5N,53.3W	-2.2	0.8
Denmark Strait	64.5N,40.3W – 64.5N, 24.4W	-2.0	1.8
Iceland-Faeroes	64.8N, 12.2W – 62N, 8.3W	1.5	1.3
Hebrides-Faeroes	58-61.7N, 7.6W	1.5	1.7

section	location	mean	std dev
Newfoundland	40-43N,50.1W	-16.3	24.8
St. Johns-Fl Cap	47N,44.9-47.7W	-4.1	1.5
N. Atl. Current	47-58N, 47.7W	24.3	4.4
EUC 35W	-3-2.5N,35W	51.6	28.0
EUC 28W	-3 – 2.5N, 28W	-5.2	32.6
EUC 23W	-3 – 2.5N, 23W	-75.8	10.4
EUC 4W	-3 – 2.5N, 4W	-36.4	11.1
Drake Passage	55.6-67.2S – 68.8 W	163.8	7.0
Atl. Trn. 62.0N	62N, 65.6W – 13.4E	-1.0	1.9
Atl. Trn. 47.0N	47N, 4.8-47.7W	-0.1	2.8
Atl. Trn. 40.0N	40N,5-71.6W	-0.8	2.9
Atl. Trn. 34.0N	34N, 7.6-80.7W	0.0	0.0
Atl. Trn. 27.0N	27N,13.2-80.7W	-1.0	3.2
Atl. Trn. 9.0N	9N,14.6-59.6 W	-1.2	3.6
Atl. Equator	0N, 44.9W – 9.3E	-2.5	3.6
Atl. Trn. 30S	30S,48.6W – 15.9E	-0.3	4.0
Alaska Stream	54.4N, 152.6W – 56.8N, 99.4W	-16.2	8.2
Bering Strait	65.9N, 167.5-172W	0.9	1.0
Pacific EUC	3S-3N, 153.1W	17.1	15.1
Kuroshio 24N	24N, 122-124.6E	22.3	3.3
Kuroshio 135E	13.05 – 34.58N, 135E	78.6	18.3
Luzon Strait	18.5-21.9N, 120.7E	-5.7	2.6
Taiwan Strait	24.5N, 118.3-120.7E	2.0	0.9
Tokara Strait	28.5-30.8N,130E	20.7	3.8
Tsushima Strait	35.1N,129-132.5E	2.6	0.5
Tsugaru Strait	41.3-41.5N, 140.3E	1.7	0.1
Soya Strait	45.3-46N, 142E	0.8	0.3
E China Sea	24.4N,121.6-123.7E	22.3	3.3
South Sulu Sea	6.4N,118.2-120.6E	-3.4	1.5
Aust-Bali	8.8-20.6S, 117E	-14.6	3.2
Ind Throughflow	8.4S,114.1E – 22.1S,112.3E	-20.4	4.9

Table 3 – Mean and standard deviation of 2002 1/8° assimilative Global NCOM transport (Sv) through various straits and sections around the world. Transports are calculated over the full depth of the water column.

Station ID	SWAFS northworld boundary conditions	NCOM/OSU Tides boundary conditions
H350	.9549	.9777
H351	.9222	.9734
H352	.9439	.9741
H354	.9503	.9798
H362	.9716	.9770
H364	.9322	.9513

Table 4 – Correlation coefficients between observed water levels and model hindcast values for the GLOSS stations used above, for the 24 May to 19 July time series. The higher correlations obtained using the NCOM/OSU boundary conditions suggest that the NCOM/OSU boundary condition values do not degrade the tidal height predictions of the SWAFS pacnest configuration.